UNIVERSITAT POLITÈCNICA DE VALÈNCIA
DEPARTAMENTO DE QUÍMICA
INSTITUTO UNIVERSITARIO MIXTO DE TECNOLOGÍA QUÍMICA
(UPV-CSIC)

DOCTORAL THESIS

Photoremovable protecting groups for carbonyl compounds of biological interest

---

Mauricio Lineros Rosa

Supervisors:

Prof. Miguel Ángel Miranda Alonso
Dr. Virginie Lhiaubet-Vallet

Valencia, February 2021

CERTIFICATION

Miguel Ángel Miranda Alonso, full Professor of the Universitat Politècnica de València (UPV) and Virginie Lhiaubet-Vallet, tenured scientist of the Consejo Superior de Investigaciones Científicas (CSIC),

CERTIFY that the Doctoral Thesis entitled "Photoremovable protecting groups for carbonyl compounds of biological interest" has been developed by Mauricio Lineros Rosa under their supervision in the Instituto Universitario Mixto de Tecnología Química (UPV-CSIC).

Prof. Miguel A. Miranda Alonso Dr. Virginie Lhiaubet-Vallet

A mi primo Marcos

Agradecimientos:

La presente tesis doctoral representa el final de una etapa académica repleta de aprendizajes y de muy buenos momentos, por los que he de agradecer a muchas personas que han formado parte de ellos y sin quienes estos no habrían sido posibles.

En primer lugar, me gustaría dar las gracias a mis directores de tesis Miguel Ángel Miranda y Virginie Lhiaubet por haberme brindado la oportunidad de realizar el doctorado y por el gran apoyo que siempre me han ofrecido. Sin duda, a ellos les debo en gran medida el buen recuerdo que me llevo de mi paso por el ITQ.

No sólo he sido afortunado con mis directores sino también con mis compañeros del 11A1: Ofelia, Cristina, Paloma y Óscar. Muchos han sido los buenos momentos compartidos con ellos dentro y fuera del laboratorio. No quisiera tampoco olvidar al resto de integrantes del grupo de fotoquímica: Alice, Rebeca, Gemma, Faber, Jenny, Isa, Juan Antonio, Paco, Marisa, Chelo, Nacho, Inma, Alex, Jorge, Nacho…quienes han puesto color día tras día a las horas de trabajo de estos años.

Igualmente, quiero agradecer a todo el personal del ITQ-CSIC, que de una u otra forma ha contribuido a que mi paso por el instituto haya sido una buena experiencia. Además, me gustaría agradecer a mis amigos del ITQ: Sergio, Miguel, María, Javi, Pilar, Jordan, Ximo, Ferrán, Jose Miguel, Marcos, Iván, Elena, Eva… quienes han formado mi familia valenciana junto con mis compañeros de piso: Mailén, Marquinho, Guille, Elvis, Claudia, Edu y Sergio.

Gracias a mi madre y hermanos por todo el apoyo que siempre me han dado y por alentar la toma de decisiones que me llevaron a comenzar esta etapa. Gracias a los padres y hermano de Bea por siempre acogerme como a uno más de la familia. Por último, quiero darle las gracias a Bea por su apoyo incondicional a pesar de la distancia y por las innumerables horas al teléfono repletas de risas y buenos consejos.

Abbreviations and symbols

[d_6]-DMSO – Deuterated dimethylsulfoxide

$^1O_2$ – Singlet oxygen

^{3}EXC – Triplet exciplex

5hmU – 5-Hydroxymethyluracil

6-4 PP – Pyrimidine (6-4) pyrimidone

8-oxoGua – 8-Oxo-7,8- dihydroguanine

A – Absorption

AB – Avobenzone

AB(E) – Avobenzone in its *enol* form

AB(K) – Avobenzone in its *diketonic* form

AcOEt – Ethyl acetate

AP – Acetophenone

c – Light velocity (3×10^8 m s^{-1})

caC – 5-Carboxylcytosine

CASSCF – Complete-active space self-consistent field

CD_3CN – Acetonitrile

CD_3OD – Deuterated methanol

$CDCl_3$ – Deuterated chloroform

CPD – Cyclobutane pyrimidine dimers

Cy – Cyclohexane

Cyt – Cytosine

D_2O – Deuterated water

DAD – Diode array detector

DBM – Dibenzoylmethane

DCA – Dichloroacetic acid

DCM – Dichloromethane

Dew – Dewar valence

DIAD – Di*iso*propyl azodicarboxylate

DIPEA – *N,N*-Di*iso*propylethylamine

DMF – *N,N*-dimethylformamide

DMFA – (2,4-dimethoxyphenyl)acetic acid

DMT-Cl – 4,4'-Dimethoxytrityl chloride

DNA – Deoxyribonucleic acid

E – Energy

e^-_{aq} – Hydrated electron

ESHT – Excited state hydrogen transfer mechanism

ESI – Electrospray ionization

eT – Electron transfer

E_T – Triplet energy

EtOH – Ethanol

eV – Electronvoltio

F – Fluorescence

FapyGua – 2,6-Diamino-4-hydroxy-5- formamidopyrimidine

FC – Franck-Condon

FDA – Food and drug administration

ForC – 5-Formylcytosine

ForU – 5-Formyluracil

FRET – Förster resonance energy transfer

fs – Femtosecond

GlyThy – 5,6- Dihydroxy-5,6-dihydrothymine

GSHT – Ground state hydrogen atom transfer

Gua – Guanosine

h – Planck's constant (6.626×10^{-34} J s)

hmC – 5-Hydroxymethyl cytosine

HOMO – Highest occupied molecular orbital

HPLC – High-performance liquid chromatography

HRMS – High-resolution mass spectroscopy

HSQC – Heteronuclear Single-Quantum Correlation Spectroscopy

Hz – Hertz

IC – Internal conversion

ISC – Intersystem crossing

IUPAC – International union of pure and applied chemistry

J – Coupling constant

J – Jules

k – Rate constant

KP – Ketoprofen

k_q – Quenching constant

LCAO – Linear combination of atomic orbitals

LED – Light emitting diode

LFP – Laser flash photolysis

LUMO – Lowest unoccupied molecular orbital

M – Molarity

MALDI – Matrix assisted laser desorption ionization

mC – 5-Methylcytosine

MeCN - Acetonitrile

MeOH – Methanol

MNP – 1-Methylnaphthalene

MO – Molecular orbital

MS/MS - Tandem mass spectrometry

N – Avogadro number (6.022×10^{23} mol^{-1})

nm – Nanometer

NMR – Nuclear Magnetic Resonance

NOESY – Nuclear overhauser effect spectroscopy

NPX – Naproxen

ns - Nanosecond

NSAID – Nonsteroidal anti-inflammatory drug

NTO – Natural transition orbital

$O_2^{\bullet-}$ – Superoxide radical anion

ODN – Oligodeoxynucleotides

$OH^{\bullet}$ – Hydroxyl radical

P – Phosphorescence

PABA – *p*-Aminobenzoic acid

PBS – Phosphate-buffered saline

PES – Potential energy surface

PG – Protecting group

Phs – Photosensitizer

PPG – Photolabile protecting group

ppm – Parts per million

ps – Picosecond

Pur – Purine

Pyo – 5-Methyl-2-pyrimidone

Pyr – Pyrimidine

ROS – Reactive oxygen species

s – Second

SIM – Selected ion monitoring

SOC – Spin-orbit coupling

SSET – Singlet-singlet energy transfer

SSL – Simulated sunlight

STC – Singlet-triplet crossing

TBAF – Tetrabutylammonium fluoride

TBDMSCl – *tert*-Butyldimethylsilyl chloride

TD-DFT – Time-dependent density functional theory

THF – Tetrahydrofuran

Thy – Thymine

Thy<>Thy – Cyclobutane thymine dimers

TICT – Twisted intramolecular charge transfer

TL – α-Tetralone

TLC – Thin layer chromatography

TOF – Time of flight

TTET – Triplet-triplet energy transfer

UPLC – Ultra performance liquid chromatography

US – United States

UV – Ultraviolet

UV-Vis – Ultraviolet-Visible

UVA – Ultraviolet A

UVB – Ultraviolet B

UVC – Ultraviolet C

VET – Vibrational energy transfer

VR – Vibrational relaxation

1,5–H – δ-Hydrogen abstraction

Φ – Quantum yield

Φ_S – Topological index

Φ_Δ – Singlet oxygen quantum yield

δ – Chemical shift

λ – Wavelength

λ_{em} – Emission wavelength

λ_{exc} – Excitation wavelength

λ_{irr} – Irradiation wavelength

μs – Microsecond

τ – Lifetime

Summary of chemical compounds

Chapter 3

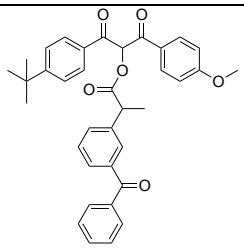

AB-KP

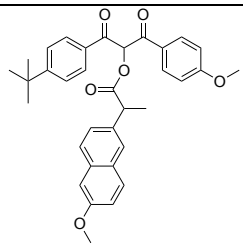

AB-NPX

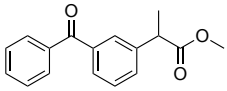

KP-Me

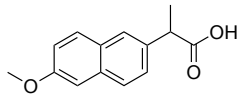

NPX

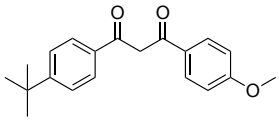

AB(K)

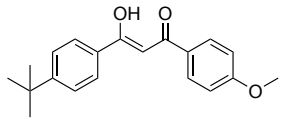

AB(E)

Chapter 4

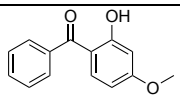

OB

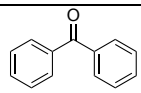

BP

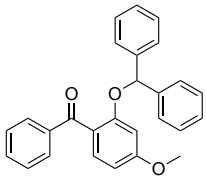

OB-BP

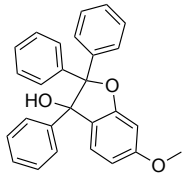

OB-BP-C

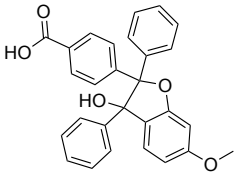

OB-CBP-C

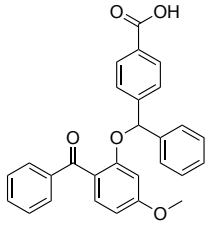

OB-CBP

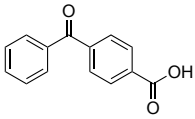

CBP

AP

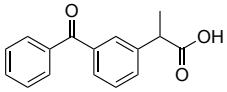

KP

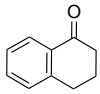

TL

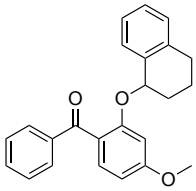

OB-TL

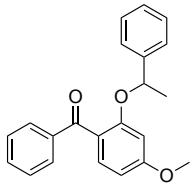

OB-AP

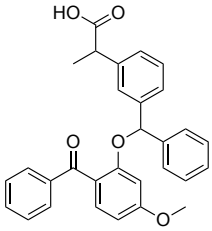

OB-KP

Chapter 5

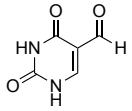

ForU

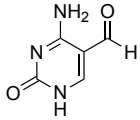

ForC

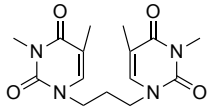

Thy-Thy

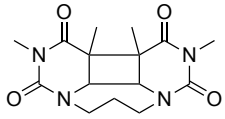

Thy<>Thy

Chapter 6

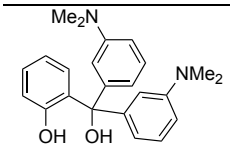

PPG-1

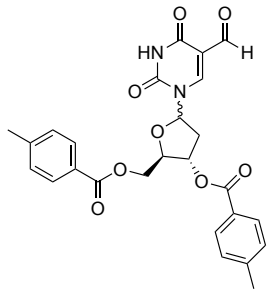

dForU-Tol

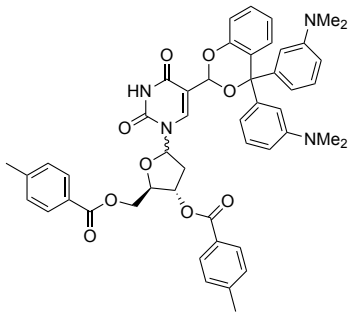

dForU-Tol-PPG-1

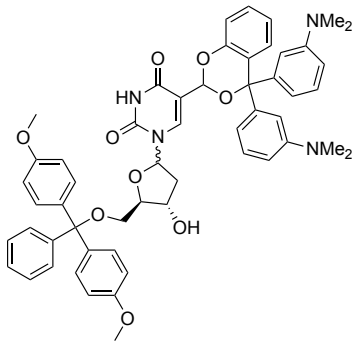

dForU-Trityl-PPG-1

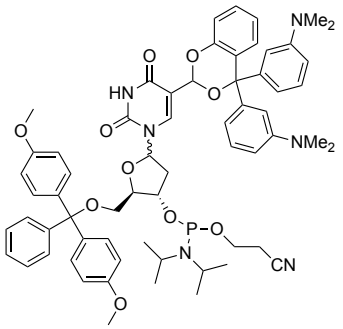

dForU-BB-PPG-1

Outline

Chapter 1:

General introduction

1.1. Introduction to photochemistry

Molecular photochemistry is the branch of chemistry concerned with chemical reactions undergone by photoexcited molecules. In general, after light absorption an electronically excited state is reached from which different processes can happen.[1] Upon absorption of a photon, an electron can be promoted not only from the highest occupied molecular orbital (HOMO) but also from lower energy HOMOs (HOMO-1, HOMO-2, etc) to a higher unoccupied molecular orbital. Molecular orbitals (MO) are formed from linear combination of atomic orbitals (LCAO) and they can be divided into four types: bonding (σ, π), antibonding (σ*, π*), non-bonding (n) and Rydberg orbitals. As a result, molecules can exhibit different kinds of transitions depending on their functional groups. The most common types of electronic transitions, which involve the three first types of the above-mentioned MOs, are represented in Figure 1.1.

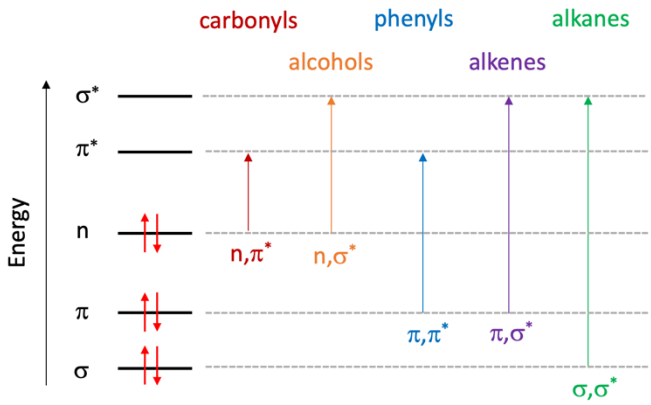

Figure 1.1. Electronic transitions and examples of functional groups where they take place.

Among all possible electronic transitions, the most relevant one is that which takes place from the HOMO to the lowest unoccupied molecular orbital (LUMO), since it is the less energetic transition. Once in an electronically excited state the molecule can relax by photochemical and photophysical processes or can absorb a second photon promoting the population of upper excited states (represented as A_1 and A_2, respectively, in Figure 1.2). This latter process (A_2) occurs in the case of bright excited state which are able to absorb light. The Jablonski diagram (Figure 1.2) summarizes these processes which are classified into non-radiative (vibrational relaxation, internal conversion, intersystem crossing and triplet-triplet energy transfer) and radiative (fluorescence and phosphorescence) processes. In this diagram, the electronic states of a molecule are represented with thick horizontal lines, while thin horizontal lines depict vibrational levels. Each of these vibrational levels can be further divided into rotational levels, however, such level of detail is usually omitted. The electronic states of same multiplicity and different energy are arranged in the same column according to their energies. The straight and curved arrows represent transitions that can occur after exposure of a molecule to light. Straight ones refer to absorption or emission of a photon, whereas curved ones correspond to radiationless transitions.

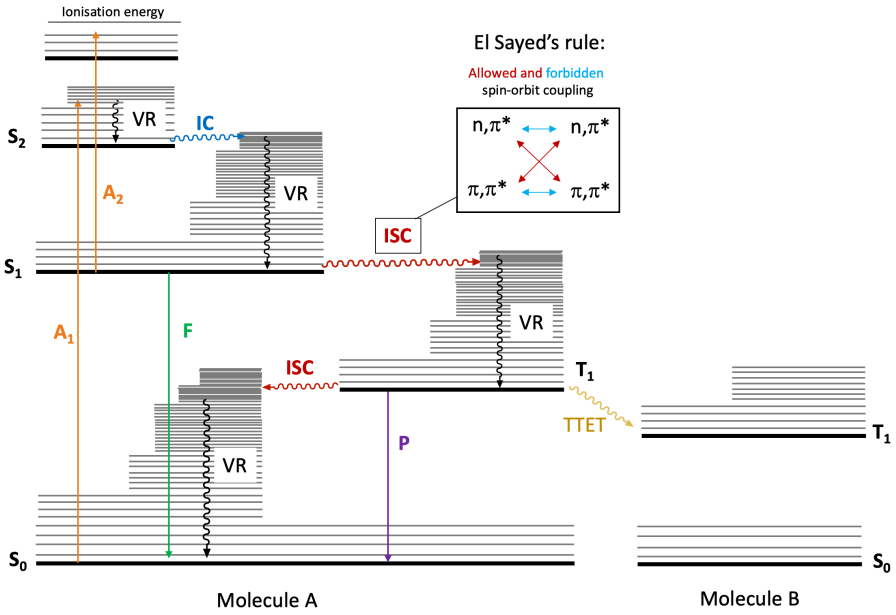

Figure 1.2. Jablonski diagram.

The starting point in a Jablonski diagram is the absorption (A_1) of a photon that promotes an electron from the ground electronic state to an excited electronic state. This transition is called a vibronic transition, since it could happen between any of the vibrational states on each electronic state. Once excited, there are multiple ways by which a molecule can dissipate that energy. One of them is through vibrational relaxation (VR), which releases the energy by means of non-radiative decay processes and occurs between vibrational levels within the same electronic level. Other two processes are fluorescence (F) and phosphorescence (P). Although both involve spontaneous emission of radiation, the first one takes place with retention of spin multiplicity; while the second entails a change in spin multiplicity, and hence, it is a slower process. These two radiative transitions usually happen with an appreciable yield only from the lowest electronic excited state of a

given multiplicity, this statement is known as Kasha's rule. A molecule can also redistribute its energy over vibrational modes of different electronic states by means of isoenergetic transitions. When these transitions take place between states of same multiplicity, they are called internal conversion (IC); while if they involve a change in multiplicity, they are known as intersystem crossing (ISC). These latter transitions are favored when they involve a change of molecular orbital type (El-Sayed's rule). Additionally, interactions between a molecule (A) in an electronically excited state and a second species (B) can take place. Here, triplet-triplet energy transfer (TTET) and electron transfer are two of the most important.

Photochemical processes are always competing with photophysical ones, which tend to bring back the excited molecule to its ground state. Thus, photoreactions can only occur if they are fast enough to compete with photophysical processes. In general, and as an extension of the Kasha´s rule, excited molecules will react with an appreciable yield only from the lowest excited state of a given multiplicity.

All those abovementioned processes play an essential role in many beneficial applications not only in nature (*ie.* photosynthesis, vision or formation of vitamin D) but also in medicine (*ie.* photodynamic therapy or dentistry). Unfortunately, they are also responsible for many harmful effects on living organisms. In this context, photosensitized reactions make a substantial contribution since they can extend the photobiologically active spectrum of solar light beyond UVB radiation. This results in a higher incidence of skin disorders, which can ultimately derive in skin cancer development.

This Thesis focuses on developing new photocages systems for biological applications and on the understanding of their mechanism of action.

This includes: (*i*) the study of new compounds able to release photosensitive agents along with an UV-filter shield and (*ii*) the design of a new methodology based on photoremovable protecting groups for the insertion of potential intrinsic DNA photosensitizers (Phs) in oligonucleotides, *i.e.* the oxidatively generated 5-formylpyrimidines.

1.2. Photolabile protecting groups

As previously mentioned, light plays an important role not only in natural processes but also in several applications developed by humans. Since the beginning, chemists have made use of light in their favor to induce chemical and physical changes that otherwise could not happen.[2] In this context, this section deals with photoremovable protecting groups (also known as photolabile protecting groups, PPGs), which allow using light as an external and non-invasive stimulus for their deprotection in a spatially and temporally controlled manner.

Since the early reports on PPG by Barltrop[3] and Barton[4] in 1962, a large number of photolabile protecting groups have been developed, which have found applications in a huge number of fields as diverse as biology, organic synthesis,[5,6] biochemistry,[7] volatiles release,[8] etc. However, along this section the attention will be focused only on those more related to this Thesis, *i.e.* phenacyl, anthraquinone and salicyl alcohol derivatives.

1.2.1. Phenacyl-like PPGs

The ability of phenacyl groups to act as a PPG for the carboxyl function was first reported in 1973 by John C. Sheehan and Kazuo Umezawa.[9] In their study, the p-methoxyphenacyl and the α-methylphenacyl groups were used for the release of carboxylic acids attached in α-position, which works in good yield in the presence of H-donor solvents, such as ethanol.

From a mechanistic point of view, the photorelease can take place through different pathways depending on factors such as the presence of aromatic ring substituents.[10] For example, in the case of the p-methoxyphenacyl group the mechanism has been demonstrated to occur through an initial intermolecular hydrogen abstraction step (Figure 1.3A).[11] However, when a methyl group is incorporated in position 2, the hydrogen abstraction happens intramolecularly making the deprotection feasible regardless of the presence of H-donor solvents (Figure 1.3B).[12] By contrast, the presence of p-hydroxy group leads the process through a concerted release of the leaving group and the phenolic proton followed by a photo-Favorskii rearrangement (Figure 1.3C).[13]

Nonetheless, a first stage involving the formation of a phenacyl-like triplet state is common to all of them. In this context, the influence on the photorelease process of the relative triplet energy of the phenacyl group with regards to that of its caged compound will be analyzed in Chapter 3. For this purpose, the recently published system based on the dibenzoylmethane derivative avobenzone will be employed.[14,15]

(A) Intermolecular hydrogen abstraction

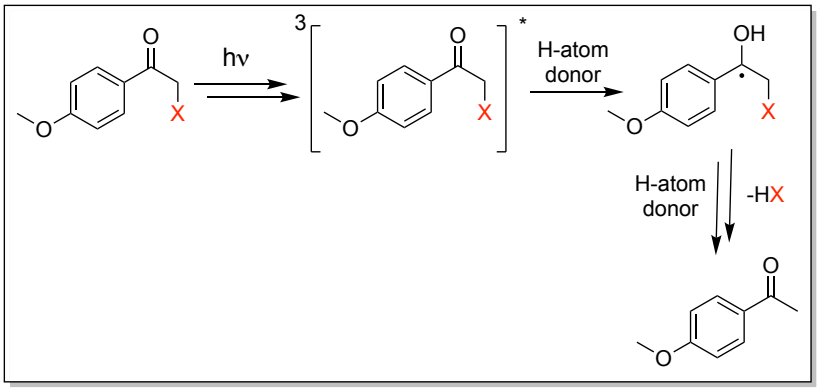

(B) Intramolecular hydrogen abstraction

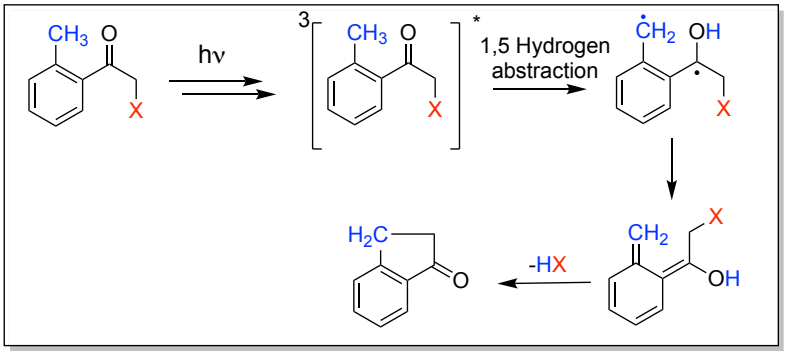

(C) Photo-Favorskii reaction

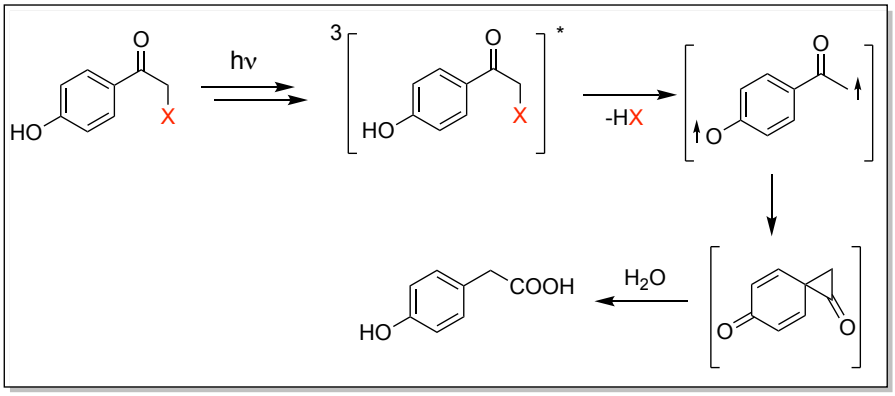

Figure 1.3. Proposed release mechanisms of different phenacyl-like PPGs.

1.2.2. Anthraquinone derivatives

Derivatives of 1-alkoxy-9,10-anthraquinones have been found of great value as PPGs for carbonyl compounds. The first studies were carried out by Blankespoor and co-workers.[16,17] They proposed a mechanism involving a first δ-hydrogen abstraction (1,5-H) followed by electron transfer (eT) that leads to a zwitterion formation, which is then trapped by methanol. Finally, upon oxidation of the formed hydroquinone to anthraquinone, hydrolysis of the acetal or ketal occurs readily affording the desired aldehyde or ketone, respectively (Scheme 1.1).[18]

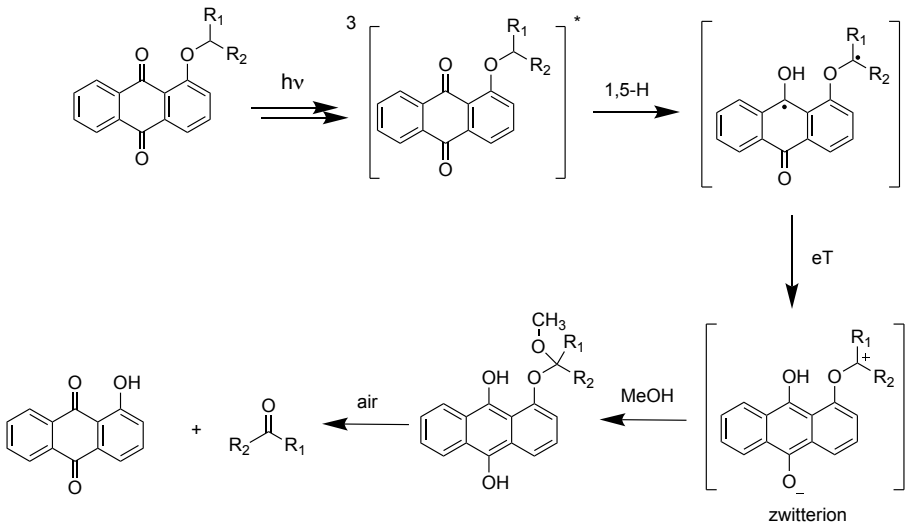

Scheme 1.1. Proposed mechanism for the photorelease of ketones and aldehydes from 1-alkoxy-9,10-anthraquinone derivatives.

These anthraquinone derivatives have found utility on applications as diverse as synthesis of biologically active aldehydes[19], solid-phase synthesis[20] and functional perfumery.[21,22]

Inspired by these studies, a novel photoremovable carbonyl protecting group based on oxybenzone solar filter, and sharing structural similarities, is presented in Chapter 4

1.2.3. α,α-Diaryl salicyl alcohol derivatives

Another photolabile carbonyl protecting group is based on the α,α-diaryl salicyl alcohol backbone and was first introduced by Pengfei and co-workers.[23] In their work, they proposed a photorelease mechanism involving a zwitterionic intermediate as depicted in Scheme 1.2.

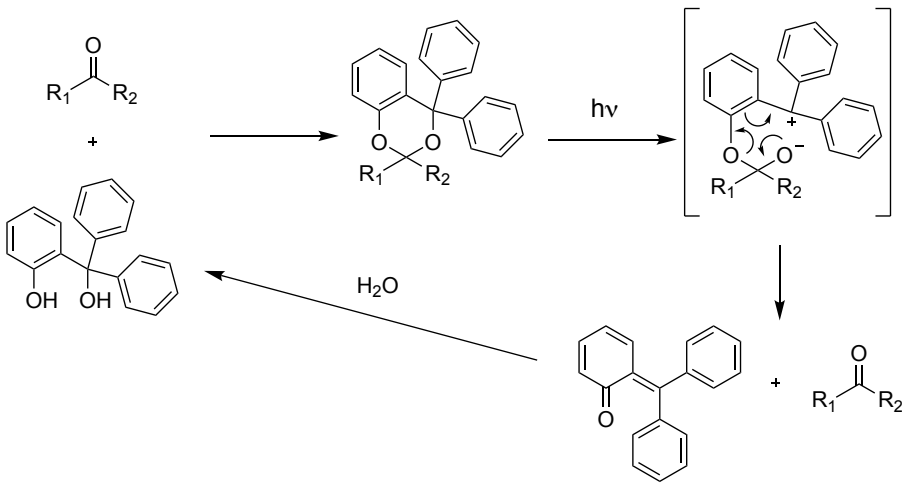

Scheme 1.2. General mechanism for the photorelease process from α,α-diaryl salicyl alcohol derivatives.

Further efforts have been made on these PPGs in order to optimize their caging conditions,[24] as well as their photochemical and photophysical

properties. In this respect, introduction of substituents at different positions of the aromatic rings makes it possible to improve their deprotection efficiencies and to tune their absorption spectra, thus enabling their sequential deprotection by controlling the irradiation wavelength.[25,26]

These PPGs have already been used in drug delivery and in multi-steps synthesis.[27,28] Their robustness to acidic condition together with their efficient caging and photouncaging yields confers them appropriate properties for the new application in the synthesis of modified oligonucleotides presented in Chapter 6.

1.3. Discovering the dark side of the light

The solar spectrum that reaches the Earth´s surface is comprised of ultraviolet, visible and infrared radiation. The ultraviolet radiation was discovered in 1801 by Johann Wilhem Ritter[29], and along the 19th century further studies were published regarding the ability of sunlight to trigger skin adverse effects by mechanisms different from simple burns.[30–32] Although Charcot, in 1858, reported that UV radiation produced by electric arcs was able to produce conjunctivitis and skin erythema, it was Widmark, in 1889, the first scientist to experimentally prove that UV radiation coming from sunlight is responsible for the observed harmful effects. Since then, a huge number of works have been reported regarding the radiation noxious impact (especially in the UV range) on biological components.

The UV radiation is divided into three regions: UVA, B and C. Fortunately, UVC (200-290 nm), which is the most energetic, is completely filtered by the atmosphere. On the other hand, the UVB (290-320 nm) represents approximately 5% of the total UV energy that reaches the Earth´s

surface, and the remaining 95% corresponds to UVA radiation (320-400 nm). The former can be directly absorbed by biomolecules triggering photochemical reactions that can lead to cellular damages. Conversely, UVA is not directly absorbed, but it can activate other molecules called photosensitizers that can, in turn, react with the biological components. Interestingly, since UVA is not directly absorbed by biomolecules, it can reach a deeper portion of the dermis (Figure 1.4). Thus, from a photobiological point of view, ultraviolet light is considered as the most photobiologically relevant part of sunlight since it can interact with biomolecules by direct and indirect mechanisms.

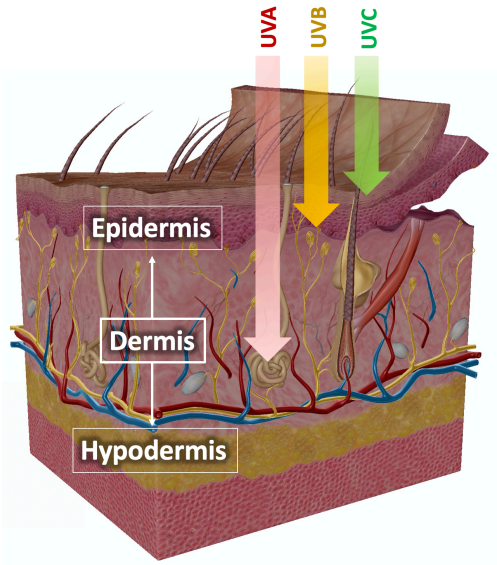

Figure 1.4. Schematic representation of the UV light penetration into the skin.

1.3.1. Direct and indirect interaction of light with biomolecules

Direct or indirect absorption of light by biological components can lead to the formation of damages on them. Here, these processes are summarized, paying particular attention to their consequences for DNA damage.

1.3.1.1. Direct absorption

For most of the biological components, damages resulting from direct absorption of sunlight are mainly due to the UVB part of its electromagnetic spectrum. In this respect, chemical modifications produced on DNA molecules are of particular interest due to their potential mutagenicity. UVB photons are directly absorbed by DNA bases producing two major modifications that involve pyrimidine bases: cyclobutane pyrimidine dimers (CPD) and pyrimidine (6-4) pyrimidone (6-4 PP) photoproducts. These lesions have been found in cellular DNA, on average, in a 3:1 ratio[33]; however, these values may vary depending on the employed assay.[34,35] CPDs results from a [2+2] photocycloaddition between the C5-C6 double bond of two adjacent pyrimidine bases, giving rise to a cyclobutane ring. A Paterno-Buchi photoreaction is at the origin of the formation of 6-4 PP. It consists of a formal [2+2] cycloaddition between the C5-C6 double bond of the 5'-end pyrimidine base and the C4 carbonyl group (or imine group) of a 3'-end thymine (or cytosine). This finally results in the formation of a new covalent bond between the C6 and C4 of two adjacent pyrimidine bases. Furthermore, 6-4 PP can further turn into its Dewar valence (Dew) isomer after absorption of a second photon (Scheme 1.3).[36–38]

After direct absorption of UVB photons, the CPDs formed between two Thy (Thy<>Thy) or a 5'-Thy and 3'-Cyt (Thy<>Cyt), and the 6-4 PP resulting from reaction between 5'-Thy and 3'-Cyt (Thy(64)Cyt) have been

found as the major bipyrimidine photoproducts being in a ratio of 2:1:1, respectively.[39,40] Interestingly, the relative formation of these photoproducts is similar regardless of whether isolated or cellular DNA is irradiated. Direct UVC and UVB irradiation of DNA also induces photooxidation of 2´-deoxyguanosine (dGuo) and formation of 8-oxo-2´-deoxyguanosine (8-oxodGuo) (Scheme 1.3).[41] The proposed mechanism points toward the involvement of the guanine radical cation generated through photoionization of the nucleobase, as expected from the ionization potential of 2´-deoxyguanosine that is the lowest among the DNA bases.

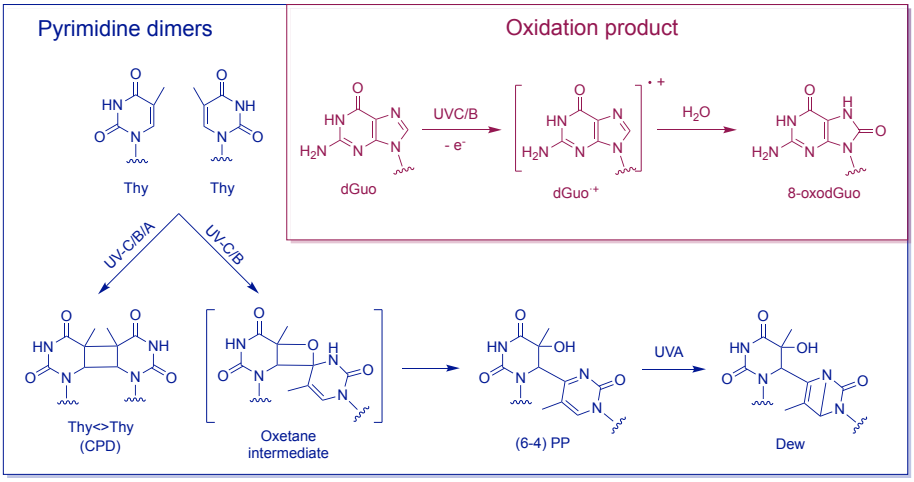

Scheme 1.3. DNA damages obtained by direct UV light absorption.

Regarding the UVA radiation, DNA or oligonucleotides present a very weak absorption in this region, with a molar absorption coefficient lower than 10 M^{-1} cm^{-1}, which has been reported and assigned to the effect of base stacking along the double-stranded structure.[42] In this context, the only lesions are CPDs (mainly Thy<>Thy)[43,44] and, although 6-4PP have not been

evidenced, it is noteworthy that UVA photons play an important role in their conversion to their Dewar valence isomers.[45,46]

1.3.1.2. Indirect light absorption

Even if light is not directly absorbed by the biomolecules, it can generate lesions through a photosensitization process. The IUPAC Gold Book defines photosensitization as "a process by which a photochemical or photophysical alteration occurs in one molecular entity as a result of initial absorption of radiation by another molecular entity called a photosensitizer". This definition, from a more medical point of view, is described as an enhanced skin sensitivity to radiation emitted from the sun and from other light sources. These unusual reactions are triggered by harmless light doses in combination with photosensitizers (such as drugs, skin care products, porphyrins, etc).

The first study describing the ability of a molecule to act as a photosensitizer was carried out in 1899 by a student of Tappeiner named Raab who showed that acridine has the ability to sensitize protozoans, such as paramecia, using sunlight transmitted through a window-glass.[47] Raab´s work triggered many studies that revealed the ability of other dyes (like eosin) to photosensitize cells. Ultimately, these findings not only led to the development of the current photodynamic therapy, which takes advantage of light to eliminate cancerous or precancerous cells, but also allowed a better understanding regarding the development of certain skin conditions like hydroa aestivale.[47]

Many studies have been run to establish the mechanisms involved in the photoreactivity of sensitizing compounds with biomolecules. Next, a summary of these photoreactions is presented paying special attention to their

effect on DNA components. These reactions are generally classified into three main types of processes: (*i*) Type I photoreactions, which involve mainly the formation of neutral or ionic radicals (*ii*) Type II processes that refer to energy transfer from the photosensitizer towards molecular oxygen to yield singlet oxygen, a reactive oxygen species (ROS), and (*iii*) triplet-triplet energy transfer to biological components with triplet states of lower energy (see Scheme 1.4).

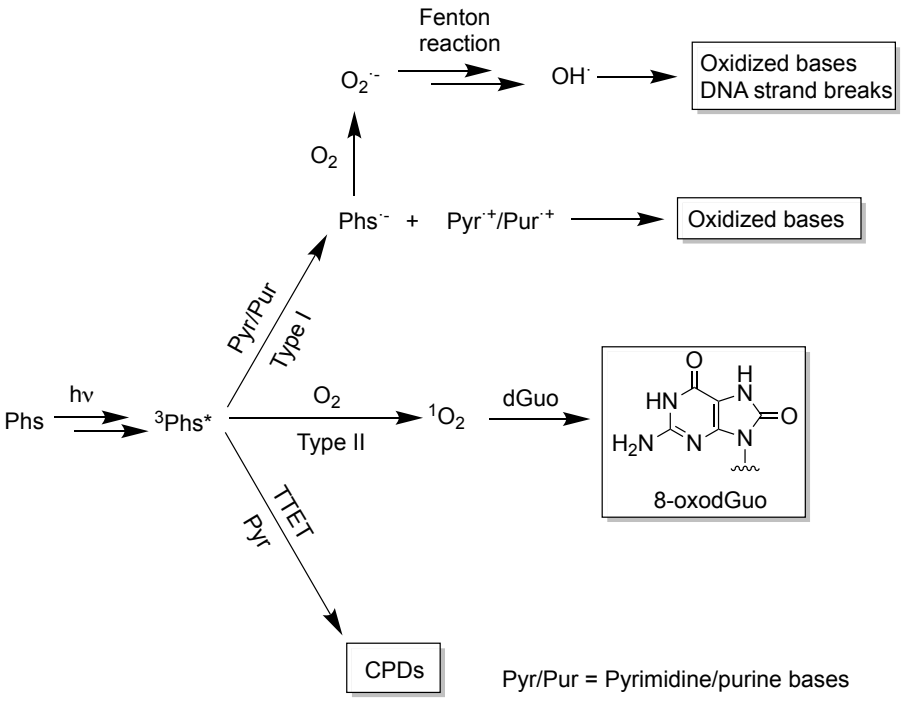

Scheme 1.4. General representation of the photosensitized mechanisms and their main effects on DNA.

1.3.1.2.1. Type I reactions

Type I processes involve the formation of neutral or ionic radicals as products of H-abstraction or electron transfer, respectively. Hydrogen abstraction by carbonyl groups have been abundently studied, being one of the most fundamental reactions in organic photochemistry. Generally, this reactivity takes place from the triplet state. The reactivity of carbonyl groups towards hydrogen donors depends on the electronic configuration of the lowest triplet excited state (n,π* or π,π*), with the ketones having n,π* as their lowest triplet excited state being the most reactive. During this reaction, an excited carbonyl compound abstracts a hydrogen from a donor to form a ketyl radical, which subsequently may abstract a second hydrogen from the media or recombine to form either alcohols or diols (Scheme 1.5).

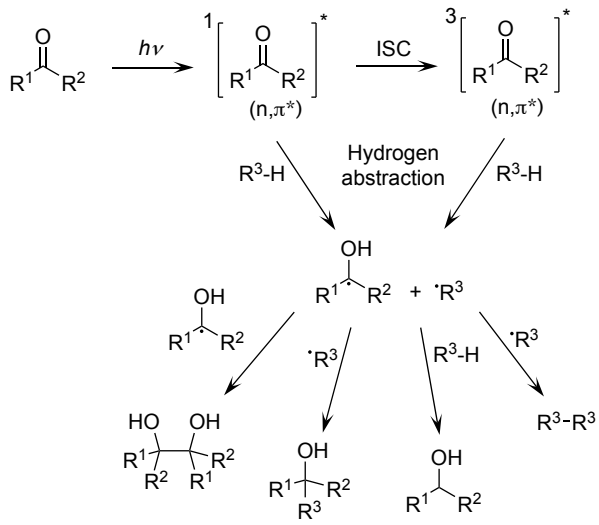

Scheme 1.5. Possible products obtained by hydrogen abstraction from carbonyl compounds.

However, with DNA bases the predominant process is the one-electron oxidation, which is favored in the case of guanines as they have the lowest ionization potential among the nucleobases.[48] The radical cation of guanine ($Gua^{\cdot+}$) can further react with water giving the 8-hydroxy-7,8-dihydroguanyl radical that can be finally transformed into 8-oxo-7,8-dihydroguanine (8-oxoGua) or 2,6-diamino-4-hydroxy-5-formamidopyrimidine (FapyGua) by means of competitive one-electron oxidation and one-electron reduction, respectively (Scheme 1.6).[33] Additionally, radical cation of deoxyguanosine can also suffer a hydrogen abstraction at the anomeric carbon giving rise to formation of an abasic site.[49]

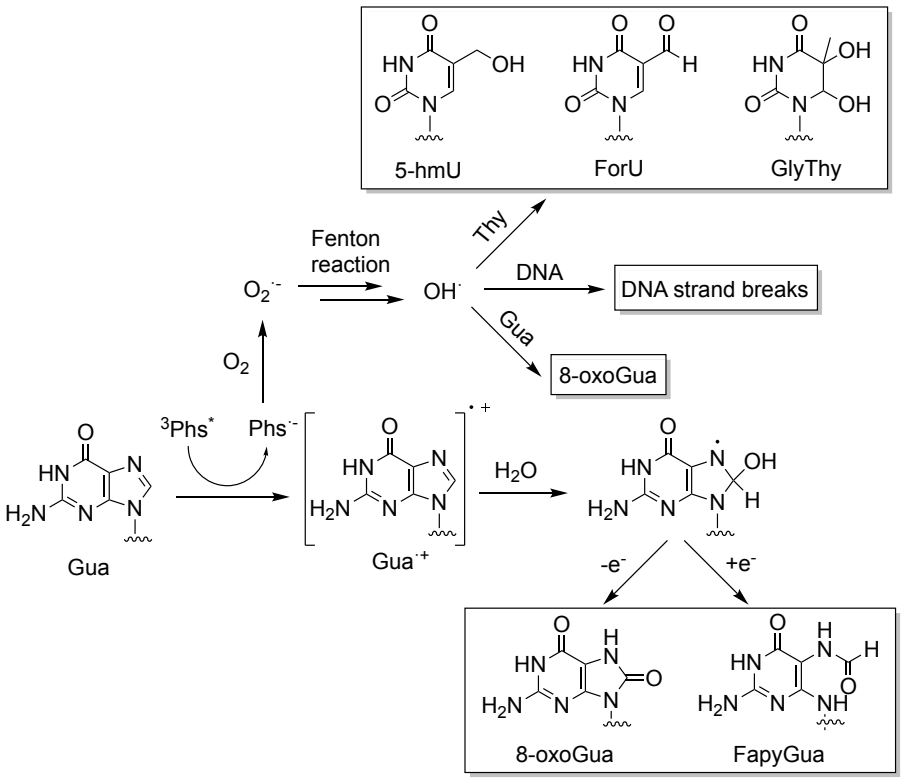

Scheme 1.6. Different types of oxidatively generated DNA damages triggered by photosensitized Type I processes.

On the other hand, the radical anion of the photosensitizer ($Phs^{\cdot -}$) can react with molecular oxygen (O_2) yielding superoxide radical anion ($O_2^{\cdot -}$) that can be finally converted into $OH^{\cdot}$ through $O_2^{\cdot -}$ conversion into H_2O_2 by superoxide dismutase enzyme and its further reduction by Fe^{2+} (Fenton reaction). $OH^{\cdot}$ also reacts with DNA bases, but in this case, it leads to the unselective formation of oxidized purine and pyrimidine. As a result, $OH^{\cdot}$ can give rise to DNA strand breaks,[50] to guanine oxidatively generated products such as 8-oxoGua and FapyGua, and to other pyrimidine products like 5,6-dihydroxy-5,6-dihydrothymine (GlyThy), 5-hydroxymethyluracil (5hmU) and 5-formyluracil (ForU) (Scheme 1.6).[51,52]

1.3.1.2.2. Type II reactions

Type II processes refer to reactions derived from singlet oxygen ($^1O_2$) production. This species is classified as a reactive oxygen species (ROS) and is obtained by energy transfer from an excited photosensitizer (generally in its triplet excited state) to O_2. Molecular oxygen has a triplet configuration in its ground state, being a paramagnetic biradical with two electrons of parallel spin that are placed in separate π^* orbitals (Figure 1.5). Due to its electronic configuration, oxygen has to react with other molecules accepting two electrons with the same spin. For this reason, ground-state oxygen is unable to efficiently oxidize biomolecules. By contrast, singlet oxygen is much more reactive since the spin restriction is removed. In consequence, this species can easily oxidize biomolecules such as fatty acids, proteins and DNA.[53]

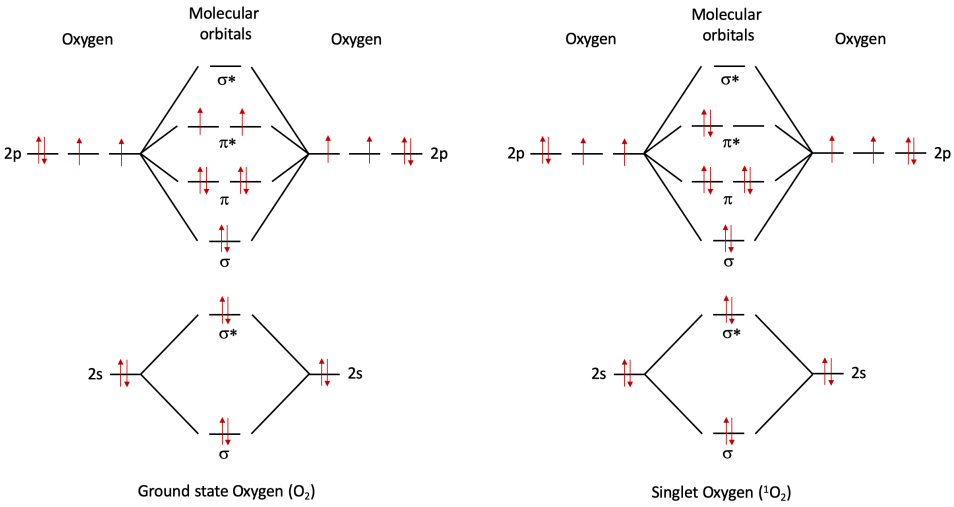

Figure 1.5. Molecular orbital diagrams of ground-state molecular oxygen ($O_2(^3\Sigma_g^-)$, denoted as O_2) and of first excited state molecular oxygen ($O_2(^1\Delta_g)$, denoted as $^1O_2$).

In the DNA environment, $^1O_2$ selectively reacts with dGuo leading to its major oxidative product, 8-oxodGuo.[54]

1.3.1.2.3. Triplet-triplet energy transfer

The energy transfer process allows excitation of a molecule at a wavelength where it does not absorb light. It is a process of paramount importance in nature, as photosynthetic organisms make use of it to transport the energy captured by the chlorophyll antenna. The energy transfer process can be expressed, in a general way, following eq. 1.1.

$$D^* + A \rightarrow D + A^* \quad (1.1)$$

Where D^* represents the energy donor, which transfers its energy to a neighboring acceptor molecule A. For this process to be favored, the energy of the donor (D^*) in its excited state has to be higher than that of the acceptor (A^*). The overall process generally occurs between excited states having the same multiplicity, *i.e.* singlet-singlet energy transfer (SSET) or a triplet-triplet energy transfer (TTET). As it is the case for emission and photochemical processes, the energy transfer takes place from the lowest singlet or triplet excited state.

Energy transfer processes can be divided into two different types: radiative and non-radiative processes.[55] On the one hand, radiative energy transfer, also known as trivial energy transfer, involves the emission of a photon by the donor molecule (D^*), which is absorbed by the acceptor molecule (A). Therefore, the emitter (D*) and the energy acceptor (A) can be in a different container.

On the other hand, non-radiative processes are classified as two types: Förster and Dexter mechanisms. The Förster resonance energy transfer (FRET) occurs by means of a dipole-dipole coupling, and requires a good overlap of the donor emission and acceptor absorption spectra. An important characteristic of this energy transfer mechanism is that its efficiency is inversely proportional to the sixth power of the distance between donor and acceptor, which makes this process highly distance dependent. Nevertheless, its effectiveness has been reported for “long” distances between donor and acceptor up to 100 Å. As a result, FRET is widely used to measure the dynamics of biological molecules within the nanoscale.

Dexter mechanism involves an energy transfer by electron exchange, and as a consequence, this mechanism requires an appreciable overlap between the molecular orbitals of D and A. The reaction rate constant

exponentially decays as the distance between A and D increases. Thus, the exchange mechanism is known as the short-range energy transfer and it typically occurs within 10 Å. By contrast with FRET, it can give rise to both SSET and TTET.

TTET processes to DNA bases lead to the formation of CPDs. In this reaction the relative energies of the photosensitizer, which acts as the donor (D), and of the nucleobases, which are the acceptors (A), are key.[56,57] In this sense, thymine is the major target since it is the base with lower triplet energy. It has been established that the triplet energy threshold for a Phs to photosensitize CPDs in DNA is of *ca.* 270 kJ mol^{-1}.[58]

1.3.1.2.4. Exogenous and endogenous photosensitizers

Along the years numerous photosensitizing compounds have been reported.[59–62] Here, the attention is focused on exogenous and endogenous chemicals in close connection with the investigation developed in this Doctoral Thesis. In this context, photochemical/photobiological properties of benzophenone-derived nonsteroidal anti-inflammatory drugs (NSAIDs) are reported, in the first section, to illustrate the case of exogenous photosensitizers, while endogenous photosensitizers are addressed through the example of DNA lesions, since some of them have been reported to act as intrinsic photosensitizers, a concept styled as “Trojan Horse” effect.

Exogenous photosensitizers

Due to contemporary lifestyle, we are continuously exposed to an increasing number of xenobiotics like drugs, perfumes, cosmetics or

sunscreens. Their presence in the skin in combination with light (from sunlight or artificial sources) results in an increasing number of cases dealing with clinical photosensitization. These side effects are generally classified as photoallergic or phototoxic, being these latter the most predominant. Hence, it is of outmost importance to get knowledge about the photosafety profile of new xenobiotics before their commercialization in order to determine if risk minimization measurements are needed to avoid adverse effects. In this sense, the International Conference on Harmonization of Technical Requirements for Registration of Pharmaceuticals for Human Use (ICH) established the ICH S10 guideline.[63] This document discusses the existing nonclinical and clinical photosafety tests to evaluate drug phototoxicity and photoallergy and provides international standards for photosafety assessment. So far, the most widely used in vitro assay for phototoxicity is the 3T3 neutral red uptake, which compares the cytotoxic potential of the considered chemicals to Balb/c 3T3 mouse fibroblasts in the presence or in the absence of UV light.[64] However, in spite of its usefulness, it only reveals the phototoxic potential of the compound without informing on other undesired side effects such as photoallergy, photomutagenicity, etc. Thus, other *in vitro* methods, like the use of reconstructed human skin models, are needed to test final clinical formulations.

Additionally, a detailed knowledge about drug photophysical and photochemical properties is important in order to understand the molecular basis of their adverse effects. In this sense, benzophenone (BP) derivatives, such as some of the nonsteroidal anti-inflammatory drugs (NSAIDs), are well known for their strong photosensitizing properties.[65] Among them, ketoprofen (KP) has been widely reported in the medical literature and has been mainly associated to photosensitive effects.[66–70] These adverse effects are in close connection with the photophysical properties of their parent benzophenone:

(i) UV light absorption up to 360 nm, (ii) intersystem crossing quantum yield close to unity, (iii) lowest triplet excited state (*ca.* 290 kJ·mol^{-1}) of n,π* nature, (iv) singlet oxygen quantum yield (Φ_Δ) of *ca.* 0.3. Thus, KP (as its parent compound BP) is able to photoinduce CPD formation through TTET mainly towards thymine, which is the base with the lowest triplet energy value.[71] In this context, after irradiation of calf thymus DNA in the presence of BP, Thy<>Thy, 5'-Cyt<>Thy-3' and 5'-Thy<>Cyt-3' are formed in a distribution of 1:0.23:0.25, respectively.[72] Moreover, oxetanes formation through a Paterno-Büchi is also competing with TTET, being the contribution of the latter higher in DNA environment because of the thymidine triplet energy stabilization. Indeed, oxetanes between carbonyl-derived Phs and thymine have only been characterized in the case of isolated nucleosides,[73] or when the carbonyl compound is covalently inserted in the DNA structure.[74] Besides, KP (as well as BP) is also able to oxidize both purine and pyrimidine[75,76] bases through one electron transfer mechanism, this process being favored for dGuo since it is the nucleobase with the lowest oxidation potential. The nature of the one electron oxidation process has been studied by laser flash photolysis (LFP) and steady-state photolysis experiments.[77] BP has also shown the ability to oxidize thymine by formal hydrogen abstraction at the C-5,[78] and to produce $^1O_2$, which in turn reacts with guanine affording 8-oxodGuo.

Due to all the above, the development of new strategies is of paramount importance to counteract the adverse effects derived from the use of benzophenone derived xenobiotics. In this connection, in Chapters 3 and 4, the use of sunscreen-based photocage systems based on avobenzone (AB) and oxybenzone (OB) is developed for the photorelease of the mentioned UV filters along with carbonyl compounds (like BP and acetophenone derivatives), with the goal of avoiding their known photoreactivity.

Endogenous photosensitizers

In our organism there are numerous molecules that can act as endogenous photosensitizers. Among them, pterins, which are a family of heterocyclic compounds, are known to be capable of photoinducing oxidation of some biomolecules such as DNA.[79–82] Melanin has also been reported to play an important role as a DNA photosensitizer increasing the risk of developing melanoma.[83] Porphyrins and flavins are also recognized endogenous photosensitizers.[84–87]

Moreover, our group has shown that some DNA damages could behave as endogenous photosensitizers inducing chemical changes in their proximity, leading to the generation of multiple lesions (cluster lesions). In this process, a first irradiation gives rise to the formation of the DNA lesion, which is able to absorb in the UVA and act, after a second excitation, as an intrinsic photosensitizer generating more damages in its neighborhood (Figure 1.6). This has been named "Trojan horse" concept.[84]

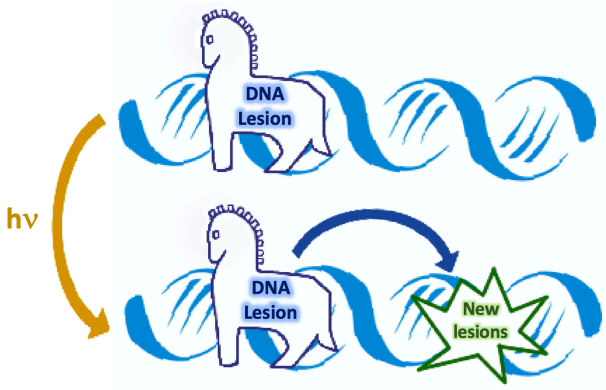

Figure 1.6. Representation of the "Trojan horse" concept.

The first reported example of Trojan horse has been that of the 6-4 PP.[84] Indeed, the presence of the 5-methyl-2-pyrimidone (Pyo) chromophore in 6-4 PP, with an absorption band centered at 320 nm, which allows UVB/UVA irradiation, is the main responsible for its photosensitizing properties. Moreover, its triplet excited state, with an energy (E_T *ca.* 297 kJ mol^{-1}) higher than that of thymine in DNA, is efficiently formed (ϕ_{ISC} *ca.* 0.86). Under UVA irradiation, formation of singlet oxygen and of hydroxyl radical has also been evidenced. These photochemical properties are in line with the DNA damages observed after UVA irradiation of Pyo and 6-4PP in the presence supercoiled circular DNA, which have shown their ability to induce DNA lesions, such as. oxidatively generated damage and cyclobutane pyrimidine dimers.[85,86] Moreover, a recent study goes a step further by studying intrinsic 6-4PP, obtained by pre-irradiating DNA with UVB. However, no significant differences were detected in the yields of CPDs induced by UVB or mixed UVB/UVA irradiation, whereas photoisomerization of 6-4PP into their Dewar valence isomers is very efficient. The authors concluded that 6-4PP-mediated TTET does not significantly contribute to UV-induced DNA damage.[87]

Similar studies were run with 5-formyluracil (ForU), an oxidatively generated lesion of thymine generated through endogenous or exogenous processes. As in the case of 6-4PP, ForU fulfils the photophysical requirements to act as an efficient photosensitizer with the efficient formation of an energetic triplet excited state able to photoinduce formation of both thymine-thymine and cytosine-cytosine CPDs (Thy<>Thy and Cyt<>Cyt, respectively) in model systems and plasmid DNA.[88]

The presence of intrinsic photosensitizers represents a threat for the integrity of the DNA molecule as it can lead to the formation of multiple damage sites, such as cluster lesions, that signify a challenge for the DNA

repair machinery. In this context, it is important to map the known DNA photolesions to establish their potential to act as Trojan horses. Moreover, a clear evaluation of their intrinsic photosensitizing potential should be obtained through their insertion in oligonucleotides of different sequences. However, synthesis of oligonucleotides containing 6-4PP and ForU is not straightforward and requires new developments (see Chapter 6).

1.4. Solar filters

For all those abovementioned reasons, it is important to choose an appropriate photoprotection in order to minimize the adverse effects caused by UV light exposure. In this sense, different actions can be taken, such as avoiding sun exposure around noon, wearing clothing and sunglasses, and using sunscreens. The latter ones are especially useful in some daily situations that involve a greater sun exposure during professional or recreational activities.

Ultraviolet filters are the active ingredients in sunscreen formulations and they can be classified as physical or chemical depending on their nature. Physical filters are inorganic compounds that mainly act by scattering and reflecting the light. On the other hand, chemical filters, which are the most widely used, are organic compounds able to absorb light. However, there are some common desirable properties among them, *i.e.* provide protection against UVA/B radiation and being photostable and non-toxic.

Concerning the approval of UV filters in cosmetic formulations there is not a global criterion. For example, in the United States of America (USA), it is regulated by the Food and Drug Administration (FDA), whereas in Europe it is ruled by the European Cosmetic and Perfumery Association

(Colipa).[89,90] Then, some UV filters such as ethylhexyl triazone or bisoctrizole are allowed for their use in sunscreens formulations in Europe, while in the US they are only allowed in personal care products and cosmetics but not in sunscreen products.[91] Figure 1.7 shows the classification of the UV filters that are currently approved for their use in Europe.

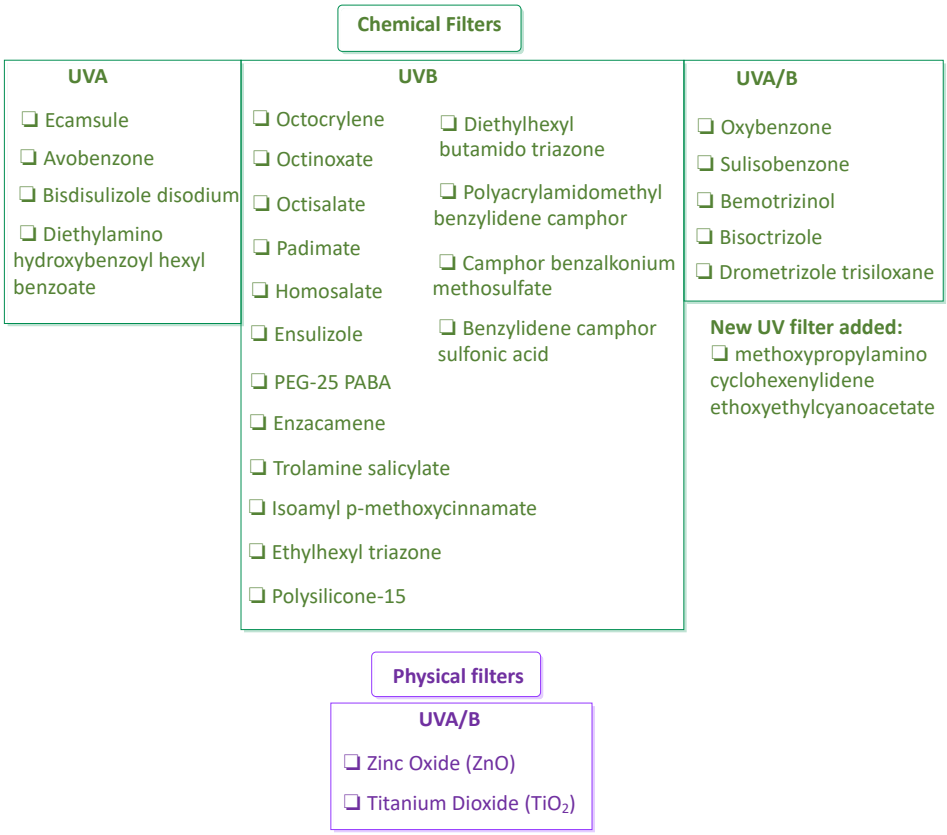

Figure 1.7. Ultraviolet filters currently approved in Europe and their classification according to their UV protection.

Chemical filters are classified into different groups based on their molecular structure, which makes special sense since their properties vary

accordingly. In this context, both the absorption spectra and the nonradiative relaxation pathways of UV filters can be understood based on their structures. These relationships for four of the most common classes of sunscreens are illustrated below.

The p-aminobenzoic acid (PABA) derivatives, like the currently approved ethylhexyl triazone, have an electron donating group in *para* position to an electron accepting group. As a result, after absorption of a photon an efficient electron delocalization takes place (Figure 1.8) responsible for its absorption around 290 nm.[92] Besides, this structural configuration allows its deactivation through a twisted intramolecular charge transfer (TICT).[93] The use of PABA in cosmetics has been forbidden due to its photosensitizing properties (allergic contact dermatitis).[94,95]

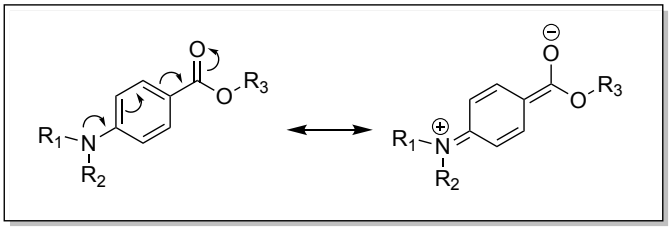

Figure 1.8. Charge transfer in a PABA molecule.

Cinnamates, as PABA, possess electron donor and acceptor groups in *para* positions. However, in this case an added double bond between the phenyl and the caboxyl group results in an extended conjugation (Figure 1.9), which causes a redshift of the absorption maximum. Moreover, the presence of this additional double bond is also responsible for photoisomerization

between the cis (*Z*) and trans (*E*) isomers, which plays an important role in the relaxation from its excited state.[96,97]

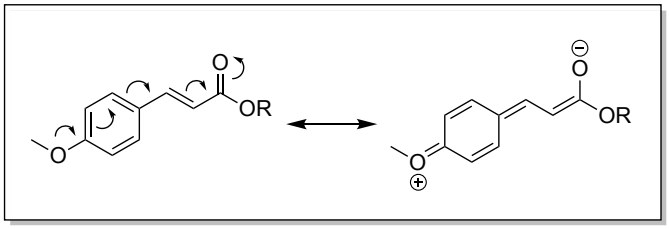

Figure 1.9. Charge transfer in a cinnamate molecule.

Dibenzoylmethane (DBM) derivatives have been extensively used in cosmetic industry, being avobenzone (AB) the most employed UVA filter by far. In the ground state, AB exhibits a *keto-enol* equilibrium, being the *enol* tautomer, AB(E), the most stable species and responsible for its strong UVA absorption (Figure 1.10A). However, after light absorption it undergoes a photoisomerization to its *keto* tautomer, AB(K), which exhibits an absorption maximum at *ca.* 260 nm, thus, losing its efficacy as a sunscreen. In the dark, the *enol* form is recovered by thermal tautomerization.[98]

After UVA excitation of AB, a vibrationally excited chelated *enol*, $AB(CE)_{vib}$*, and three different nonchelated AB isomers, AB(NCE1-3), are formed (Figure 1.10B). These relax on an ultrafast time scale with the exception of AB(NCE1) that persists far longer.[99] Besides, the AB(E)-AB-(K) phototautomerization has been suggested to occur favorably through the geometry of AB(NCE1), though, this intermediate can be stabilized in protic solvents preventing such isomerization. In this context, the photoreactivity of AB has been found to be solvent dependent, being photolabile in nonpolar

solvents, whereas in polar protic solvents it is essentially photostable.[100] The photostability in this latter case is attributed to a fast proton exchange mechanism *via* intermolecular hydrogen bonding with the solvent molecules.[101]

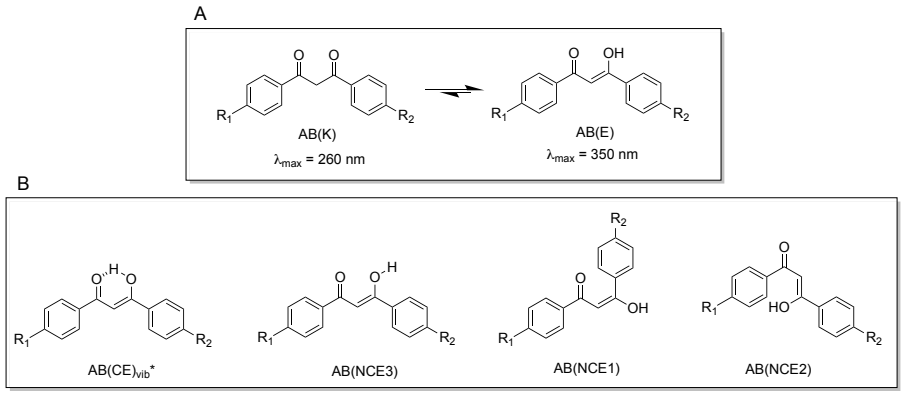

Figure 1.10. Tautomeric equilibrium of avobenzone (A) and the structures of the vibrationally excited chelated *enol*, $AB(CE)_{vib}$*, and nonchelated isomers, AB(NCE1-3), obtained after excitation of avobenzone (B). R^1 = -OCH_3 and R^2 = -$C(CH_3)_3$ and *vice versa*.

Photodegradation through AB(K) tautomer involves bond cleavage at alpha position of the carbonyl group (Norrish Type I process) from its triplet state (^{3}AB(K)*) followed by radical recombination or H abstraction and/or oxidation (Scheme 1.7).[102,103] Besides, ^{3}AB(K)* is also able to generate singlet oxygen which can react, in turn, with AB(E) leading to oxidative products.[104] To overcome its photoinstability, AB is usually formulated with other additives, such as solar filters[105] and antioxidants,[106,107] which can act through mechanisms that include quenching of ^{3}AB(K)* and singlet oxygen quenching

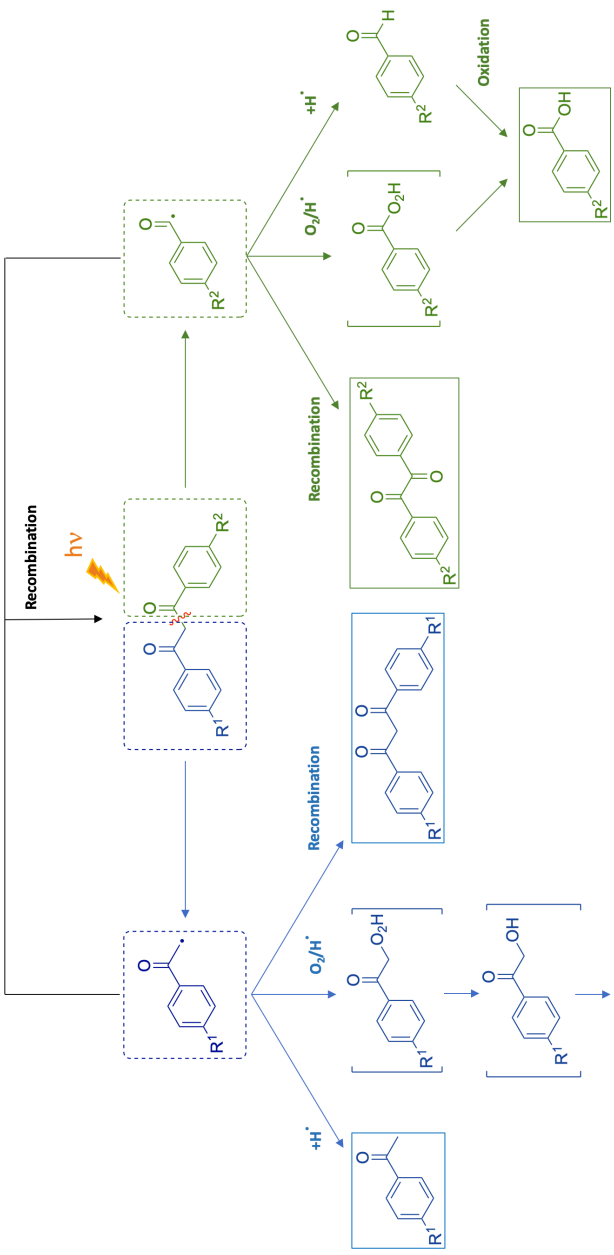

Scheme 1.7. Possible photodegradation products of avobenzone, where R^1 = -OCH_3 and R^2 = -$C(CH_3)_3$ and *vice versa*.

In the case of the benzophenone filter family, the presence of at least two electron donating groups in *ortho* and *para* position to the *keto* moiety are common to all of the worldwide approved BP filters. Oxybenzone and sulisobenzone, which are currently approved in Europe, possess a methoxy and a hydroxy group in *para* and *ortho* position, respectively (Figure 1.11A). The presence of these groups results in two absorption maxima, at 286 nm (UVB) and at 324 nm (UVA). Here, the UVB transition can be attributed to the electron delocalization depicted in Figure 1.11B,[108] while absorption in the UVA range is attributed to the intramolecular hydrogen bond between the hydroxyl and carbonyl groups.[109,110]

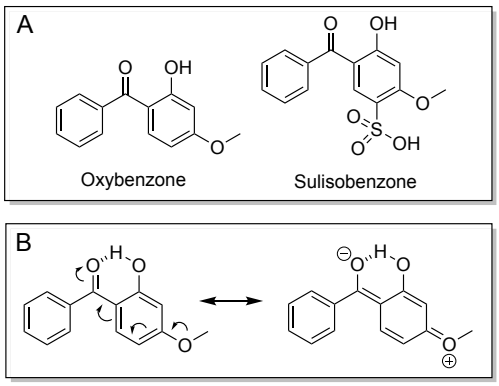

Figure 1.11. Oxybenzone and sulisobenzone structures (A) and the electron delocalization in the oxybenzone.

Besides, this hydroxy group is involved in the excited state relaxation that occurs through an excited state hydrogen transfer mechanism (ESHT) which is responsible for its high photostability.[111] In Scheme 1.8 is shown the proposed mechanism for the nonradiative relaxation pathways of oxybenzone in the UVA region. According to this mechanism, after excitation at *ca.* 325 nm an S_2 (π,π^*) is populated, which relaxes by internal conversion (IC) to the

S_1 (n,π*) followed by excited state hydrogen atom transfer (ESHT) to form a *keto* isomer. Then, rotation around the C-C bond links the S_1 state to a conical intersection with the S_0 state. Finally, the initial chelated *enol* in the S_0 is regenerated (*ca.* 90%) through ground state hydrogen atom transfer (GSHT) and vibrational energy transfer (VET) to the solvent bath. The remaining 10% is attributed to the formation of a *trans keto* isomer which is trapped in that form over a nanosecond time scale.[112] A similar study has also proposed a similar relaxation mechanism after excitation in the UVC and UVB spectral regions.[113]

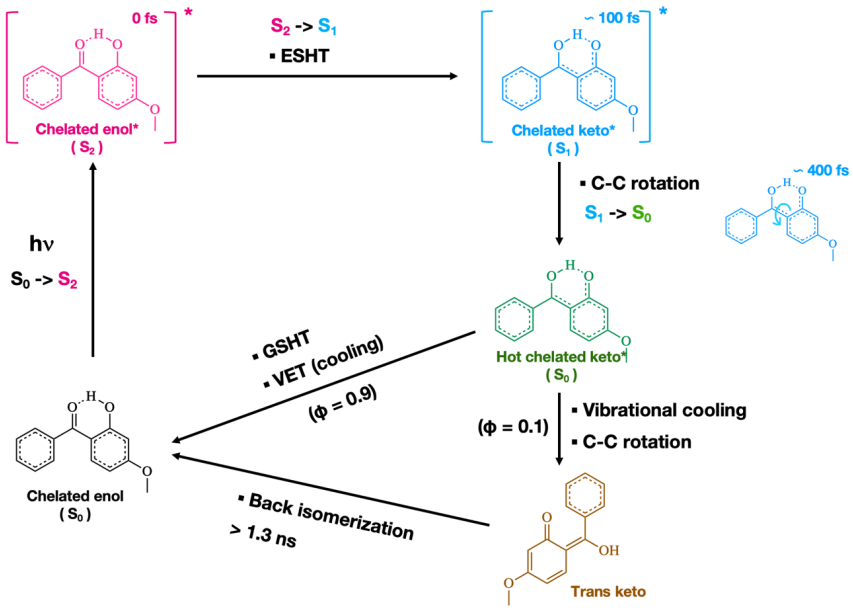

Scheme 1.8. Proposed oxybenzone deactivation mechanim.[112]

1.5. Bibliography

1 J. W. Verhoeven, *Pure Appl. Chem.*, 1996, **68**, 2223–2286.

2 H. D. Roth, *Angew. Chem. Int. Ed.*, 1989, **28**, 1193–1207.

3 J. A. Barltrop and P. Schofield, *Tetrahedron Lett.*, 1962, 697–699.

4 D. H. R. Barton, Y. L. Chow, A. Cox and G. W. Kirby, *Tetrahedron Lett.*, 1962, **3**, 1055–1057.

5 N. Hoffmann, *Chem. Rev.*, 2008, **108**, 1052–1103.

6 J. Sankaranarayanan, S. Muthukrishnan and A. D. Gudmundsdottir, *Adv. Phys. Org. Chem.*, 2009, **43**, 39–77.

7 C. Brieke, F. Rohrbach, A. Gottschalk, G. Mayer and A. Heckel, *Angew. Chem. Int. Ed.*, 2012, **51**, 8446–8476.

8 A. Herrmann, *Photochem. Photobiol. Sci.*, 2012, **11**, 446.

9 J. C. Sheehan and K. Umezawa, *J. Org. Chem.*, 1973, **38**, 3771–3774.

10 P. Klan, T. Solomek, C. G. Bochet, R. Givens, M. Rubina, V. Popik, A. Kostikov and J. Wirz, *Chem. Rev.*, 2012, **113**, 119–191.

11 A. Banerjee and D. E. Falvey, *J. Am. Chem. Soc.*, 1998, **120**, 2965–2966.

12 M. Zabadal, A. P. Pelliccioli, P. Klan and J. Wirz, *J. Phys. Chem. A*, 2001, **105**, 10329–10333.

13 R. S. Givens, D. Heger, B. Hellrung, Y. Kamdzhilov, M. Mac, P. G. Conrad, E. Cope, J. I. Lee, J. F. Mata-Segreda, R. L. Schowen and J. Wirz, *J. Am. Chem. Soc.*, 2008, **130**, 3307–3309.

14 I. Aparici-Espert, M. C. Cuquerella, C. Paris, V. Lhiaubet-Vallet and M. A. Miranda, *Chem. Commun.*, 2016, **52**, 14215–14218.

15 I. Aparici-Espert, M. A. Miranda and V. Lhiaubet-Vallet, *Molecules*, 2018, **23**, 673–683.

16 R. L. Blankespoor, R. Hsung and D. L. Schutt, *J. Org. Chem.*, 1988, **53**, 2877–2878.

17 R. L. Blankespoor, R. L. De Jong, R. Dykstra, D. A. Hamstra, D. B. Rozema, D. P. Vanmeurs and P. Vink, *J. Am. Chem. Soc.*, 1991, **113**, 3507–3513.

18 R. L. Blankespoor, R. P. Smart, E. D. Batts, A. A. Kiste, R. E. Lew and M. E. Vander Vliet, *J. Org. Chem.*, 1995, **60**, 6852–6859.

19 R. G. Brinson and P. B. Jones, *Org. Lett.*, 2004, **6**, 3767–3770.

20 R. L. Blankespoor, T. Devries, E. Hansen, J. M. Kallemeyn, A. M. Klooster, J. A. Mulder, R. P. Smart and D. A. Vander Griend, *J. Org. Chem.*, 2002, **67**, 2677–2681.

21 B. Levrand and A. Herrmann, *Flavour Fragr. J.*, 2006, **21**, 400–409.

22 S. Rochat, C. Minardi, J. Y. De Saint Laumer and A. Herrmann, *Helv. Chim. Acta*, 2000, **83**, 1645–1671.

23 W. Pengfei, H. Huayou and W. Yun, *Org. Lett.*, 2007, **9**, 1533–1535.

24 P. Wang, Y. Wang, A. Hu and X. Liang, *Eur. J. Org. Chem.*, 2009, 208–211.

25 H. Yang, X. Zhang, L. Zhou and P. Wang, *J. Org. Chem.*, 2011, **76**, 2040–2048.

26 P. Wang, Y. Wang, H. Hu, C. Spencer, X. Liang and L. Pan, *J. Org. Chem.*, 2008, **73**, 6152–6157.

27 P. Wang, M. Mondal and Y. Wang, *Eur. J. Org. Chem.*, 2009, 2055–2058.

28 J. H. Kim, F. Huang, M. Ly and R. J. Linhardt, *J. Org. Chem.*, 2008, **73**, 9497–9500.

29 J. W. Ritter and C. W. Böckman, *Ann. für Phys.*, 1801, **7**, 527.

30 T. Veiel, *Vierteljahresschr. Dermatol. Syph.*, 1887, **14**, 113–116.

31 E. Home, *Philos. Trans.*, 1820, **11**, 1–10.

32 F. Urbach, *J. Photochem. Photobiol. B Biol.*, 2001, **64**, 99–104.

33 J. L. Ravanat, T. Douki and J. Cadet, *J. Photochem. Photobiol. B Biol.*, 2001, **63**, 88–102.

34 D. L. Mitchell, J. P. Allison and R. S. Nairn, *Radiat. Res.*, 1990, **123**, 299–303.

35 D. Perdiz, P. Gróf, M. Mezzina, O. Nikaido, E. Moustacchi and E. Sage, *J. Biol. Chem.*, 2000, **275**, 26732–26742.

36 J. A. Meador, A. J. Baldwin, J. D. Pakulski, W. H. Jeffrey, D. L. Mitchell and T. Douki, *Environ. Microbiol.*, 2014, **16**, 1808–1820.

37 P. H. Clingen, C. F. Arlett, L. Roza, T. Mori, O. Nikaido and M. H. L. Green, *Cancer Res.*, 1995, **55**, 2245–2248.

38 T. Douki and E. Sage, *Photochem. Photobiol. Sci.*, 2016, **15**, 24–30.

39 T. Douki and J. Cadet, *Biochemistry*, 2001, **40**, 2495–2501.

40 J. Cadet, E. Sage and T. Douki, *Mutat. Res. - Fundam. Mol. Mech. Mutagen.*, 2005, **571**, 3–17.

41 M. Gomez-Mendoza, A. Banyasz, T. Douki, D. Markovitsi and J. L. Ravanat, *J. Phys. Chem. Lett.*, 2016, **7**, 3945–3948.

42 S. Mouret, C. Philippe, J. Gracia-Chantegrel, A. Banyasz, S. Karpati, D. Markovitsi and T. Douki, *Org. Biomol. Chem.*, 2010, **8**, 1706–1711.

43 Y. Jiang, M. Rabbi, M. Kim, C. Ke, W. Lee, R. L. Clark, P. A. Mieczkowski and P. E. Marszalek, *Biophys. J.*, 2009, **96**, 1151–1158.

44 H. Ikehata, *Photochem. Photobiol. Sci.*, 2018, **17**, 1861–1871.

45 T. Douki, *Photochem. Photobiol.*, 2016, 587–594.

46 S. Courdavault, C. Baudouin, M. Charveron, B. Canguilhem, A. Favier, J. Cadet and T. Douki, *DNA Repair (Amst).*, 2005, **4**, 836–844.

47 F. Urbach, P. D. Forbes, R. E. Davies and D. Berger, *J. Invest. Dermatol.*, 1976, **67**, 209–224.

48 C. J. Burrows and J. G. Muller, *Chem. Rev.*, 1998, **98**, 1109–1151.

49 C. Paris, S. Encinas, N. Belmadoui, M. J. Climent and M. A. Miranda, *Org. Lett.*, 2008, **10**, 4409–4412.

50 W. K. Pogozelski and T. D. Tullius, *Chem. Rev.*, 1998, **98**, 1089–1107.

51 J. Cadet, T. Delatour, T. Douki, D. Gasparutto, J. P. Pouget, J. L. Ravanat and S. Sauvaigo, *Mutat. Res. - Fundam. Mol. Mech. Mutagen.*, 1999, **424**, 9–21.

52 J. Cadet, S. Mouret, J. L. Ravanat and T. Douki, *Photochem. Photobiol.*, 2012, **88**, 1048–1065.

53 K. Krumova, G. Cosa, J. Aubry and J. R. Kanofsky, *Singlet Oxyg. Appl. Biosci. Nanosci.*, 2016, 1–4.

54 J. Cadet, T. Douki and J. L. Ravanat, *Photochem. Photobiol.*, 2015, **91**, 140–155.

55 P. Klán and J. Wirz, in *Photochemistry of Organic Compounds: From Concepts to Practice*, eds. J. Coxon, P. Bailey, L. Field, J. A. Gladdysz, P. Parsons and P. Stang, John Wiley and Sons, 2009, pp. 25–72.

56 V. Lhiaubet-Vallet, M. C. Cuquerella, J. V. Castell, F. Bosca and M. A. Miranda, *J. Phys. Chem. B*, 2007, **111**, 7409–7414.

57 M. C. Cuquerella, V. Lhiaubet-Vallet, M. A. Miranda and F. Bosca, *Phys. Chem. Chem. Phys.*, 2017, **19**, 4951–4955.

58 F. Bosca, V. Lhiaubet-Vallet, M. C. Cuquerella, J. V. Castell and M. A. Miranda, *J. Am. Chem. Soc.*, 2006, **128**, 6318–6319.

59 M. C. Cuquerella, V. Lhiaubet-Vallet, F. Bosca and M. A. Miranda, *Chem. Sci.*, 2011, **2**, 1219–1232.

60 D. E. Moore, *Drug Saf.*, 2002, **25**, 345–372.

61 F. Boscá and M. A. Miranda, *J. Photochem. Photobiol. B Biol.*, 1998, **43**, 1–26.

62 V. Lhiaubet-Vallet and M. A. Miranda, in *CRC Handbook of Organic Photochemistry and Photobiology, Third Ed. - Two Vol.*, eds. A. Griesbeck, M. Oelgemöller and F. Guetti, 2012, pp. 1541–1556.

63 *International Conference on Harmonization of Technical Requirements for Registration of Pharmaceuticals for Human Use*

(ICH) (2014) ICH Guideline S10 Guidance on Phototoxicity Evaluation of Pharmaceuticals, ICH, Geneva, Switzerland., .

64 H. Spielmann, M. Balls, J. Dupuis, W. J. Pape, G. Pechovitch, O. De Silva, H. G. Holzhütter, R. Clothier, P. Desolle, F. Gerberick, M. Liebsch, W. W. Lovell, T. Maurer, U. Pfannenbecker, J. M. Potthast, M. Csato, D. Sladowski, W. Steiling and P. Brantom, *Toxicol. Vitr.*, 1998, **12**, 305–327.

65 F. Boscá, M. L. Marín and M. A. Miranda, *Photochem. Photobiol.*, 2001, **74**, 637.

66 F. Boscá and M. A. Miranda, *J. Photochem. Photobiol. B Biol.*, 1998, **43**, 1–26.

67 J. de la Cuadra-Oyanguren, A. Pérez-Ferriols, M. Lecha-Carrelero, A. M. Giménez-Arnau, V. Fernández-Redondo, F. J. Ortiz de Frutos, J. F. Silvestre-Salvador and E. Serra-Baldrich, *Actas Dermosifiliogr*, 2007, **98**, 96–101.

68 I. Karlsson, E. Persson, A. Ekebergh, J. Mårtensson and A. Börje, *Chem. Res. Toxicol.*, 2014, **27**, 1294–1303.

69 A. C. Kerr, J. Ferguson, S. H. Ibbotson, R. S. Dawe, A. K. Haylett, L. E. Rhodes, H. Adamski, A. Alomar, E. Serra, C. Antoniou, F. Aubin, M. Vigan, T. Biedermann, J. Fischer, J. L. Bourrain, D. Bruynzeel, T. Rustemeyer, J. M. Carrascosa, M. M. U. Chowdhury, J. dela Cuadra, C. Foti, J. Gardeazabal, D. J. Gawkrodger, A. Gimenez-Arnau, M. Goncalo, A. Goossens, M. Lecha, M. C. Marguery, N. J. Neumann, B. Niklasson, J. L. Peyron, P. Pigatto, R. Spiewak, N. Stone, A. Tanew, P. Thomas, A. Bonnevalle, S. M. Wilkinson, P. Wolf, A. Gruber-Wackernagel and H. C. Wulf, *Br. J. Dermatol.*, 2012, **166**, 1002–1009.

70 A. F. Monteiro, M. Rato and C. Martins, *Clin. Dermatol.*, 2016, **34**, 571–581.

71 P. D. Wood and R. W. Redmond, *J. Am. Chem. Soc.*, 1996, **118**, 4256–4263.

72 T. Douki, A. Reynaud-Angelin, J. Cadet and E. Sage, *Biochemistry*, 2003, **42**, 9221–9226.

73 M. C. Cuquerella, V. Lhiaubet-Vallet, J. Cadet and M. A. Miranda, *Acc. Chem. Res.*, 2012, **45**, 1558–1570.

74 K. Nakatani, T. Yoshida and I. Saito, *J. Am. Chem. Soc.*, 2002, **124**, 2118–2119.

75 T. Douki and J. Cadet, *Int. J. Radiat. Biol.*, 1999, **75**, 571–581.

76 V. Lhiaubet, N. Paillous and N. Chouini-Lalanne, *Photochem. Photobiol.*, 2001, **74**, 670–678.

77 V. Lhiaubet-Vallet, N. Belmadoui, M. J. Climent and M. A. Miranda, *J. Phys. Chem. B*, 2007, **111**, 8277–8282.

78 N. Belmadoui, S. Encinas, M. J. Climent, S. Gil and M. A. Miranda, *Chem. - A Eur. J.*, 2005, **12**, 553–561.

79 Y. Hiraku, K. Ito, K. Hirakawa and S. Kawanishi, *Photochem. Photobiol.*, 2007, **83**, 205–212.

80 E. V. Khaydukov, K. E. Mironova, V. A. Semchishen, A. N. Generalova, A. V. Nechaev, D. A. Khochenkov, E. V. Stepanova, O. I. Lebedev, A. V. Zvyagin, S. M. Deyev and V. Y. Panchenko, *Sci. Rep.*, 2016, **6**, 1–9.

81 G. T. Wondrak, M. K. Jacobson and E. L. Jacobson, *Photochem. Photobiol. Sci.*, 2006, **5**, 215–237.

82 L. Kaestner, A. Juzeniene and J. Moan, *Photochem. Photobiol. Sci.*, 2004, **3**, 981–989.

83 F. P. Noonan, M. R. Zaidi, A. Wolnicka-Glubisz, M. R. Anver, J. Bahn, A. Wielgus, J. Cadet, T. Douki, S. Mouret, M. A. Tucker, A. Popratiloff, G. Merlino and E. C. De Fabo, *Nat. Commun.*, 2012, **3**, 1–10.

84 V. Vendrell-Criado, G. M. Rodríguez-Muñiz, M. C. Cuquerella, V. Lhiaubet-Vallet and M. A. Miranda, *Angew. Chemie - Int. Ed.*, 2013, **52**, 6476–6479.

85 V. Vendrell-Criado, G. M. Rodriguez-Muniz, M. C. Cuquerella, V. Lhiaubet-Vallet and M. A. Miranda, *Angew. Chem. Int. Ed.*, 2013, **52**, 6476–6479.

86 V. Vendrell-Criado, G. M. Rodríguez-Muñiz, V. Lhiaubet-Vallet, M. C. Cuquerella and M. A. Miranda, *ChemPhysChem*, 2016, **17**, 1979–1982.

87 T. Douki, *ChemPhotoChem*, 2020, **4**, 294–299.

88 I. Aparici-Espert, G. Garcia-Lainez, I. Andreu, M. A. Miranda and V. Lhiaubet-Vallet, *ACS Chem. Biol.*, 2018, **13**, 542–547.

89 *Official Journal of the European Union, Cosmetic products Regulation EC Nº1223/2009., 2009.*, .

90 *Official Journal of the European Union, Cosmetic products Commission Regulation EU 2020/1684., 2020.*, .

91 N. Sabzevari, S. Qiblawi, S. A. Norton and D. Fivenson, *Int. J. Women's Dermatology*, 2021, **7**, 28–44.

92 N. A. Shaath, *Photochem. Photobiol. Sci.*, 2010, **9**, 464–469.

93 N. d. N. Rodrigues, N. C. Cole-Filipiak, M. A. P. Turner, K. Krokidi, G. L. Thornton, G. W. Richings, N. D. M. Hine and V. G. Stavros, *Chem. Phys.*, 2018, **515**, 596–602.

94 *Official Journal of the European Union, Cosmetic products Commission directive 2008/123/EC, 2008.*, .

95 T. Mathias and H. I. Maibach, *Arch Dermatol*, 1978, **114**, 1665–1666.

96 S. Pattanaargson, T. Munhapol, P. Hirunsupachot and P. Luangthongaram, *J. Photochem. Photobiol. A Chem.*, 2004, **161**, 269–274.

97 X. P. Chang, C. X. Li, B. Bin Xie and G. Cui, *J. Phys. Chem. A*, 2015, **119**, 11488–11497.

98 M. Yamaji and M. Kida, *J. Phys. Chem. A*, 2013, **117**, 1946–1951.

99 A. D. Dunkelberger, R. D. Kieda, B. M. Marsh and F. F. Crim, *J. Phys. Chem. A*, 2015, **119**, 6155–6161.

100 G. J. Mturi and B. S. Martincigh, *J. Photochem. Photobiol. A Chem.*, 2008, **200**, 410–420.

101 S. Tobita, J. Ohba, K. Nakagawa and H. Shizuka, *J. Photochem. Photobiol. A Chem.*, 1995, **92**, 61–67.

102 S. P. Huong, E. Rocher, J. D. Fourneron, L. Charles, V. Monnier, H. Bun and V. Andrieu, *J. Photochem. Photobiol. A Chem.*, 2008, **196**,

106–112.

103 W. Schwack and T. Rudolph, *J. Photochem. Photobiol. B Biol.*, 1995, **28**, 229–234.

104 M. Yoshioka, Y. Sakuma and M. Saito, *J. Org. Chem.*, 1999, **64**, 9247–9250.

105 V. Lhiaubet-Vallet, M. Marin, O. Jimenez, O. Gorchs, C. Trullas and M. A. Miranda, *Photochem. Photobiol. Sci.*, 2010, **9**, 552–558.

106 S. Afonso, K. Horita, J. P. Sousa E Silva, I. F. Almeida, M. H. Amaral, P. A. Lobão, P. C. Costa, M. S. Miranda, J. C. G. Esteves Da Silva and J. M. Sousa Lobo, *J. Photochem. Photobiol. B Biol.*, 2014, **140**, 36–40.

107 P. C. V. Govindu, B. Hosamani, S. Moi, D. Venkatachalam, S. Asha, V. N. John, V. Sandeep and K. H. Gowd, *Photochem. Photobiol. Sci.*, 2019, **18**, 198–207.

108 N. A. Shaath, *Photochem. Photobiol. Sci.*, 2010, **9**, 464–469.

109 B. M. Baughman, E. Stennett, R. E. Lipner, A. C. Rudawsky and S. J. Schmidtke, *J. Phys. Chem. A*, 2009, **113**, 8011–8019.

110 B. A. M. Corrêa, A. S. Gonçalves, A. M. T. De Souza, C. A. Freitas, L. M. Cabral, M. G. Albuquerque, H. C. Castro, E. P. Dos Santos and C. R. Rodrigues, *J. Phys. Chem. A*, 2012, **116**, 10927–10933.

111 A. R. Abid, B. Marciniak, T. Pędziński and M. Shahid, *J. Photochem. Photobiol. A Chem.*, 2017, **332**, 241–250.

112 L. A. Baker, M. D. Horbury, S. E. Greenough, P. M. Coulter, T. N. V. Karsili, G. M. Roberts, A. J. Orr-Ewing, M. N. R. Ashfold and V. G.

Stavros, *J. Phys. Chem. Lett.*, 2015, **6**, 1363–1368.

113 L. A. Baker, M. D. Horbury, S. E. Greenough, M. N. R. Ashfold and V. G. Stavros, *Photochem. Photobiol. Sci.*, 2015, **14**, 1814–1820.

Chapter 2:

General objectives

This Doctoral Thesis focuses on the understanding, development and use of photolabile protecting groups with biological applications. Here, these applications include the simultaneous photorelease of photosensitive compounds along with commercially available solar filters, as well as the development of new synthetic strategies for the incorporation of carbonyl derivatives into oligonucleotides. More specifically, the objectives of the present Thesis could be outlined as follows:

➤To gain a deeper understanding regarding the photophysical and photochemical processes that take place during the photouncaging process of two prodrug/profilter systems formed between the avobenzone (AB) solar filter and two different NSAIDs.

➤To expand the use of solar filters as photocages for carbonyl compounds by making use of the well-known oxybenzone UVB/A filter, and to obtain information about its photorelease mechanism and its substrate scope.

➤To analyze the photophysical and photochemical properties of two oxidatively generated DNA damages, namely 5-formyluracil (ForU) and 5-formylcytosine (ForC), paying special attention to their role as potential intrinsic photosensitizers.

➤To develop a new synthetic approach for the insertion of ForU into oligodeoxynucleotides using a photoremovable carbonyl protecting group.

Chapter 3:

Mechanistic insights into the avobenzone-based drug photocages

3.1. Introduction

Significant advances have been made since the early reports on photoremovable protecting groups (also known as photolabile protecting groups, PPG), [1–3] which are now essential in a multitude of research fields as diverse as organic synthesis, catalysis, therapeutic application, imaging, sensing, modulation of protein−DNA binding, etc.[4-14] The main advantage of PPG is the use of light as an external and non-invasive stimulus, which results in minimal secondary processes and offers a fully complementary alternative to conventional chemical and biological tools such as protecting groups (PG) and chemotherapeutic agents. In addition, the photorelease can be performed with a high spatiotemporal control and without additional chemicals, thus holding promise for the development of a wide range of applications in organic chemistry, biochemistry, biology, polymer science, lithography, toiletry, etc.[4-14]

Phenacyl derivatives are among the most used PPG as they provide an extensive toolkit for protection of chemical functions such as carboxylic acids, alcohols, thiols, phosphates, sulfonates, amines, etc.[4,10,15,16] They operate through different mechanisms including inter- or intramolecular H-abstraction, electron transfer from suitable donors or photo-Favorskii rearrangement. In most of these processes, triplet excited states have been established as the key intermediates.[4] Thus, an efficient intersystem crossing (ISC) is often a prerequisite for high photorelease efficacy.

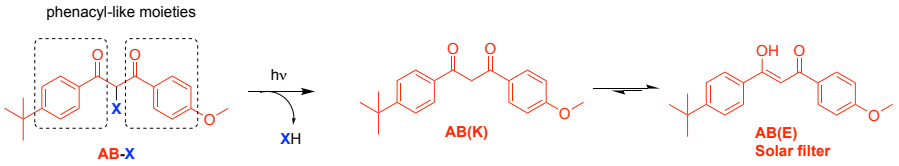

Scheme 3.1. General representation of the photorelease from avobenzone-based systems.

Recently, the dibenzoylmethane derivative avobenzone (AB, 4-*tert*-butyl-4-methoxydibenzoylmethane) has been proposed as a valuable phenacyl-like PPG for carboxylic acid photorelease (Scheme 3.1).[17,18] Interestingly, this compound not only behaves as an ordinary PPG, *i.e.* being released upon irradiation, but it also presents an added value since it acts as a well-established UVA filter. Indeed, AB is already largely used to achieve photoprotection in commercial sunscreens and cosmetics formulations. This combined action has given rise to the new concept of synergic prodrug/profilter, which results in a perfect combination to provide the phototriggered delivery of a photosensitive drug together with its UVA protective filter. This concept has been successfully proven with ketoprofen (KP) and diclofenac, two highly photosensitive non-steroidal anti-inflammatory drugs (NSAIDs)[19,20] used as topical pain relievers.[17,18] Photochemical studies have demonstrated the controlled and simultaneous photorelease of the drug and the filter. The avobenzone in its *enol* form, AB(E), is responsible for the large UVA absorption, due to the formation of intramolecular hydrogen bond that enforces the planarity of the molecular skeleton as compared to its diketonic form, AB(K), thus increasing the π-conjugation, red-shifting the absorption spectrum and providing photoprotection.[21,22] Indeed, thanks to the filtering action of AB(E), the

NSAID photoreactivity is inhibited and, consequently, the risk of adverse skin reactions, such as phototoxicity and photoallergy, is minimized.

In the AB-derivative systems above mentioned, the photorelease process has been proposed to take place from the excited triplet state of the AB moiety in its diketonic form, ^{3}AB(K)*, following a reaction mechanism similar to the one previously established for phenacyl derivatives.[4] Hence, the efficient population of ^{3}AB(K)* appears essential to reach the optimal conditions for the photorelease. Since AB-based systems can be partitioned into two basic constituent fragments, the energetic order of the triplet states centered on one or another unit can be crucial to dictate the global photodissociation efficiency. More precisely, under the photoreaction conditions, the triplet excited state centered on the carboxylate moiety should be located at a higher energy than the one localized over AB(K); otherwise, a triplet-triplet energy transfer would occur, deactivating the photoreactive ^{3}AB(K)*.

With this background, in the present chapter, thorough spectroscopic and molecular modeling studies are employed to assess the importance of the relative location of ^{3}AB(K)* versus the triplet state of its caged compound. Specifically, the photophysics of the prodrug/profilter dyads (AB-KP and AB-NPX) formed by linking AB to two different NSAIDs, namely ketoprofen (KP) and naproxen (NPX), have been assessed and compared with the properties of their basic components (Chart 3.1). In this regards, to study the photophysical properties of the AB(K) fragment, we used the methylated derivative of AB (AB-Me) in order to block the *keto-enol* equilibrium.

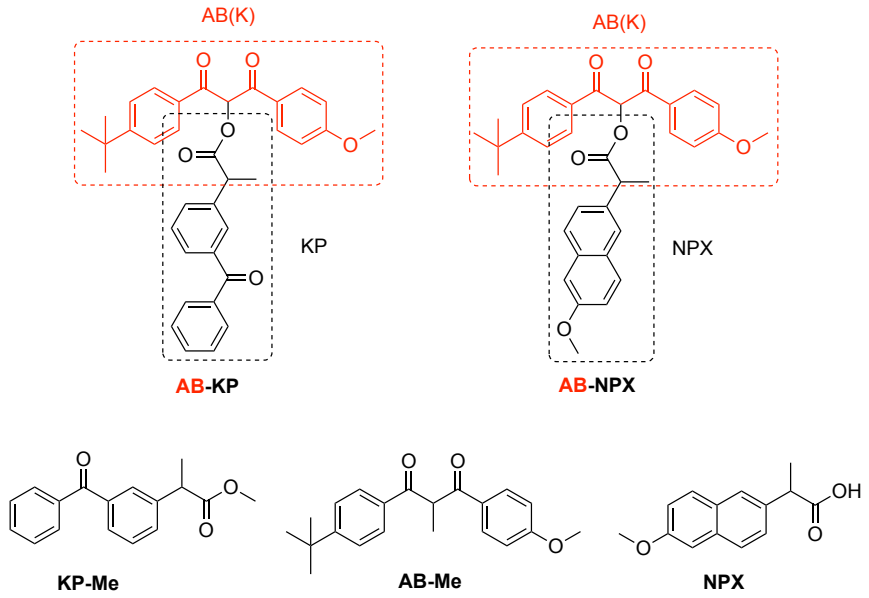

Chart 3.1. Structure of the studied compounds.

3.2. Results and discussion

3.2.1. Influence of the solvent on the photorelease of AB-KP

Along this section, the influence of the solvent on the photorelease of AB-KP will be evaluated using EtOH, hexane and acetonitrile, three solvents with different polarities (dielectric constant, ε, of *ca.* 24.55, 1.89 and 35.94, respectively)[23] and H-donor capabilities. This analysis makes special sense in the case of AB-KP dyad since both fragments are based on aromatic ketones, whose excited states energies are in general sensitive to solvent polarity, especially when their electronic configuration is of n,π* nature.[24]

3.2.1.1. Preliminary steady-state photolysis studies of AB-KP in EtOH and hexane

First, steady-state photolysis of N_2 deaerated solutions of AB-KP (7 x 10^{-5} M) were carried out using simulated sunlight (SSL), and the course of the reaction was followed by UV-Vis absorption spectrophotometry monitoring the photorelease of AB through the appearance of its characteristic 355 nm absorption band.[17] Irradiation performed in ethanol solution resulted in an evident increase of the intensity of the AB(E) signature band with irradiation time (Figure 3.1A).[17] By contrast, the irradiation of the hexane solutions showed a markedly slower photorelease. Indeed, even after 30 min of irradiation the AB(E) UVA band is barely noticeable and more specifically seven-fold lower than for ethanol solutions (Figure 3.1B). Besides, different spectral changes below 250 nm are also observed, which point toward a different photoreactivity of the dyad in these solvents. Further experiments, performed in acetonitrile (Figure 3.1C) showed the inefficiency of the photorelease process when a polar solvent with poor H-donor capability is used. Thus, results in hexane could, in a first approximation, be explained by the lack of H-donor capability of the solvent, which is a crucial step to assure the release mechanism. However, an alternative explanation can be considered taking into account that the photorelease is initiated by the population of the phenacyl-like triplet excited state ^{3}AB(K)*.[17] In this context, aromatic ketones are well-known for the marked solvent-dependence of the energetic levels of their excited states, especially for the n,π* ones.[24] Thus, we performed spectroscopic analysis and theoretical calculations to get deeper insight into the lowest singlet and triplet excited state landscape when ethanol and hexane are used as solvents.

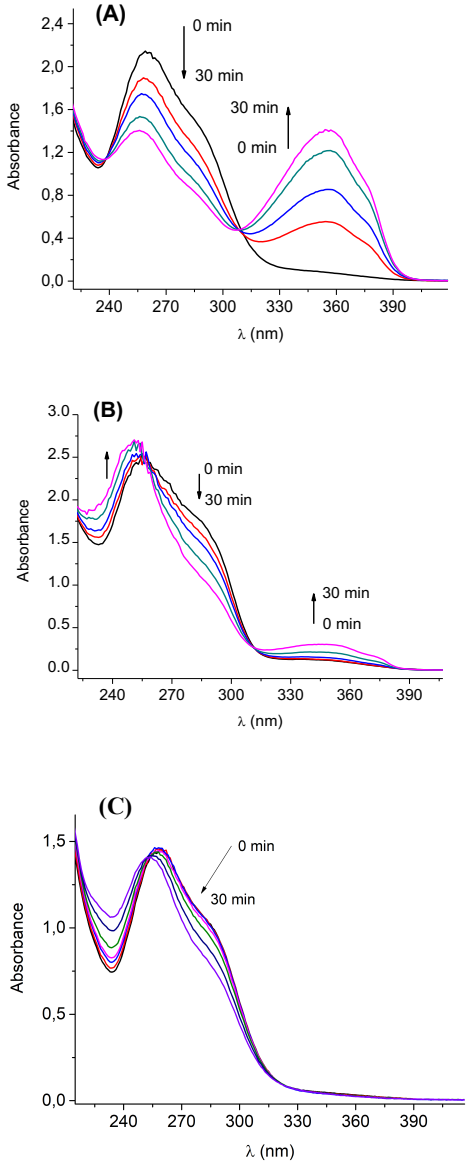

Figure 3.1. UV absorption changes for AB–KP in deaerated ethanol (7 x 10^{-5} M) (A), hexane (7 x 10^{-5} M) (B) or acetonitrile (4 x 10^{-5} M) (C) under SSL irradiation (from 0 to 30 min).

3.2.1.2. Studies on the nature of the singlet excited states

Solvatochromism, due to the singlet excited states ordering, was studied for AB-KP and its basic chromophores AB-Me and KP-Me using UV-Vis absorption spectroscopy. In the case of the dyad, the main absorption band, located in the UVC region, experiences only a weak bathochromic shift (from 254 to 260 nm) when changing the solvent from hexane to ethanol, which is consistent with a transition of π,π* nature (Figure 3.2). In contrast, a shoulder, observed in the UVA at ~355 nm, is shifted to the red and becomes clearly more resolved when hexane is used as solvent (Figure 3.2, inset), confirming its n,π* character.

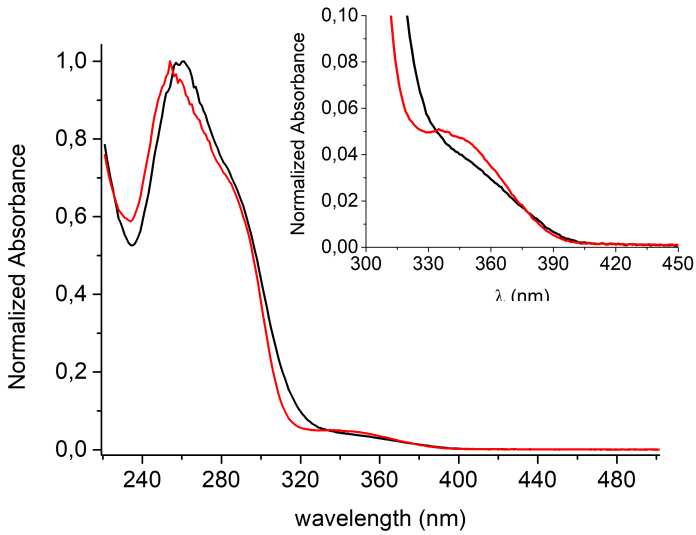

Figure 3.2. Normalized UV-Vis absorption spectra of AB-KP in hexane (red) and ethanol (black). Inset: zoom of the absorption in the 300-450 nm range.

Concerning the isolated chromophores of the dyad, AB-Me (Figure 3.3A) and KP-Me (Figure 3.3B), they also present both UVC and UVA absorption bands of π,π* and n,π* nature,[21,25] respectively, which exhibit the typical shift, associated with their respective electronic configurations, as a function of solvent polarity.

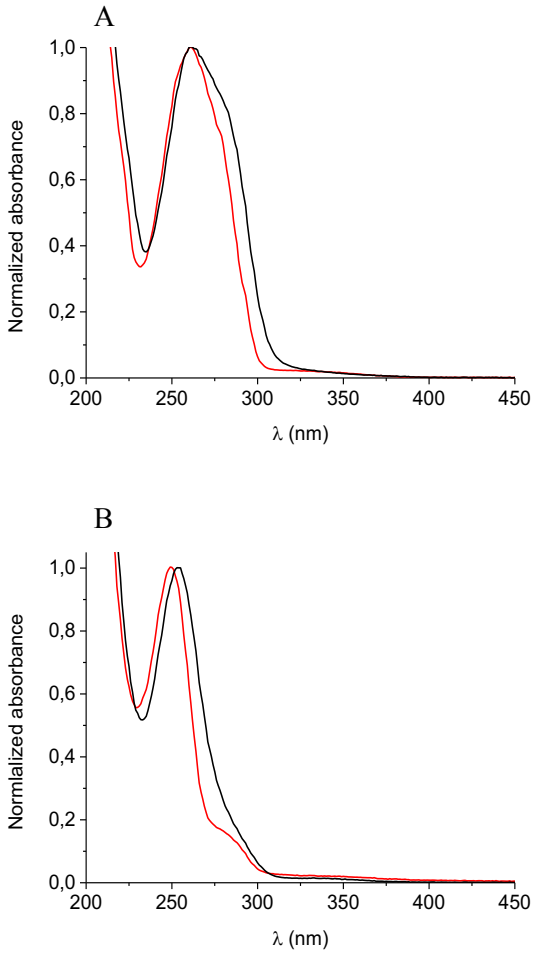

Figure 3.3. Normalized UV-Vis absorption spectra of AB-Me in hexane (red) and ethanol (black) (A). Normalized UV-Vis absorption spectra of KP-Me in hexane (red) and ethanol (black) (B).

The nature of the transitions was also confirmed by theoretical calculations in collaboration with Prof. A. Monari and Dr. A. Francés-Monerris from University of Lorraine (France). The theoretical absorption spectra (Figure 3.4) was obtained as vertical transitions from an ensemble of geometries of the Franck-Condon region. The low energy transitions at *ca*. 300 nm reproduce the experimentally observed blue shift with the increase of the solvent polarity.

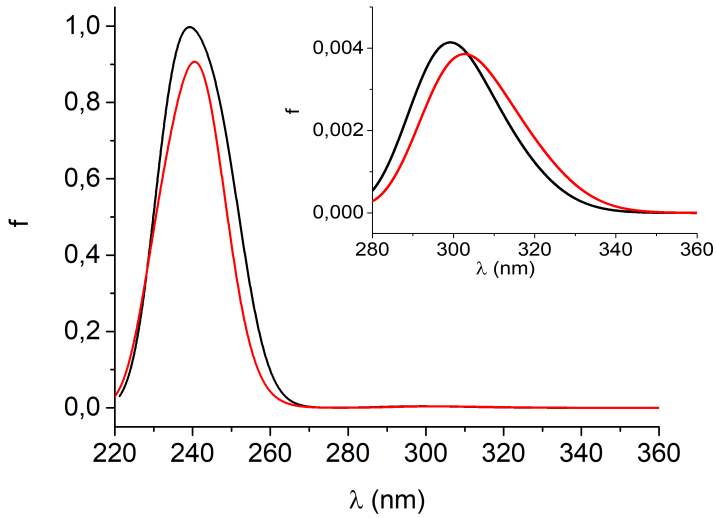

Figure 3.4. Calculated absorption spectrum (oscillator strength (f) versus wavelength (λ)) obtained from the 10 lowest excited states of the dyad in ethanol (black) and hexane (red). Inset: absorption in the UVA region. Calculations were performed at the Density Functional Theory (DFT) level using ωB97-XD as exchanged correlation functional and the 6-31G(d) basis set.

A more detailed analysis of the electronic density reorganization confirms the presence of an almost dark (S_1, n,π*) and a much brighter (π,π*)

absorption. As can be seen from the natural transition orbitals (NTOs) reported in Figure 3.5, the π-stacking between the AB and KP chromophores also induces an excitonic coupling leading to the delocalization of the hole and electron densities over the two moieties.

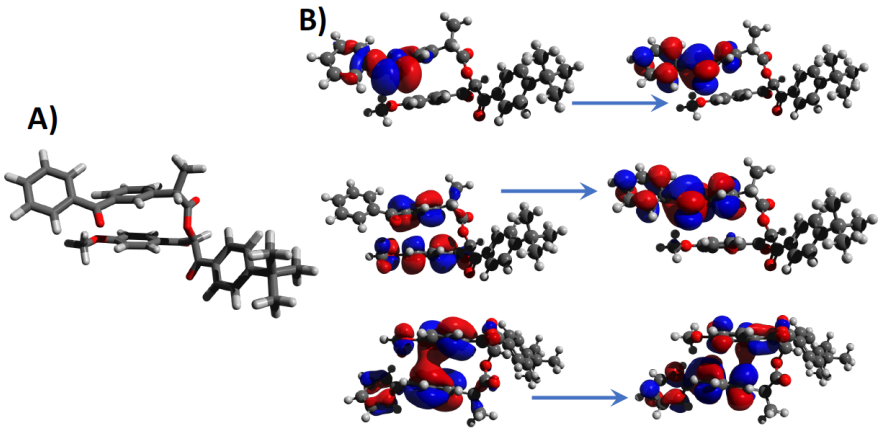

Figure 3.5. DFT equilibrium geometry for the ground state of the AB-KP dyad calculated using ωB97-XD as exchanged correlation functional and the 6-31G(d) basis set. Note the π-stacking between the AB and KP units (A). Hole and particle NTOs for three lowest-lying singlet excited states (B).

3.2.1.3. Nanosecond laser flash photolysis experiments

As mentioned above, triplet excited states are key species in the photochemistry of phenacyl-based PPG. Therefore, to evaluate the population and reactivity of ^{3}AB-KP*, ^{3}AB-Me* and ^{3}KP-Me*, laser flash photolysis (LFP) experiments were performed by means of a nanosecond pulsed laser (Nd:YAG) using 355 nm as excitation wavelength.

Transient absorption spectra obtained for deaerated solutions of KP-Me in EtOH and hexane (Figure 3.6A and 3.6B) are in agreement with those described in the literature for ketoprofen.[25,26] In ethanol, the typical benzophenone-like behavior was observed with the generation of a very short-lived triplet excited state centered at 520 nm (τ of *ca.* 0.05 μs) that gives rise to the formation of the ketyl radical peaking at 550 nm. While the same species were observed in hexane, the triplet decay was slower with a characteristic time τ of *ca*. 0.4 μs. Deaerated ethanol or hexane solutions of AB-Me showed only one transient absorption peaking at *ca.* 400 nm and with lifetime of *ca.* 1.3 and 0.4 μs, respectively (Figure 3.6C and 3.6D), which was assigned to the triplet excited state of AB-Me by comparison with the literature data.[21]. No signal corresponding to ketyl radical formation was detected under the experimental conditions.

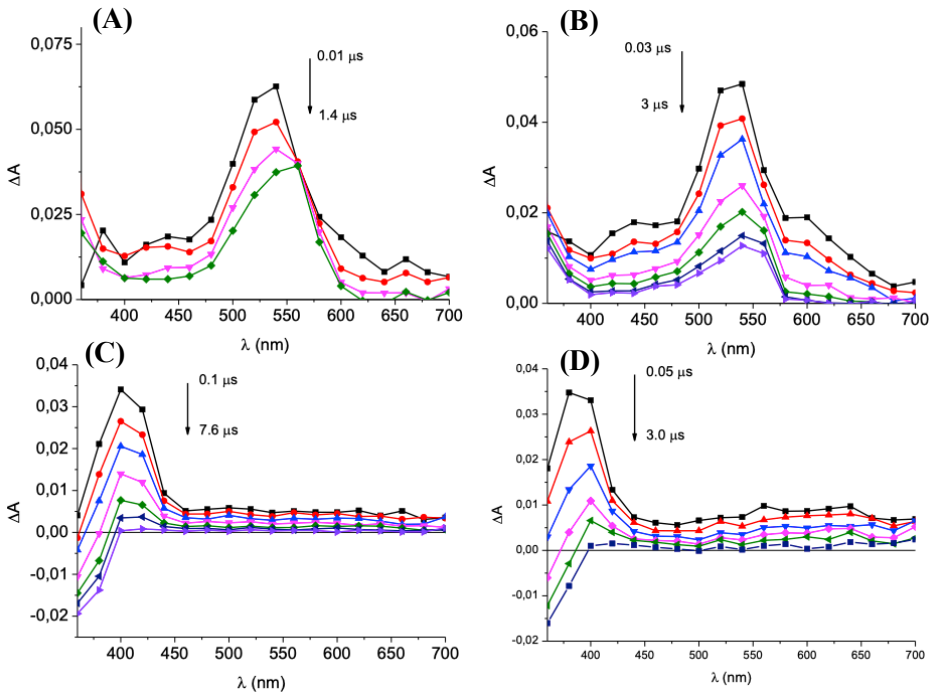

Figure 3.6. Transient absorption spectra of KP-Me in EtOH (A), or hexane (B) and of AB-Me in EtOH (C) or hexane (D) at different time after the 355 nm laser pulse.

Interestingly, in the case of AB-KP, a marked difference of the spectra was observed depending on the solvent (Figure 3.7). In ethanol, a transient absorption peaking at 400 nm was detected (Figure 3.7A) and assigned, by comparison with AB-Me, to the triplet-triplet transition of the avobenzone-like moiety in its *diketo* form ^{3}AB(K)*. This band decays in the sub-µs range with a lifetime τ of *ca.* 0.2 µs. At longer times (*i.e.* 0.9 µs after the laser pulse), a weak signal, similar to the one of ketoprofen ketyl radical, was observed at *ca.* 550 nm. However, in MeCN, as expected for its poor H-donor capability, only the signal corresponding to ^{3}AB(K)* was observed at 400 nm (Figure 3.7C). Interestingly, in hexane (Figure 3.7B), the AB(K) triplet band at 400

nm (τ of *ca.* 0.2 μs) was observed, although to a lesser extent, while a transient absorption at *ca.* 520 nm (τ of ca. 0.2 μs) similar to the well-known triplet absorption of KP was detected decaying without (apparently) giving rise to any ketyl radical formation.

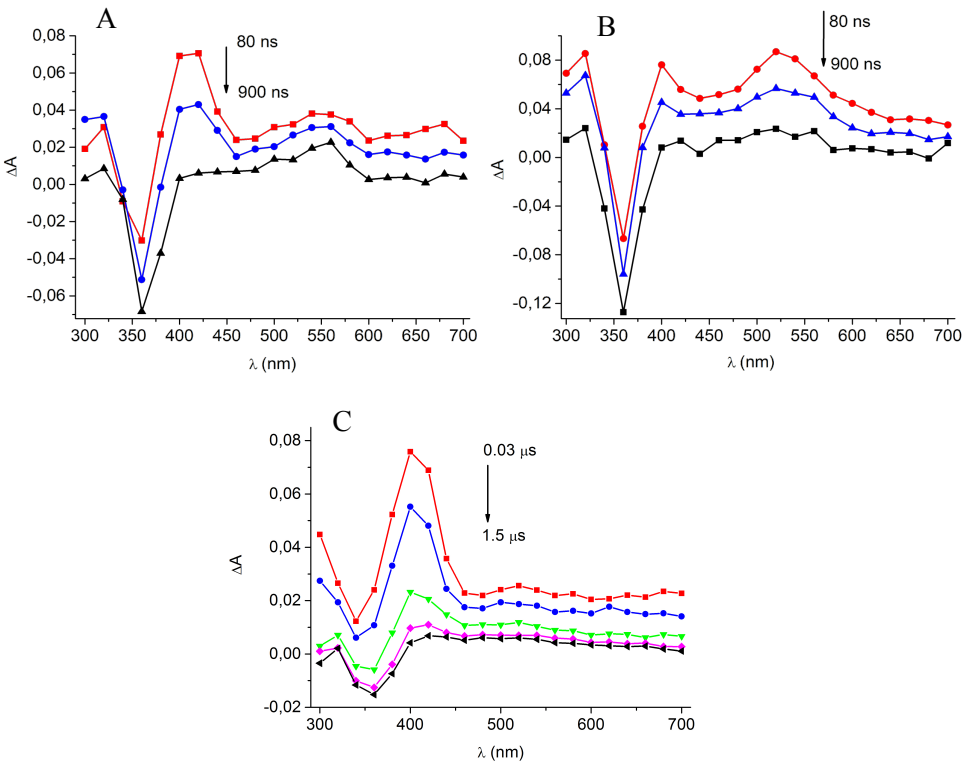

Figure 3.7. Transient absorption spectra of AB-KP (carried out with 14 cuvettes to avoid photodecomposition of AB-KP during the experiment) in ethanol (A), hexane (B) and MeCN (C) under N_2, at different times after the 355 nm laser pulse.

In order to investigate whether this intriguing behavior was only observable in the covalently bound AB-KP dyad, the photophysical study was

also extended to mixtures of 1:1 (3 mM: 3 mM) ratio of AB-Me and KP-Me in either deaerated EtOH or hexane (Figure 3.8). At 355 nm, most of the incoming light is absorbed by AB-Me (64% in EtOH or 72% in hexane). Interestingly, the transient absorption spectra observed in both solvents are quite similar to those obtained for the AB-KP dyad. In EtOH, ^{3}AB-Me* and some ketyl radical (that could arise from direct irradiation of the KP moiety), were detected (Figure 3.8A). The lifetime of the 400 nm species in the 1:1 mixture was 0.8 μs, which corresponds to a bimolecular quenching rate constant of *ca.* 10^{8} $M^{-1}s^{-1}$. The hexane spectra, as in the case of the dyad, only exhibited the absorption band of ^{3}KP-Me* with τ of *ca.* 0.4 μs, evidencing a very efficient quenching of ^{3}AB-Me* by KP-Me through a triplet-triplet energy transfer process (Figure 3.8B). All these spectra data are summarized in table 3.1.

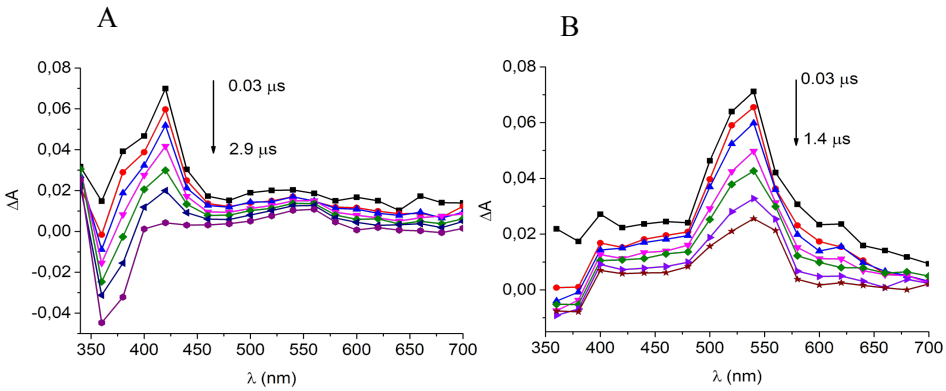

Figure 3.8. Transient absorption spectra of a degassed 1:1 mixture of AB-Me:KP-Me in ethanol (A) or in hexane (B) at different time after the 355 nm laser pulse.

Table 3.1. Summary of the observed transient absorption bands of AB-Me, KP-Me and AB-KP together with their assigned species and lifetimes.

	AB-Me	KP-Me	AB-Me:KP-Me (1:1)	AB-KP
Ethanol	^{3}AB-Me*:	^{3}KP-Me*:	^{3}AB(K)*:	^{3}AB(K)*:
	400 nm (1.3 μs)	520 nm (0.05μs)	400 nm (0.8μs)	400 nm (0.2μs)
		Ketyl radical:	Ketyl radical:	Ketyl radical:
		550 nm	550 nm	550 nm
Hexane	^{3}AB-Me*:	^{3}KP-Me*:	^{3}KP-Me*:	^{3}KP-Me*:
	400 nm (0.4 μs)	520 nm (0.4μs)	520 nm (0.4μs)	520 nm (0.2μs)
		Ketyl radical:	Ketyl radical:	^{3}AB(K)*:
		550 nm	550 nm	400 nm (0.2 μs)

3.2.1.4. Ultrafast transient absorption spectroscopy experiments

In order to analyze the sub-nanosecond processes and to shed light on the population of ^{3}KP* in hexane, ultrafast transient absorption spectroscopy was performed using a mode-locked Ti-sapphire laser of a compact Libra HE (4W power at 4 kHz) regenerative amplifier delivering 100 fs pulses at 800 nm (1 mJ/pulse). At this timescale, KP-Me and AB-Me were measure separately in ethanol and hexane (Figure 3.9). KP-Me alone in ethanol (Figure 3.9A) or in hexane (Figure 3.9B) exhibited the characteristic singlet–singlet transition at 580 nm, which gave rise to the 525 nm triplet-triplet absorption band through an efficient intersystem crossing in less than 20 ps.[17]

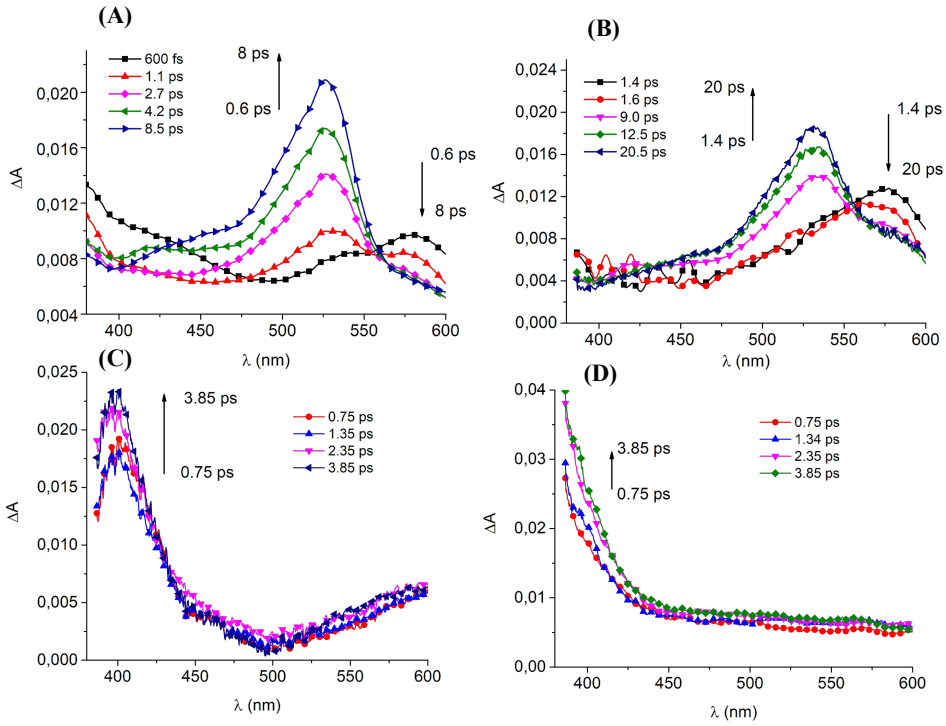

Figure 3.9. Transient absorption spectra of KP-Me in EtOH (A), or hexane (B) and of AB-Me in EtOH (C) or hexane (D) at different time after the laser pulse at 355 nm.

As shown in Figure 3.10A, the signals derived from KP singlet-singlet or triplet-triplet transient absorption were hardly detected for the dyad AB-KP in ethanol or hexane within the first 20 ps. At long delay times (up to 2.2 ns), no new band appeared in the 500-620 nm region when the spectrum was obtained in ethanol (Figure 3.10B).

Notably, when hexane was used as solvent the same behavior was detected for AB-KP up to 50 ps (Figure 3.11A); however, after this delay time, a signal centered at 525 nm emerges (Figure 3.11B). It is noteworthy that, in

the dyad, the characteristic singlet-singlet transient absorption of KP was not detected, and the KP triplet state absorption band increased with a time constant higher than in the case of KP alone (Figure 3.9B). This supports formation of ^{3}KP* in hexane through a triplet-triplet energy transfer from ^{3}AB(K)*, rather than by intersystem crossing from the corresponding excited singlet state, a process that was not detected in ethanol. A possible explanation for this solvent-related difference would be an inversion of the relative excited state energy levels of AB(K) and KP, which in the case of hexane could favor energy transfer from AB to KP.

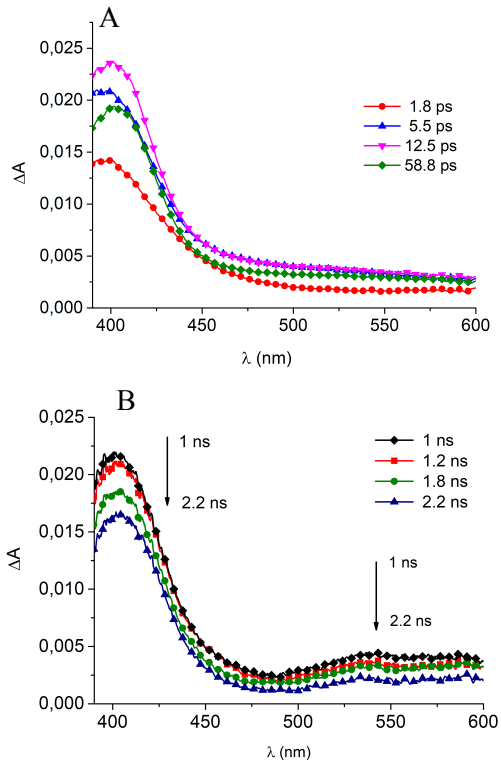

Figure 3.10. Transient absorption spectra of AB-KP in ethanol (A) from 1.8 ps to 58.8 ps and (B) from 1 ns to 2.2 ns after the laser pulse at 355 nm.

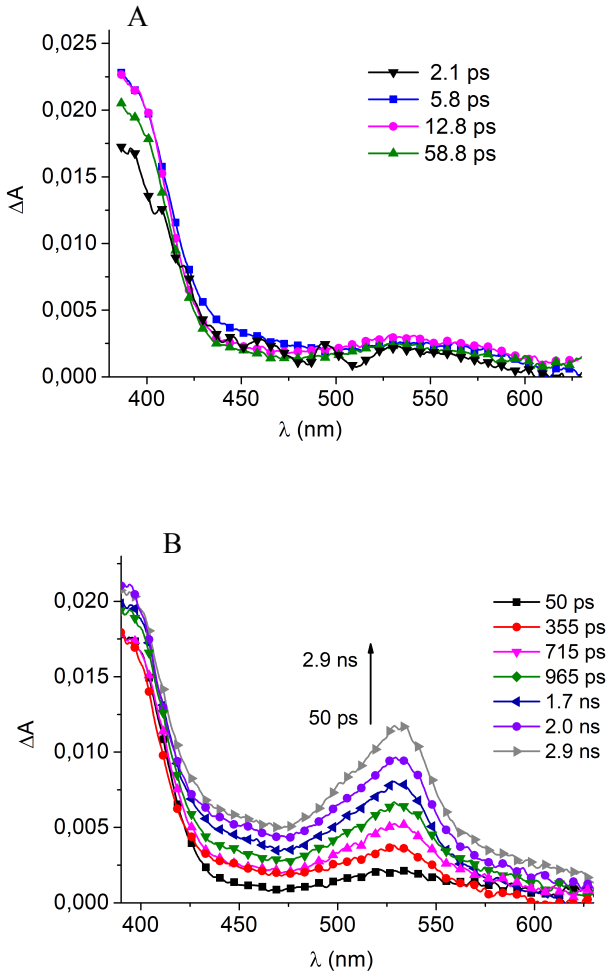

Figure 3.11. Transient absorption spectra of AB-KP in hexane (A) from 0.3 ps to 58.8 ps and (B) from 50 ps to 2.0 ns after the laser pulse at 355 nm.

3.2.1.5. Theoretical analysis on the influence of solvent in the triplet energy order of AB(K) and KP in the AB-KP system

The above results are further supported by the exploration of the triplet potential energy surfaces of the AB-KP dyad at a time-dependent

density functional theory (TD-DFT) level making use of the Tamm-Dancoff approximation (TDA),[27] and the singlet and triplet electronic densities have been analyzed in terms of Natural Transition Orbitals (NTOs) making use of the NANCY_EX code.[28,29] These calculations have been performed in collaboration with Prof. A. Monari and Dr. A. Francés-Monerris from University of Lorraine (France). As shown in Figure 3.12 and Table 3.2, the two lowest-lying triplet states are centered over the KP and the AB subsystems, as revealed by the analysis of their spin densities and the NTOs describing the lone-pair electrons (Figure 3.12C). At the Franck-Condon geometry, irrespectively of the solvent, ^{3}KP* is always lower in energy than ^{3}AB*. However, the energy gap between them is closer in ethanol due to the increase of solvent polarity.

Upon triplet geometry optimization, while the state of interest is strongly stabilized, a noticeable increase in energy is observed for the other triplet (Figure 3.12A and 3.12B and Table 3.2). In hexane, when considering the corresponding adiabatic energy difference, ^{3}KP* is the lowest state, being 0.06 eV lower than ^{3}AB*. Conversely, the energetic ordering of the states is inverted in the case of ethanol, in which ^{3}AB* at its equilibrium geometry is now 0.02 eV more stable than ^{3}KP*.

Even though the energy differences are small, the nature of the states (Figure 3.12C) correlate well with the different photophysics experienced as a function of the solvent described in detail by the experimental measurements. Indeed, after the initial intersystem crossing, leading most probably to the population of ^{3}KP*, the diabatic nature of the triplet state is conserved in hexane, while in ethanol the most stable triplet localized over ^{3}AB* supports a formal triplet-triplet energy transfer towards this molecular moiety. The observed small energy difference raises the question of the behaviour of the dyad in intermediate polarity solvents, or in inhomogeneous

media. Even if the precise characterization of such complex systems goes clearly beyond the scope of the present contribution, we may speculate that a competition between the pathways leading to the population of ^{3}KP* or ^{3}AB* could be envisaged that in turn could affect the photouncaging quantum yield. Even if the energetic barrier related to the triplet transfer has not been explicitly modeled here, the relatively small energy difference, and the rather moderate geometric reorganization, should point towards a relatively facile and a fast process, coherently with the spectroscopic measurements.

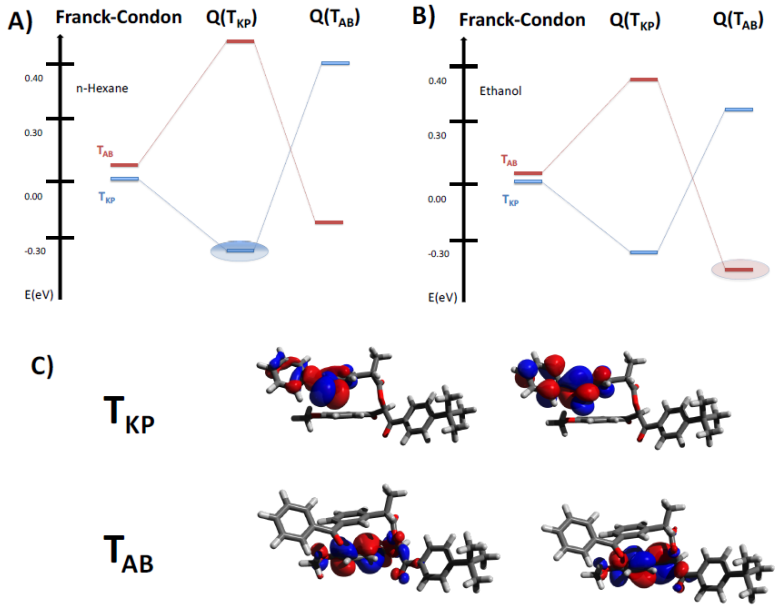

Figure 3.12. Energy diagram of the lowest triplet states of the dyad in hexane (A) and ethanol (B) and NTOs describing the lone pair electrons of the triplet state centered on the ketoprofen (T_{KP}) and avobenzone (T_{AB}) moiety, respectively (C). All energies are relative to the triplet state localized over KP (^{3}KP*) at the Franck-Condon region.

Table 3.2. Relative energies (E) in eV of ^{3}AB* and ^{3}KP* states at Franck-Condon (FC) and at the relative equilibrium geometries Q(^{3}AB*) and Q(^{3}KP*), respectively, in hexane and ethanol.

	FC	**Q(^{3}KP*)**	**Q(^{3}AB*)**
		n-Hexane	
E(^{3}KP*)	0.000	-0.322	0.404
E(^{3}AB*)	0.151	0.471	-0.265
		Ethanol	
E(^{3}KP*)	0.000	-0.326	0.320
E(^{3}AB*)	0.084	0.370	-0.350

Altogether these results show the influence of solvent polarity on the triplet excited state location in AB-KP. These differences are because both ^{3}AB-Me* and ^{3}KP-Me* are n,π* triplets, whose energies are influenced by the solvent polarity. This could provoke an inversion of their relative triplets leading, in few ns-μs, to an excitation located on one or another of the fragments.

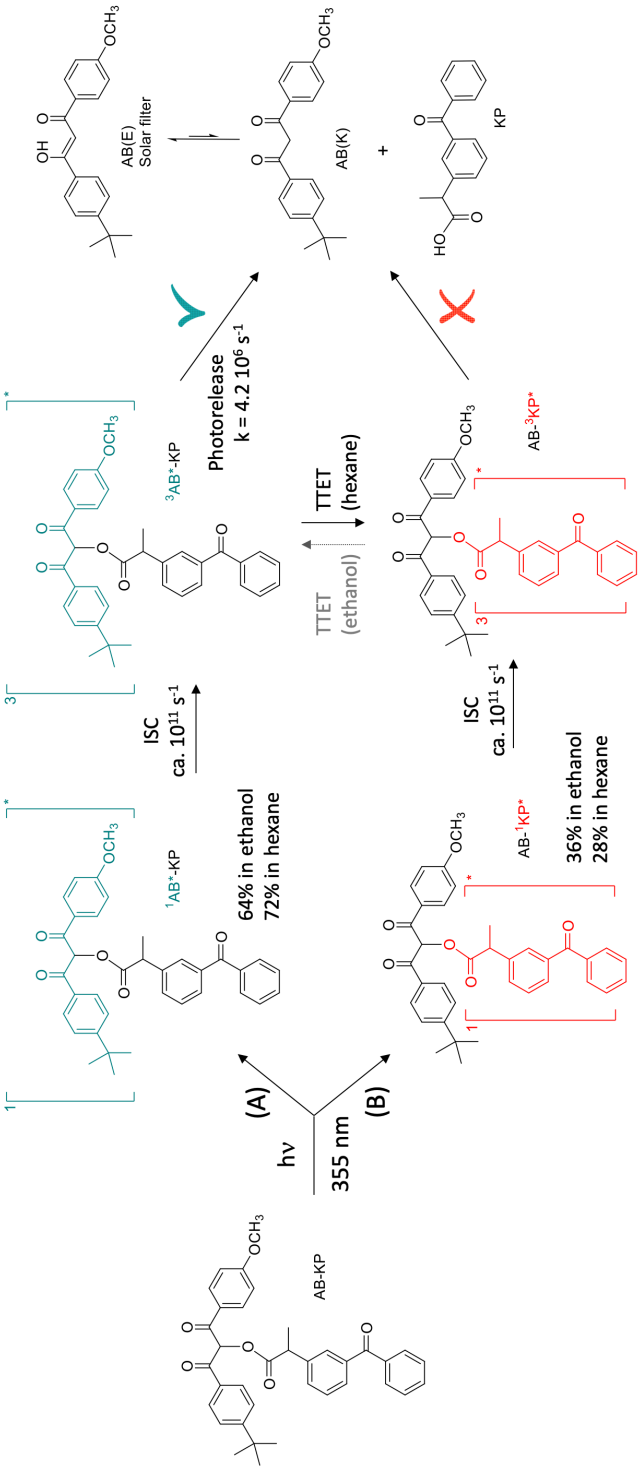

Scheme 3.2. Photodeactivation processes of AB-KP.

As shown in Scheme 3.2, after excitation, two different routes are possible depending on the excited chromophore. In the case of a 355 nm irradiation, most of the light is absorbed by AB (64% and 72% in ethanol and hexane, respectively). Pathway A leads to formation of a singlet excited state localized on the AB(K) moiety, followed by efficient population of ^{3}AB(K)*, which finally gives rise to the photouncaging process. If the light is absorbed by the KP moiety, a similar route (pathway B) takes place giving rise to KP singlet and triplet excited states. However, no photorelease is expected from this pathway.

In hexane, experimental and theoretical data have clearly demonstrated that the lowest triplet state is ^{3}KP*. Excitation of AB results in the formation, after ISC, of its triplet excited state ^{3}AB(K)*. However, an efficient triplet-triplet energy transfer (TTET) from ^{3}AB(K)* to the KP moiety deactivates the reactive phenacyl-like and decreases the proportion of the photorelease. Indeed, this latter process, with a rate constant k of *ca*. 4.2 x 10^6 s^{-1} (determined by using the equation: $1/\tau_0 = 1/\tau + k$, where τ_0 is lifetime of unreactive ^{3}AB-Me* and τ is the lifetime of ^{3}AB-KP*), competes with TTET (k of *ca*. 10^8 s^{-1}), and thus cannot represent more than 4% of the deactivation paths. The TTET process is evidenced by the ultrafast transient absorption experiments, which show a delayed formation of ^{3}KP* beginning 50 ps after the laser pulse. This has been unequivocally associated with TTET. Indeed, the lack of a ^{1}KP* signal at a short and long timescale is in complete agreement with this mechanism, ruling out not only the formation of ^{3}KP* by direct excitation, but also as a consequence of a singlet-singlet energy transfer between ^{1}AB(K)* and KP, followed by ISC. The TTET is moreover in accordance with the computational results that establish a ^{3}KP* as the lowest state as compared to the ^{3}AB(K)* excitation. Once, populated, ^{3}KP* should

deactivate through nonradiative processes or giving rise to the typical BP-like photochemistry (*ie*. mainly photoreduction).

By contrast, in ethanol, the excitation remains localized on the AB(K) moiety as demonstrated by the spectroscopic studies with the only detection of the ^{3}AB(K)* signal at 400 nm. This trend is again further confirmed by TD-DFT calculations, which demonstrated that in ethanol the optimized triplet on the AB moiety is lower in energy with respect to the optimized triplet on the KP moiety, thus allowing the photouncaging process to occur from the reactive phenacyl-like triplet state.

3.2.2. Photophysics of AB systems linked to a drug of lower triplet energy value

Thus far, the photophysical and photochemical properties of the AB-KP dyad have been studied in two different solvents (EtOH and hexane) for the purpose of assessing the solvent polarity effect on the photorelease process. These data point towards an important role of the relative triplet energy values (E_T) of both parts of the dyad. In this regard, in order to get an efficient photorelease of both components, it is postulated that the ^{3}AB(K)* should possess a lower energy than its caged compound. In this section, to get further evidences that support this statement, the new dyad made with naproxen (Chart 3.1), a NSAID with an E_T of *ca.* 40 kJ·mol^{-1} lower than E_T (AB(K)),[30,31] has been synthesized and compared in EtOH with AB-KP by means of spectroscopic techniques.

3.2.2.1. Fluorescence experiments

Since NPX exhibits fluorescent emission, we decided to investigate how its emission could be affected within the AB-NPX system. First of all, the absorption spectra of AB-NPX (Figure 3.13A) and of its components (Figure 3.13B) were registered in EtOH at same concentration (9 x 10^{-6} M). The UV-Vis spectrum of NPX in ethanol shows six absorption bands at 230, 261, 271, 281, 316 and 330 nm. Whereas AB-NPX shows two bands, one of them at 270 nm mainly coming from AB-Me, and the other one at 330 nm accounting for NPX.

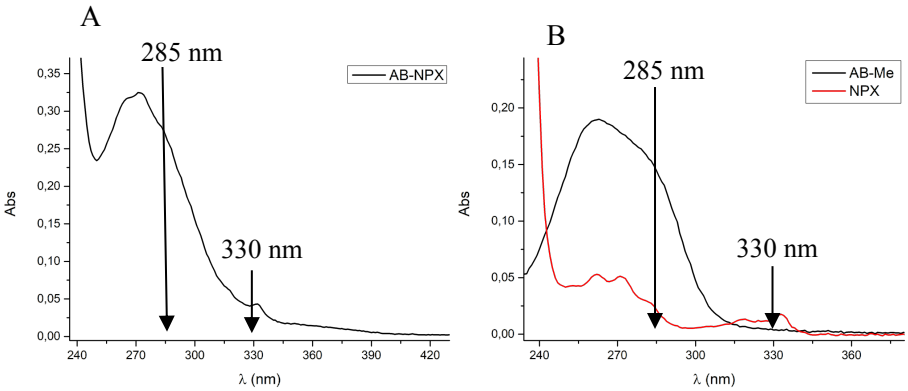

Figure 3.13. UV-Vis spectra of AB-NPX (A) and AB-Me and NPX (B) in ethanol at 9.5 x 10^{-6} M.

The fluorescence spectra of NPX and AB-NPX were recorded in EtOH. The concentration of NPX was adjusted in order to get an absorbance of *ca.* 0.1 at two different excitation wavelengths (λ_{exc}), 285 and 330 nm. Then, the sample of AB-NPX was prepared at the same concentration as NPX. The drug shows an emission band centered at 352 nm, which agrees with literature data[32,33] (Figure 3.14A), while the AB-NPX lacks of fluorescence (Figure 3.14B). Interestingly, the outcomes were the same, regardless of the

λ_{exc}, which indicates that the results are not affected by the percentage of light absorbed by each components of the dyad.

The lack of fluorescence in the AB-NPX system can be explained assuming that the n,π* singlet energy of AB(K) is lower than that of NPX. As a consequence, a singlet-singlet energy transfer from ^{1}NPX* to populate the non-fluorescent ^{1}AB(K)* occurs resulting in the deactivation of the singlet excited state of NPX.

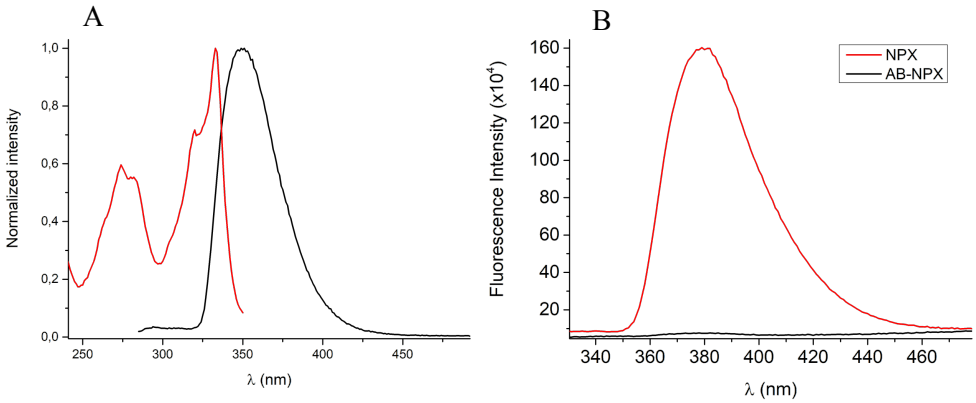

Figure 3.14. Normalized emission (λ_{exc} = 270 nm) and excitation spectra (λ_{em} = 370 nm) of NPX in EtOH (A). Fluorescence spectra of AB-NPX and NPX in EtOH (λ_{exc} = 285 nm) at 4 x 10^{-5} M (B).

Furthermore, the singlet energy of NPX was also calculated using eq. 3.1:

$$E_S = \frac{N\,h\,c}{\lambda_{0,0}} \quad (3.1)$$

Where N is the Avogadro number (6.022 x 10^{23} mol^{-1}), h is the Planck constant (6.626 x 10^{-34} J s), c is the light velocity (3 x 10^8 m s^{-1}), and $\lambda_{0,0}$ (337

x 10^{-9} m) is the wavelength obtained from the crossing point between its normalized emission and excitation spectra (Figure 3.14A). The obtained E_S of *ca.* 355 kJ·mol^{-1} is in agreement with literature data.[31]

3.2.2.2. Steady-state photolysis of the new system

Then, the new system AB-NPX was irradiated in deaerated ethanol solution, but in this case, contrary to what happened with AB-KP, no AB band was observed at any extent after 30 min of irradiation with SSL. According to our previous studies, this can be easily explained based on the low energy of ^{3}NPX*. As previously postulated for AB-KP in hexane, the ^{3}AB(K)* is quenched by NPX by means of TTET, so the photouncaging process is suppressed. This experiment supports that regardless of the presence of protic solvent, if the avobenzone-based system is made up of AB linked to a molecule with a lower triplet energy than AB(K), then the photorelease process does not work.

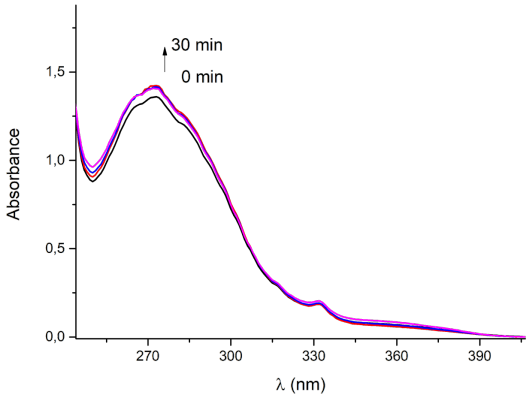

Figure 3.15. UV absorption changes for AB-NPX at 6.6 x 10^{-5} M in N_2 deaerated EtOH under SSL.

3.2.2.3. Laser flash photolysis experiment

Finally, LFP experiments were carried out to evaluate the population of ^{3}AB(K)* and ^{3}NPX* in the AB-NPX system. The transient absorption spectra of each compound were recorded in deaerated ethanol by means of a nanosecond pulsed laser (Nd:YAG) using 355 nm as excitation wavelength for AB-Me and AB-NPX, while NPX was measured using a laser pulse at 266 nm.

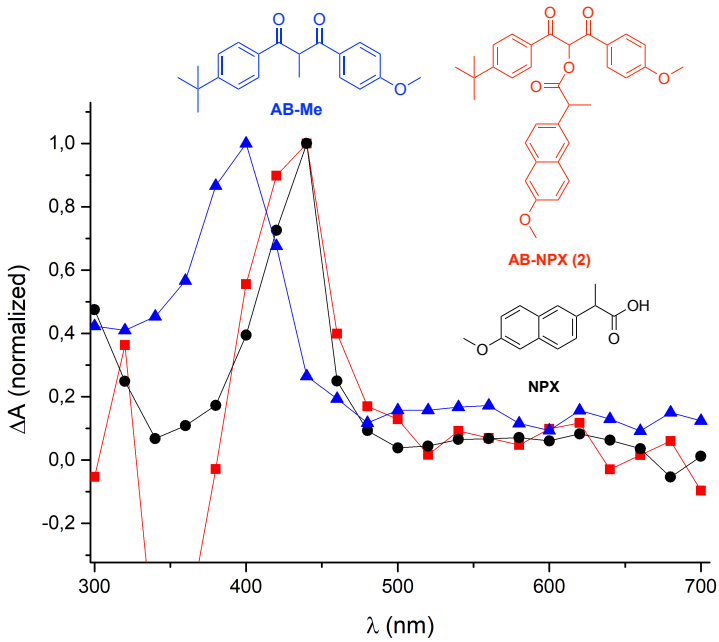

Figure 3.16. Normalized transient absorption spectra of AB-NPX (red line), NPX (black line) and AB-Me (blue line) in ethanol under N_2 at 1 μs after the laser pulse at 355 nm or 266 nm.

In Figure 3.16, the normalized transient absorption spectra of ^{3}AB-Me*, ^{3}NPX* and ^{3}AB-NPX* registered in deaerated ethanol, have been overlapped. Interestingly, after excitation of AB-NPX at 355 nm, no signal at

400 nm corresponding to ^{3}AB-Me* was detected. However, its transient absorption spectrum shows a band peaking at 440 nm, which can be safely assigned, by comparison with NPX, to the triplet-triplet transition of NPX fragment.

Besides, this band decays with a lifetime of 8.6 μs, which is consistent with the lifetime of NPX.[34] These LFP results, together with those obtained for AB-KP in hexane, support the deactivation of the photouncaging process by means of a TTET process from the ^{3}AB(K)* towards the drug-derived moiety. Depending on the excited chromophore in the AB-NPX system, two different pathways can happen (Scheme 3.3). After light absorption of AB(K) chromophore, route A, the result is mainly the same than in the case of AB-KP in hexane, its triplet state is deactivated by TTET towards the drug moiety. However, after direct excitation of NPX, route B, a SSET to AB(K) occurs (as previously mentioned in section 3.2.2.1), followed by ISC to give the ^{3}AB(K)* which is finally deactivated by TTET to NPX. Consequently, no photorelease is observed in the system AB-NPX in ethanol.

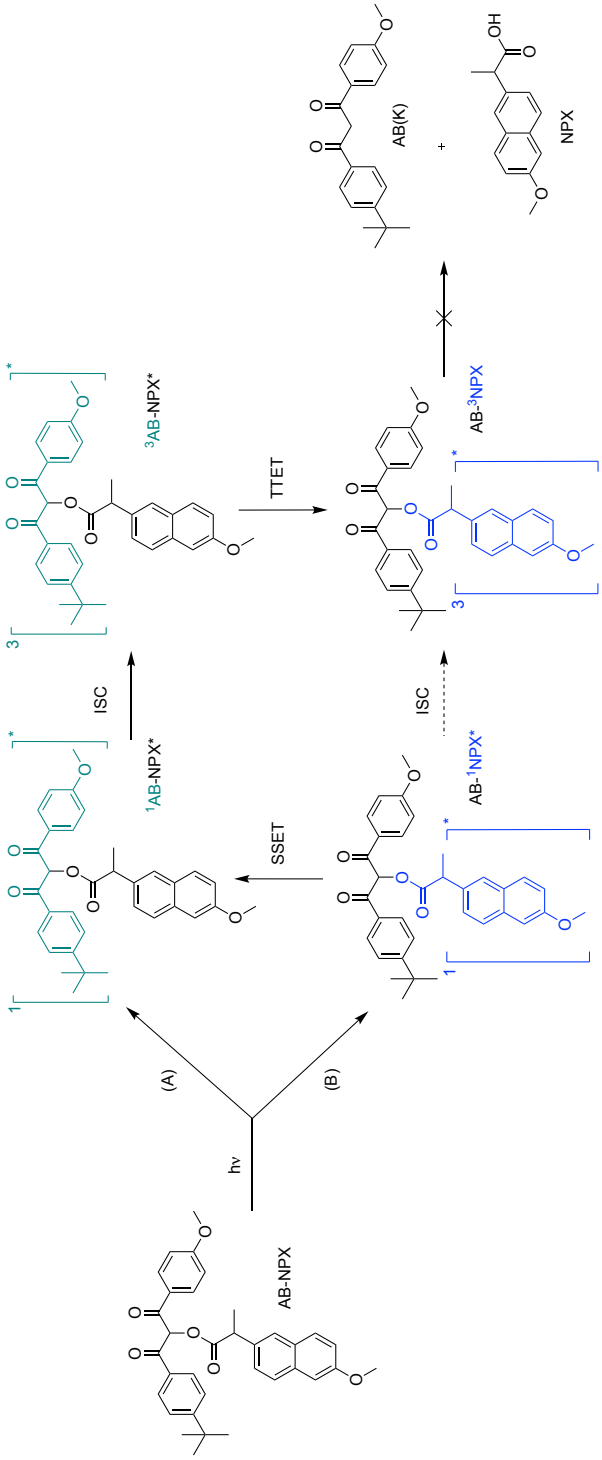

Scheme 3.3. Photodeactivation process of AB-NPX in ethanol.

3.3. Conclusion

In the present chapter, mechanistic studies of a sunscreen-based drug photocage containing the UVA-filter avobenzone and the photosensitizing drugs ketoprofen and naproxen are reported. For this purpose, both spectroscopic analysis and molecular modeling have been employed. The obtained results constitute an unambiguous proof of the importance of the relative energy value of the avobenzone triplet manifold with regard to its caged compound for an efficient photorelease to occur. In this regard, the avobenzone triplet has to be the component of the dyad with the lowest energy, otherwise it would be deactivated through triplet-triplet energy transfer toward the caged compound (*i.e.* ketoprofen or naproxen), resulting in the inactivation of the photouncaging process. These findings are of high value for the design and the optimization of the photorelease conditions of new sunscreen-based drug photocages.

3.4. Experimental section

3.4.1. Synthesis

AB-KP, AB-NPX, AB-Me and KP-Me were prepared following similar procedures to those previously described in the literature.[17,21,35]

Synthesis of 2-bromo-1-(4-(*tert*-butyl)phenyl)-3-(4-methoxyphenyl)propane-1,3-dione (AB-Br)[17]

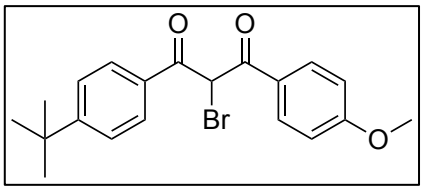

Two solids, avobenzone (AB, 2 g, 6.4 mmol) and *N*-bromosuccinimide (1.14 g, 6.4 mmol) were mixed under solvent free conditions in a mortar. The mixture was mixed each 15 minutes during 2 h. Then, water was added and the solution was filtered under vacuum. The solid was left overnight to dry up. Purification was performed by flash chromatography using cy:AcOEt (6:1, v:v) as eluent. Colorless crystals of AB-Br were obtained (1.81 g) in a 73% yield.

^{1}H NMR (300 MHz, $CDCl_3$): δ (ppm) 8.01 (d, J = 9 Hz, 2H), 7.93 (d, J = 8.6 Hz, 2H), 7.46 (d, J = 8.6 Hz, 2H), 6.93 (d, J = 9.0 Hz, 2H), 6.48 (s, 1H), 3.86 (s, 3H), 1.31 (s, 9H).

HRMS (ESI-TOF): *m/z*, $C_{20}H_{22}BrO_3$ $[M + H]^+$ calculated for 389.0752; found: 389.0746.

Synthesis of 1-(4-(*tert*-butyl)phenyl)-3-(4-methoxyphenyl)-1,3-dioxopropan-2-yl 2-(6-methoxynaphthalen-2-yl)propanoate (AB-NPX)[17]

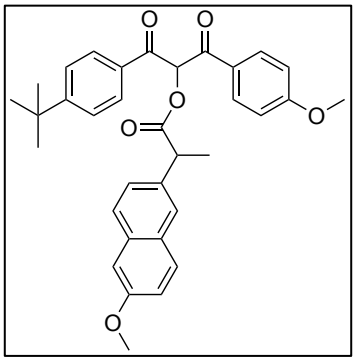

First, cesium naproxen salt was formed by titration of a naproxen water solution (0.1 M) against a cesium carbonate water solution (4 M) until pH stabilized at 7. Then, water was removed to afford the corresponding cesium salt, which was redissolved (1.41 g, 3.9 mmol) in 15 mL of DMF and added to a flask containing AB-Br (0.6 g, 1.54 mmol). After 24 hours of stirring, the solvent was evaporated and the reaction was purified by flash chromatography, cy:AcOEt, (7:1, v:v). The product, was obtained in a 69 % yield (0.572 g).

^{1}H NMR (300 MHz, $CDCl_3$): δ (ppm) 8.03 – 7.93 (m, 4H), 7.86 – 7.74 (m, 3H), 7.60 – 7.49 (m, 1H), 7.46 - 7.33 (m, 2H), 7.30 - 7.22 (m, 2H), 6.95 (s+s, 1H), 6.81 (d, J = 8.9 Hz, 1H), 6.74 (d, J = 8.9 Hz, 1H), 4.18 (q, J = 7.0 Hz, 1H), 4.05 (s, 3H), 3.84 (s+s, 3H), 1.78 (d+d, J = 6.9, 3H), 1.38 (s+s, 9H).

^{13}C NMR (75 MHz, $CDCl_3$): δ (ppm) 190.7, 190.7, 189.4, 173.0, 164.2, 164.1, 157.9, 157.8, 134.8, 133.9, 132.1, 132.0, 131.8, 131.6,

129.6, 129.5, 129.5, 129.4, 129.0, 127.4, 127.2, 127.1, 126.5, 125.6, 125.5, 119.0, 119.0, 113.8, 113.7, 105.7, 105.7, 81.1, 55.4, 55.4, 55.3, 45.3, 45.3, 35.2, 35.2, 31.0, 30.9, 18.2.

HRMS (ESI-TOF): *m/z*, $C_{34}H_{35}O_6$ $[M + H]^+$ calculated for 539.2434; found: 539.2435.

Synthesis of 1-(4-(*tert*-butyl)phenyl)-3-(4-methoxyphenyl)-1,3-dioxopropan-2-yl 2-(3-benzoylphenyl)propanoate (AB-KP)[17]

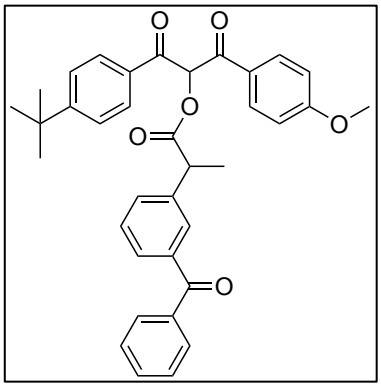

First, cesium ketoprofen salt was formed by titration of a ketoprofen water solution (0.1 M) against a cesium carbonate water solution (4 M) until pH stabilized at 7. Then, water was removed to afford the corresponding cesium salt (1.23 g, 3.2 mmol) which was redissolved in 12.8 mL of DMF and added to a flask containing AB-Br (0.5 g, 1.28 mmol). After 17 hours of stirring, the solvent was evaporated and the reaction was purified by flash chromatography, cy:AcOEt, (4:1, v:v). The product, was obtained in a 62 % yield (0.446 g, 0.79 mmol).

^{1}H NMR (300 MHz, $CDCl_3$): δ (ppm) 8.06 – 7.81 (m, 4H), 7.76-7.65 (m,, 4H), 7.64-7.52 (m, 2H), 7.51-7.33 (m, 5H), 6.91 – 6.75 (m, 3H), 3.99 (q+q, J = 7.2 Hz, 1H), 3.82 (s+s, 3H), 1.62 (d+d, J = 7.2 Hz, 3H), 1.28 (s, 9H).

Synthesis of 1-(4-(*tert*-butyl)phenyl)-3-(4-methoxyphenyl)-2-methylpropane-1,3-dione (AB-Me)[21]

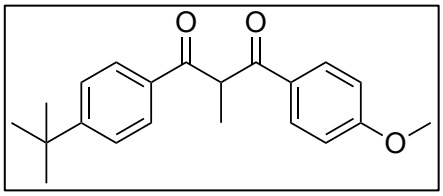

To a deaerated solution of avobenzone (1 g, 3.2 mmol) in acetone (50 mL) were added an excess of iodomethane (1.9 g, 12.9 mmol) and K_2CO_3 (0.9, 6.4 mmol). The solution was stirred overnight at 45ºC. Then, the crude product was filtered under reduced pressure to remove the KI formed as a white powder. The solvent from the collected organic phase was removed under reduced pressure. Finally, purification was performed by column chromatography (cy:AcOEt, 60:40) affording pure product AB-Me. Yield: 70%

^{1}H NMR (300 MHz, $CDCl_3$): δ (ppm) 7.94 (d, J = 9 Hz, 2H), 7.90 (d, J = 8.4 Hz, 2H), 7.41 (d, J = 8.4 Hz, 2H), 6.88 (d, J = 9 Hz, 2H), 5.19 (q, J = 6.9 Hz, 1H), 3.83 (s, 3H), 1.57 (d, J = 6.9 Hz, 3H), 1.31 (s, 9H).

Synthesis of methyl 2-(3-benzoylphenyl)propanoate (KP-Me)[35]

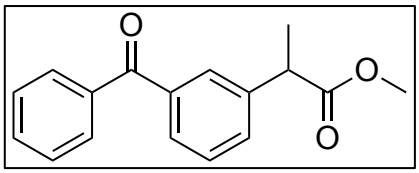

To a dry flask containing *(S)*-Ketoprofen (1 g, 3.9 mmol) in methanol (39 mL) was added H_2SO_4 (0.04 g, 0.39 mmol). The solution was stirred overnight at 75ºC and then cooled to room temperature. Then, the solvent was removed under reduced pressure. The crude was redissolved in DCM and washed with a $NaHCO_4$ saturated solution. Finally, the organic phase was dried with anhydrous $MgSO_4$, filtered, and the filtrate was concentrated in vacuo. The pure product KP-Me was used without further purification. Yield: 1.01 g (94 %).

^{1}H NMR (300 MHz, $CDCl_3$): δ (ppm) 7.90 – 7.33 (m, 9H), 3.77 (q, J = 7.2 Hz, 1H), 3.67 (s, 3H), 1.53 (d, J = 7.2 Hz, 3H).

3.4.2. NMR spectra.

^{1}H NMR ($CDCl_3$, 300 MHz)

AB-Br

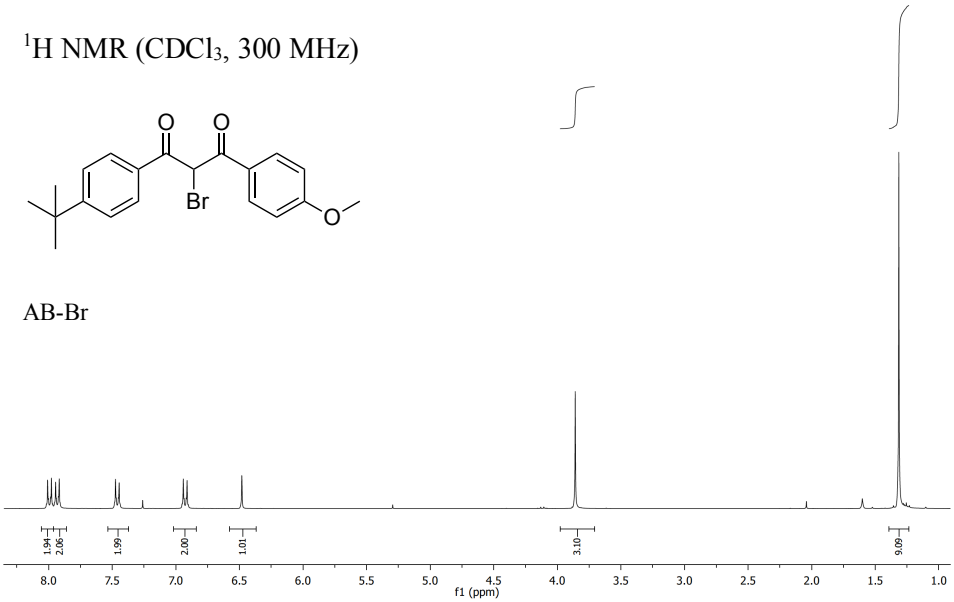

^{1}H NMR ($CDCl_3$, 300 MHz)

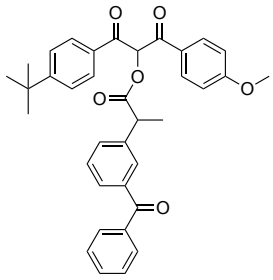

AB-KP

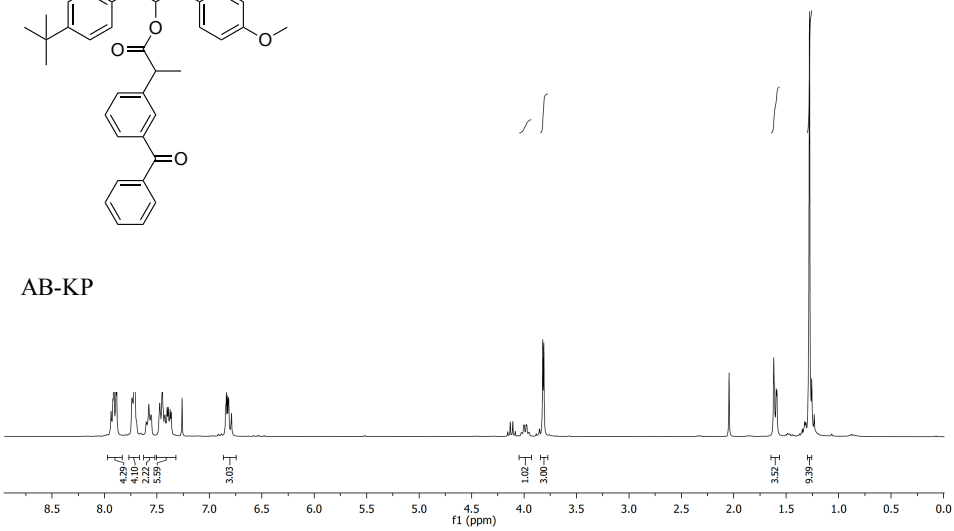

^{1}H NMR ($CDCl_3$, 300 MHz)

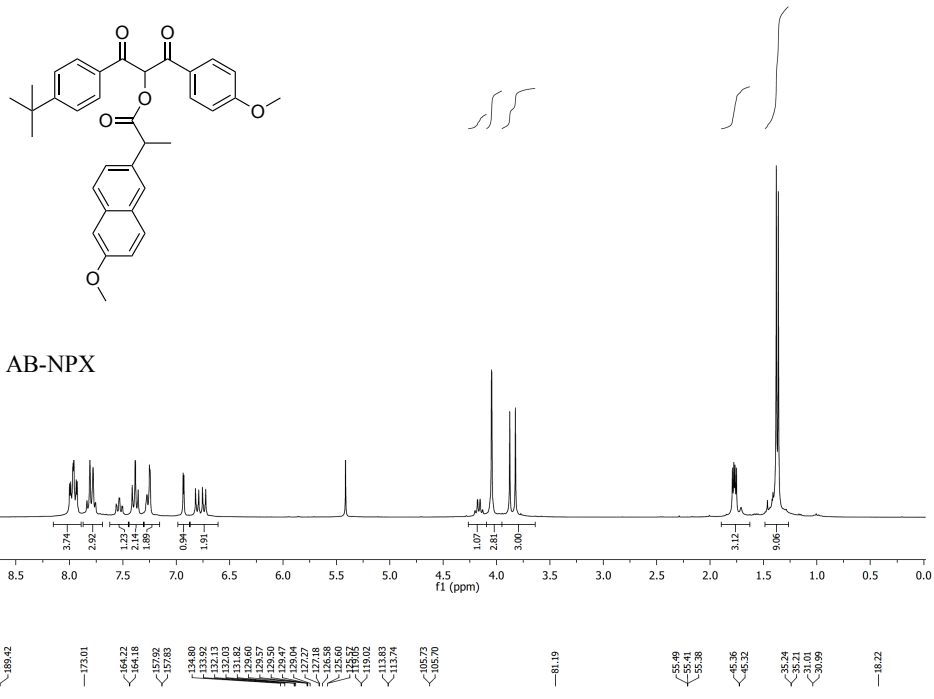

^{13}C NMR ($CDCl_3$, 75 MHz)

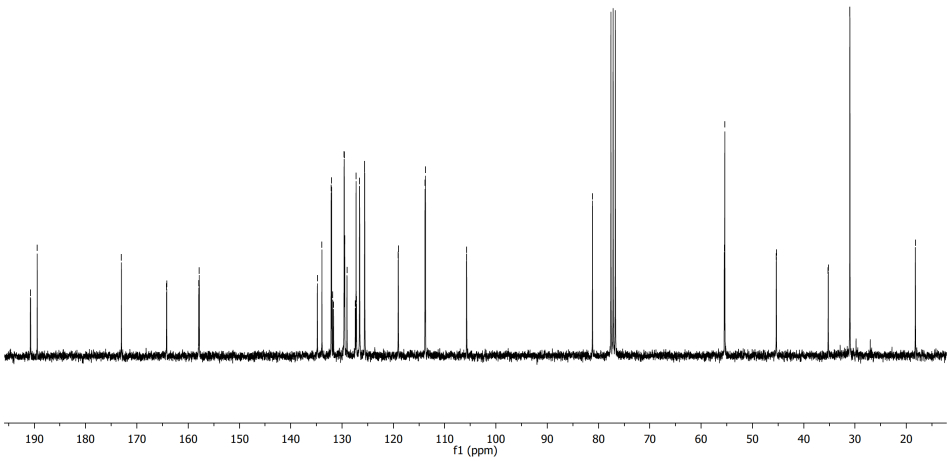

^{1}H NMR ($CDCl_3$, 300 MHz)

AB-Me

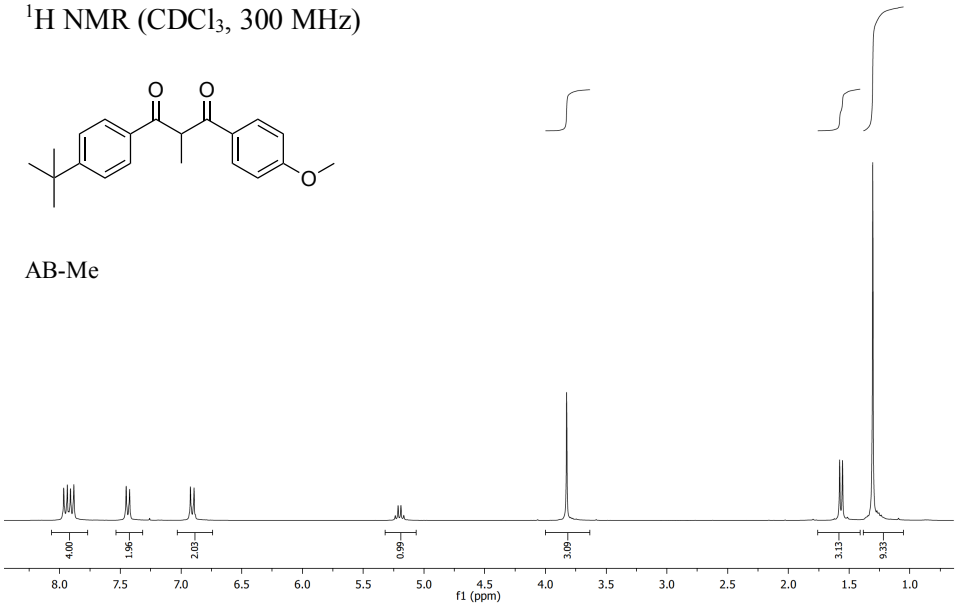

^{1}H NMR ($CDCl_3$, 300 MHz)

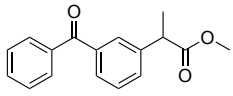

KP-Me

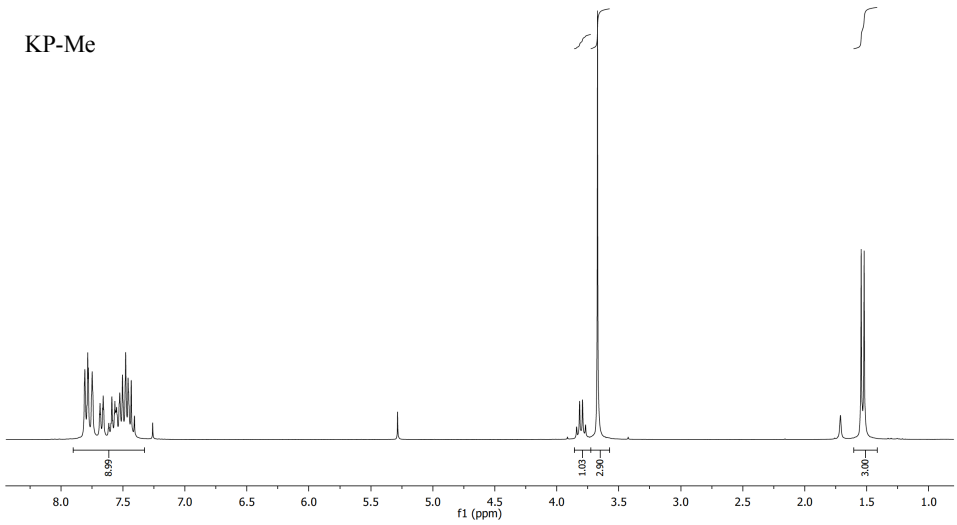

3.5. Bibliography

1 J. A. Barltrop and P. Schofield, *J. Chem. Soc.*, 1965, 4758–4765.

2 J. A. Barltrop, P. J. Plant and P. Schofield, *Chem. Commun.*, 1966, 822–823.

3 J. C. Sheehan and K. Umezawa, *J. Org. Chem.*, 1973, **38**, 3771–3774.

4 P. Klán, T. Šolomek, C. G. Bochet, A. Blanc, R. Givens, M. Rubina, V. Popik, A. Kostikov and J. Wirz, *Chem. Rev.*, 2013, **113**, 119–191.

5 J. M. Silva, E. Silva and R. L. Reis, *J. Control. Release*, 2019, **298**, 154–176.

6 A. Herrmann, *Angew. Chem. Int. Ed.*, 2007, 46, 5836–5863.

7 Y. Wu, Z. Yang and Y. Lu, *Curr. Opin. Chem. Biol.*, 2020, **57**, 95–104.

8 R. S. Stoll and S. Hecht, *Angew. Chem. Int. Ed.*, 2010, **49**, 5054–5075.

9 M. Hocek, *Acc. Chem. Res.*, 2019, **52**, 1730–1737.

10 E. Speckmeier and K. Zeitler, *ACS Catal.*, 2017, **7**, 6821–6826.

11 K. A. Korzycka, P. M. Bennett, E. J. Cueto-Diaz, G. Wicks, M. Drobizhev, M. Blanchard-Desce, A. Rebane and H. L. Anderson, *Chem. Sci.*, 2015, **6**, 2419–2426.

12 M. J. Hansen, W. A. Velema, M. M. Lerch, W. Szymanski and B. L. Feringa, *Chem. Soc. Rev.*, 2015, **44**, 3358–3377.

13 M. Klausen, V. Dubois, J. B. Verlhac and M. Blanchard-Desce, *Chempluschem*, 2019, 84, 589–598.

14 C. Brieke, F. Rohrbach, A. Gottschalk, G. Mayer and A. Heckel, *Angew. Chem. Int. Ed.*, 2012, **51**, 8446–8476.

15 Y. Q. Yang, Z. Lu and X. Xu, *Asian J. Org. Chem.*, 2019, **8**, 2192–2195.

16 E. Speckmeier, M. Klimkait and K. Zeitler, *J. Org. Chem.*, 2018, **83**, 3738–3745.

17 I. Aparici-Espert, M. C. Cuquerella, C. Paris, V. Lhiaubet-Vallet and M. A. Miranda, *Chem. Commun.*, 2016, **52**, 14215–14218.

18 I. Aparici-Espert, M. A. Miranda and V. Lhiaubet-Vallet, *Molecules*, 2018, **23**, 673–683.

19 V. Lhiaubet-Vallet and M. A. Miranda, in *CRC Handbook of Organic Photochemistry and Photobiology.*, eds. F. Ghetti, A. G. Griesbeck and M. Oelgemöller, CRC Press, 2012, pp. 1541–1555.

20 E. Bignon, M. Marazzi, V. Besancenot, H. Gattuso, G. Drouot, C. Morell, L. A. Eriksson, S. Grandemange, E. Dumont and A. Monari, *Sci. Rep.*, 2017, **7**, 8885.

21 C. Paris, V. Lhiaubet-Vallet, O. Jiménez, C. Trullas and M. A. Miranda, *Photochem. Photobiol.*, 2009, **85**, 178–184.

22 V. Lhiaubet-Vallet, M. Marin, O. Jimenez, O. Gorchs, C. Trullas and M. A. Miranda, *Photochem. Photobiol. Sci.*, 2010, **9**, 552–558.

23 M. Montalti, A. Credi, L. Prodi and T. M. Gandolfi, *Handbook of Photochemistry, Third Edition*, CRC Press, 2006.

24 N. J. Turro, V. Ramamurthy and Scaiano J. C., *Principles of Molecular Photochemistry: An Introduction*, University Science Books, 2009.

25 V. Lhiaubet, F. Gutierrez, F. Penaud-Berruyer, E. Amouyal, J. P. Daudey, R. Poteau, N. Chouini-Lalanne and N. Paillous, *New J. Chem.*, 2000, **24**, 403–410.

26 F. Boscá and M. A. Miranda, *J. Photochem. Photobiol. B Biol.*, 1998, **43**, 1–26.

27 R. L. Martin, *J. Chem. Phys.*, 2003, **118**, 4775–4777.

28 T. Etienne, X. Assfeld and A. Monari, *J. Chem. Theory Comput.*, 2014, **10**, 3896–3905.

29 T. Etienne, X. Assfeld and A. Monari, *J. Chem. Theory Comput.*, 2014, **10**, 3906–3914.

30 C. Paris, V. Lhiaubet-Vallet, O. Jiménez, C. Trullas and M. Á. Miranda, *Photochem. Photobiol.*, 2009, **85**, 178–184.

31 L. J. Martinez and J. C. Scaiano, 1998, **68**, 646–651.

32 M. A. Husain, Z. Yaseen, S. U. Rehman, T. Sarwar and M. Tabish, *FEBS J.*, 2013, **280**, 6569–6580.

33 P. Damiani, M. Bearzotti and M. A. Cabezón, *J. Pharm. Biomed. Anal.*, 2002, **29**, 229–238.

34 F. Boscá, M. L. Marín and M. A. Miranda, *Photochem. Photobiol.*, 2001, **74**, 637.

35 C. D.-T. Nielsen, A. J. P. White, D. Sale, J. Bures and A. C. Spivey, *J. Org. Chem.*, 2019, **84**, 14965–14973.

Chapter 4:

Oxybenzone-based photocages for the photorelease of carbonyl groups

4.1. Introduction

Among the available photoremovable protecting groups (PPGs), relatively few have found utility for caging carbonyl functional groups.[1–4] These PPGs are applicable not only in multi-step organic synthesis, where carbonyl groups often require protection against nucleophiles, oxidative or reductive agents, but also for biological purposes to release bioactive compounds. Early work on carbonyl caging compounds was based on acetals from o-nitrophenylethylene glycol.[5,6] Later, a series of 1,3-dioxolane and 1,3-dioxane derivatives have been investigated to optimize the photouncaging process.[3,7–13]

This chapter aims for the development of a new sunscreen-based photocage system for protecting carbonyl groups. As already mentioned in the previous chapter, the use of sunscreen-based photocages is of special interest because they offer the added value of concomitant release of a UVA filter. This design makes special sense for caging carbonyl compounds in view of their well-established photoreactivity.[14,15]

In this chapter, the commercial UVA/UVB filter oxybenzone (OB, 2-hydroxy-4-methoxybenzophenone, Figure 4.1) has been the cornerstone of our new carbonyl photocage design. Actually, as in the case of AB derived systems, this solar filter plays a dual role acting not only as a PPG but also providing an efficient UV shield effect to protect the carbonyl-derived compound after its photorelease. We have proven the concept studying new carbonyl photocages for the photorelease of OB along with benzophenone (BP) or its water-soluble derivative (4-carboxybenzophenone, CBP). This design points to a possible therapeutic approach to reduce the severe photoadverse effects of drugs containing a carbonyl chromophore. In this sense, this new photolabile protecting group has been applied for the photorelease of KP.

4.2. Results and discussion

4.2.1. Design and synthesis of a new dyad model based on oxybenzone filter

A new system made up of the oxybenzone solar filter (OB) linked to benzophenone (BP) by means of an ether linkage was designed and synthesized to evaluate the ability of the OB to act as a PPG (Chart 4.1).

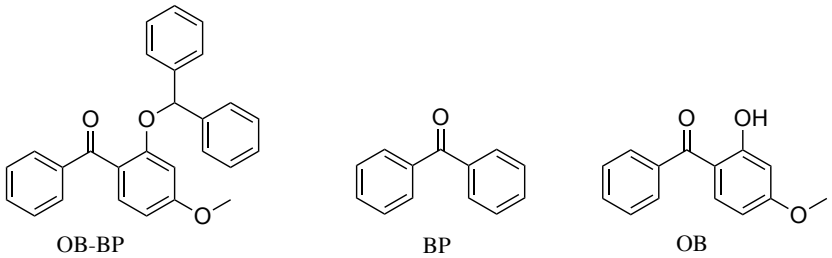

Chart 4.1. Structure of the model dyad OB-BP and its components OB and BP.

Benzophenone was chosen as the carbonyl compound for the design of our prodrug/profilter model system, since it is the main structural unit of KP which is a nonsteroidal anti-inflamatory drug (NSAID) responsible for pronounced cutaneous photosensitization. Regarding the OB filter, we chose it as a possible PPG for carbonyl compound because of its structural similarities to 1-alkoxy-9,10-anthraquinones (Scheme 4.1). These latter compounds have been extensively studied by Blankespoor and co-workers for their ability to release carbonyl compounds upon light absorption in MeOH and subsequent exposure to air (Scheme 4.1).[16–18]

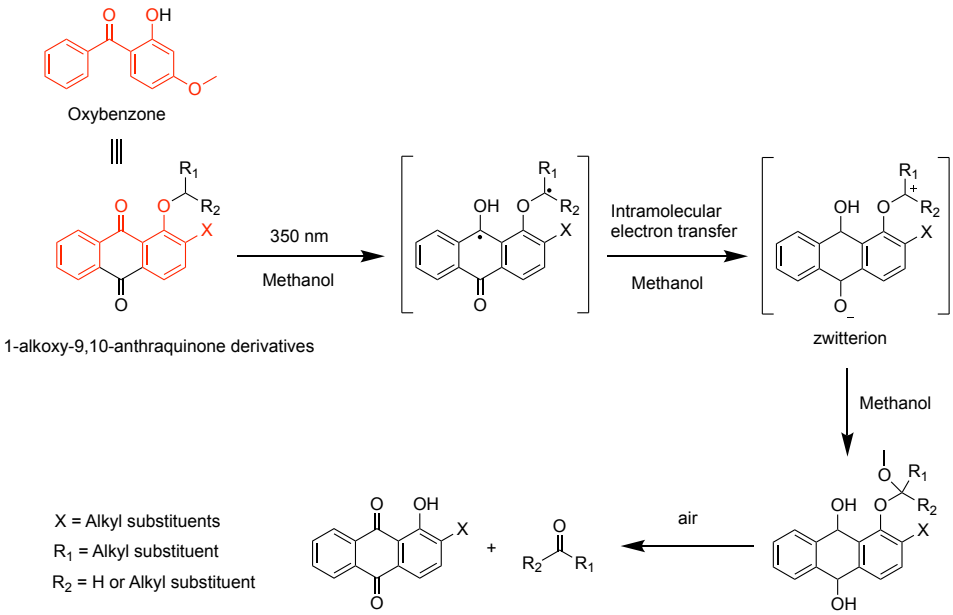

Scheme 4.1. Structural similarities between oxybenzone and 1-alkoxy-9,10-anthraquinone derivatives and the literature proposed mechanism for the photorelease of aldehydes and ketones from the latter compounds.

The synthesis of compound OB-BP was accomplished by alkylation of oxybenzone using as alkylating agent bromodiphenylmethane through a two-phase procedure using a phase-transfer catalyst (Scheme 4.2).[19]

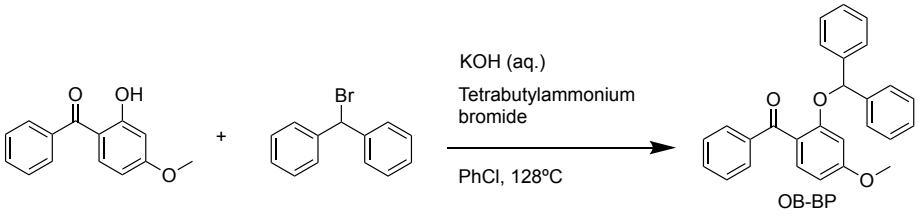

Scheme 4.2. Synthesis of compound OB-BP.

The UV-Vis spectra of OB-BP, OB and BP were registered in MeOH at same concentration to select the appropriate irradiation source for the steady-state experiments and also to evaluate whether the OB would protect, or not, the BP from such irradiation source (Figure 4.1). The UV-Vis absorption spectrum of the BP exhibits a maximum at 250 nm, whereas the OB, as expected for a UVA/UVB filter, shows two absorption bands with maxima at *ca.* 287 and 325 nm, which should protect the former from the SSL. In the case of the dyad, its absorption does not show the UVA absorption band of the oxybenzone since the hydroxy group responsible for such absorption has been converted into an ether linkage, however, it still shows a band that reaches the UVA region (up to 375 nm), allowing its irradiation using simulated sunlight (SSL). The same happened with the absorption band of the BP which was lacking since it was reduced to afford the alcohol group used to form the mentioned ether linkage through a Mitsunobu reaction.

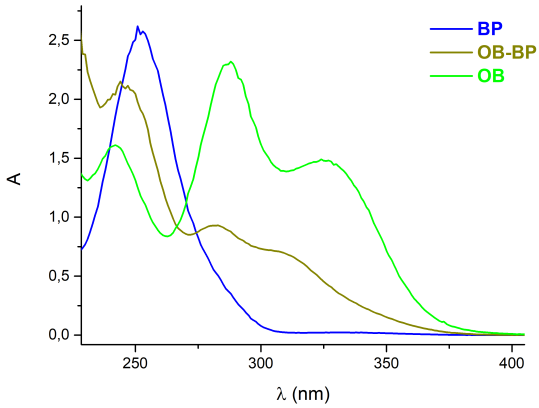

Figure 4.1. UV-Vis absorption spectra of compounds OB-BP, OB and BP at same concentration (1.3 x 10^{-4} M) in MeOH.

4.2.2. Preliminary steady-state photolysis study of OB-BP

As a first step, the capacity of the new photolabile system OB-BP to release its components was analyzed using different MeOH:H_2O proportions. This analysis was carried out to determine if the photolysis of OB-based system is affected by solvent polarity as is the case with anthraquinone-based systems.[17] For that, the dyad was irradiated with SSL provided by the filtered emission of a xenon arc lamp in aerated MeOH solution using increasing amount of H_2O (0, 10, 20, 40, 60 and 90%). The irradiations were followed by UV-Vis absorption following the characteristic band at 325 nm of the OB. From these studies, the appearance of the OB characteristic band seemed to be favored in the presence of 40% water (Figure 4.2B), while lower or higher water percentages resulted in an apparently decrease of the photorelease process. Next, to get a more accurate analysis, compound OB-BP was irradiated in MeOH (100%) and in MeOH:H_2O (60:40, v:v) and aliquots were taken at different times for their subsequent analysis by HPLC-DAD (Figure 4.2C and 4.2D). The peaks corresponding to OB-BP, OB and BP were assigned by comparison with standards and their quantification was accomplished by means of calibration curves.

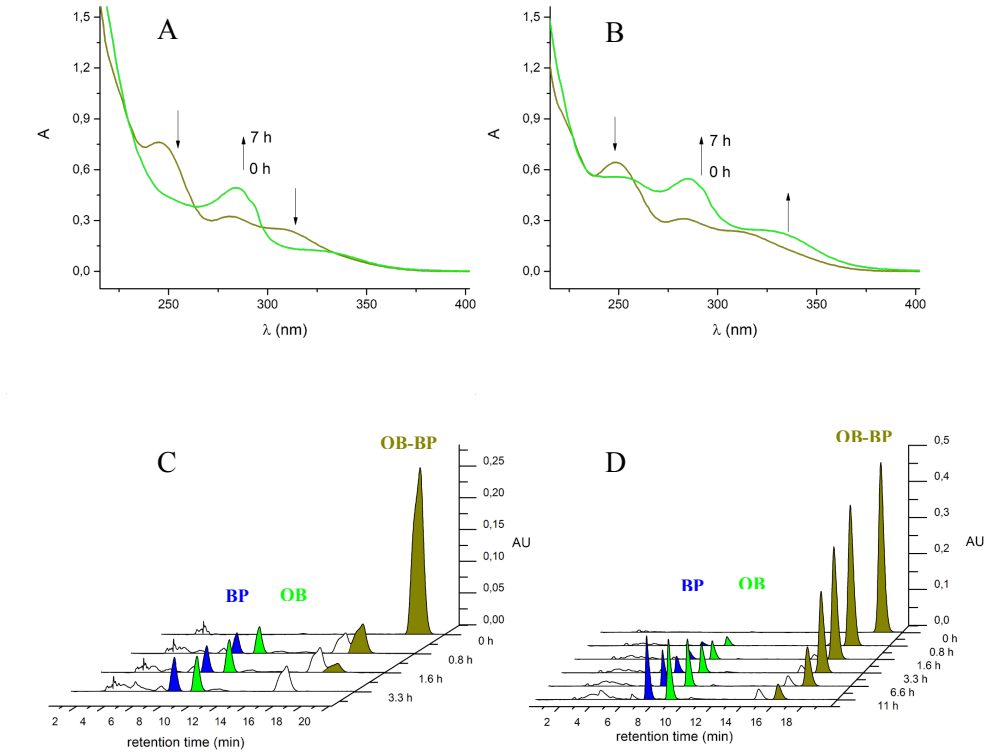

Figure 4.2. (A) and (B) UV-Vis spectra changes of aerated solutions of OB-BP (4 x 10^{-5} M) in MeOH and MeOH:H_2O (60:40, v:v), respectively, irradiated for 7h with SSL, (C) and (D) HPLC chromatograms registered at 250 nm for an aerated MeOH and for an aerated MeOH:H_2O (60:40, v:v) solution, respectively, of OB-BP ($1.7x10^{-4}$ M) upon irradiation at different times with SSL.

The photoprocess was faster in the absence of water (Figure 4.2C), where the dyad is totally consumed in 3.3 h. At that time, BP and OB were released in a yield of 11% and 24%, respectively, together with a major photoproduct of unknown identity with a retention time of 15 min. On the other hand, when the dyad was irradiated in the presence of 40% of H_2O (Figure 4.2D), it was only consumed in a 52% after 3.3 h. Under these conditions, the process was not only slower but it was also cleaner, being less

favored the formation of the unknown photoproduct. Regarding the efficiency of the process in the presence of water, after *ca.* 11 h of irradiation, a release yield of 27% and 56% of BP and OB was obtained, respectively. Some UPLC-MS analysis were carried out in order to figure out the nature of the secondary compounds responsible for the lower release yield of BP compared to OB. Unfortunately, no clear evidence was obtained from these analysis.

Moreover, the ability of OB to protect BP from its photodegradation was confirmed by HPLC analysis of SSL irradiations of BP alone and in the presence of OB. From the irradiation of BP alone, a 44% of the initial BP was consumed after 6.6 h of irradiation (Figure 4.3A). In contrast, BP was found to be photostable when irradiated in the presence of OB (Figure 4.3B). With these results, the ability of the sunscreen to protect the BP against its photodegradation under the irradiation conditions was proved.

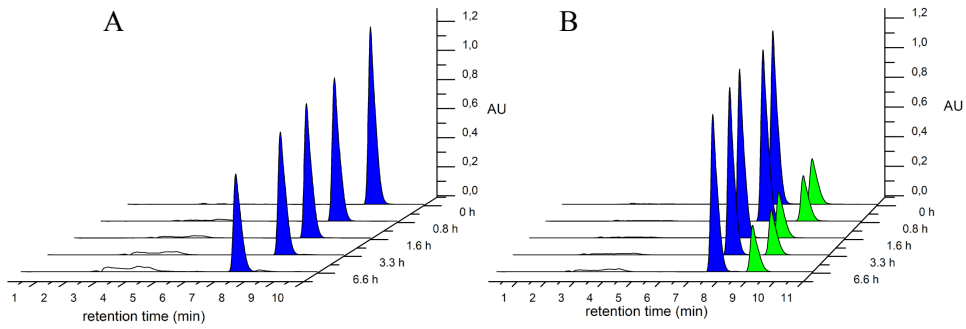

Figure 4.3. HPLC chromatograms registered at 250 nm of BP ($1.7x10^{-4}$M) (A) and of an equal mixture of BP:OB ($1.7x10^{-4}$M) (B) in aerated MeOH:H_2O (60:40, v:v) irradiated with SSL.

4.2.3. Characterization of the triplet excited state

First, laser flash photolysis experiments (LFP, using the 3rd harmonic of a Nd:YAG laser at 355 nm) of dyad OB-BP were carried out to get information on the transition species involved in the photochemical process. Transient absorption spectra with three bands centered at *ca*. 340, 500 and 680 nm were observed in MeCN and MeOH solution under N_2 (Figure 4.4). These bands decay with a similar lifetime without leading to further detectable species. For example, in the case of MeCN, these three bands decay with a lifetime in the range of 0.35-0.4 μs.

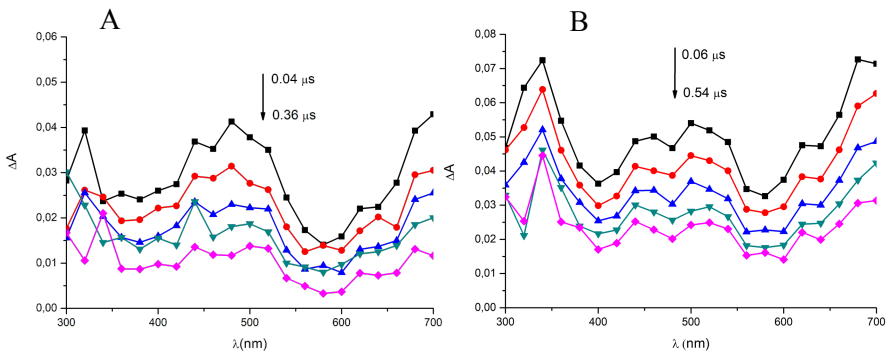

Figure 4.4. Transient absorption spectra of OB-BP in MeOH (A) and MeCN (B) under N_2 at different times after the laser pulse at 355 nm.

Moreover, oxygen quenching experiments were performed in MeOH. The oxygen quenching rate constant of OB-BP was determined at 480 and 700 nm by means of the Stern-Volmer equation (4.1).

$$\frac{\tau_0}{\tau} = 1 + k_q \tau_0 [Q] \quad (4.1)$$

Where τ_0 is the lifetime of OB-BP under deaerated conditions (s); τ is the lifetime of OB-BP at different O_2 concentrations (s); [Q] refers to the

oxygen concentrations[20] (M) and k_q refers to the oxygen quenching rate constant (M^{-1} s^{-1}). A value of k_q in the order of 10^9 M^{-1} s^{-1} was obtained at both wavelengths (Figure 4.5). Thus, these bands were assigned to triplet-triplet transitions.

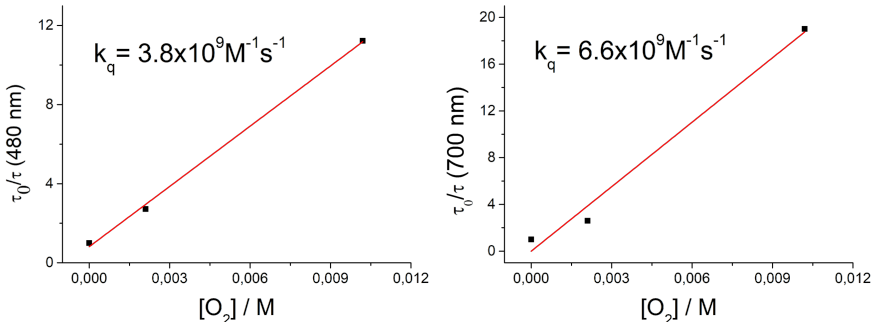

Figure 4.5. Stern-Volmer plots obtained for quenching of OB-BP by oxygen using decays registered at 480 and 700 nm. Inset: quenching rate constants

Next, the phosphorescence emission spectrum of the dyad was recorded in EtOH at 77K to determine the energy value of the triplet excited state (Figure 4.6). For that purpose, an ethanolic stock solution of OB-BP was prepared adjusting its absorbance at the excitation wavelength (λ_{exc}=306 nm) at *ca.* 0.8 with a cuvette of 1 cm optical pathway. A value of E_T of *ca*. 293 kJ mol^{-1} (70 kcal mol^{-1}) was calculated using eq. 4.2.

$$E_T = \frac{N\,h\,c}{\lambda_{0-0}} \quad (4.2)$$

Where N is the Avogadro number (6.022 x 10^{23} mol^{-1}), h is the Planck constant (6.626 x 10^{-34} J s), c is the light velocity (3x 10^{8} m s^{-1}), and $\lambda_{0\text{-}0}$ is the wavelength corresponding to the first emission band (m).

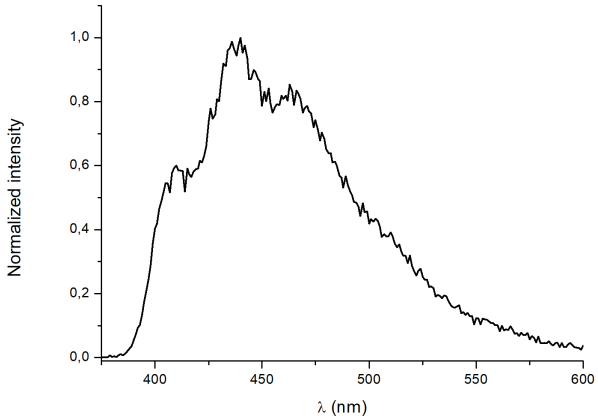

Figure 4.6. Phosphorescence emission spectrum of OB-BP in EtOH at 77K, λ_{exc}= 306 nm

Additionally, in order to characterize and confirm the triplet nature of the transition bands, TTET experiments were performed by laser flash photolysis (λ_{exc}=355 nm). For these experiments, 1-methylnaphthalene (MNP) was chosen because (*i*) it does not absorb at the excitation wavelength, (*ii*) its triplet excited state energy (254 kJ mol^{-1}) is lower than that of OB-BP and (*iii*) its triplet-triplet transient absorption spectrum does not overlap any bands of OB-BP one.[20]

Figure 4.7 shows the transient absorption spectra of the dyad OB-BP in the presence of 0.24 eq of MNP. This experiment was performed using a stock solution of OB-BP adjusted to an absorbance of 0.35 at the excitation

wavelength (λ_{exc}=355 nm) in MeCN. As expected from the relative energies of their triplet excited states, after selective excitation at 355 nm of OB-BP, a TTET to MNP occurred resulting in the disappearance of the band at 500 nm of the OB-BP concomitantly with the appearance of a new band at 420 nm corresponding to MNP.

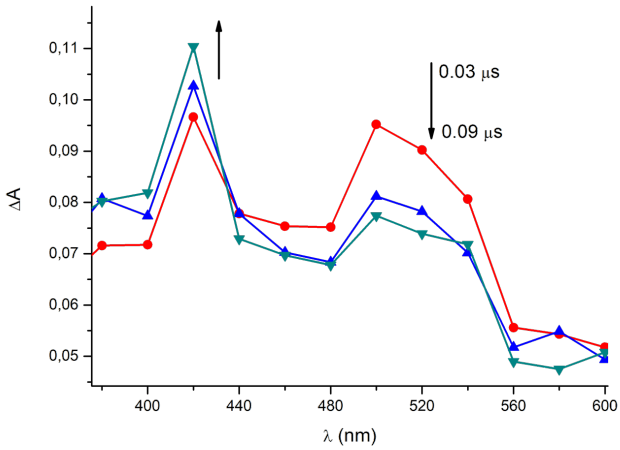

Figure 4.7. TTET from OB-BP to MNP in MeCN. Transient absorption spectra obtained for a solution of OB-BP and MNP (0.24 eq) at different time delays after the 355 nm laser excitation.

4.2.4. Nature and reactivity of the triplet excited state

Transient absorption spectra were compared in solvents of different polarities, ie. cyclohexane (Cy), acetonitrile (MeCN) and a mixture 60:40 of methanol:water (MeOH:H_2O). As expected for methoxy BP derivatives, the band at 500 nm of OB-BP shifts towards shorter wavelengths when solvent polarity increases (Figure 4.8). These spectral changes are due to a change in of the lowest excited state of the BP derivative from n,π* to π,π*.[21,22]

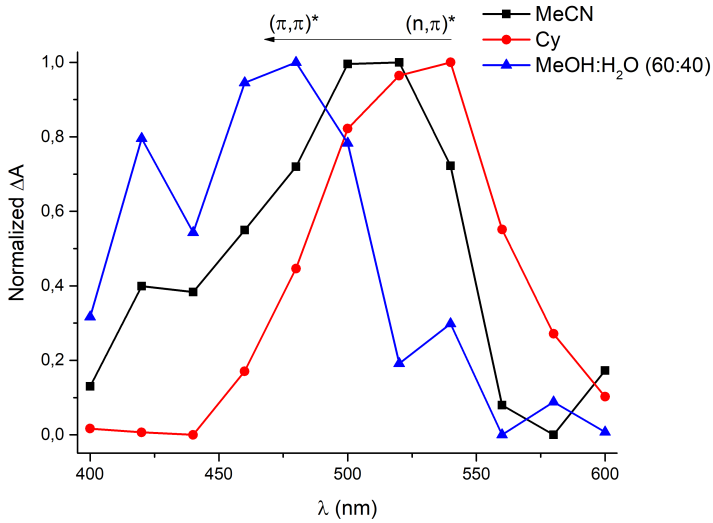

Figure 4.8. Normalized transient absorption spectra of OB-BP in different solvents under deaerated conditions at 40 ns after the 355 nm laser pulse.

In addition to this hypsochromic shift, variations in lifetime were also observed, being in cyclohexane five times shorter than in MeCN. This change may be due to the different reactivity of the triplets of π,π* or n,π* nature, being more reactive towards hydrogen abstraction those carbonyls of n,π* character. To corroborate this reactivity, dyad OB-BP was irradiated in cyclohexane (with a 4% of DCM for solubility purposes) and the main photoproduct was isolated for its characterization by NMR and MS spectrometry. Indeed, the isolated product was identified as the cyclic compound OB-BP-C which arises from an intramolecular hydrogen abstraction followed by a biradical recombination (Scheme 4.3).

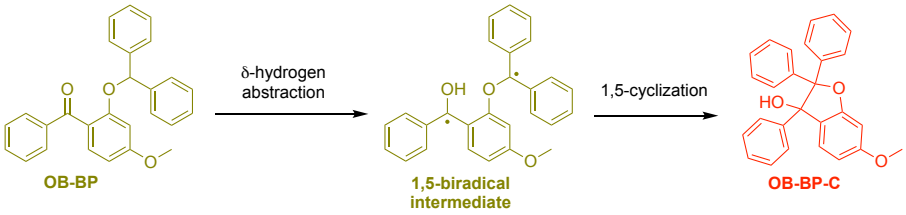

Scheme 4.3. Cyclization of OB-BP by means of hydrogen abstraction.

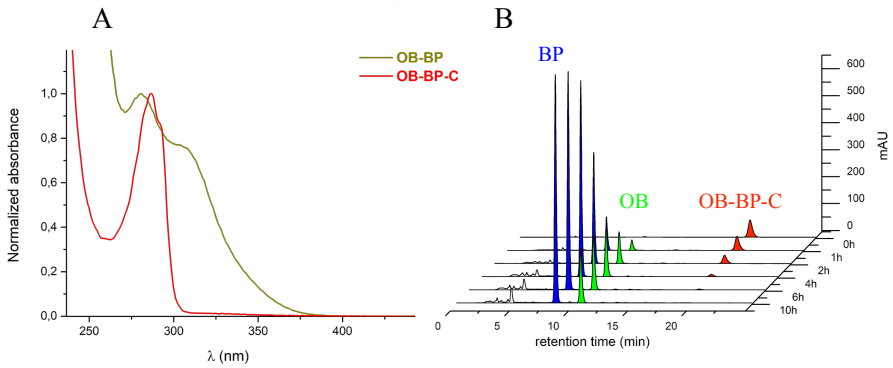

Figure 4.9. Normalized absorption spectra of OB-BP and OB-BP-C in MeCN:H_2O (60:40, v:v) (A) and HPLC chromatograms registered at 250 nm for a deaerated MeCN:H_2O (60:40, v:v) solution of OB-BP-C ($2x10^{-4}$M), upon irradiation at different times with SSL (B).

The isolated cyclic photoproduct was analyzed by UV-Vis spectrophotometry and HPLC. Due to the loss of the benzophenone chromophore, the cyclic photoproduct lacks of absorption in the UVA region (Figure 4.9A). Interestingly, both OB and BP were also released after irradiation with SSL of OB-BP-C in deaerated MeCN:H_2O (60:40, v:v) (Figure 4.9B), so this cyclic compound plays a role of a reaction intermediate.

For this reason, from now on, the studies to understand the photorelease process will be done focusing mainly on such intermediate.

4.2.5. Mechanistic insights

4.2.5.1. The role of a photooxidant in the process

First, since an oxidation is taking place along the process, we evaluated the influence that an external photooxidant such as 4-carboxybenzophenone (CBP) would have on the photorelease process. For that, the cyclic intermediate OB-BP-C was irradiated with SSL in the presence and absence of CBP in deaerated aq. MeCN solution instead of aq. MeOH. This change was made to avoid photoreaction of CBP with the solvent due to H-abstraction and CBP ketyl radical formation. During these irradiations, the reaction was accelerated in the presence of CBP (Figure 4.10), pointing toward a photoinduced oxidation of OB-BP-C.

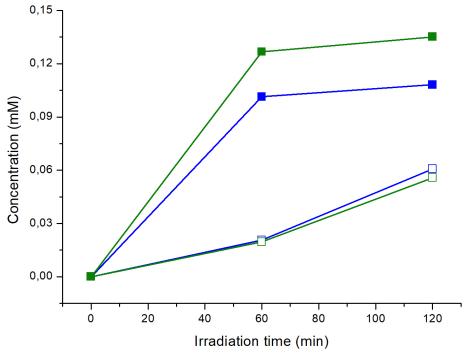

Figure 4.10. Time course of the photorelease of OB (green line) and BP (blue line) through SSL irradiation of a deaerated MeCN:H_2O (60:40, v:v) solution of OB-BP-C (2 x 10^{-4}M) in the presence (filled squares) and absence (unfilled squares) of CBP, upon irradiation with Simulated Sunlight.

Moreover, LFP experiments were carried out to get deeper insights in the interactions between the photooxidant and the cyclic intermediate OB-BP-C. Figure 4.11A shows the transient absorption spectra of the triplet state of CBP in MeCN:H_2O (60:40, v:v) with a band centered at 560 nm. As expected for a benzophenone derivative, the band at 560 nm evolves toward a red shifted transient absorption in the presence of hydrogen donor because of CBP ketyl radical formation. This spectral change is clearly observed in Figure 4.11B, where the spectra of CBP in ethanol and MeCN:H_2O (60:40, v:v) are compared. The same photobehavior was observed when adding OB-BP-C to a MeCN:H_2O solution of CBP (Figure 4.11C). Besides, the quenching rate constant of CBP by OB-BP-C in MeCN:H_2O solution is in the order of 10^9 M^{-1} s^{-1}, which agrees with a hydrogen abstraction in two steps, a first electron transfer with generation of CBP anion radical followed by a proton transfer giving rise to CBP ketyl radical (Scheme 4.4).

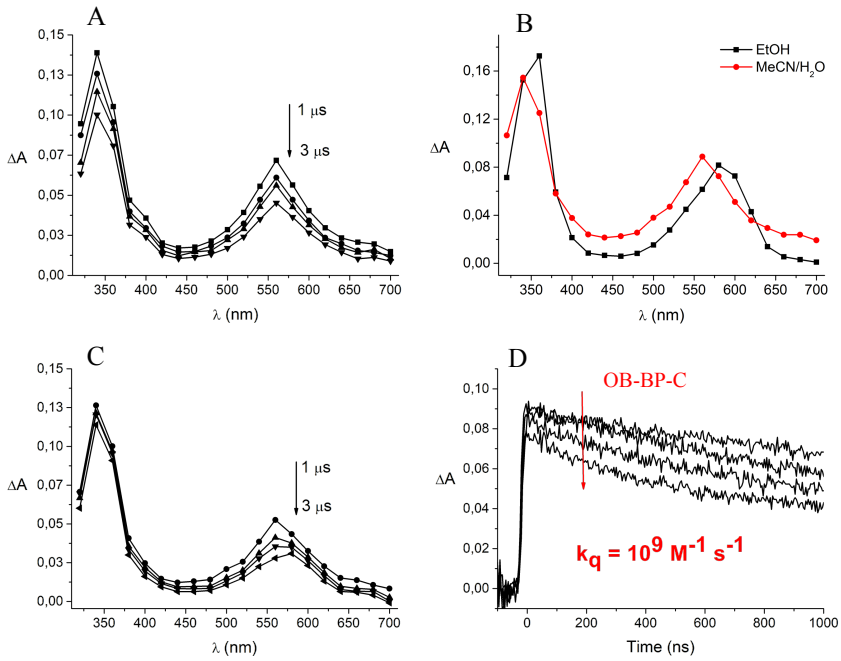

Figure 4.11. Transient absorption spectra registered at different times after the laser pulse at 355 nm of a deaerated solution of CBP in MeCN:H_2O (60:40, v:v) (A) in ethanol and MeCN:H_2O (60:40, v:v) at 80 ns after the laser pulse (B) in the presence of 0.05 equivalent of OB-BP-C in MeCN:H_2O (60:40, v:v) (C) and decays at 560 nm of CBP at different OB-BP-C concentrations in deaerated MeCN:H_2O (60:40, v:v) after the laser pulse at 355 nm (D).

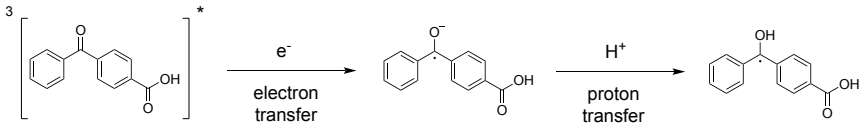

Scheme 4.4. Hydrogen abstraction in two steps.

Thus, the photorelease process is boosted by a photooxidant that abstracts an electron from the cyclic intermediate. Conversely, in the absence of such an oxidant, photoionization should be the triggering process.

4.2.5.2. A new OB based system caging the CBP

The role played by CBP along the photoliberation process led us to synthesize and study the compounds OB-CBP and OB-CBP-C (Chart 4.2), which should provide a more efficient release. Besides, these compounds offer the possibility of studying them in aqueous solution.

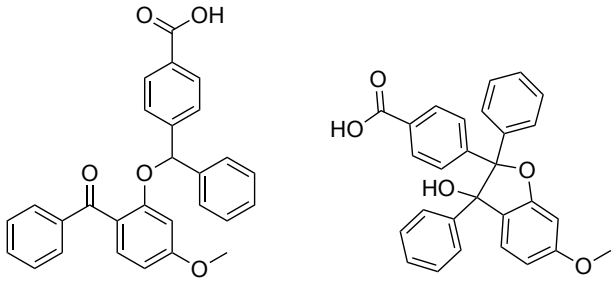

OB-CBP OB-CBP-C

Chart 4.2. Structures of compounds OB-CBP and OB-CBP-C.

Photolabile compound OB-CBP was synthesized in four steps. First, the carboxylic acid of 4-carboxybenzophenone (CBP) was esterified to CBP-Me, then selective reduction of the ketone was achieved by using $NaBH_4$. The obtained alcohol reacted with oxybenzone (OB) in the presence of triphenylphosphine (PPh_3) and diisopropyl azodicarboxylate (DIAD) through a Mitsunobu reaction[23] to yield the diaryl ether OB-CBP-Me, which finally gave rise to OB-CBP after basic hydrolysis. Regarding compound OB-CBP**,**

it was obtained using a similar procedure as for the cyclic compound OB-BP-C (Scheme 4.5).

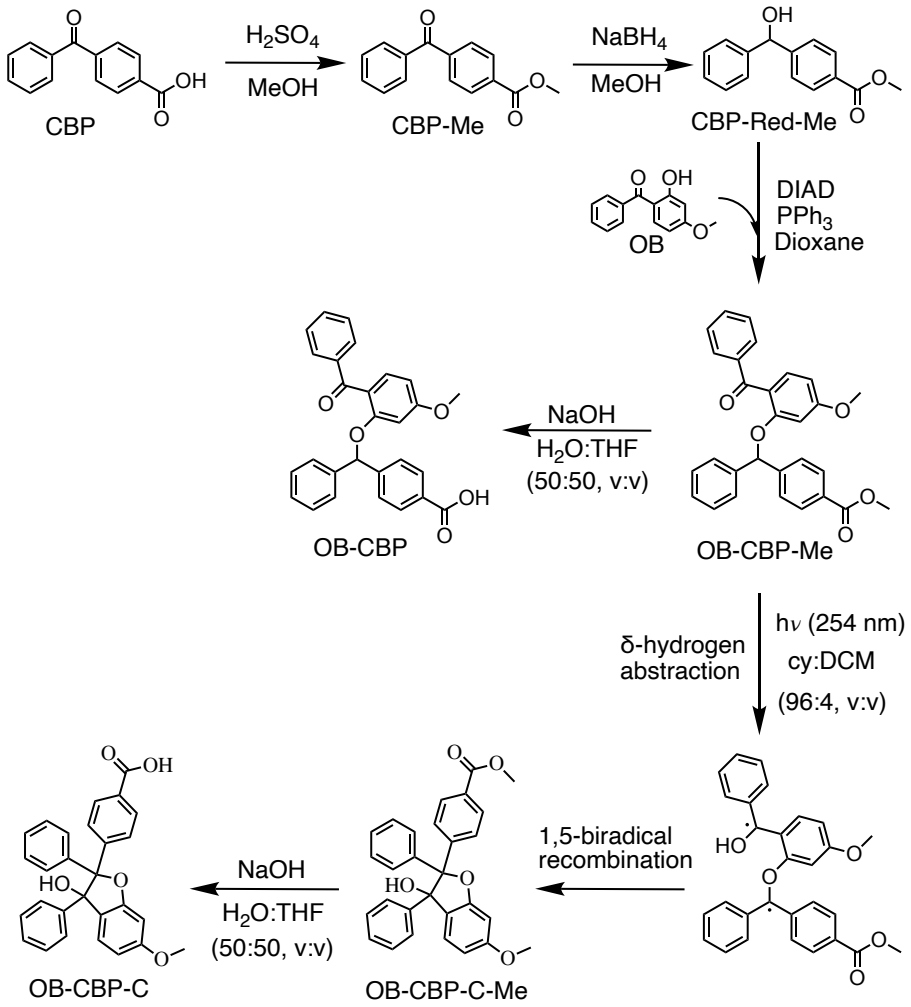

Scheme 4.5. Synthesis of compounds OB-CBP and OB-CBP-C.

The UV-Vis absorption spectra of photocage OB-CBP displays a long wavelength band peaking at 310 nm that reaches the UVA region, and making conceivable the photorelease using SSL. 4-carboxybenzophenone (CBP) and the oxybenzone (OB) absorption spectra were recorded in H_2O:MeCN (40:60, v:v) (Figure 4.12B) and showed that the OB filter provides the desired protection of the carbonyl derivative against the SSL irradiation.

The new photolabile system OB-CBP was also irradiated to corroborate its ability to release both components. The irradiation was carried out using SSL in oxygen-free MeCN:H_2O (60:40, v:v) and was followed by HPLC (Figure 4.12C). It was observed that both OB and CBP are photoreleased together with other photoproducts. The peaks corresponding to OB-CBP, OB and CBP were assigned and quantified by comparison with pure compounds to obtain the kinetic curves (Figure 4.12D).

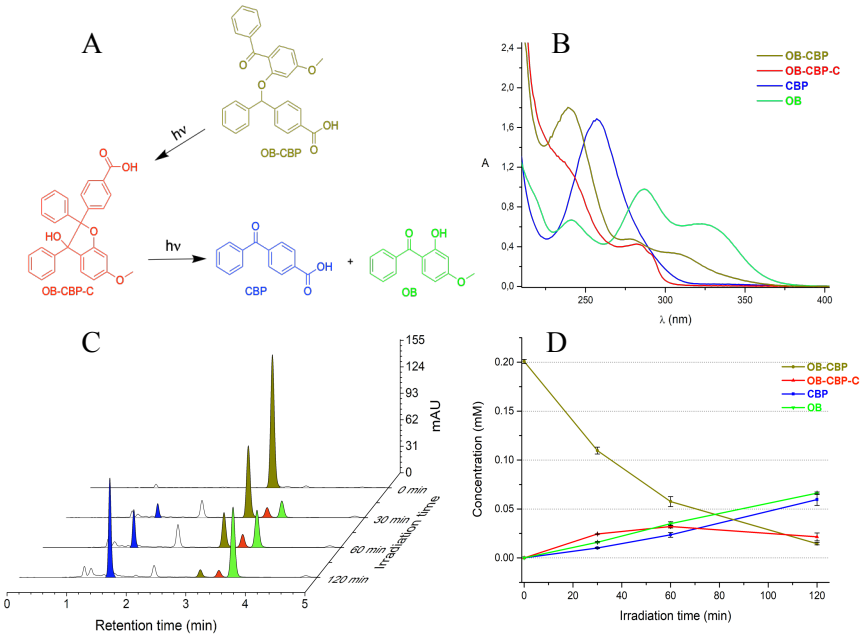

Figure 4.12. (A) Photorelease of CBP and OB from new carbonyl photocage OB-CBP (B) UV-Vis absorption spectra in MeCN:H_2O (60:40, v:v) of OB-CBP, OB-CBP-C, CBP and OB at same concentration ($6.6x10^{-5}$ M), (C) HPLC chromatograms registered at 280 nm for an oxygen-free MeCN:H_2O (60:40, v:v) solution of OB-CBP ($2x10^{-4}$ M), upon irradiation at different times with simulated solar light, and (D) kinetic traces of OB-CBP, OB-CBP-C, CBP and OB.

Moreover, peaks eluting at 2.3 and 3.4 min exhibit the kinetic behavior of an intermediate with an increase of area to a maximum after 60 min followed by a decrease. These compounds were assigned to the diastereoisomers of cyclic intermediate OB-CBP-C (Scheme 4.6).

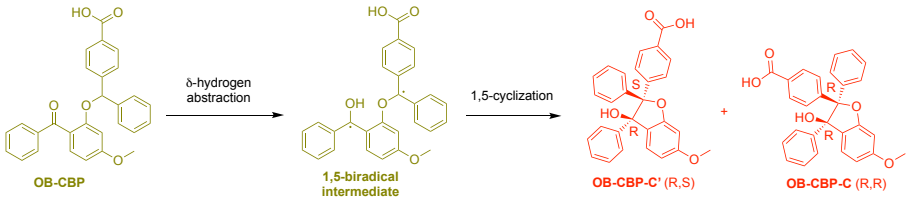

Scheme 4.6. Diastereoisomers of cyclic intermediate OB-CBP-C obtained from OB-CBP by an intramolecular hydrogen abstraction and a subsequent C-C coupling of the formed biradical.

To support this claim, a deaerated MeCN:H_2O (60:40, v:v) solution of OB-CBP was irradiated and the resulting photomixture was analyzed by mass spectrometry (Figure 4.13). From the MS analysis, two peaks with the mass corresponding to OB-CBP-C (at *m/z* 421.14 as $[M\text{-}OH]^+$) were detected. Additionally, the sample was also assessed by MS/MS, obtaining the same fragmentation pattern for both peaks.

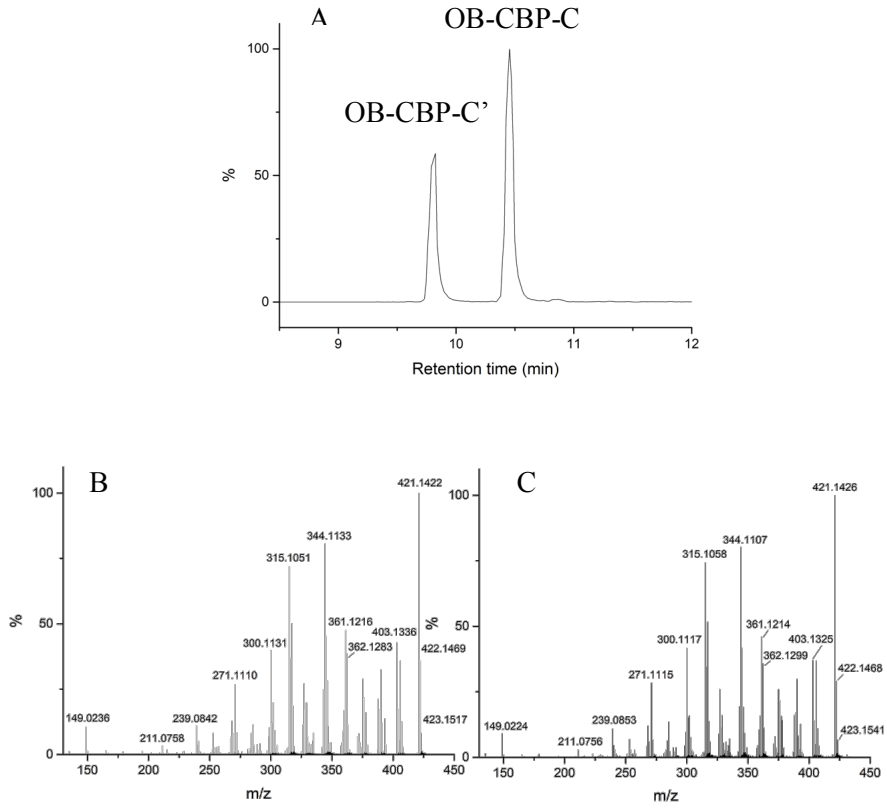

Figure 4.13. Selected ion monitoring (SIM) chromatograms at *m/z* 421.14 as $[M\text{-}OH]^+$ obtained from irradiation of photocage OB-CBP under oxygen-containing conditions in MeCN:H_2O (60:40, v:v) (A), and MS/MS spectra (parent ion with *m/z* 421.14, collision energy of *ca.* 30 V) of intermediate OB-CBP-C**'** at elution time of 9.8 min (B) and OB-CBP-C at elution time of 10.4 min (C).

In order to get a deeper understanding about the photorelease process of OB and CBP from this cyclic intermediate, OB-CBP-C was used for additional steady-state photolysis experiments. In a first stage, an oxygen-containing solution of compound OB-CBP-C in MeCN:H_2O (60:40, v:v) was

irradiated with SSL to confirm the intermediate capacity to photorelease OB and CBP (Figure 4.14).

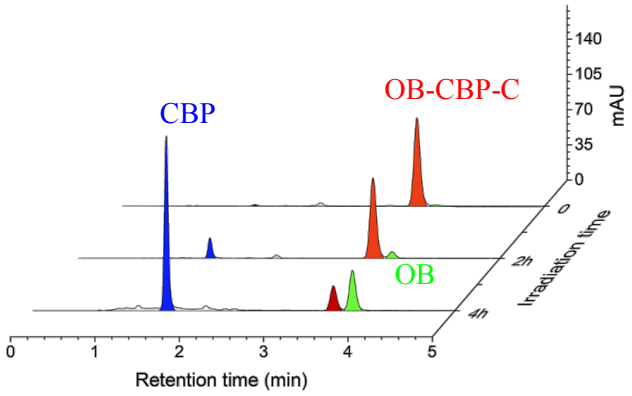

Figure 4.14. HPLC chromatogram registered at 280 nm of a solution of OB-CBP-C (2×10^{-4} M) irradiated with SSL in oxygen-containing MeCN:H_2O (60:40, v:v).

Then, to simplify the quantification process, experiments were performed using a low pressure Hg lamp with a monochromatic output at 254 nm under N_2 or air atmosphere. Compound OB-CBP-C (2×10^{-4} M) dissolved in anhydrous MeCN (obtained from a solvent purification system) or in MeCN:H_2O (60:40, v:v) was irradiated, and the reaction was followed by HPLC (Figure 4.15).

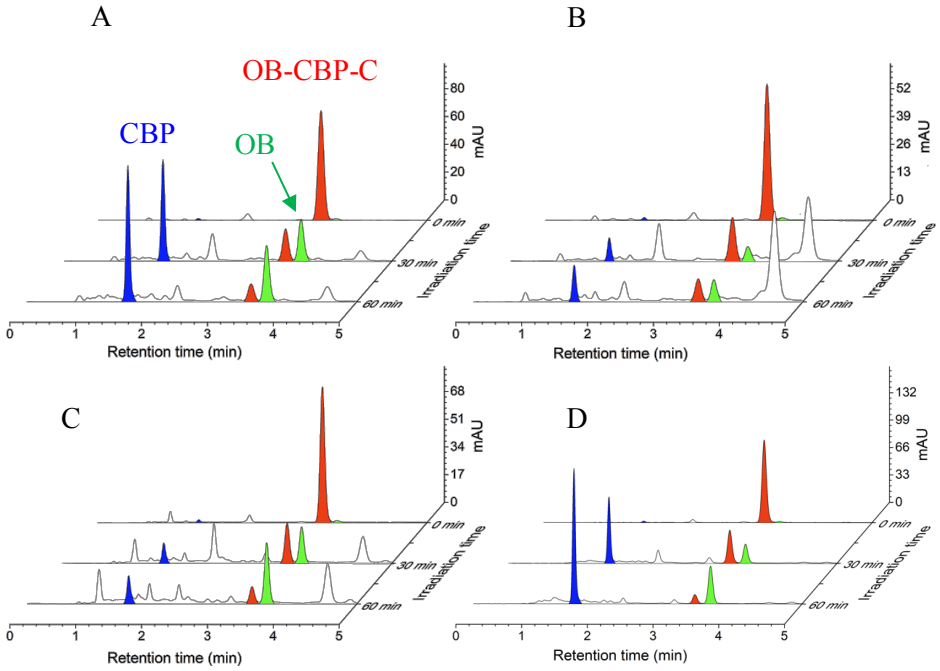

Figure 4.15. HPLC chromatograms registered at 280 nm of a solution of OB-CBP-C (2×10^{-4} M) irradiated at 254 nm in oxygen-containing anhydrous MeCN (A), oxygen-free anhydrous MeCN (B), oxygen-free MeCN:H_2O (60:40, v:v) (C), and in oxygen-containing MeCN:H_2O (60:40, v:v) (D).

Compound OB-CBP-C was consumed during the irradiation irrespective of the employed conditions, whereas the release of CBP strongly differed depending on the presence of oxygen and/or water. As shown in Figure 4.15D for an oxygen-containing MeCN:H_2O solution, the peak of compound OB-CBP-C, eluting at 3.4 min, decreased giving basically rise to the formation of the desired CBP (at 1.5 min), together with OB (at 3.7 min). The yields of the photoproducts determined after 60 min of irradiation are

summarized in Table 4.1. The results were clearly affected by the presence of O_2 or H_2O.

In oxygen-containing aqueous acetonitrile, the yields of CBP and OB were markedly higher and the formation of undesired byproducts was minimized. Remarkably, when oxygen and water were present in the solution, CBP yield reached 51.7%, whereas the yield of OB grew from 7.6% to 21.1%. A quantum yield of *ca.* 0.16 was determined for the photoreaction by means of an established procedure using as standard the photocyclization of *N*-methyldiphenylamine to *N*-methylcarbazole in oxygen-containing acetonitrile.[24,25]

Table 4.1. Yields of compounds OB-CBP-C, CBP and OB obtained after 60 min of irradiation under different conditions.

	Conversion (%)	CBP (%)	OB (%)
Anhydrous MeCN*, N_2	85.4±0.3	9.1±1.6	7.6±1.2
MeCN/H_2O, N_2	89.1±0.7	6.1±0.3	19.0±0.5
Anhydrous MeCN, Air	82.4±1.8	36.3±1.4	20.6±0.5
MeCN/H_2O, Air	87.8±0.7	51.7±1.2	21.1±0.4

* with the employed operating procedures it is difficult to safely exclude the possible presence of adventitious amounts of water or oxygen in the medium.

The obtained results are in accordance with the fact that incorporation of an oxygen atom to dyad OB-CBP-C is required to release CBP and OB.

To experimentally settle whether the oxygen comes from H_2O and if so where it is finally incorporated, photodeprotection was carried out using MeCN:$H_2{}^{18}O$ as solvent. In this context, an oxygen-containing solution of OB-CBP-C in either MeCN:H_2O or MeCN:$H_2{}^{18}O$ was exposed to 254 nm light, and the reaction mixture was analyzed by UPLC-HRMS. When H_2O was used, mass spectra of the CBP and OB peaks were coincident with the expected natural isotopic pattern, with *m/z* values of 227.0714 and 229.0864 as [M+H$^+$], respectively. Conversely, for the reaction in $H_2{}^{18}O$ a CBP peak at *m/z* 229.0743 increased and its exact mass corresponded to that of ^{18}O labeled CBP. By contrast, no significant changes were observed for OB (Figure 4.16).

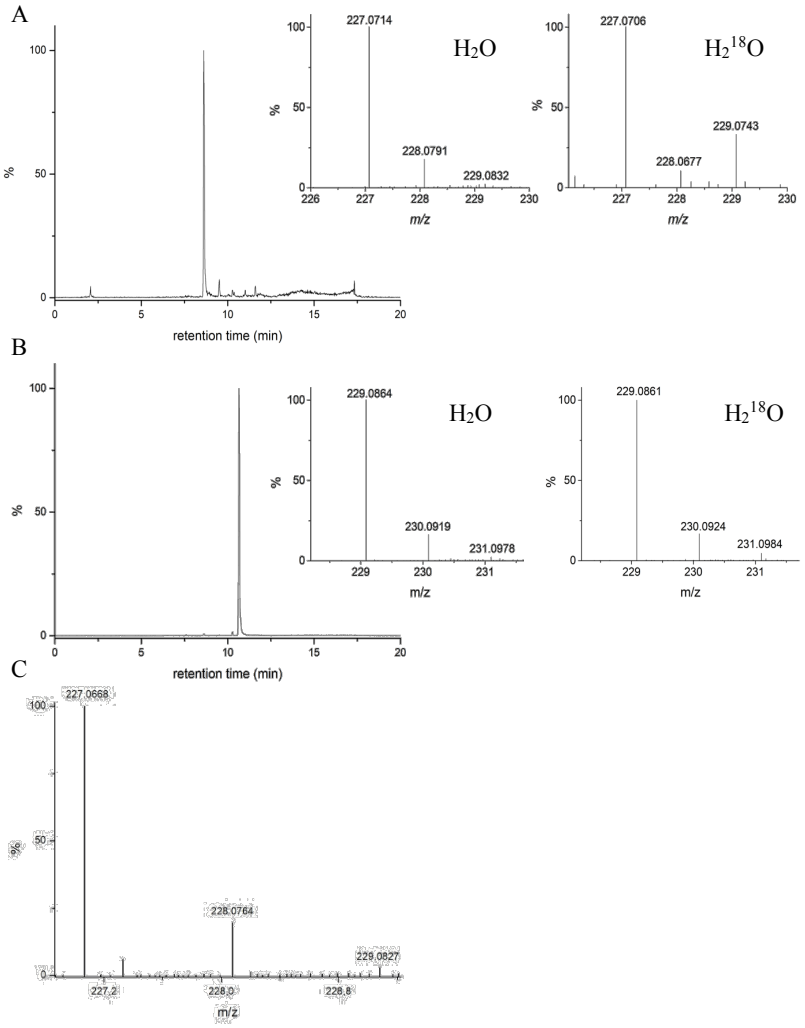

Figure 4.16. SIM chromatograms (A) at *m/z* 227.07 of CBP as $[M+H]^+$ obtained from irradiation of photocage OB-CBP-C under oxygen-containing conditions in MeCN:H_2O. Inset: ESI spectra of detected CBP peak in MeCN:H_2O and MeCN:$H_2{}^{18}O$, (B) at *m/z* 229.08 of OB as $[M+H]^+$ obtained from irradiation of photocage OB-CBP-C under oxygen-containing conditions in MeCN:H_2O. Inset: ESI spectra of detected OB peak in MeCN:H_2O and MeCN:$H_2{}^{18}O$, (C) ESI spectrum of CBP peak as $[M+H]^+$ obtained from a solution of CBP left for hours under dark conditions in MeCN:$H_2{}^{18}O$.

Thus, comparison of the MS spectra for the CBP peak showed that the ratio between the intensity of the ions at *m/z* 229.0743 and 227.0706 was higher in the presence than in the absence of $H_2{}^{18}O$ (1/3 vs 1/33, respectively). Moreover, no changes in the isotopic pattern were observed for CBP in $H_2{}^{18}O$ solution left in the dark for hours (Figure 4.16C).

Altogether, these results demonstrate that at least part of the oxygen of CBP arises from water present in the solvent, and supports that in aerobic atmosphere the yield of CBP formation is enhanced in aqueous acetonitrile. Nonetheless, the reaction still takes place under aerobic anhydrous conditions, albeit to a lesser extent, showing that atmospheric oxygen is also capable to trigger the process. Consequently, the lowest efficiency is observed for oxygen-free anhydrous acetonitrile.

In order to explain the obtained results and to get insights into the mechanistic details of the photoprocess, LFP experiments were performed at 266 nm. The transient absorption spectrum obtained for N_2-bubbled aqueous solutions of OB-CBP-C is shown in Figure 4.17. It exhibits a maximum at 350 nm together with a broad band growing until 700 nm characteristic of hydrated electron (e^-_{aq}), which was quenched under N_2O atmosphere (Figure 4.17A). The linear variation of the hydrated electron absorbance at 680 nm as a function of the laser intensity reflected a monophotonic process (Figure 4.17B). Furthermore, the log-log representation fitted linearly with a slope of 1.2 (Figure 4.18A) confirming the one-photon nature of the ionization process, which could thus occur under exposure to light intensity commonly used in steady-state photolysis experiments.

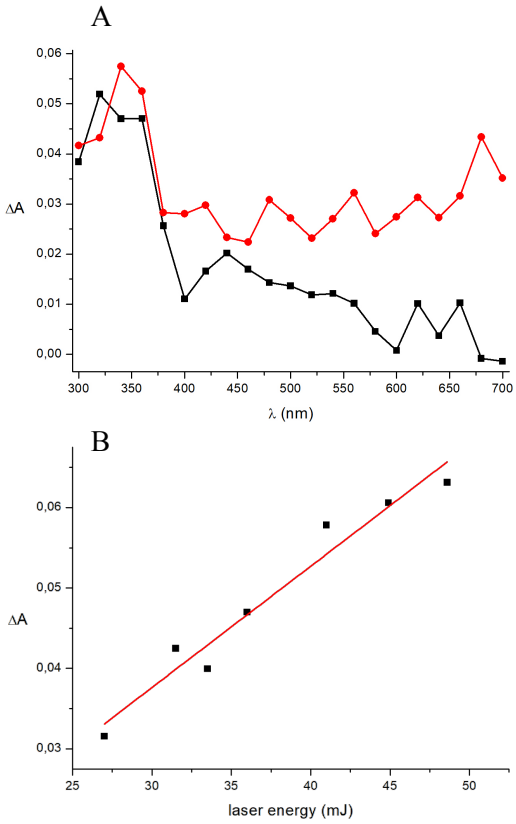

Figure 4.17. Transient absorption spectra of OB-CBP-C in H_2O under N_2 (red line) or N_2O (black line) 0.04 μs after the 266 nm laser pulse (laser energy: 33 mJ) (A). Laser energy dependence of the transient absorption intensity at 680 nm of the N_2 solution (B).

Consistently, LFP studies carried out using (2,4-dimethoxyphenyl)acetic acid (DMFA) as a model of the dialkoxyaryl group of OB-CBP-C also gave rise to e^-_{aq} (see Figure 4.18C). Interestingly, the 4-carboxyaryl moiety can act as a good electron acceptor and thus be reduced

during the process either through an intramolecular electron transfer process or through trapping of hydrated electron.

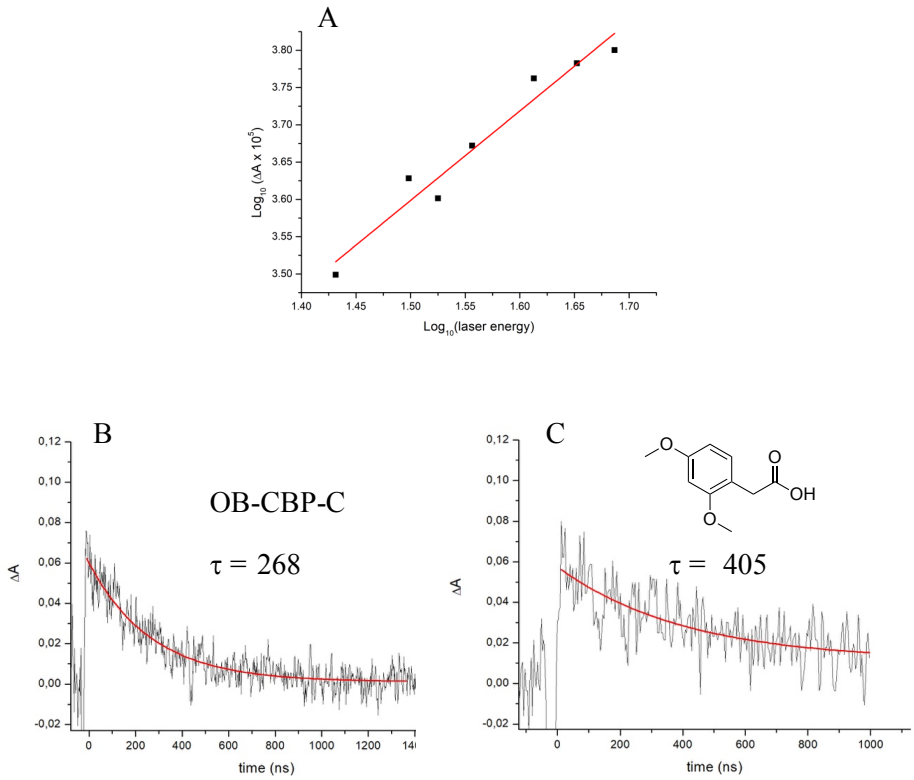

Figure 4.18. Log-log scale plot of the laser power versus the transient absorption signal of compound OB-CBP-C in MilliQ H_2O under oxygen-free conditions (A). Decays of OB-CBP-C (B) and (2,4-dimethoxyphenyl)acetic acid (2,4-DMFA) (C) monitored at 680 nm in MilliQ H_2O under oxygen-free conditions.

Actually, comparison of the kinetic traces of hydrated electron at 680 nm revealed a faster decay for OB-CBP-C (Figure 4.18B, $\tau \sim 270$ ns) than for DMFA (Figure 4.18C, $\tau \sim 400$ ns), which is in agreement with electron trapping by the 4-carboxyaryl moiety of OB-CBP-

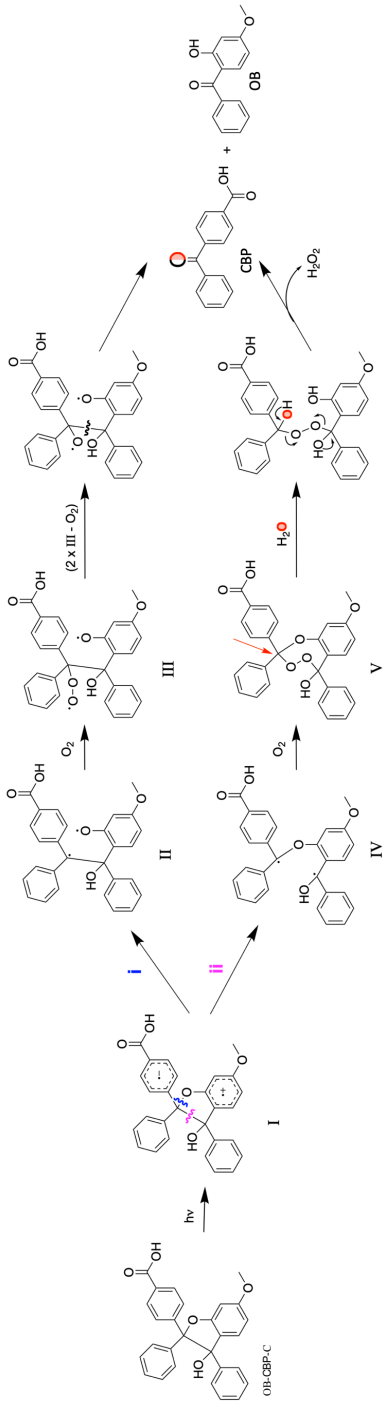

Scheme 4.7. Photorelease mechanism from photocage OB-CBP-C.

On the basis of these data, a possible mechanism is outlined in Scheme 4.7. The photorelease process might be triggered by the photoinduced formation of biradical zwitterion I. This intermediate can evolve through two different pathways depending on the mesolytic cleavage of the benzylic C-O bond (route i) or C-C bond (route ii). In the former case, the obtained biradical II is trapped by O_2 leading to III, which after dimerization and subsequent fragmentation yields the desired CBP and OB. The C-C cleavage, route ii, gives rise to biradical IV that reacts with O_2 to form the cyclic endoperoxide intermediate V. In the presence of water, it hydrolyzes to yield, after loss of H_2O_2, CBP and OB. In this context, incorporation of ^{18}O to CBP demonstrates that water attacks at the benzylic position of the carboxyaryl moiety, which is actually the most electrophilic carbon.

4.2.6. Applications

To explore the scope of the OB-based photocage approach, we have synthesized compounds containing differently substituted ketones. For that purpose, two additional systems formed by linking OB with acetophenone (OB-AP) and with α-tetralone (OB-TL) have been synthesized and tested under the optimized irradiation conditions. The study of the acetophenone derivative should inform on the influence of the lacking of one of the aryl groups, while the α-tetralone was selected to confirm the release of cyclic ketones. Furthermore, the prodrug/profilter system formed between KP and OB was synthesized as a real application for the release and subsequent protection of a benzophenone derivative.

The synthesis of the prodrug/profilter formed between ketoprofen and OB (OB-KP) was achieved by a similar synthetic route to that of the OB-CBP dyad. Firstly, the carboxylic acid of KP was esterified to its methyl ester. Then, the benzophenone was reduced with $NaBH_4$, and the afforded alcohol was linked to oxybenzone through the Mitsunobu reaction. Finally, the ester was hydrolyzed to obtain OB-KP (Scheme 4.8).

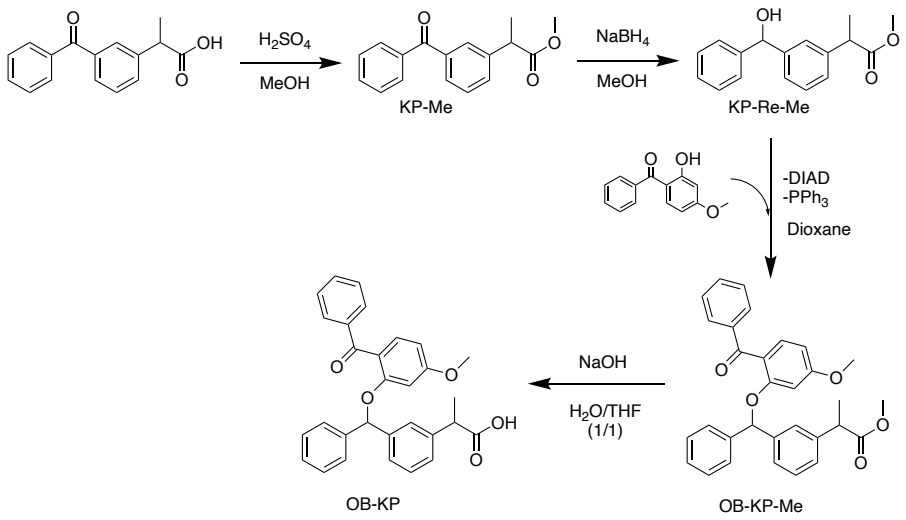

Scheme 4.8. Synthesis of OB-KP system

The synthesis of OB-AP and OB-TL was achieved straightforward, through a one-step synthesis, linking the alcohol of the oxybenzone to that of the reduced carbonyl compound by means of the Mitsunobu reaction (Scheme 4.9).

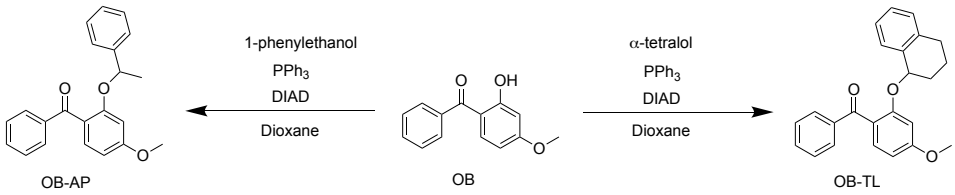

Scheme 4.9. Synthesis of OB-AP and OB-TL.

The UV-Vis spectra of these systems (Figure 4.19) have a main band in the same range as the previous dyads, reaching the UVA region up to 375 nm, which allows its irradiation with SSL.

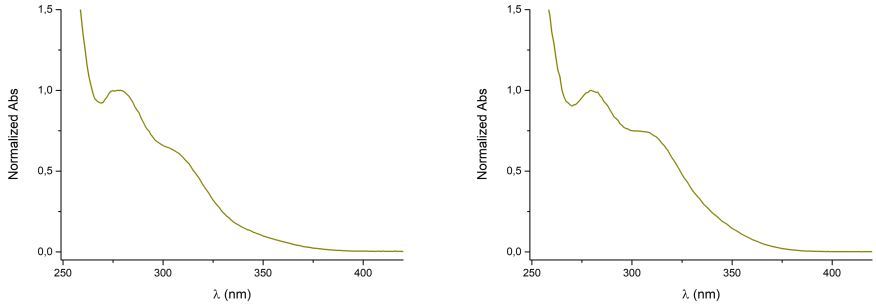

Figure 4.19. Normalized UV-Vis spectra of dyads OB-TL (left) and OB-AP (right) in MeCN:H_2O (60:40, v:v).

4.2.6.1. HPLC analysis of the steady-state photolysis of compounds OB-AP, OB-TL and OB-KP

The dyad OB-KP was irradiated for 30 min with SSL, in the presence and absence of CBP, under deaerated conditions in MeCN:H_2O (60:40, v:v)

and analyzed by HPLC (Figure 4.20). From these irradiations, it was observed that the consumption of OB-KP was not strongly affected by the presence of the photooxidant, changing from 36% to 44%. However, the release yield of both components was considerably higher in its presence. The presence of CBP increases the release of OB from 3.7 to 10 %, and of KP from 2.4 to 12%.

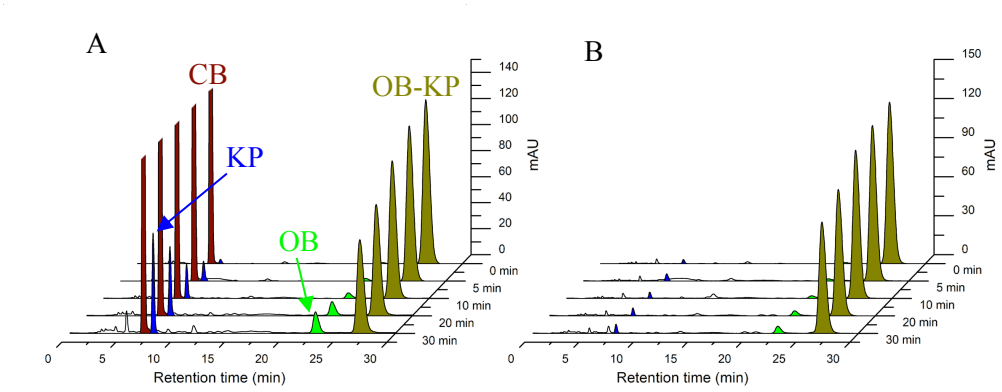

Figure 4.20. HPLC chromatogram registered at 254 nm for a deaerated MeCN:H_2O (60:40, v:v) solution of OB-KP ($2x10^{-4}$M) with 1eq. of CBP (A) and without CBP (B), upon irradiation with Simulated Sunlight.

Finally, steady state photolysis experiments of the dyads OB-TL and OB-AP were performed in deaerated MeCN:H_2O (60:40, v:v) using SSL as an irradiation source. These irradiations were also carried out in the presence and absence of the photooxidant (CBP). As previously observed in the case of OB-KP, the consumption of OB-TL and OB-AP was not affected by the presence of the CBP, while the release yield of their components strongly depends on its presence (see Table 4.2).

Table 4.2. Yields of OB-TL and OB-AP and their components in the presence and absence of CBP after two hours of irradiation with SSL in MeCN:H_2O (60:40, v:v).

	With CBP (%)	Without CBP (%)
OB-TL	92	92
OB	69	22
α-tetralone	41	8
OB-AP	50	63
OB	50	5
Acetophenone	28	2

As shown in Figures 4.21 and 4.22, the cyclic intermediates (red peaks) are only observed in the absence of CBP, which agrees with the fact that the photooxidant only interact with the cyclic intermediates promoting their photooxidation.

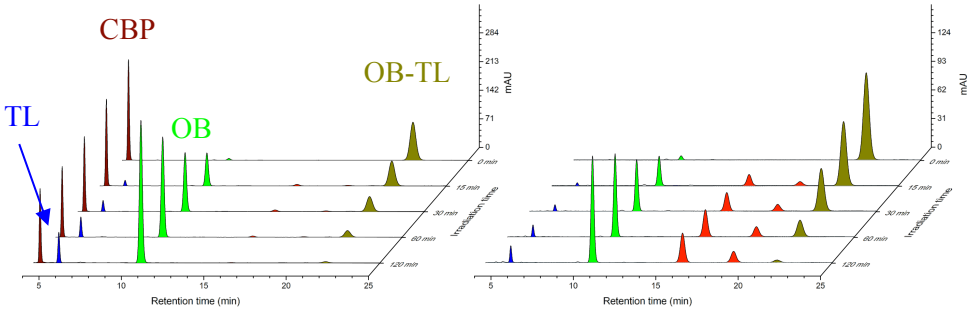

Figure 4.21. HPLC chromatogram registered at 300 nm for a deaerated MeCN:H_2O (60:40, v:v) solution of OB-TL ($2x10^{-4}$ M) with 1 eq. of CBP (left) and without CBP (right), upon irradiation with Simulated Sunlight.

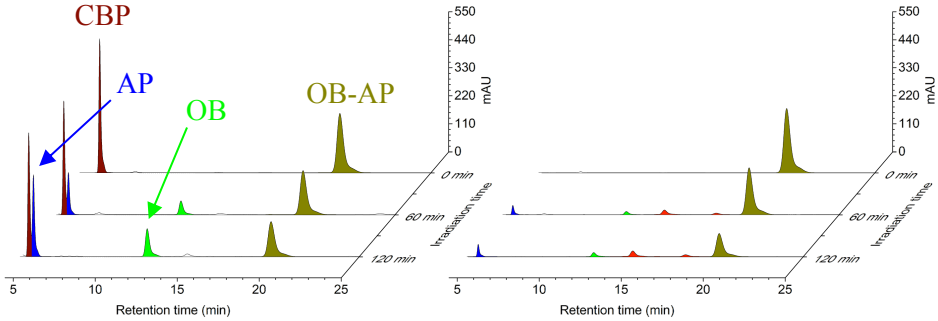

Figure 4.22. HPLC chromatogram registered at 240 nm for a deaerated MeCN:H_2O (60:40, v:v) solution of OB-AP ($2x10^{-4}$ M) with 1 eq. of CBP (left) and without CBP (right), upon irradiation with Simulated Sunlight

4.3. Conclusion

In summary, the concept of sunscreen-based photocages for carbonyl compounds has been proven, using compounds OB-BP, OB-BP-C, OB-CBP and OB-CBP-C, which serve as precursors for the photouncaging of the target aromatic ketone along with its UV-filter shield. Furthermore, this approach has been applied for the release of ketoprofen, a NSAID for topical use responsible for pronounced skin photosensitization. Thus far, the concept has also been extended to two other ketones, acetophenone and α-tetralone. Further work is in progress to improve the uncaging process and to explore the scope of this approach with differently substituted ketones.

4.4. Experimental section

4.4.1. Synthesis

Synthesis of (2-(benzhydryloxy)-4-methoxyphenyl)(phenyl)methanone (OB-BP)

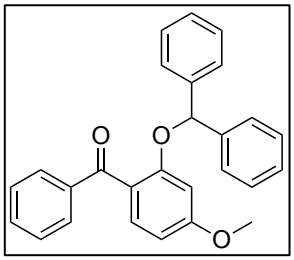

A solution of KOH (0.68 g, 12.1 mmol) in H_2O (12.3 mL) was added to a well stirred solution of oxybenzone (1 g, 4.38 mmol), bromodiphenylmethane (2,7 g, 10.9 mmol) and tetrabutylammonium bromide (0.144 g, 0.437 mmol) in chlorobenzene (9.8 mL). The solution was stirred at 128°C for 18 h. After cooling to room temperature, the reaction mixture was taken up in AcOEt, washed with H_2O (2X), dried ($MgSO_4$) and concentrated. Purification was performed by column chromatography (cy/AcOEt, 9:1; silica gel) to give the pure product OB-BP. Yield: 0.62 g (36%).

^{1}H NMR (300 MHz, $CDCl_3$): δ (ppm) 7.88 – 7.75 (m, 2H), 7.58 – 7.37 (m, 4H), 7.23 – 7.03 (m, 10H), 6.53 (dd, J = 8.5, 2.1 Hz,1H), 6.45 (d, J = 2.1 Hz, 1H), 6.09 (s, 1H), 3.73 (s, 3H).

^{13}C NMR (75 MHz, $CDCl_3$): δ (ppm) 196.4, 163.3, 157.7, 141.1, 139.7, 132.4, 132.4, 129.7, 128.6, 128.2, 127.7, 126.3, 122.7, 105.7, 101.5, 82.6, 55.5.

HRMS (ESI-TOF): *m/z*, $C_{27}H_{23}O_3$ $[M + H]^+$ calculated for 395.1639; found: 395.1647.

Synthesis of 6-methoxy-2,2,3-triphenyl-2,3-dihydrobenzofuran-3-ol (OB-BP-C)

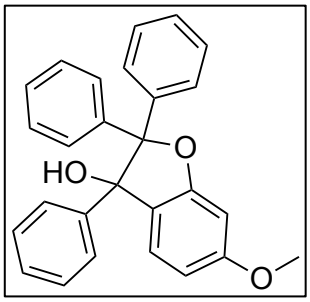

A deaerated solution of 0.098 g OB-BP in 24mL cy and 1mL DCM was irradiated for 40 min using SSL. Then, the solvent was removed under vacuum. Purification was performed by preparative TLC plates silica gel, using cy:AcOEt as eluent (9:1, v:v). Colorless crystals of OB-BP-C were obtained (0.017g) in a 87% yield.

^{1}H NMR (300 MHz, $CDCl_3$): δ (ppm) 7.76 (d, J = 7.7 Hz, 2H), 7.34 (m, 3H), 7.24 – 7.03 (m, 7H), 6.99 (m, 3H), 6.84 (d, J = 8.3 Hz, 1H), 6.80 (d, J = 2.2 Hz, 1H), 6.48 (dd, J = 8.3, 2.2 Hz, 1H), 3.87 (s, 3H).

^{13}C NMR (75 MHz, $CDCl_3$): δ (ppm) 162.4, 160.3, 141.5, 141.4, 140.7, 128.1, 127.9, 127.8, 127.6, 127.3, 127.3, 127.2, 127.1, 126.9, 126.8, 125.9, 108.2, 99.6, 96.4, 87.7, 55.8.

HRMS (ESI-TOF): *m/z*, $C_{27}H_{21}O_2^+$ $[M - OH]^+$ calculated for 377,1542; found: 377,1526.

Synthesis of methyl 4-benzoylbenzoate (CBP-Me)

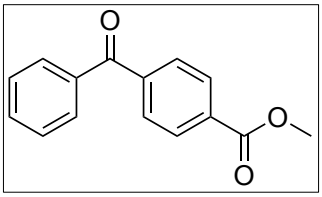

Concentrated sulfuric acid (0.025 mL, 0.44 mmol) was added to a solution of 4-carboxybenzophenone (0.5 g, 2.2 mmol) in anhydrous MeOH (15 mL). The solution was stirred at 75 ºC for 17 h and then cooled to room temperature. The solvent was removed under reduced pressure. The crude product was redissolved in DCM and washed with saturated sodium bicarbonate. Finally, the organic phase was dried with anhydrous magnesium sulfate, filtered, and the filtrate was concentrated in vacuo. The pure product CBP-Me was obtained without further purification. Yield: 0.421 g (77%).

^{1}H NMR (300 MHz, $CDCl_3$): δ (ppm) 8.15 (d, J = 8.6 Hz, 2H), 7.82 (m, 4H), 7.68 – 7.57 (m, 1H), 7.55 – 7.42 (m, 2H), 3.97 (s, 3H).

HRMS (ESI-TOF) *m/z* $[M+H]^+$ calculated for $C_{15}H_{13}O_3$: 241.0865; found: 241.0859.

Synthesis of methyl 4-[hydroxy(phenyl)methyl]benzoate (CBP-Red-Me)

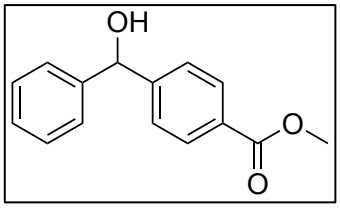

Compound CBP-Me (0.328 g, 1.36 mmol) was dissolved in a mixture of anhydrous MeOH (5 mL) and anhydrous DCM (2 mL). The resulting solution was cooled to 0 ºC, and then $NaBH_4$ (0.072 g, 1.9 mmol) was added portionwise during 2 h. Subsequently, the solution was allowed reaching room temperature, and stirred for 3 h. To quench the excess of $NaBH_4$, the solution was cooled in an ice bath, and then water (5 mL) was added. The resulting mixture was stirred for 30 min. The mixture of solvents was removed under reduced pressure, then the afforded crude was redissolved with DCM (20 mL) and washed with water. Finally, the combined organic extracts were dried with $MgSO_4$, filtered, and the solvent was removed under reduced pressure. The pure product CBP-Red-Me was obtained without further purification. Yield: 0.282 g (85%).

^{1}H NMR (300 MHz, $CDCl_3$): δ (ppm) 7.91 (d, J = 8.4 Hz, 2H), 7.38 (d, J = 8.1 Hz, 2H), 7.33 – 7.11 (m, 5H), 5.79 (d, J = 3.3 Hz, 1H), 3.81 (s, 3H), 2.40 (d, J = 3.3 Hz, 1H).

HRMS (ESI-TOF) *m/z* $[M+H]^+$ calculated for $C_{15}H_{15}O_3$: 243.1021; found: 243.1021.

Synthesis of methyl 4-[(2-benzoyl-5-methoxyphenoxy)(phenyl)methyl]benzoate (OB-CBP-Me)

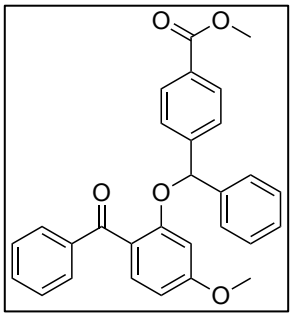

To a solution of compound CBP-Red-Me (0.249 g, 1.03 mmol) and triphenylphosphine (PPh_3) (0.324 g, 1.23 mmol) in anhydrous dioxane (5.5 mL) was added oxybenzone (0.353 g, 1.55 mmol) and diisopropyl azodicarboxylate (DIAD) (0.350 mL, 2 mmol). The solution was stirred at room temperature for 4 h. The crude reaction mixture was concentrated under reduced pressure and purified by column chromatography (cy/AcOEt, 4:1; silica gel) to give the pure product OB-CBP-Me. Yield: 0.340 g (73%).

^{1}H NMR (300 MHz, $CDCl_3$): δ (ppm) 7.95 – 7.80 (m, 4H), 7.60 – 7.41 (m, 4H), 7.20 (m, 7H), 6.55 (dd, J = 8.5, 2.0 Hz, 1H), 6.48 (d, J = 2.0 Hz, 1H), 6.19 (s, 1H), 3.86 (s, 3H), 3.71 (s, 3H).

^{13}C NMR (75 MHz, $CDCl_3$): δ (ppm) 195.9, 166.5, 163.1, 157.2, 145.9, 140.2, 139.5, 132.3, 132.3, 129.8, 129.5, 129.2, 128.6, 128.1, 127.9, 126.1, 125.9, 122.4, 105.6, 101.4, 81.8, 55.3, 51.9.

HRMS (ESI-TOF) *m/z* $[M+H]^+$ calculated for $C_{29}H_{25}O_5$: 453.1702; found: 453.1713.

Synthesis of 4-(3-hydroxy-6-methoxy-2,3-diphenyl-2,3-dihydrobenzofuran-2-yl)benzoic acid (OB-CBP)

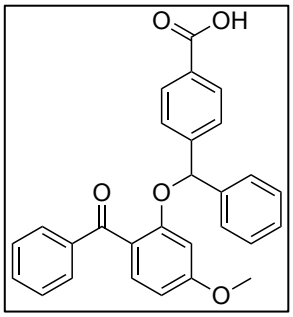

Compound OB-CBP-Me (0.191 g, 0.42 mmol) was dissolved in a mixture of 1 M aq. NaOH (2 mL) and THF (2 mL). The resulting solution was stirred for 22 h at room temperature. The mixture was acidified to pH 1 using 1 M aq. HCl, then the resulting mixture was extracted with DCM (3 x 10 mL), dried over anhydrous $MgSO_4$, and rotary evaporated to afford compound OB-CBP (0.127 g) in a 69% yield.

^{1}H NMR (300 MHz, $CDCl_3$): δ (ppm) 7.88 (d, J = 8.1 Hz, 2H), 7.80 (d, J = 7.2 Hz, 2H), 7.47 (m, 4H), 7.25 – 6.98 (m, 7H), 6.54 (dd, J = 8.7, 1.8 Hz, 1H), 6.41 (d, J = 1.8 Hz, 1H), 6.12 (s, 1H), 3.73 (s, 3H).

^{13}C NMR (75 MHz, $CDCl_3$): δ (ppm) 196.3, 163.3, 157.4, 146.6, 140.3, 139.6, 132.5, 132.5, 130.5, 129.7, 129.3, 128.9, 128.3, 128.09, 126.3, 126.1, 122.7, 105.8, 101.6, 82.1, 55.5.

HRMS (ESI-TOF) *m/z* $[M+H]^+$ calculated for $C_{28}H_{23}O_5$: 439.1545; found: 439.1550. Molar absorption coefficients in MeCN:H_2O (60:40, v:v): log ε = 3.9 (280 nm), 3.7 (310 nm).

Synthesis of methyl 4-(3-hydroxy-6-methoxy-2,3-diphenyl-2,3-dihydrobenzofuran-2-yl)benzoate (OB-CBP-C-Me)

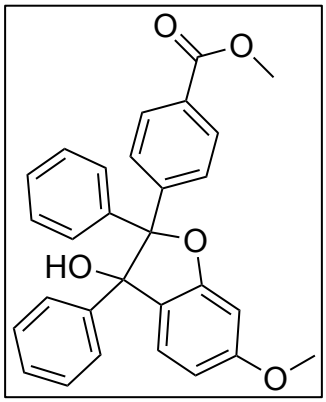

An oxygen-free solution of compound OB-CBP-Me (0.170 g, 0.376 mmol) in 211 mL cy and 9 mL DCM was irradiated for 90 min using a Luzchem photoreactor (model LZC-4V) with 8 lamps with a maximum output at 355 nm. Then, the solvent was removed under vacuum. Purification was performed by column chromatography (cy/AcOEt, 6:1; silica gel). Product OB-CBP-C-Me was obtained by resolution of the diastereoisomeric mixture (0.058 g) in a 34% yield.

^{1}H NMR (300 MHz, $CDCl_3$): δ (ppm) 8.07 – 7.96 (d, J = 8.7 Hz, 2H), 7.95 -7.83 (d, J = 8.7 Hz, 2H), 7.15 (m, 5H), 7.08 – 6.90 (m, 5H), 6.82 (m, 2H), 6.48 (dd, J = 8.3, 2.2 Hz, 1H), 3.88 (s, 3H), 3.86 (s, 3H).

^{13}C NMR (75 MHz $CDCl_3$): δ (ppm) 166.9, 162.6, 160.2, 146.0, 140.9, 140.8, 129.2, 129.1, 128.1, 127.8, 127.4, 127.4, 127.3, 127.2, 127.0, 126.5, 125.9, 108.3, 99.5, 96.4, 87.8, 55.8, 52.2.

HRMS (ESI-TOF) *m/z* $[M\text{-}OH]^+$ calculated for $C_{29}H_{23}O_4$: 435.1596; found: 435.1595.

Based on the spectroscopic data, this compound corresponds to the (R,R) configuration. This is clearly observed by comparing the chemical shift of the phenyl hydrogens of the aryl group linked to the ester group, which are deshielded in the (R,R) configuration with respect to the (R,S).

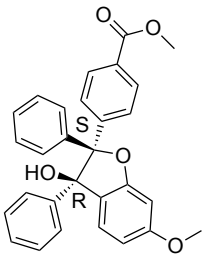

OB-CBP-C (R,S)

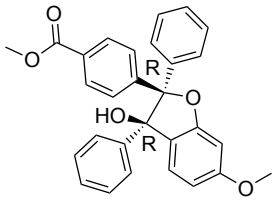

OB-CBP-C (R,R)

Synthesis of 4-(3-hydroxy-6-methoxy-2,3-diphenyl-2,3-dihydrobenzofuran-2-yl)benzoic acid (OB-CBP-C)

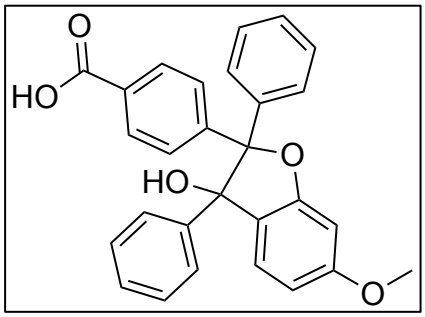

Compound OB-CBP-C-Me (0.057 g, 0.13 mmol) was dissolved in a mixture of 1 M aq. NaOH (0.56 mL) and THF (0.56 mL). The resulting solution was stirred for 22 h at room temperature. The mixture was acidified to pH 1 using 1 M aq. HCl, then the resulting mixture was extracted with DCM (3 x 10 mL), dried over anhydrous MgSO4, and rotary evaporated to afford compound OB-CBP-C (0.013 g) in a 23% yield.

^{1}H NMR (300 MHz, CD_3OD): δ (ppm) 7.97 (d, J = 8.5 Hz, 2H), 7.90 (d, J = 8.5 Hz, 2H), 7.21 – 6.88 (m, 10H), 6.84 (d, J = 2.2 Hz, 1H), 6.77 (d, J = 8.3 Hz, 1H), 6.50 (dd, J = 8.3, 2.2 Hz, 1H), 3.86 (s, 3H).

^{13}C NMR (75 MHz, CD_3OD): δ (ppm) 162.3, 160.1, 146.4, 141.9, 141.6, 128.1, 127.8, 127.5, 126.8, 126.6, 126.5, 126.1, 125.5, 107.4, 99.1, 95.4, 86.9, 54.6.

HRMS (ESI-TOF) *m/z* $[M\text{-}OH]^+$ calculated for $C_{28}H_{21}O_4$: 421.1440; found: 421.1439.

Molar absorption coefficient in MeCN:H_2O (60:40, v:v): log ε = 3.8 (283 nm).

Synthesis of methyl 2-(3-benzoylphenyl)propanoate (KP-Me)

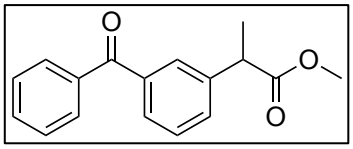

Prepared following the same procedure to that previously described in chapter 3.

Synthesis of methyl 2-(3-(hydroxy(phenyl)methyl)phenyl)propanoate (KP-Red-Me)

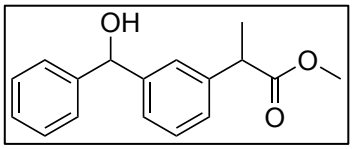

Compound KP-Me (0.9 g, 3.35 mmol) was dissolved in anhydrous MeOH (17 mL). The resulting solution was cooled to 0 ^{O}C, and then $NaBH_4$ (0.177 g, 4.67 mmol) was added portionwise during 3 h. Finally, the solution was allowed to reach room temperature and stirred for 3.5 h. To quench the excess of $NaBH_4$, the solution was cooled in an ice bath, and then DCM (50mL) and H_2O (15 mL) was added. The resulting mixture was stirred for 30 min. The mixture was extracted with DCM (3 x 15 mL) and the combined organic extracts were dried with $MgSO_4$ and filter, and the solvent was removed under reduced pressure. The pure product KP-Red-Me was obtained without further purification. Yield: 0.87 g (95.5%).

^{1}H NMR (300 MHz, $CDCl_3$): δ (ppm) 7.52 – 7.11 (m, 9H), 5.85 (d, J = 2.3 Hz, 1H), 3.76 (q, J = 7.2 Hz, 1H), 3.68 (s, 3H), 1.53 (d, J = 7.2 Hz, 3H).

Synthesis of methyl 2-(3-((2-benzoyl-5-methoxyphenoxy)(phenyl)methyl)phenyl)propanoate (OB-KP-Me)

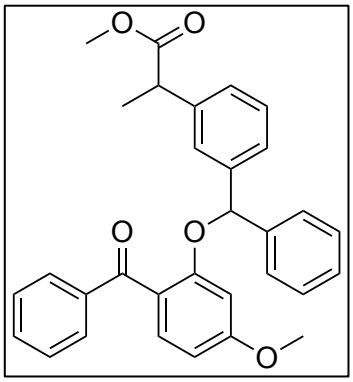

To a solution of compound KP-Red-Me (0.435 g, 1.6 mmol) and triphenylphosphine (0.525 g, 2 mmol) in anhydrous dioxane (8 mL) was added oxybenzone (0.548 g, 2.4 mmol) and DIAD (0.550 mL, 2.79 mmol). The solution was stirred at room temperature for 4 h. The crude reaction mixture was concentrated and purified by column chromatography (cy/AcOEt, 4:1; silica gel) to give the pure product OB-KP-Me. Yield: 0.543g (68%).

^{1}H NMR (300 MHz, $CDCl_3$): δ (ppm) 7.91 – 7.76 (m, 2H), 7.59 – 7.36 (m, 4H), 7.24 – 7.04 (m, 8H), 6.97 (m, 1H), 6.53 (dd, J = 8.5, 2.0 Hz, 1H), 6.44 (d, J = 2.0 Hz, 1H), 6.08 (s, 1H), 3.72 (s, 3H), 3.67-3.48 (m, 4H), 1.49 – 1.38 (m, 3H).

^{13}C NMR (75 MHz, $CDCl_3$): δ (ppm) 196.2, 174.9, 174.8, 163.2, 157.6, 141.5, 141.4, 140.9, 140.8, 139.6, 132.4, 132.3, 129.7, 129.0, 128.6, 128.2, 127.7, 126.7, 126.5, 126.2, 125.6, 125.5, 125.1, 125.0, 122.7, 105.8, 101.4, 82.5, 55.4, 52.0, 45.4, 45.3.

HRMS (ESI-TOF): *m/z*, $C_{31}H_{29}O_5$ $[M + H]^+$ calculated for 481.2005; found: 481.2015.

Synthesis of 2-(3-((2-benzoyl-5-methoxyphenoxy)(phenyl)methyl)phenyl)propanoic acid (OB-KP)

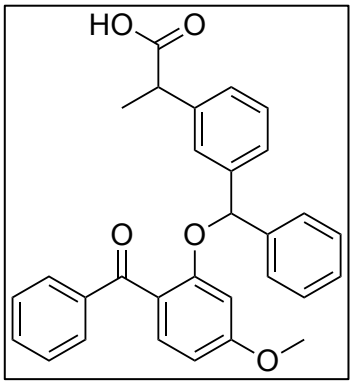

Compound OB-KP-Me (0.114 g, 0.237 mmol) was dissolved in a mixture of 1M aq. NaOH (0.53 mL) and THF (0.53 mL). The resulting solution was stirred for 20 h at room temperature. The mixture was acidified to pH 1 using 1 M aq. HCl, extracted with DCM (3 x 10 mL), dried ($MgSO_4$), and rotary evaporated to afford carboxylic acid.

^{1}H NMR (300 MHz, $CDCl_3$): δ (ppm) 8.86 (s, br, 1H), 7.81 (d, J = 7.8 Hz, 2H), 7.55-7.35 (m, 4H), 7.23-7.04 (m, 8H), 7.00-6.92 (m, 1H), 6.50 (dd, J = 6.3, 1.5 Hz, 1H), 6.43 (d, J = 1.5 Hz, 1H), 6.07 (s, 1H), 3.68 (2s, 3H), 3.65-3.52 (m, 1H), 1.50-1.33 (m, 3H).

^{13}C NMR (75 MHz, $CDCl_3$): δ (ppm) 196.5, 179.9, 163.2, 163.2, 157.6, 141.5, 141.5, 140.9, 140.9, 140.4, 139.5, 132.5, 132.3, 132.3, 129.7, 128.7, 128.2, 127.7, 126.2, 126.2, 122.6, 106.0, 101.4, 55.5, 55.4, 45.7, 18.6, 18.4.

HRMS (ESI-TOF): *m/z*, $C_{30}H_{27}O_5$ $[M + H]^+$ calculated for 467.1852; found: 467.1834.

Synthesis of (4-methoxy-2-((1,2,3,4-tetrahydronaphthalen-1-yl)oxy)phenyl)(phenyl)methanone (OB-TL)

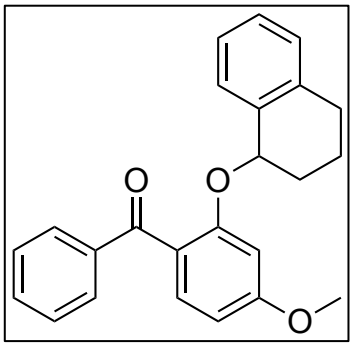

To a solution of α-tetralol (0.296 g, 2 mmol) and triphenylphosphine (0.630 g, 2.4 mmol) in anhydrous dioxane (10 mL) was added oxybenzone (0.685 g, 3 mmol) and DIAD (0.690 mL, 3.5 mmol). The solution was stirred at room temperature for 5 h. The crude reaction mixture was concentrated and purified by column chromatography (cy/AcOEt, 4:1; silica gel) to give the pure product OB-TL. Yield: 0.223 g (31%).

^{1}H NMR (400 MHz, $CDCl_3$): δ (ppm) 7.70-7.60 (m, 2H), 7.50-7.41 (m, 2H), 7.32 – 7.23 (m, 2H), 7.16-7.10 (m, 1H), 7.02 – 6.88 (m, 3H), 6.68 (d, J = 2.0 Hz, 1H), 6.62 (dd, J = 8.4, 2.0 Hz, 1H), 5.23 (t, J = 4.8 Hz, 1H), 3.88 (s, 3H), 2.61 (t, J = 6.3 Hz, 2H), 1.93 – 1.84 (m, 2H), 1.65 – 1.53 (m, 2H).

^{13}C NMR (101 MHz, $CDCl_3$) δ (ppm) 196.40, 163.25, 157.91, 139.22, 137.58, 134.88, 132.17, 129.56, 128.96, 128.95, 128.04, 127.89, 125.72, 123.81, 105.81, 102.33, 75.54, 55.70, 28.83, 28.32, 18.56.

HRMS (ESI-TOF): *m/z*, $C_{24}H_{22}O_3Na$ $[M+Na]^+$ calculated for 381.1467; found: 381.1454.

Synthesis of (4-methoxy-2-(1-phenylethoxy)phenyl)(phenyl)methanone (OB-AP)

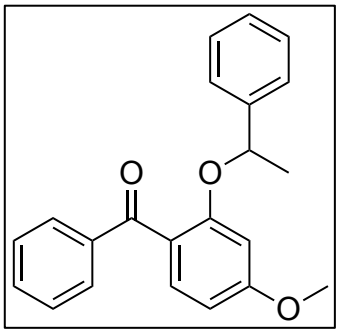

To a solution of 1-phenylethanol (0.244 g, 2 mmol) and triphenylphosphine (0.630 g, 2.4 mmol) in anhydrous dioxane (10 mL) was added oxybenzone (0.685 g, 3 mmol) and DIAD (0.690 mL, 3.5 mmol). The solution was stirred at room temperature overnight. The crude reaction mixture was concentrated and purified by column chromatography (cy/AcOEt, 4:1; silica gel) to give the pure product OB-AP. Yield: 0.306 g (46%).

^{1}H NMR (400 MHz, $CDCl_3$) δ (ppm) 7.75-7.66 (m, 2H), 7.4-7.40 (m, 1H), 7.40-7.26 (m, 3H), 7.22-7.06 (m, 3H), 7.04-6.97 (m, 2H), 6.42 (dd, J = 8.8, 2.4 Hz, 1H), 6.24 (d, J = 2.4 Hz, 1H), 5.08 (q, J = 6.4 Hz, 1H), 3.63 (s, 3H), 1.16 (d, J = 6.4 Hz, 3H).

^{13}C NMR (101 MHz, $CDCl_3$) δ (ppm) 196.46, 163.21, 157.90, 142.65, 139.74, 132.24, 132.10, 129.54, 128.65, 128.08, 127.64, 125.50, 122.58, 105.33, 101.19, 77.06, 55.45, 23.79.

HRMS (ESI-TOF): *m/z*, $C_{22}H_{21}O_3$ $[M+H]^+$ calculated for 333.1491; found: 333.1487.

4.4.2. NMR spectra

^{1}H NMR ($CDCl_3$, 300 MHz)

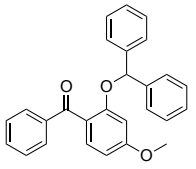

OB-BP

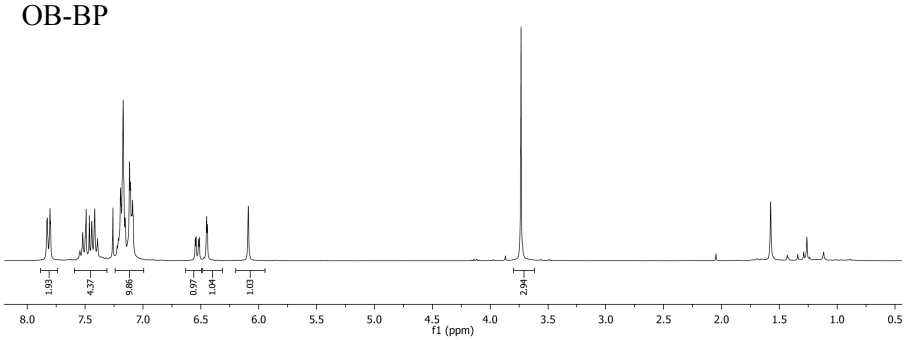

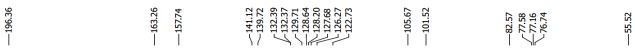

^{13}C NMR ($CDCl_3$, 75 MHz)

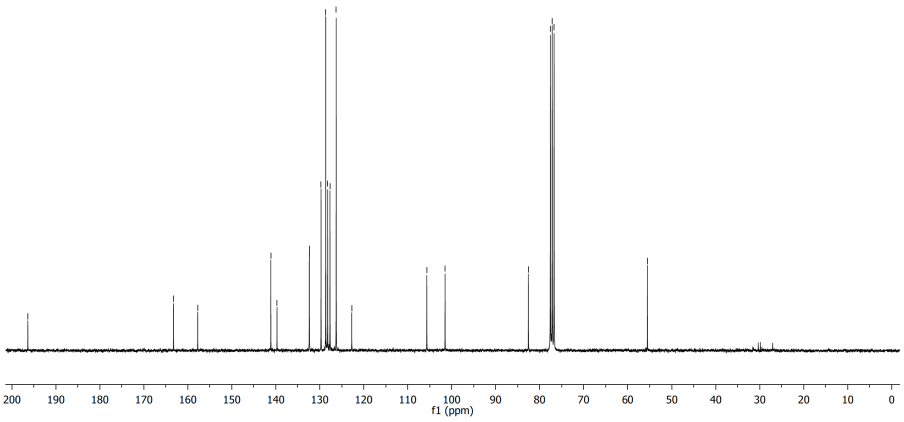

^{1}H NMR ($CDCl_3$, 300 MHz)

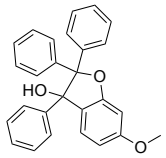

OB-BP-C

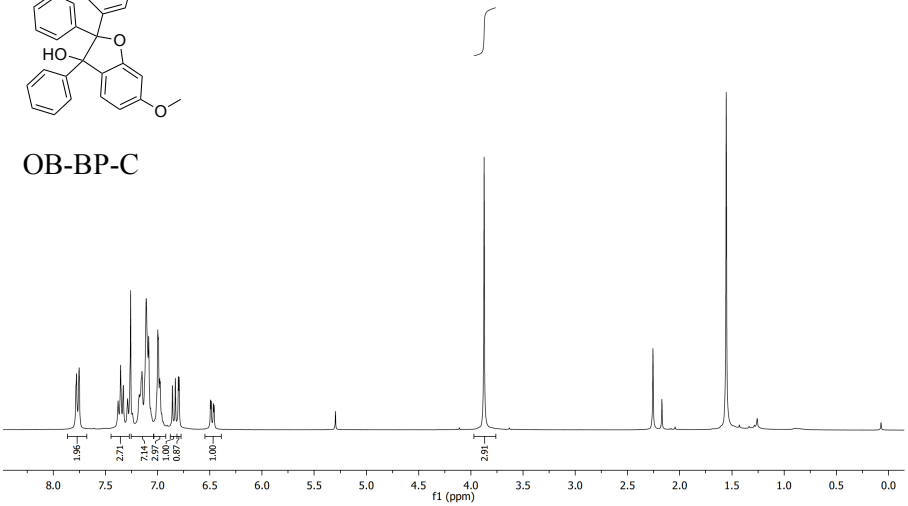

^{13}C NMR ($CDCl_3$, 75 MHz)

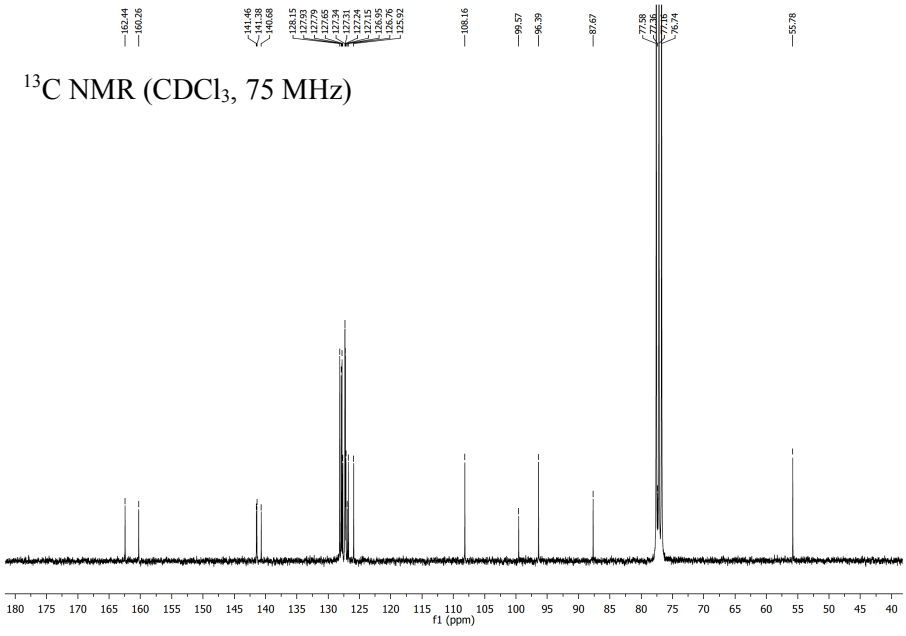

^{1}H NMR ($CDCl_3$, 300 MHz)

CBP-Me

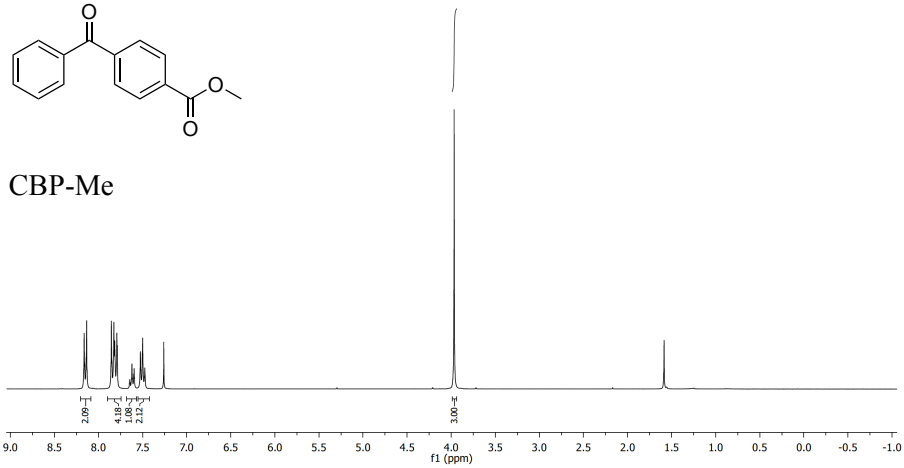

^{1}H NMR ($CDCl_3$, 300 MHz)

CBP-Red-Me

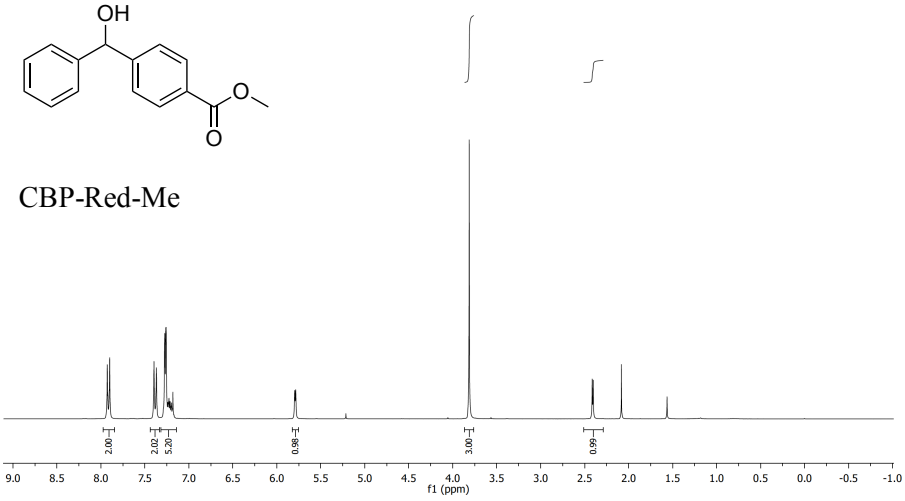

^{1}H NMR ($CDCl_3$, 300 MHz)

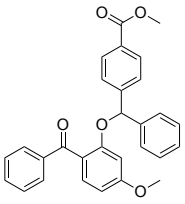

OB-CBP-Me

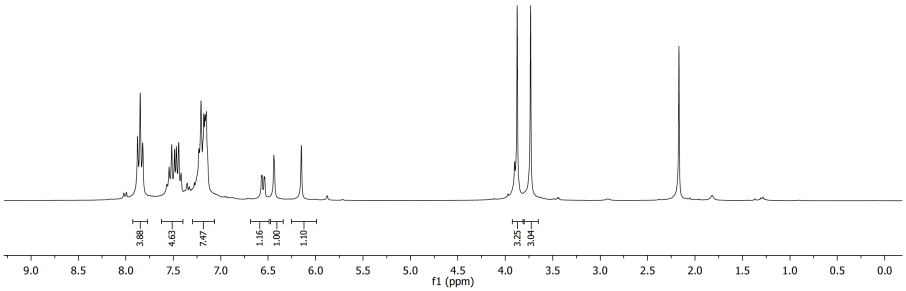

^{13}C NMR ($CDCl_3$, 75 MHz)

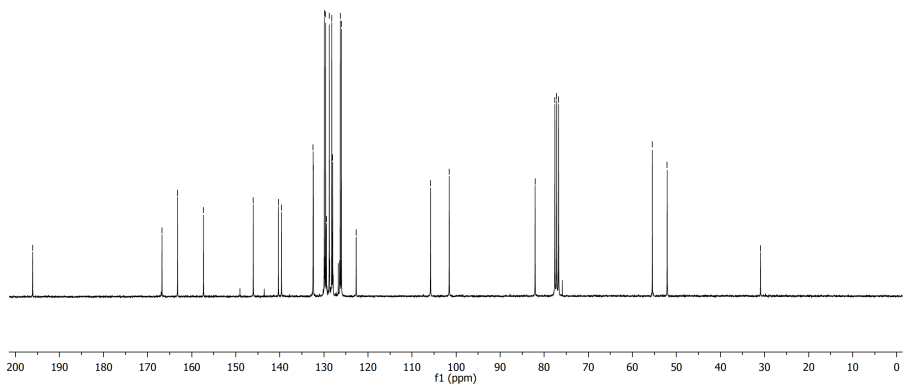

^{1}H NMR ($CDCl_3$, 300 MHz)

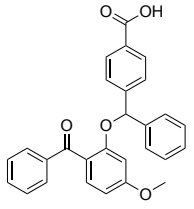

OB-CBP

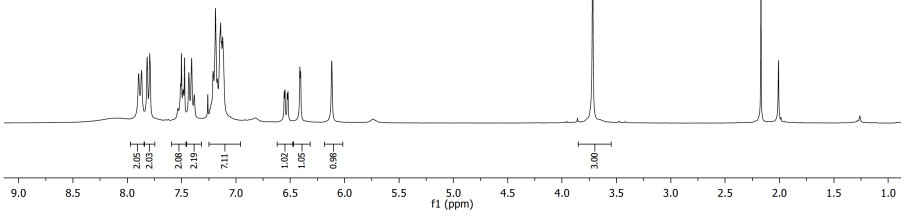

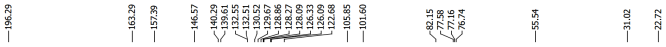

^{13}C NMR ($CDCl_3$, 75 MHz)

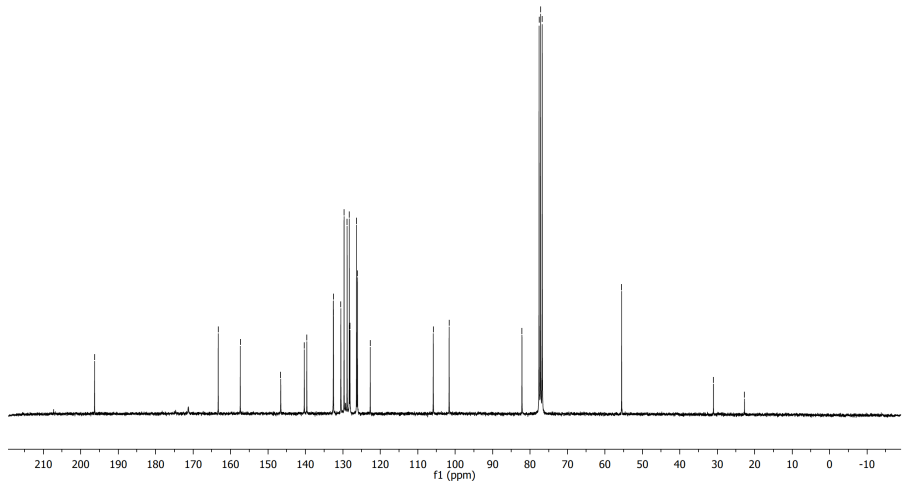

^{1}H NMR ($CDCl_3$, 300 MHz)

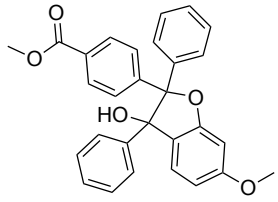

OB-CBP-C-Me

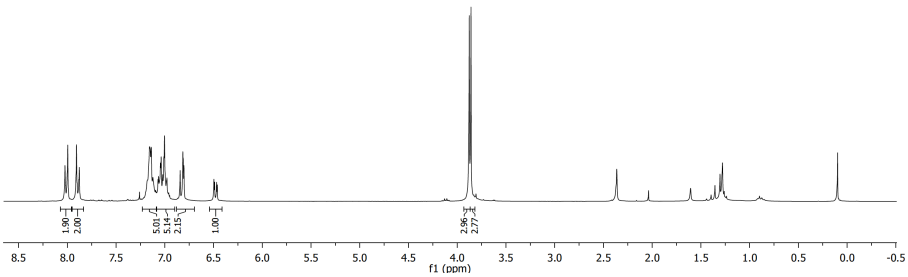

^{13}C NMR ($CDCl_3$, 75 MHz)

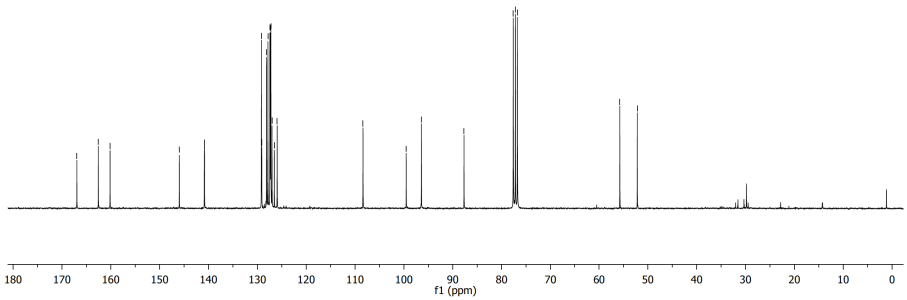

^{1}H NMR (CD_3OD, 300 MHz)

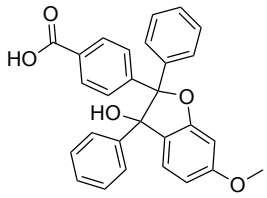

OB-CBP-C

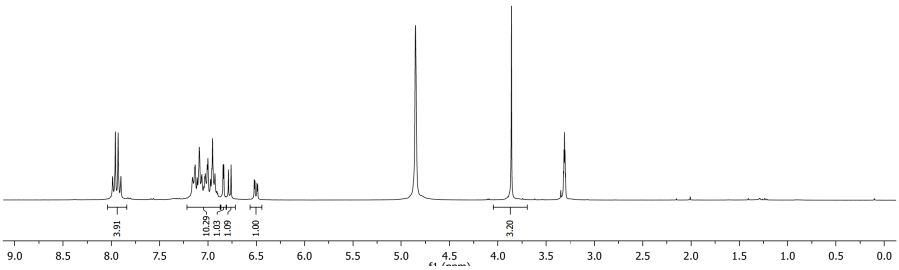

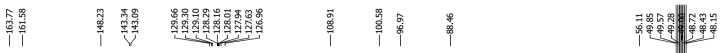

^{13}C NMR (CD_3OD, 75 MHz)

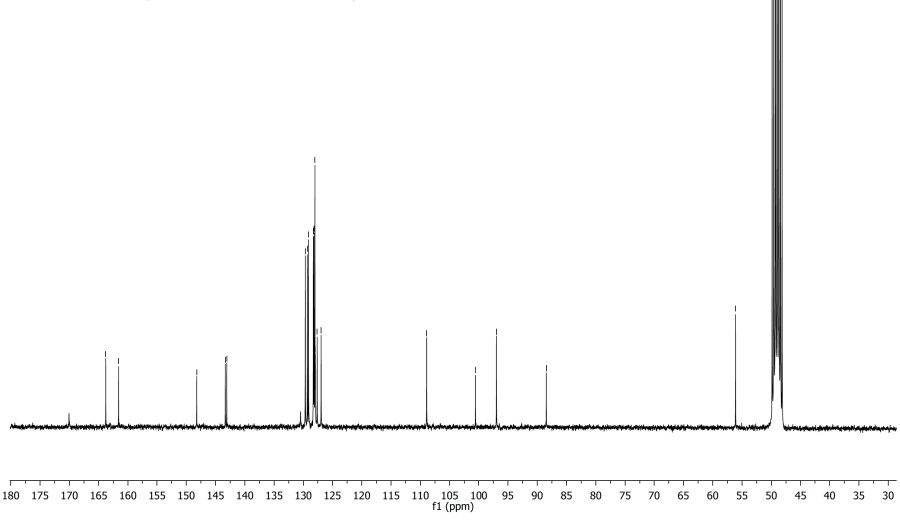

^{1}H NMR ($CDCl_3$, 300 MHz)

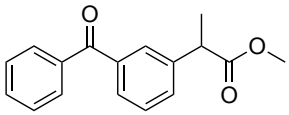

KP-Me

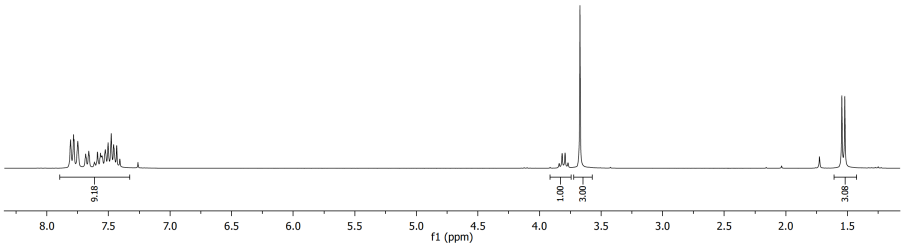

^{1}H NMR ($CDCl_3$, 300 MHz)

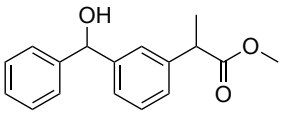

KP-Red-Me

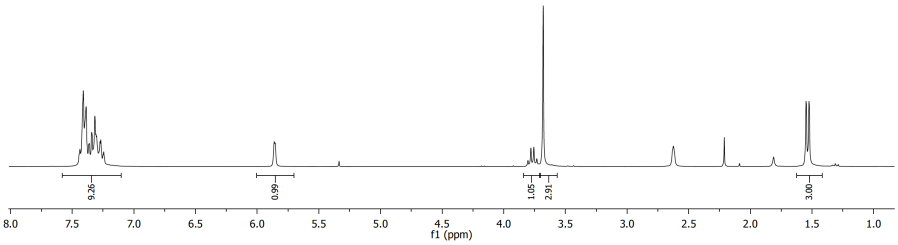

^{1}H NMR ($CDCl_3$, 300 MHz)

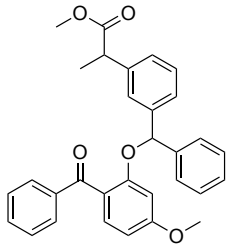

OB-KP-Me

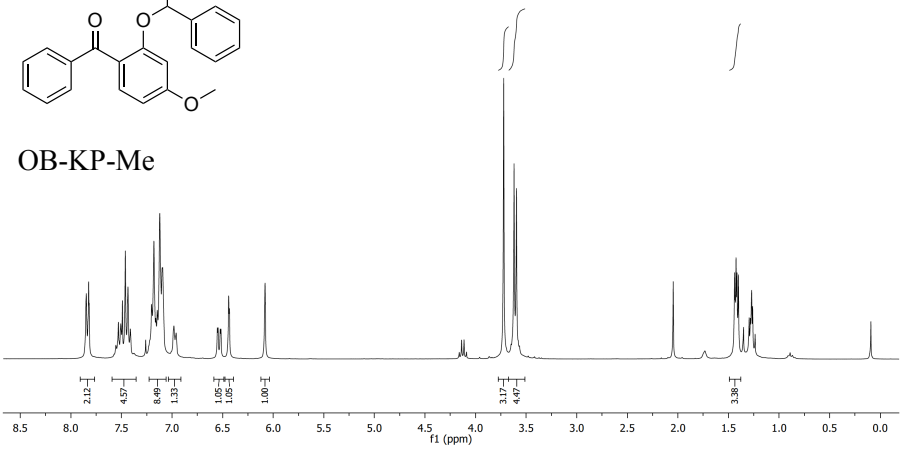

^{13}C NMR ($CDCl_3$, 75 MHz)

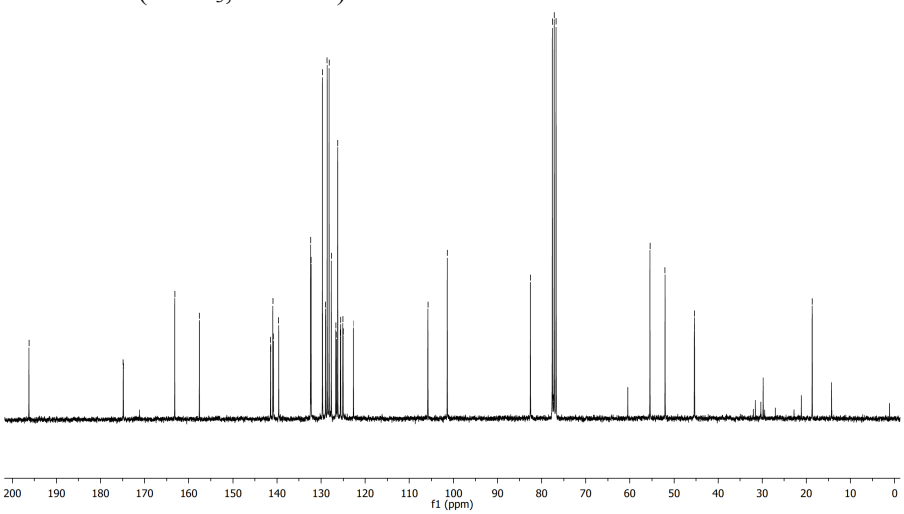

^{1}H NMR ($CDCl_3$, 300 MHz)

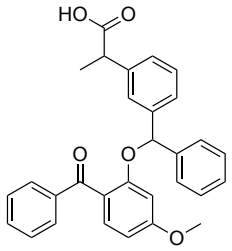

OB-KP

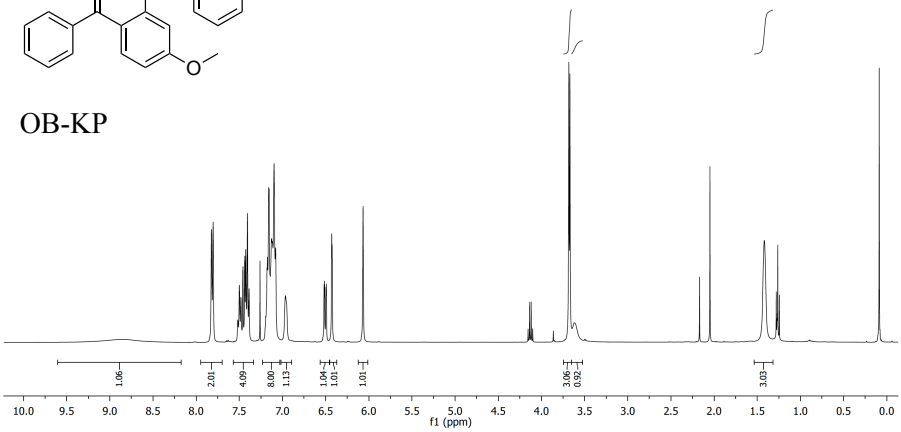

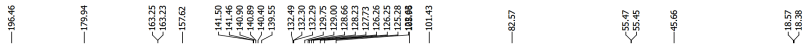

^{13}C NMR ($CDCl_3$, 75 MHz)

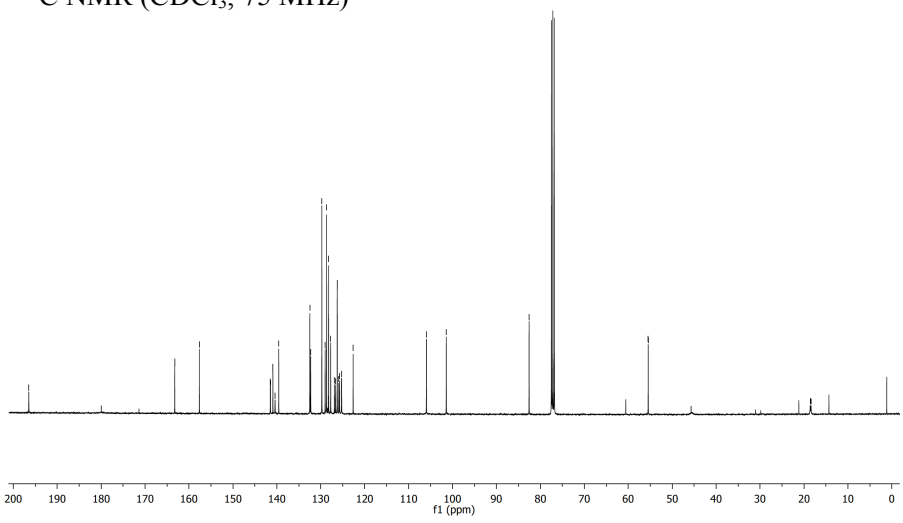

^{1}H NMR ($CDCl_3$, 400 MHz)

OB-TL

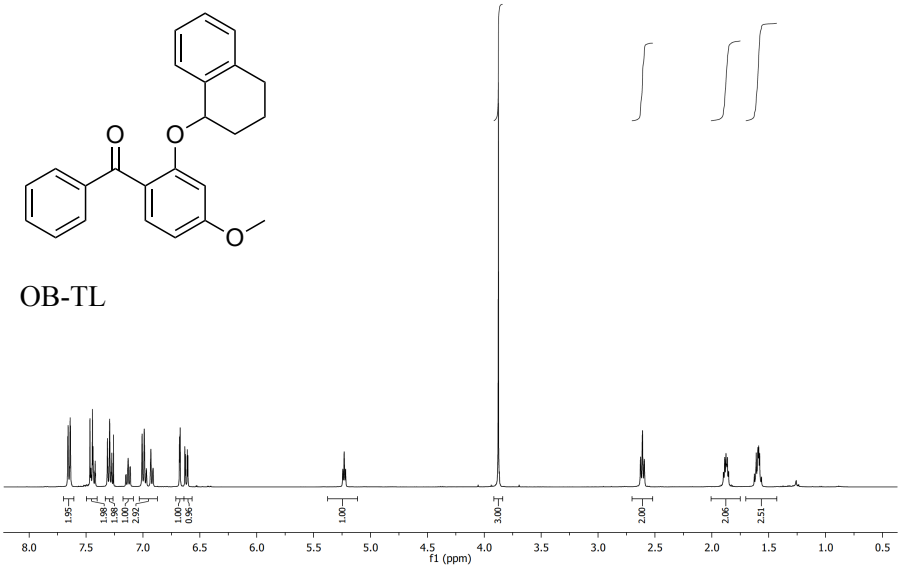

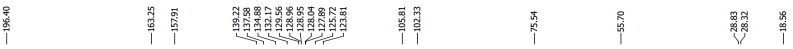

^{13}C NMR ($CDCl_3$, 101 MHz)

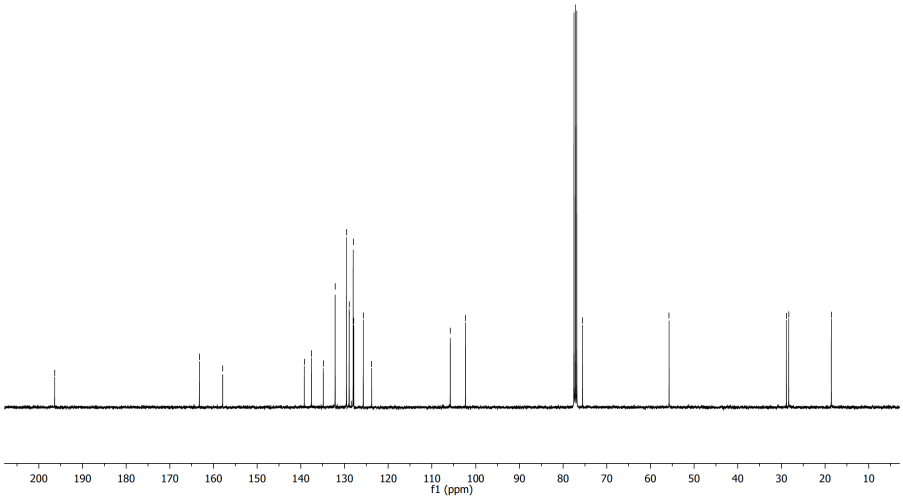

^{1}H NMR ($CDCl_3$, 400 MHz)

OB-AP

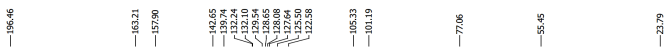

^{13}C NMR ($CDCl_3$, 101 MHz)

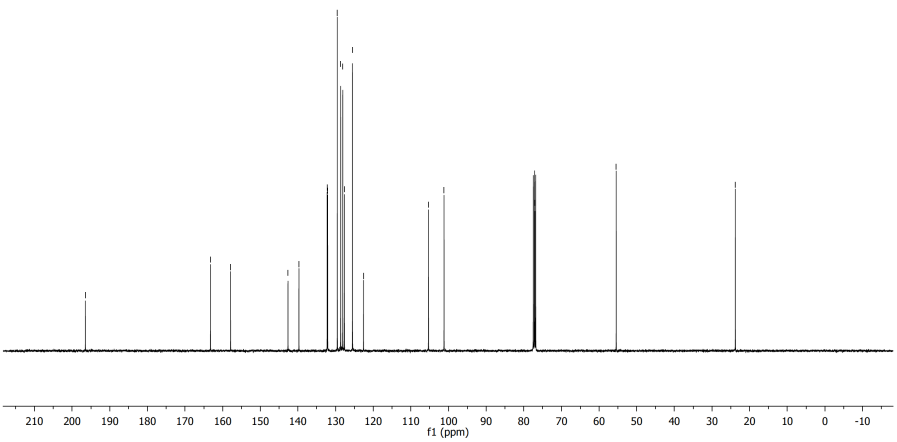

4.5. Bibliography

1 P. Klán, T. Šolomek, C. G. Bochet, A. Blanc, R. Givens, M. Rubina, V. Popik, A. Kostikov and J. Wirz, *Chem. Rev.*, 2013, **113**, 119–191.

2 A. Herrmann, *Angew. Chem. Int. Ed.*, 2007, **46**, 5836–5863.

3 P. Wang, *J. Photochem. Photobiol. A Chem.*, 2017, **335**, 300–310.

4 A. G. Griesbeck, B. Porschen, C. Kropf, A. Landes, O. Hinze, U. Huchel and T. Gerke, *Synthesis (Stuttg).*, 2017, **49**, 539–553.

5 J. Hébert and D. Gravel, *Can. J. Chem.*, 1974, **52**, 187–189.

6 D. Gravel, J. Hebert and D. Thoraval, *Can. J. Chem.*, 1983, **61**, 400–410.

7 P. Wang, A. Hu and Y. Wang, *Org. Lett.*, 2007, **9**, 2831–2833.

8 W. Pengfei, H. Huayou and W. Yun, *Org. Lett.*, 2007, **9**, 1533–1535.

9 H. Yang, X. Zhang, L. Zhou and P. Wang, *J. Org. Chem.*, 2011, **76**, 2040–2048.

10 A. P. Kostikov, N. Malashikhina and V. V. Popik, *J. Org. Chem.*, 2009, **74**, 1802–1804.

11 A. Blanc and C. G. Bochet, *J. Org. Chem.*, 2003, **68**, 1138–1141.

12 J. yu Yu, W. J. Tang, H. B. Wang and Q. H. Song, *J. Photochem. Photobiol. A Chem.*, 2007, **185**, 101–105.

13 M. Lu, O. D. Fedoryak, B. R. Moister and T. M. Dore, *Org. Lett.*, 2003, **5**, 2119–2122.

14 I. Aparici-Espert, M. C. Cuquerella, C. Paris, V. Lhiaubet-Vallet and M. Miranda, *Chem. Commun.*, 2016, **22**, 768.

15 I. Aparici-Espert, M. A. Miranda and V. Lhiaubet-Vallet, *Molecules*, 2018, **23**, 673–683.

16 R. L. Blankespoor, R. P. Smart, E. D. Batts, A. A. Kiste, R. E. Lew and M. E. Vander Vliet, *J. Org. Chem.*, 1995, **60**, 6852–6859.

17 R. L. Blankespoor, R. L. De Jong, R. Dykstra, D. A. Hamstra, D. B. Rozema, D. P. Vanmeurs and P. Vink, *J. Am. Chem. Soc.*, 1991, **113**, 3507–3513.

18 R. L. Blankespoor, T. Devries, E. Hansen, J. M. Kallemeyn, A. M. Klooster, J. A. Mulder, R. P. Smart and D. A. Vander Griend, *J. Org. Chem.*, 2002, **67**, 2677–2681.

19 D. R. Robello, T. D. Eldridge and E. J. Urankar, *Org. Prep. Proced. Int.*, 1999, **31**, 433–439.

20 M. Montalti, A. Credi, L. Prodi and T. M. Gandolfi, *Handbook of Photochemistry, Third Edition*, CRC Press, 2006.

21 D. Jornet, R. Tormos and M. A. Miranda, *J. Phys. Chem. B*, 2011, **115**, 10768–10774.

22 F. Boscá, G. Cosa, M. A. Miranda and J. C. Scaiano, *Photochem. Photobiol. Sci.*, 2002, **1**, 704–708.

23 D. L. Hughes, *New J. Org. Synth.*, 2009, **23**, 127–164.

24 M. Marin, V. Lhiaubet-Vallet and M. A. Miranda, *Org. Lett.*, 2012, **14**, 1788–1791.

25 H. Görner, *J. Phys. Chem. A*, 2008, **112**, 1245–1250.

Chapter 5:

Photochemistry of DNA lesions: 5-formyluracil versus 5-formylcytosine

5.1. Introduction

Nucleic acids are constantly exposed to endogenous and exogenous agents that can modify their chemical structure and therefore compromise their normal biological function.[1,2] Among such agents, ultraviolet light is known to trigger different photophysical and photochemical processes leading to the development of the so-called DNA photolesions.[3–6] Although DNA nucleobases are known for their high photostability,[7–11] dangerous DNA modifications are constantly produced and may be accumulated in the skin, inducing mutation and carginogenesis.[12,13] In this sense, the unprotected exposure to UV light is nowadays recognized as one of the main causes of malignant skin cancer such as melanoma.[4,14,15]

Generally speaking, DNA photolesions can be generated by direct UV light absorption or by photosensitization. Regarding DNA photodamages produced by direct UV light absorption, they mainly involve absorption of UVB radiation leading to the dominant production of cyclobutane pyrimidine dimers (CPD), along with 6-4-photoproduct (64-PP) as minor components.[5,16–18]. With respect to photosensitization, it proceeds through initial UVA light absorption by a chromophore located spatially close to DNA, which in turn can produce DNA lesions by indirect photochemical processes.[19] These usually involve the population of triplet states of the chromophores by means of intersystem crossing (ISC) followed by several photochemical routes traditionally categorized in three classes: (*i*) triplet-triplet energy transfer (TTET) to DNA, (*ii*) photoinduced electron transfer processes usually involving guanine (type I process), and (*iii*) activation of molecular oxygen to its singlet excited state (type II process). While electron transfer and singlet oxygen activation usually produce oxidative DNA lesions, triplet-triplet energy transfer has been shown, both computationally and experimentally, to favor thymine dimerization.[12,20,21] Here, we focus on the

first class of photosensitization, *i.e.* the triplet-triplet energy transfer from the chromophore to canonical bases of DNA.

A wide range of external photosensitizers have been studied in the last years,[12,22–25] a representative example being the paradigmatic case of benzophenone.[26–28] Nevertheless, it has been recently proposed that DNA lesions can themselves act as photosensitizers, since the modifications of their chemical structure may alter their optical and photophysical properties. This phenomenon was named as "Trojan horse" after recognizing that 64-PP acts as an internal photosensitizer.[29] It was found that the presence of the pyrimidone moiety leads to absorption in the UVA range and induces CPD production after ISC and subsequent triplet-triplet energy transfer. The possibility of TTET was also confirmed using molecular modeling and simulations.[30]

Recently, the role as potential Trojan horse of the oxidative lesion 5-formyluracil (ForU)[31] has been studied through experiments[32] and theoretical calculations.[33,34] It has indeed been recognized, both in model systems and in DNA oligomers, that the inclusion of ForU is correlated with a significant increase in the yield of CPD damages.[32] Furthermore, molecular modeling and simulations have shown that ForU is prone to a facile ISC, leading to an energetically favorable TTET to thymine and that those conditions are maintained in the DNA environment.[33]

Indeed, the behavior of its cytosine counterpart, 5-formylcytosine (ForC) is extremely intriguing, not only from a photophysical perspective, but also due to its biological relevance. ForC can be considered an oxidative lesion, but also an epigenetic intermediate in the demethylation process of 5-methylcytosine (mC). Indeed, the methylation of cytosine at 5 position, occurring in non-coding DNA regions with a high density of guanine and

cytosine, the so-called CpG islands, results in the silencing of the specific gene expression.

In eukaryotic cells, gene expression as a response to external stress is controlled by the active demethylation process, which may proceed through two different mechanisms involving each of them two phases (Figure 5.1). The first phase is shared by both mechanisms and involves the ten-eleven translocation family dioxygenase enzymes (TET1, TET2 and TET3) that produce the consecutive oxidation of mC to 5-hydroxymethyl cytosine (hmC), 5-formylcytosine (ForC) and 5-carboxylcytosine (caC).[35] In relation with the second phase, two different approaches have been proposed so far. A first proposal involves the identification and excision of ForC or caC by thymine-DNA glycosylase (TDG) forming an AP sites that is further cleaved by an AP endonuclease and finally filled in with the unmodified cytosine by the action of polymerase β (Pol β).[36] A second proposal involves direct C-C bond cleavage that turn ForC directly into cytosine. The mechanism proposed for the direct demethylation requires a still unknown nucleophile to attack the C6-position.[37]

The fact that an epigenetic intermediate, ForC, can potentially induce DNA photolesions, clearly opens fundamental questions concerning the subtle interplay between epigenetic phenomena and DNA photolesions, and hence can contribute to solve the molecular grounds of the problems related to the cellular tumorigenesis and the protective mechanisms that cells may have developed as a result of evolutionary pressure.

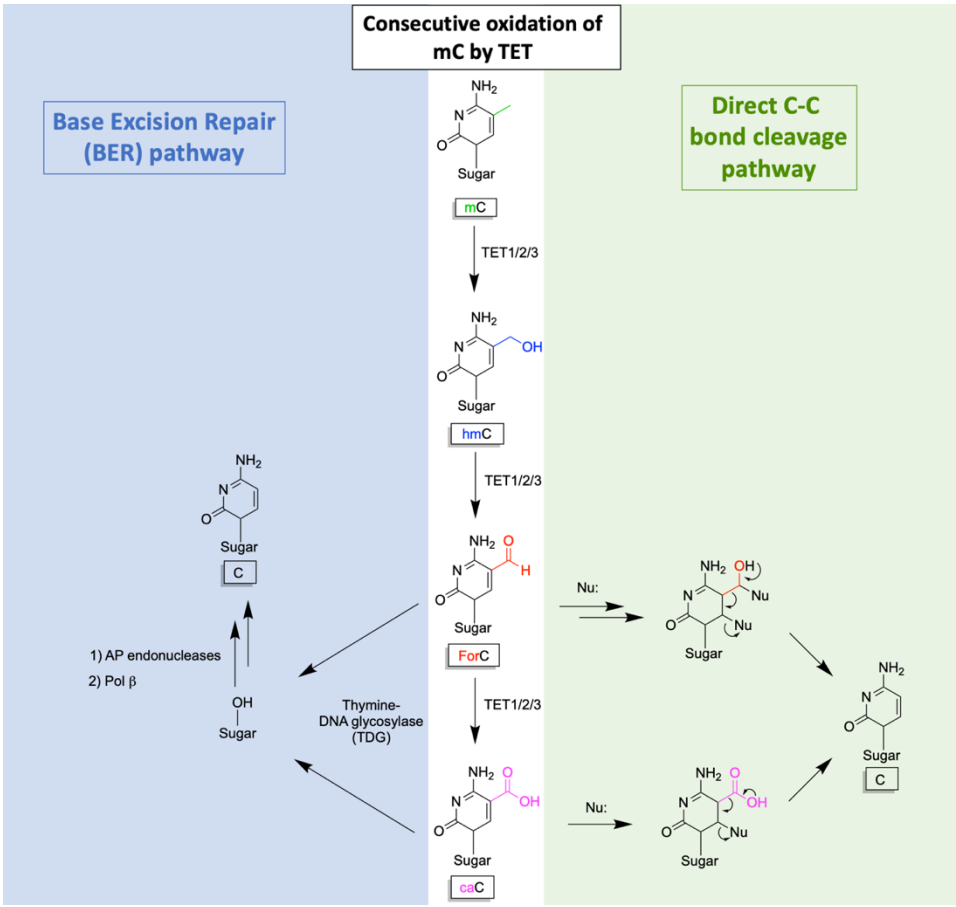

Figure 5.1. Proposal mechanisms for the active demethylation process.

In this chapter, it is rationalized and compared, by means of experimental and theoretical approaches, the propensity of ForU and ForC to photoinduce the formation of cyclobutane pyrimidine dimers. The crucial differences between the two chromophores and their effects on thymine dimerization are duly analyzed.

5.2. Results and discussion

5.2.1. Characterization of the singlet excited state

First of all, the UV-Vis spectra of both oxidized nucleobases (ForU and ForC) were recorded in different solvents (Figure 5.2A and 5.2B). ForU optical properties are solvent dependent showing the stronger bathochromic shift in phosphate buffer solution (PBS) with a maximum at around 300 nm and a tail reaching up to 340-350 nm. Conversely, the absorption maximum for ForC does not show solvatochromism, peaking at around 275 nm while the tail cuts off at 320-330 nm.

The absorption spectra of both modified nucleobases in different solvents were also simulated at Time-Dependent Density Functional Theory (TD-DFT) level. These simulations have been performed in collaboration with Prof. A. Monari and Dr. A. Francés-Monerris from University of Lorraine (France). The TD-DFT spectra (Figure 5.2C and 5.2D) reproduce well the global band shape both in the maximum and the tail regions, however, a global blue-shift is observed.

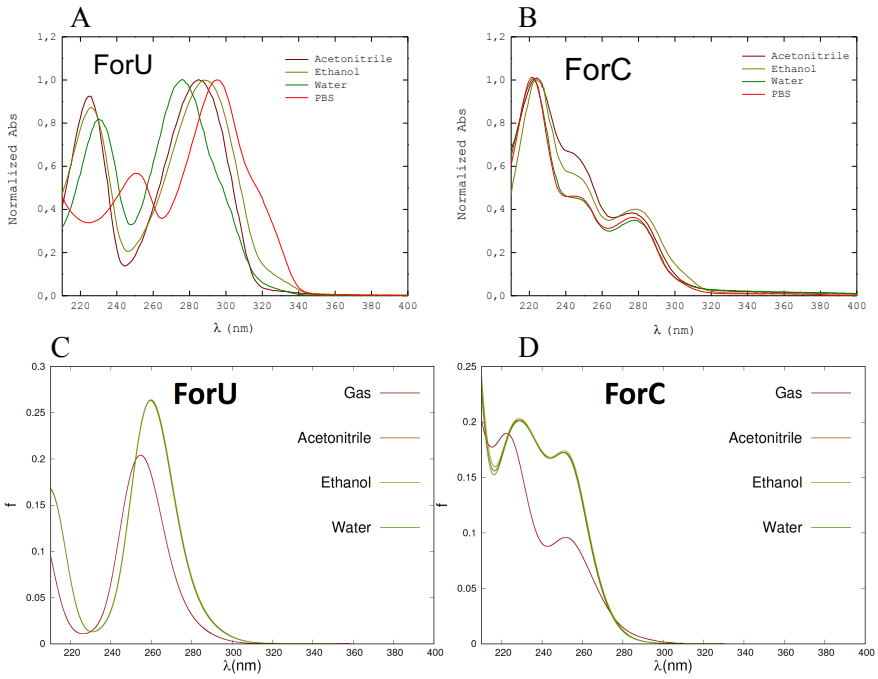

Figure 5.2. Experimental absorption spectra of ForU (A) and ForC (B) in different solvents. TD-DFT computed absorption spectra of ForU (C) and ForC (D) in different solvents.

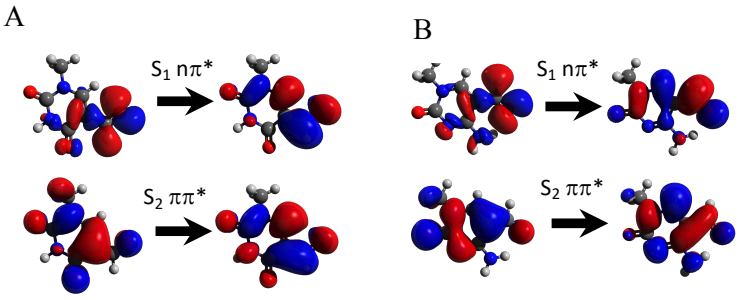

Figure 5.3. NTOs for the first lowest transition of ForU (A) and ForC (B) are shown confirming the presence of n,π* and π,π* states.

Analysis of the Natural Transition Orbitals (NTOs, Figures 5.3A and 5.3B)[38] shows that for both nucleobases the lowest transition, giving rise to the long-wavelength tail, is of ^{1}n,π* nature, hence darker, while the S_2 state corresponds to ^{1}π,π* with electronic density reorganization delocalized over the full aromatic ring.

No evident differences in the nature of the low-lying excited singlet state of ForC and ForU can be highlighted, however, the energy gap between the two states is larger for ForU, amounting to 1.1 eV at Franck-Condon geometry, while it decreases to 0.6 eV in the case of ForC. The calculated energy gaps between the first two excited states are also in good agreement with the spectra recorded in water that give two peaks at 276 and 230 nm, *i.e.* a gap of 0.9 eV for ForU, while ForC presents absorption at 278 and 245 nm leading to a gap of 0.6 eV. The local nature of the transition (*i.e.* absence of charge transfer) is also confirmed by the value of the topological ϕ_S index[39,40] that is close to 1.0 for both chromophores.

None of the compounds show fluorescence emission, pointing toward an efficient deactivation of the singlet excited state by nonradiative pathways such as internal conversion or ISC.

5.2.2. Phosphorescence emission

Experimental information on the triplet energy value of both nucleobases was obtained from the phosphorescence spectra registered in ethanol glass at 77K (see Figure 5.4). Both compounds exhibit a broad emission band, with a maximum markedly blue shifted at a λ_{em} of *ca.* 425 nm for ForC, whereas the phosphorescent emission of ForU peaks at λ_{em}= 445 nm. This emission informs not only on the occurrence of ISC, which populates

the triplet excited state, but also on the triplet energy (E_T) of the uracil and cytosine derivatives. From the wavelength corresponding to the 20% of the emission we have estimated the energy levels of the lowest triplet state, that amount to 304 kJ·mol^{-1} (3.15 eV) and 326 kJ·mol^{-1} (3.38 eV) for ForU and ForC, respectively. These measurements indicate that the triplet energy is lower for ForU, as observed from both band origin and maximum wavelengths of the corresponding phosphorescence spectra.

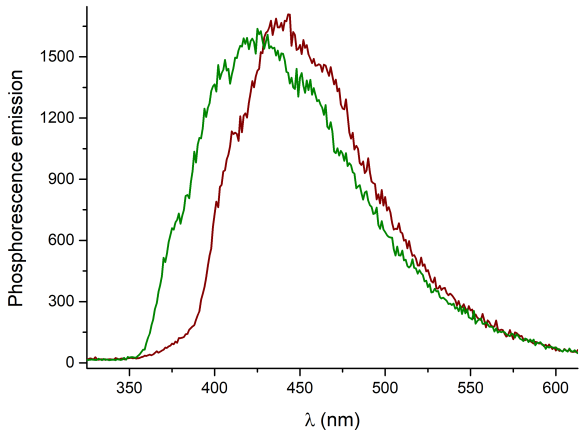

Figure 5.4. Low temperature phosphorescence spectra of ForC (green) and ForU (red) in Ethanol after excitation at 280 nm.

In order to identify the emissive triplet states for both compounds, the band origin and the band peak have been determined with the TD-DFT method (see Table 5.1). These results allow to identify the ^{3}n,π* state as the emissive state for ForU, whereas the ^{3}π,π* state is responsible of the ForC phosphorescence. This assignment is based on the good agreement between the experimental and computational values, and especially on the fact that the vertical emission wavelength of the ^{3}π,π* state of ForU is predicted at 513

nm, far from the 445 nm peak recorded experimentally, which matches much better with the $^3n,\pi^*$ vertical emission (427 nm).

5.2.3. Characterization by laser flash photolysis

5.2.3.1. Characterization of the transient species

The triplet excited state behavior of both oxidized bases at room temperature was monitored using laser flash photolysis. These experiments and also the following ones in the presence of thymine dimer (Thy-Thy), are performed in a mixture of MeCN:H_2O (1:1, v:v) for a better solubility of ForU, ForC and Thy-Thy. As shown in Figure 5.5, in this solvent mixture, ForU and ForC exhibit an absorption band with maximum at 276 nm, reaching the UVA region in both cases.

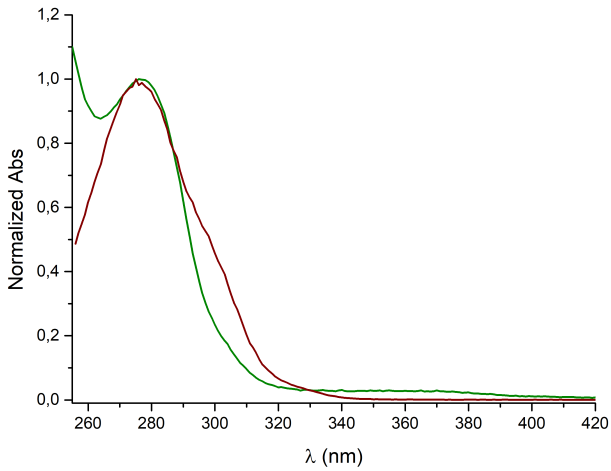

Figure 5.5. Normalized UV-vis absorption spectra of 5-formyluracil (ForU, red) and 5-formylcytosine (ForC, green) in MeCN:H_2O (1:1, v:v).

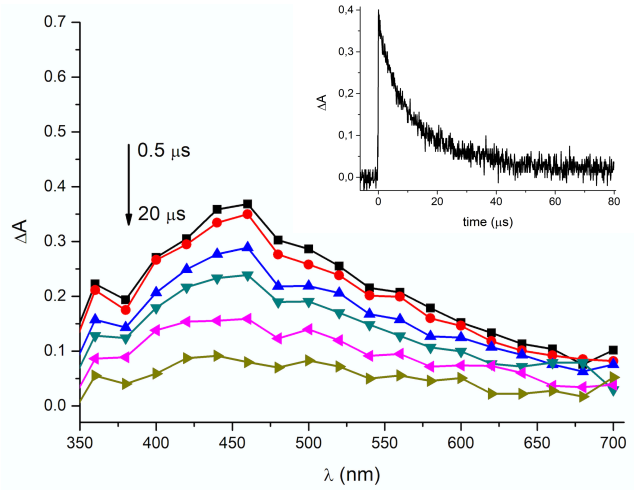

Figure 5.6. Transient absorption spectra of 5-formyluracil in MeCN:H_2O (1:1, v:v) under N_2 at different times after the 266 nm laser pulse. Inset: decay of ForU monitored at 440 nm.

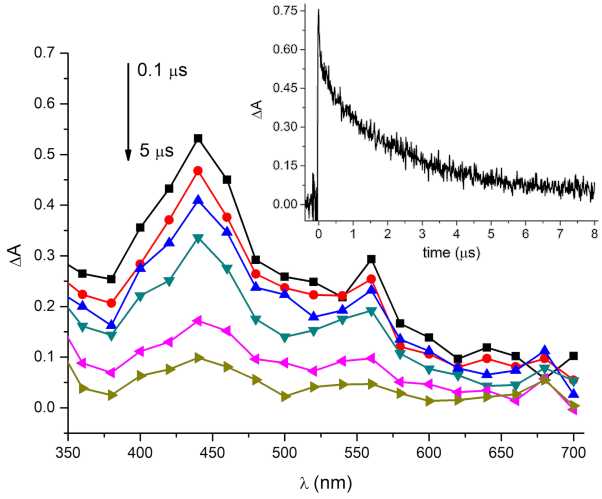

Figure 5.7. Transient absorption spectra of 5-formylcytosine in MeCN:H_2O (1:1, v:v) under N_2 at different times after the 266 nm laser pulse. Inset: decay of ForC monitored at 440 nm.

The transient absorption spectrum of ForU (Figure 5.6) showed a single broad band with maximum at 440-460 nm that completely disappeared after 40 μs without giving rise to any other species. This transient signal was assigned to the triplet-triplet absorption by comparison with our previously published data in PBS, but the spectrum in aqueous acetonitrile was cleaner and much less noisy.[32] The decay monitored at 440 nm can be fitted with a monoexponential function, $f(t) = A \exp(-t/\tau)$, yielding a lifetime τ of *ca.* 12 μs (Figure 5.6, inset) that is much longer than the one found in PBS.

The cytosine derivative, ForC, also displayed a signal centered at 440 nm together with a shoulder at 560 nm, both bands decreasing with the same kinetics (Figure 5.7); this transient signal was assigned to the triplet excited state of ForC.[34]

Concerning the kinetics, a biexponential behavior was found for the 440 and 560 nm decays, which were adjusted using the equation $f(t) = A_1 \exp(-t/\tau_1) + A_2 \exp(-t/\tau_2)$. The obtained lifetimes are $\tau_1 = 0.07$ μs ($A_1 = 0.25$) and $\tau_2 = 2.3$ μs ($A_2 = 0.75$) (Figure 5.7, inset). Both characteristic lifetimes are significantly shorter than that of ^{3}ForU*, and thus, the dynamic range for ^{3}ForC* intermolecular quenching is reduced, especially in the case of τ_1. Thus, bimolecular rate constants for ^{3}ForC* quenching were further determined using the changes of τ_2, only.

The above results establish that, upon excitation, both ForU and ForC populate triplet excited states with energies (304 kJ·mol^{-1} and 326 kJ·mol^{-1}, respectively) higher than that of thymine (*ca*. 270 kJ·mol^{-1})[41] and with a lifetime in the microsecond timescale, hence they can potentially induce energy transfer. Thus, the next step was to evaluate the ability of these excited states to photosensitize CPDs formation by means of time-resolved and steady-state experiments.

5.2.3.2. Triplet-triplet energy transfer rates to Thy-Thy

The photochemistry of ForU and ForC (Scheme 5.1) was tackled in aqueous media at room temperature in order to evaluate their potential to act as intrinsic photosensitizers. In this context, triplet excited states have been well-established as key intermediates in the photosensitized generation of damages.[12,42] Therefore, in addition to the spectroscopic characterization of the formyl derivatives, particular attention was paid here to thymine dimer formation as an analytical tool to compare the harmfulness of ForU and ForC triplet excited states. Indeed, the photosensitization of cyclobutane thymine dimer (Thy<>Thy, Scheme 5.1) is a clean reaction that occurs by TTET from the photosensitizer excited state to the pyrimidine base. To be efficient, this process requires a photosensitizer with a high triplet energy (higher than that of thymine), a high ISC quantum yield to allow significant population of the triplet manifold, and a triplet lifetime long enough to maximize the likelihood of the energy transfer process. Hence, monitoring Thy<>Thy formation provides valuable information on the overall strength of photosensitizing compounds.

As previously shown, both compounds exhibit in MeCN:H_2O (1:1, v:v) a band that reaches the UVA region allowing their selective excitation in the presence of canonical DNA bases. Nonetheless, the uracil derivative has a larger band, which broadens the spectral range available for its excitation.

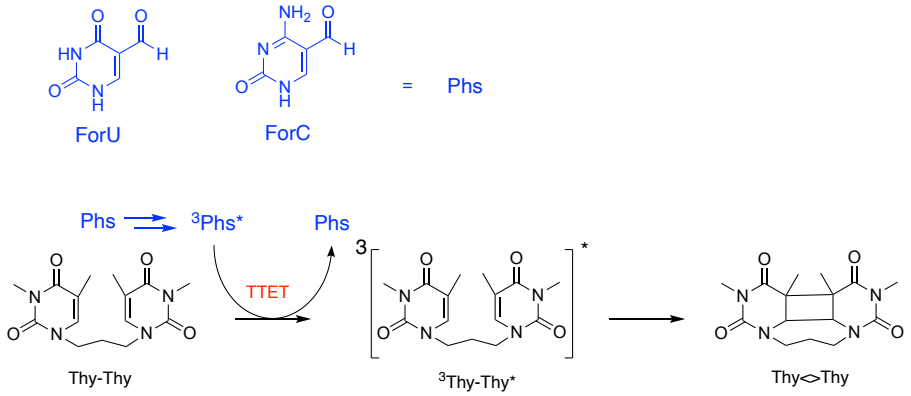

Scheme 5.1. Structures of both photosensitizers (Phs) under study (ForU and ForC) and the photosensitized [2+2] cycloaddition of Thy-Thy to afford Thy<>Thy.

First, laser flash photolysis was employed to determine the rate of the triplet-triplet energy transfer from ^{3}ForU* and ^{3}ForC* to Thy-Thy (Scheme 5.1), used as a model of adjacent nucleobases. As shown in Figure 5.8A and B, the addition of increasing amounts of Thy-Thy resulted in the shortening of the triplet excited state decay of the formyl derivatives, together with a decrease of the end-of-pulse signal intensity, which is the filter effect produced by the thymine chromophore at the excitation wavelength. Stern-Volmer plot representation of τ_0/τ as a function of the quencher concentration, reported as inlay, provided the bimolecular TTET rate constant (k_q) for both sensitizers (see Figure 5.8C). A value of 1.3 x 10^9 $M^{-1}s^{-1}$ was obtained for the ^{3}ForU* quenching, while the process was almost three times slower for ^{3}ForC* with a k_q of *ca.* 4.6 x 10^8 M^{-1} s^{-1}. Taking into account that the model system has two thymine units, the obtained values are in agreement with those previously given in the literature for TTET processes involving thymine as energy acceptor using other photosensitizers.[12,43]

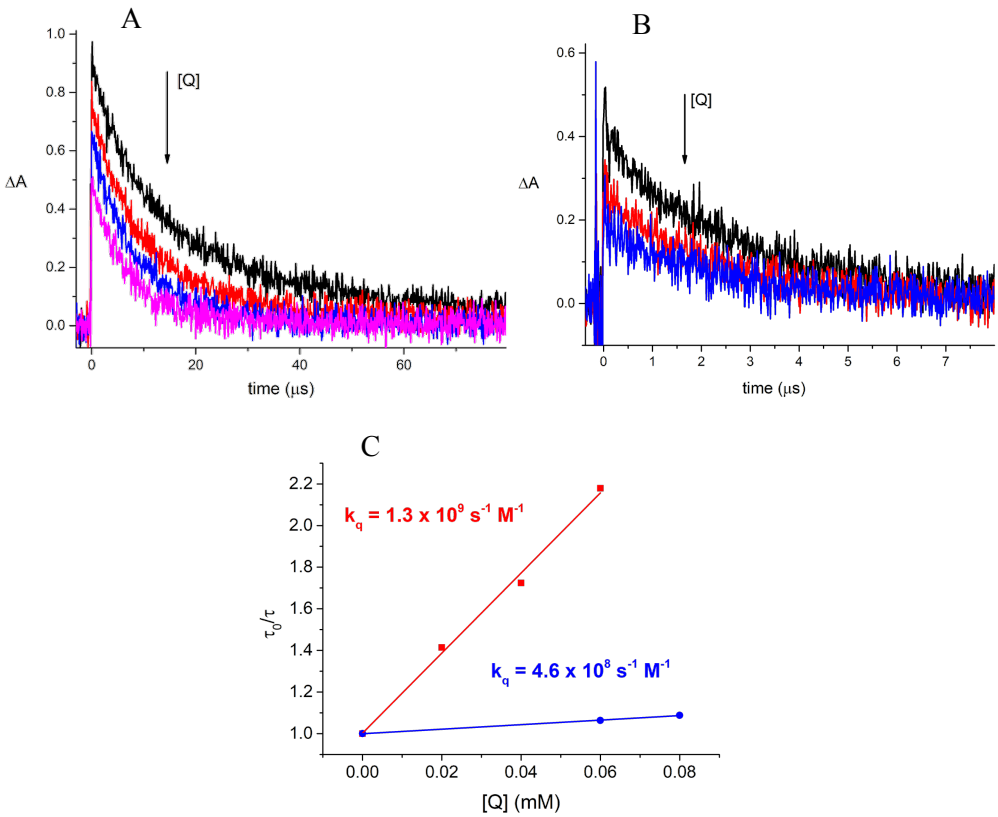

Figure 5.8. Decays of ForU (A) and ForC (B) in deaerated MeCN:H_2O (1:1,v:v) at 440 nm after the laser pulse at 266 nm in the presence of different Thy-Thy concentrations (Q from 0 to 0.08 mM). (C) Stern-Volmer plot of ForC (blue) and ForU (red) by Thy-Thy.

Curiously, an inverted order for the rate constants was expected based on the triplet energies, higher for ForC than for ForU, and on the Sandros´ equation.[44] This equation establishes that, for triplet-triplet energy transfer processes, the larger the energy difference between the donor (ie. formyl

derivatives) and the acceptor (ie. the Thy-Thy dyad), the higher the rate constant. The data obtained here pointed toward the occurrence of a more complex process than a typical energy transfer.

5.2.4. Steady-state photolysis of Thy-Thy in the presence of ForU and ForC

Next, steady-state photolysis was performed on deaerated MeCN:H_2O (1:1, v:v) solutions of Thy-Thy in the presence of ForU or ForC and using monochromatic light at λ_{exc} = 310 nm. All samples contained the same concentration of Thy-Thy (3.5 mM), ForC concentration was fixed at 1 mM, while in the case of ForU, the photosensitizer concentration was adjusted in order to obtain the same absorbance at λ_{exc} as for ForC.

The course of the photoreaction was followed by ^{1}H NMR and HPLC (Figures 5.9 and 5.11). In both cases, a clean process was observed with the formation of the *cis-syn* cyclobutane dimer of Thy-Thy (Thy<>Thy) as the only photoproduct. This assignment was based on the comparison with the NMR chemical shifts of synthetized Thy<>Thy (see Figure 5.10).

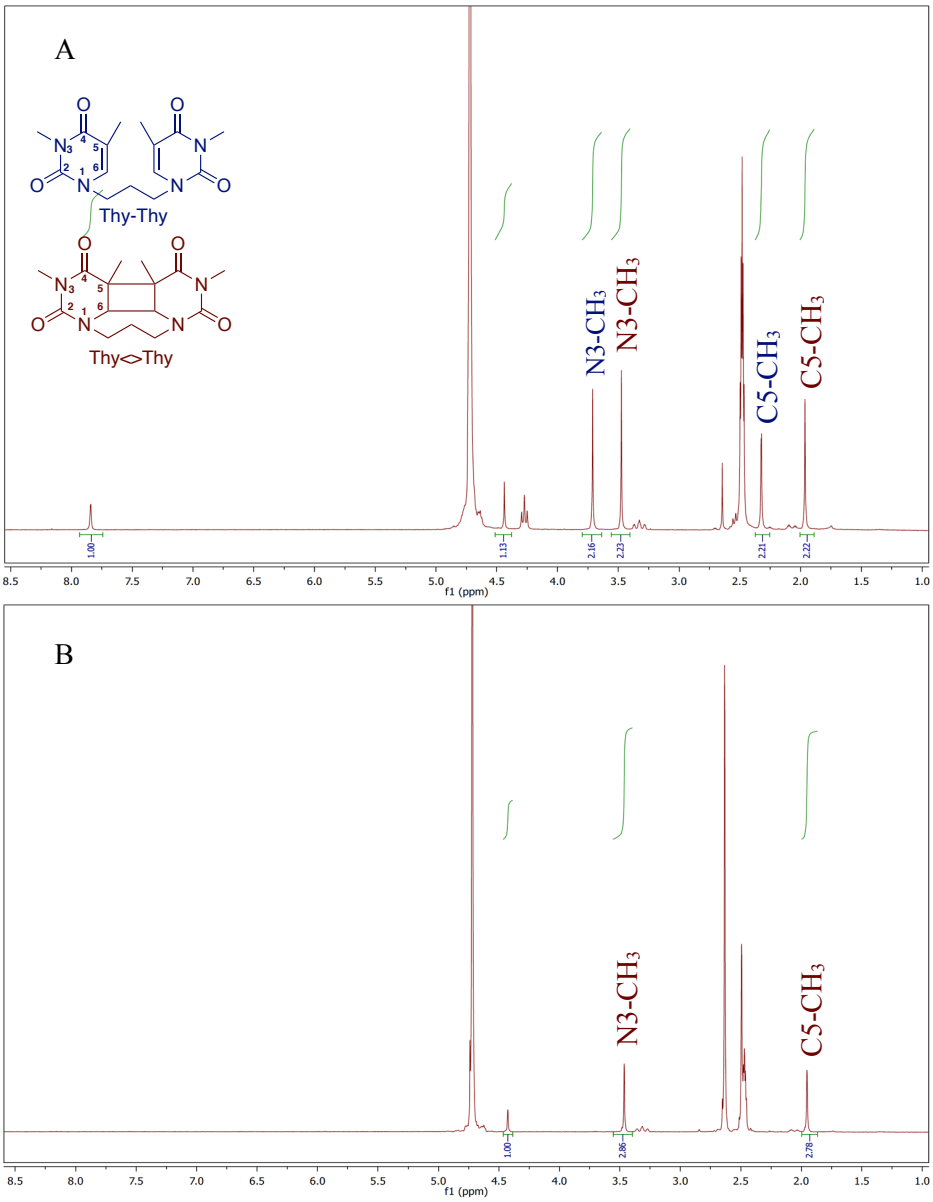

Figure 5.9. ^{1}H NMR spectrum in D_2O/CD_3CN (1:1, v:v) of the 60 min irradiation at 310 nm of ForC:Thy-Thy (1 mM:3.5 mM) (A) and ForU:Thy-Thy (0.38 mM:3.5 mM) (B).

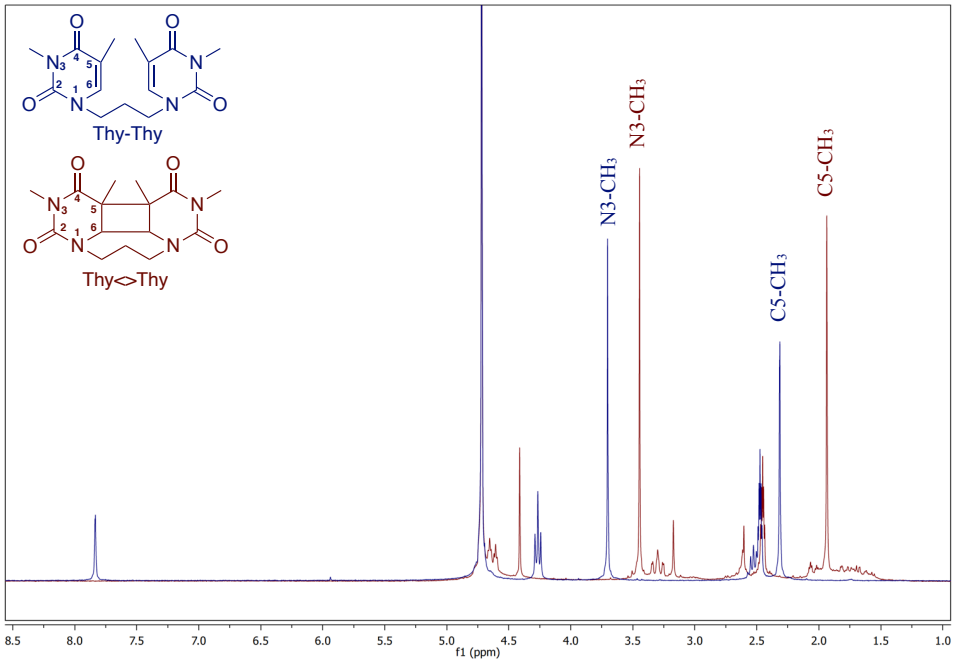

Figure 5.10. ^{1}H NMR (D_2O:CD_3CN, v:v, 300 MHz) of pure Thy-Thy (blue line) and Thy<>Thy (red line).

The NMR spectra of irradiated samples gave relevant information on the course of the photoreaction and on the nature of the photoproducts. They show that the [2+2] photocycloaddition leading to Thy<>Thy formation results in the saturation of the C5-C6 double bond and induces characteristic changes in the chemical shifts (δ) of the protons belonging to the nucleobase and to the trimethylene bridge. The most pronounced change was observed for the H6 proton that shifted from 7.90 to upper fields at *ca.* 4.48 ppm (Figure 5.10). Signals of the methyl group at N3 also experienced shielding passing from 3.77 to 3.51 ppm, while those of the C5 methyl moved from 2.38 to 2.00 ppm. The ratio of the integrals of these signals (taken as pairs) can be used to

evaluate the reaction course. In the case of ForC irradiation, it was observed that after 1h, 50% of Thy-Thy was decomposed to yield Thy<>Thy as the sole product (Figure 5.9A). Interestingly, when using ForU as a photosensitizer, the initial dyad is completely consumed under the same conditions (Figure 5.9B).

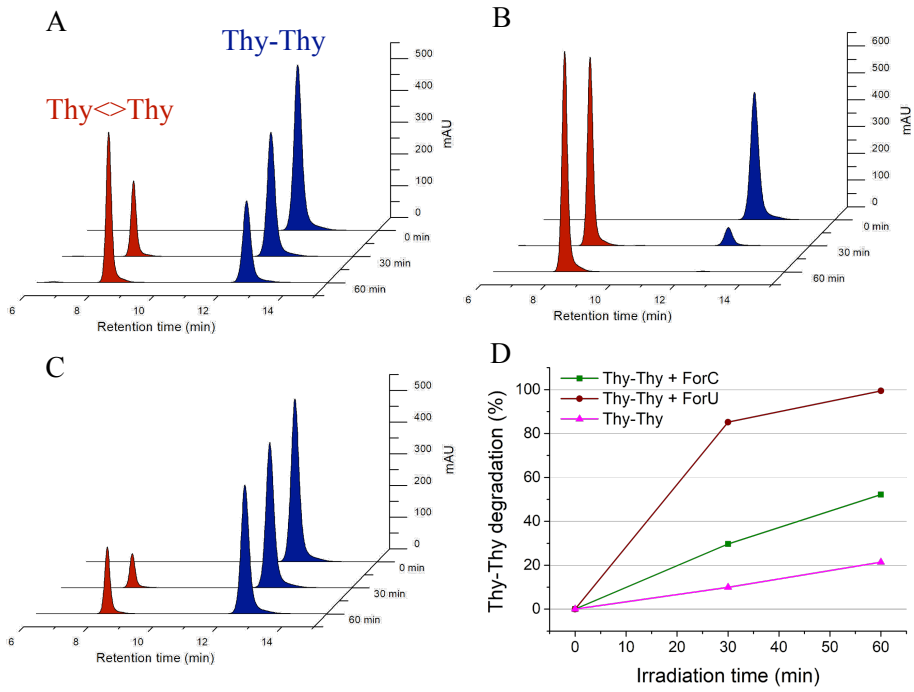

Figure 5.11. HPLC chromatograms registered at 240 nm for monochromatic irradiation (λ_{exc}= 310 nm) from 0 to 60 min of Thy-Thy (3.5 mM) in H_2O:MeCN (1:1, v:v) in the presence of ForC (1 mM) (A), in the presence of ForU (0.38 mM) (B) or alone (C). Time-dependent photodegradation of Thy-Thy, in the presence of ForU (red), ForC (green) and alone (pink) (λ_{irr} = 310 nm) (D).

The HPLC analysis provided similar results. Figure 5.11A shows the chromatograms registered for different irradiation times of ForC in presence of Thy-Thy. The peak corresponding to the Thy-Thy signal, that is eluting at 12 min, decreases concomitantly with the appearance and the increase of a new peak corresponding to Thy<>Thy (8 min). A qualitatively analogous behavior was observed for the irradiation of the mixture ForU:Thy-Thy (Figure 5.11B). A control experiment performed with Thy-Thy alone irradiated at λ_{exc}= 310 nm (Figure 5.11C) was also carried out and confirmed the lower yields for the direct CPD formation in the absence of photosensitizer. As expected from the difference in the bimolecular rate constants, Thy-Thy was more efficiently consumed when ForU is acting as photosensitizer. This is clearly illustrated in Figure 5.11D showing that the complete consumption of Thy-Thy was achieved after 1h of irradiation in presence of ForU, while only 50% of Thy-Thy is depleted in the presence of ForC, and 20% without any sensitizer.

Altogether, these experimental results showed that in spite of its higher triplet excited state energy, ForC is a less efficient Thy<>Thy photosensitizer than ForU. Thus, in order to shed more light on the molecular aspects responsible for this difference, molecular modeling was performed for a mixture of each formyl derivative and thymine.

5.2.5. Mechanistic aspects revealed by molecular modeling

5.2.5.1. Potential energy landscapes of ForU and ForC

The following theoretical calculations have been performend in collaboration with Prof. A. Monari and Dr. A. Francés-Monerris from University of Lorraine (France). As already evidenced by the different energy

levels of the singlet ^{1}n,π* and ^{1}π,π* states at the Franck-Condon geometry, the potential energy surface (PES) of the two chromophores differ quite significantly. Their exploration using the CASPT2 and TD-DFT/B3LYP methods (see chapter 7 for more information about the difference between both methods), and in particular the positioning of the most relevant points, *i.e.* singlet and triplet minima are reported in Figure 5.12. Indeed, in the case of ForU, the populated S_1 state of ^{1}nπ* diabatic nature, evolves to its equilibrium geometry (^{1}n,π* min) that also represents a singlet-triplet crossing (STC) region with the T_2 state (^{3}π,π*). Interestingly, an inversion of the diabatic triplet state ordering compared with the Franck-Condon region should be pointed out in the ForU PES at the n,π* minimum. Further exploration of the PES in the triplet manifold reveals the existence of two well defined minima for the ^{3}n,π* and ^{3}π,π* states, which are separated by less than 0.2 eV in favor of the former (see Table 5.1), hence suggesting a possible coexistence of the two spectroscopic states. In contrast, ForC presents not only a larger singlet-triplet gap at the S_1 equilibrium geometry (about 0.3 eV), but also a lack of inversion zone between the ^{3}n,π* and the ^{3}π,π* states, with the latter always happening to be the adiabatic T_1 state presenting a well-defined minimum.

Table 5.1. Experimental and computed values of the phosphorescence band origin and maxima, related to the adiabatic triplet energy levels and vertical singlet-triplet energy gaps, respectively, for ForU and ForC. Energies are in eV and wavelengths, in nm, are given within parenthesis.

Compound	State	Band origin (TD-DFT)	Band origin (Exp)	Band maximum (TD-DFT)	Band maximum (Exp)
ForU	^{3}n,π*	3.23 (384)	3.15 (394)	2.90 (427)	~2.79 (445)
	^{3}π,π*	3.03 (409)		2.42 (513)	
ForC	^{3}π,π*	3.38 (367)	3.38 (367)	3.01 (411)	~2.92 (425)

Interestingly, the CASPT2 features of the PES matches very well to the profile obtained at TD-DFT level using B3LYP functional, in particular for the STC regions of ForU. The good agreement validates the forthcoming non-adiabatic dynamics performed at the TD-B3LYP level of theory. Finally, it is also important to underline that, in agreement with the El-Sayed rule,[45] the SOC values, reported in Figures 5.12B and 5.12D, are larger between ^{1}n,π* and ^{3}π,π* with respect to ^{1}n,π* and ^{3}n,π*, providing a further argument in favor of a more efficient ISC for ForU than ForC.

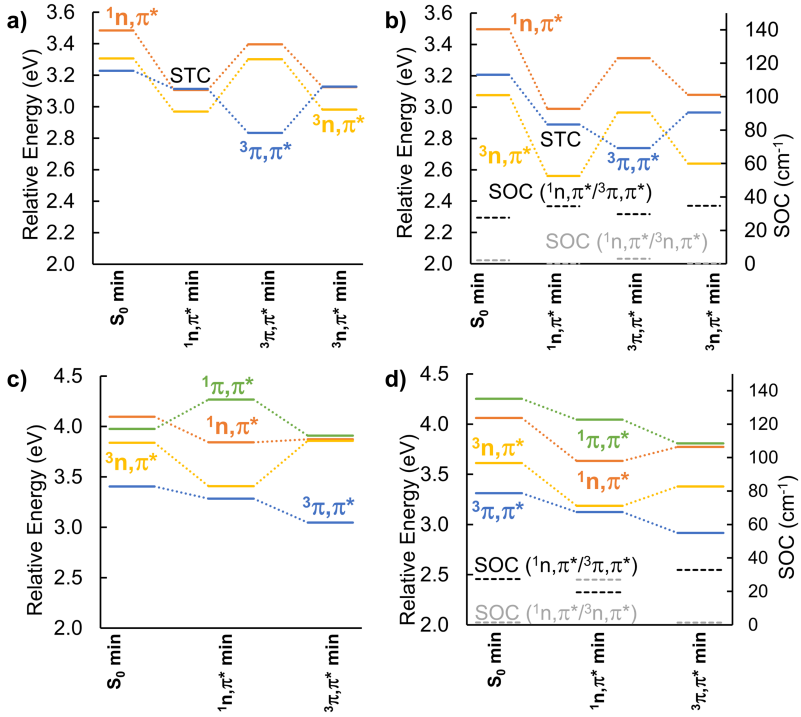

Figure 5.12. Static profile positioning the most relevant critical points on the PES of ForU calculated at CASPT2 (a) and TD-DFT/B3LYP level (b) and ForC again at CASPT2 (c) and TD-DFT/B3LYP level (d). Note that the calculated SOC between the two lowest triplet and first excited singlet state are also reported at TD-DFT level. All energies are relative to the ground state at the S_0 min geometry. STC = singlet-triplet crossing.

5.2.5.2. Non-adiabatic dynamics in the TD-DFT framework

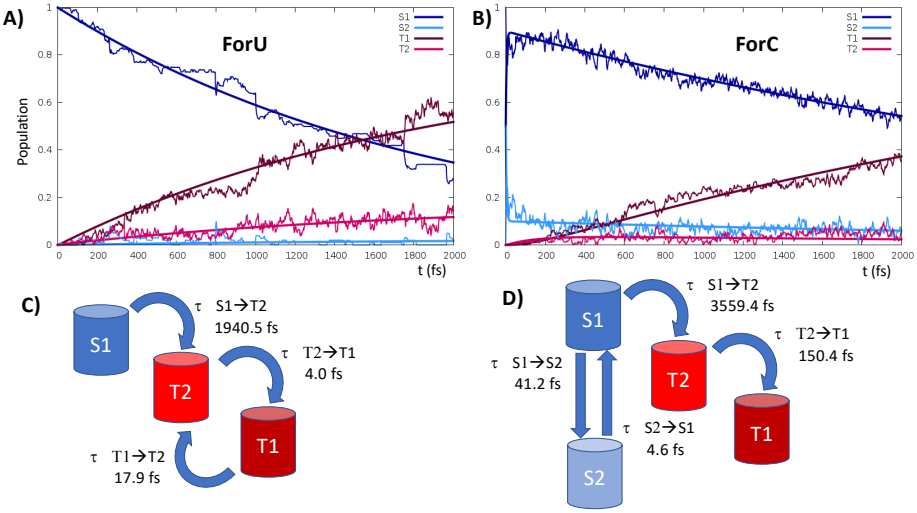

Figure 5.13. Time evolution of the population of the different excited states as obtained from the quantum amplitude of the ensemble of 100 trajectories starting from S_1 for ForU (A) and 200 trajectories (100 starting from S_1 and 100 from S_2) for ForC (B). The curves obtained fitting the obtained population to the kinetic model are also shown, while the characteristic time constants are provided in panel C) and D) for ForU and ForC, respectively.

To identify the relationship between the crucial differences in the PESs presented in Figure 5.12 and the photophysical outcomes, non-adiabatic dynamics in the TD-DFT framework for both oxidized nucleobases have been performed. The time evolution of the population of the different states is reported in Figure 5.13, from which it clearly appears that ISC is much more efficient for ForU than ForC. Thus, after 2 ps more than 60% of ForU populates the triplet manifold, whereas the population of the triplet state in ForC only reaches 40%. Moreover, while in the case of ForU a persistent

population of T_2 is observed all along the dynamics, in ForC T_1 is the only triplet state that is significantly populated. This difference can be better understood from the analysis of the hopping transitions between the states: in ForU back and forward hops between the two lowest lying triplet states are observed, while in ForC only hops from T_2 to T_1 are evidenced. This observation points to the establishment of an equilibrium inside the triplet state manifold of ForU leading to the persistent population of T_2, in a situation that was already observed in the case of benzophenone.[27]

Analysis of the hopping transitions also allows sketching the kinetic models reported in Figure 5.13C and 5.13D for ForU and ForC, respectively. In the case of ForU, after an irreversible transition from S_1 to T_2, an equilibrium between the two triplet states is achieved, as also evidenced by back and forward hops between the two surfaces. The fitting of the evolution of the population to the kinetic model also gives the characteristic time constants, which are of about 1940 fs for the $S_1 \rightarrow T_2$ transition, representing the ISC rate limiting step, and of 4 and 17 fs for the $T_2 \rightarrow T_1$ and $T_1 \rightarrow T_2$ transitions, respectively, indicating that the equilibrium is displaced towards the population of T_1. Instead, the picture of the kinetic model for ForC previews an initial equilibrium between S_1 and S_2, followed by two sequential irreversible transitions $S_1 \rightarrow T_2$ and $T_2 \rightarrow T_1$. The equilibrium in the singlet manifold is extremely rapid showing characteristic time constants of about 41 and 5 fs for $S_1 \rightarrow S_2$ and $S_2 \rightarrow S_1$, respectively. The rate limiting step is once again the $S_1 \rightarrow T_2$ transition that has a time constant of 3559 fs, *i.e.* almost double than the one of ForU, while the subsequent internal conversion in the triplet manifold is fast and the time constant for the $T_2 \rightarrow T_1$ transition is of 150 fs.

5.2.5.3. Analysis of the most active modes of ForU and ForC

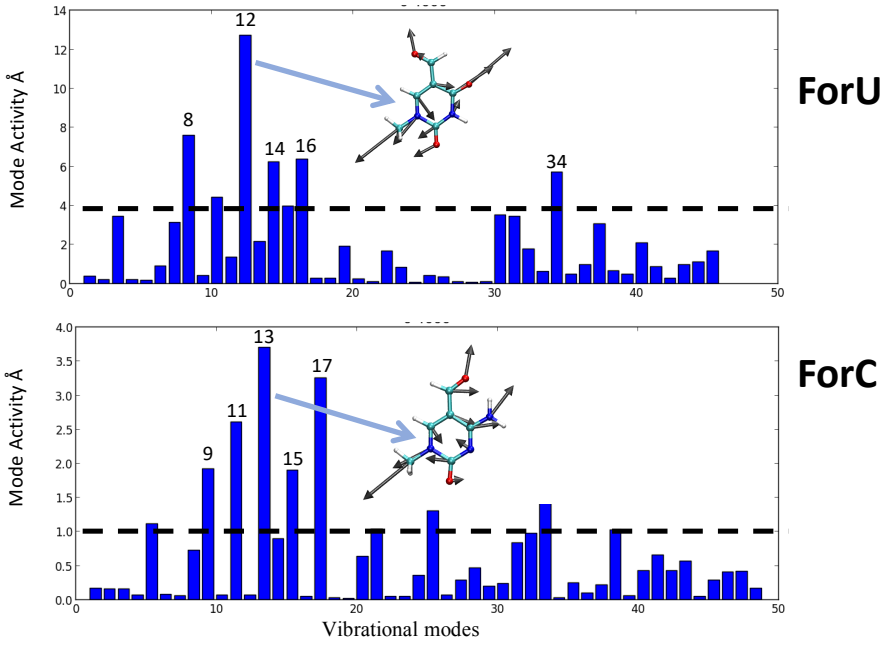

Figure 5.14. Coherent activity of the vibrational normal modes for ForU (top) and ForC (bottom) expressed in term of the standard deviation of the average trajectory projected over the normal modes. The most active modes for the two chromophores, *i.e.* the ones having an activity superior to the dotted black line roughly indicating 1/4 of the y-axis scale, are labeled. The most active mode for ForU and ForC is also represented as an inset.

Despite the different mechanism, and the different ISC rate limiting time, the behavior of the two oxidized nucleobases in terms of the normal

mode leading to the triplet population, and hence the coupling of the singlet and triplet electronic and nuclear degrees of freedom, is quite similar. Figure 5.14 reports the normal mode analysis providing a measure of the coherent activity of the different normal modes, estimated by the analysis of the average displacements and their standard deviations projected on the normal modes.[46] Interestingly, the total displacement, *i.e.* the analysis of the total activity of a normal mode disregarding its coherence over the ensemble of trajectories provides the same picture (see Figure 5.15). The analysis of the most active modes (see Figures 5.16 and 5.17) shows that the displacements driving the ISC are related to ring breathing and deformation, coupled with some stretching and in plane bending of the aromatic ring substituents. However, out-of-plane deformations of the nucleobase aromatic ring are totally absent, as confirmed by analysis of the ring puckering parameters along the trajectories (see Figure 5.18) that only slightly deviates from the ideal planarity. Interestingly, it turns out that the coherent activity of ForC is much smaller than the one of ForU, the most active normal mode having a coherent activity of about 4 and 14 Å, respectively. This fact can also partially correlate with the less efficient ISC exhibited by ForC.

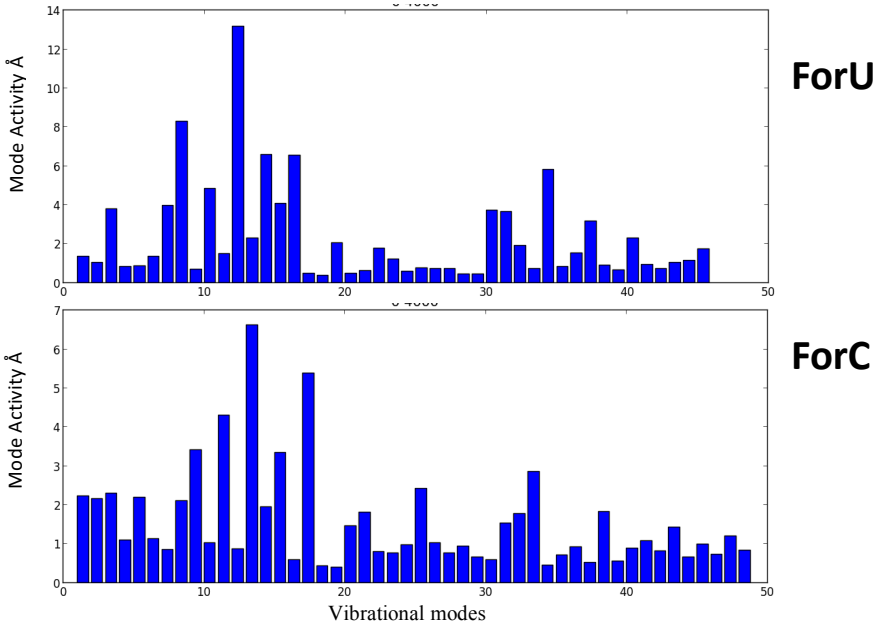

Figure 5.15. Total standard deviation of the trajectories projected on the vibrational normal modes and yielding the total activity of each mode.

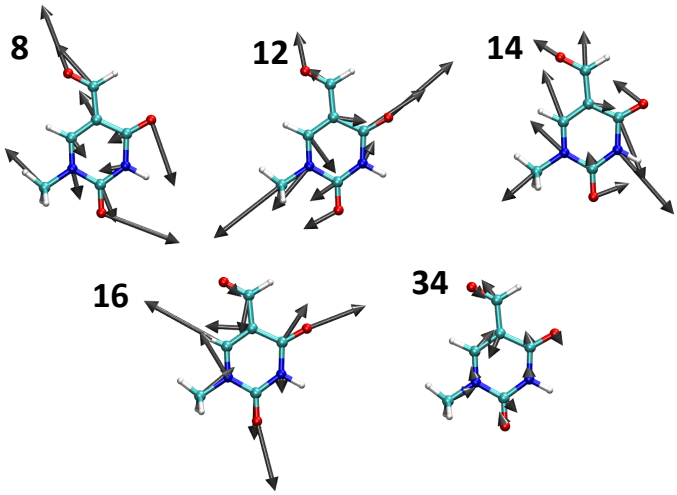

Figure 5.16. Representation of the ForU most active vibrational normal modes.

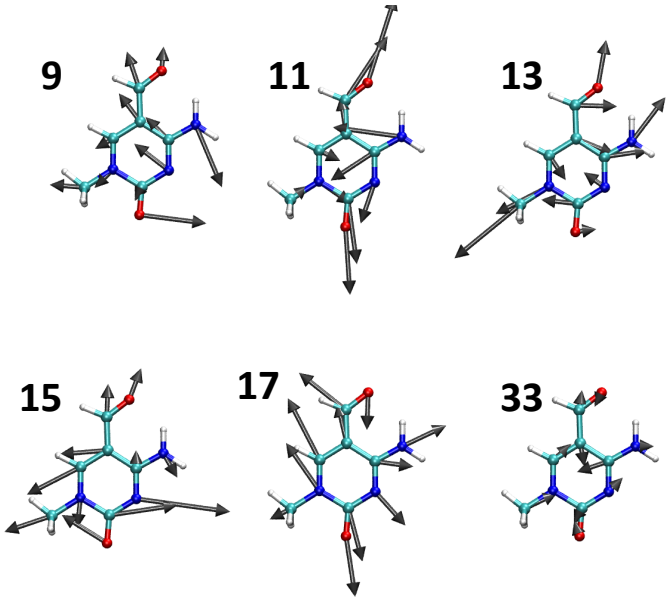

Figure 5.17. Representation of the ForC most active vibrational normal modes.

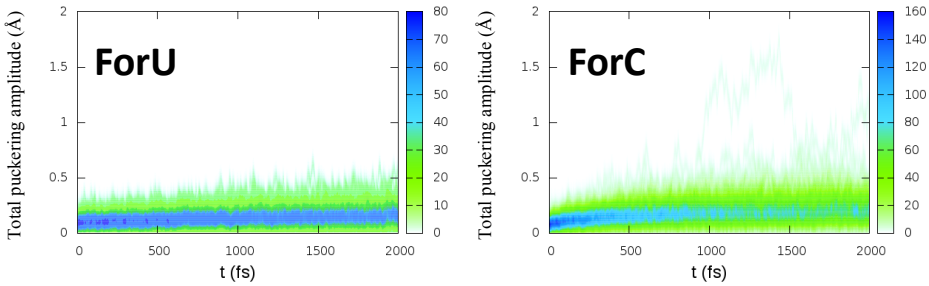

Figure 5.18. Time evolution of the aromatic ring puckering convoluted over the ensemble of the trajectories for ForU and ForC.

5.2.5.4. Potential energy landscape of ForU-Thy and ForC-Thy systems

Several factors explain the different yields of triplet-triplet energy transfer and CPD formation induced by ForU and ForC. First, the population of the triplet excited state is slower for ForC than for ForU, as shown by the respective time constants (τ_{ISC} = 1940.5 and 3559.4 fs, respectively) determined by non-adiabatic molecular dynamics. Second, the triplet state of ForC decays faster, as evidenced by the time-resolved spectroscopic data shown in Figures 5.6 and 5.7, in coherence with the nature of the lowest triplet state (^{3}n,π* and ^{3}π,π* for ForU and ForC, respectively). These intrinsic differences in the triplet lifetimes correlate very well with the nature of the emissive triplet states predicted by previous calculations for the two monomers. The emissive triplet states have been identified as ^{3}n,π* and ^{3}π,π*, for ForU and ForC respectively, on the basis of their vertical emissions. Thus, the ^{3}n,π* state of ForU has a longer lifetime given the lowest transition dipole moment with the singlet ground state and hence a smaller oscillator strength, resulting in a slower radiative decay as compared to the ^{3}π,π* of ForC. Finally, further calculations of the ForU-Thy and ForC-Thy systems have revealed

important differences in the potential energy landscape of the electronic states involved in the dimerization photoprocess. Figure 5.19 provides an overview of the energetic level of the most important electronic states calculated for relevant points of the potential energy surfaces, namely Franck-Condon, *i.e.* the ground state equilibrium geometry, and the optimized structures of the lowest singlet and triplet states.

In the case of ForC-Thy (Figure 5.19A) and as in the case of the monomer (Figure 5.12), the first excited singlet state of ^{1}n,π* nature is localized over ForC (^{1}n,π*ForC), and lies, at its equilibrium geometry, 0.48 eV below the triplet state of ^{3}π,π* nature (^{3}π,π* ForC), *i.e.* the other player involved in the ISC, justifying the slower population of the triplet manifold. Notably, and again coherently with non-adiabatic dynamics previously performed for the monomer, spin-orbit couplings corroborate the role of ^{3}π,π*ForC state as the doorway to ISC (Table 5.2). In contrast, in ForU, the corresponding states (^{1}n,π*ForU and ^{3}π,π*ForU) are quasi-degenerated at the ^{1}n,π*ForU equilibrium geometry, leading to a much more efficient triplet population (Figure 5.19B).[33]

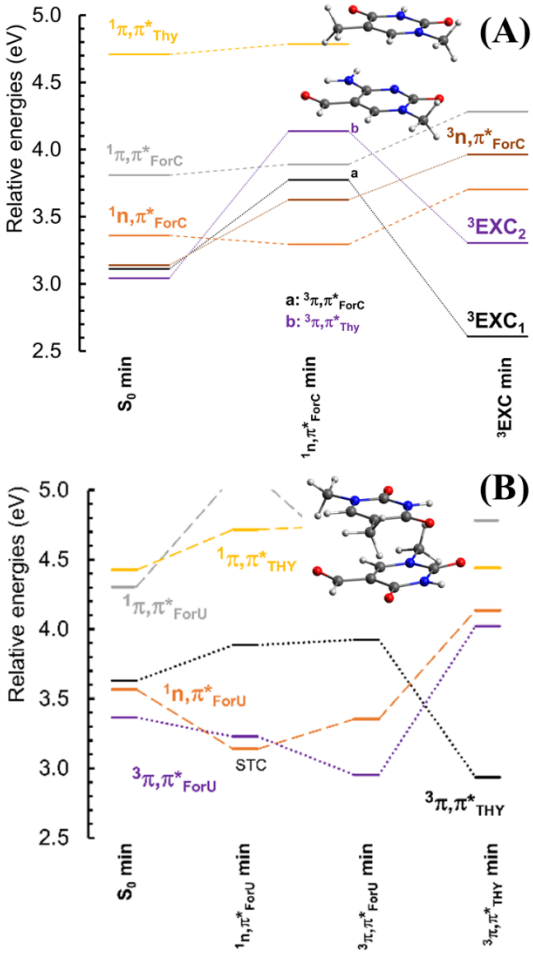

Figure 5.19. (A) CASPT2 energy profiles for the most relevant excited states of the ForC-Thy system. (B) CASPT2 energy profiles for the most relevant excited states of the ForU-Thy system, taken from Ref. [33]. STC = singlet-triplet crossing. The horizontal axis defines the equilibrium geometry of the most important states, obtained via geometry optimization, the dashed lines are used to connect the states having the same diabatic nature as a guide for the eyes. ^{3}EXC = triplet exciplex.

Table 5.2. SOC values (in cm^{-1}) between the most relevant singlet and triplet states of ForC-Thy.

	$^3EXC_1$	$^3EXC_2$	$^3(n,\pi^*)_{ForC}$
	S_0 min		
$^1(n,\pi^*)_{ForC}$	6.6–18.9	5.6–16.1	~0.1
$^1(\pi,\pi^*)_{ForC}$	0.1	0.1	2.1–5.0
$^1(\pi,\pi^*)_{Thy}$	0.1	0.1	0.5–1.4
	$^1(n,\pi^*)_{ForC}$ min		
$^1(n,\pi^*)_{ForC}$	14.7–42.8[a]	0.2–0.7[b]	2.9–7.9
$^1(\pi,\pi^*)_{ForC}$	1.8–3.4	0.0	3.3–9.1
$^1(\pi,\pi^*)_{Thy}$	0.2–0.5	0.0–0.1	1.0–2.8
	$^3EXC_1$ min		
$^1(n,\pi^*)_{ForC}$	4.2–11.1	10.0–26.1	1.0–2.4
$^1(\pi,\pi^*)_{ForC}$	0.3–0.4	0.4–1.5	0.1–0.3
$^1(\pi,\pi^*)_{Thy}$	1.6–4.2	4.4–11.4	2.5–6.3

[a] At this $^1(n,\pi^*)_{ForC}$ min geometry, the first triplet state can be labeled as $^3(\pi,\pi^*)_{ForC}$. The relatively high SOC value with the $^1(n,\pi^*)_{ForC}$ state is coherent with this fact.[b] At this $^1(n,\pi^*)_{ForC}$ min geometry, the second triplet state can be labelled as $^3(\pi,\pi^*)_{Thy}$. The low SOC value with the $^1(n,\pi^*)_{ForC}$ state is coherent with this fact.

Other significant differences between the two sensitizers are due to the distribution of the spin density between the couple photosensitizer-nucleobase. The triplet states of ForC-Thy are characterized by a marked delocalization of the π clouds, describing the unpaired electrons, over both ForC and thymine moieties, especially involving the antibonding π* orbitals (see Figure 5.20). Hence, the triplet states can be classified as exciplex (EXC_1, EXC_2). The delocalization is especially pronounced at the S_0 min and the T_1 min, that in diabatic notation is labelled as ^3EXC min. On the contrary, in the case of ForU, the spin density is much better localized over the two moieties,

also giving rise to two well distinct electronic states, with a small but non-negligible driving force favoring the transfer of spin density to Thy, in a process requiring to bypass only a relatively small energy barrier. The presence of the low energy $^3EXC_1$ in For**C** can contribute to further explain the different observed yields. Indeed, the possibility of the formation of a delocalized state involving the sensitizer and two thymine bases attached to a rigid scaffold has been previously invoked in the case of benzophenone, another photosensitizer.[47] Different mechanisms could be at play here (see Scheme 5.2) for For**C**, in which (*i*) the exciplex state is too stable to be dissociated, and act as the energy donor for TTET to Thy, however the decreased energy of $^3EXC_2$ (2.61 eV) locates this state below of Thy triplet excited state (at 2.87 eV)[21], which makes TTET process unfavored; or (*ii*) the exciplex $^3EXC_1$ can eventually further delocalize involving a second Thy unit forming a triplet triplex that evolves forming Thy<>Thy; nonetheless, such a trimolecular process can clearly be seen as slower and less efficient than the most direct route operative in the case of For**U** involving localized states (Scheme 5.2).

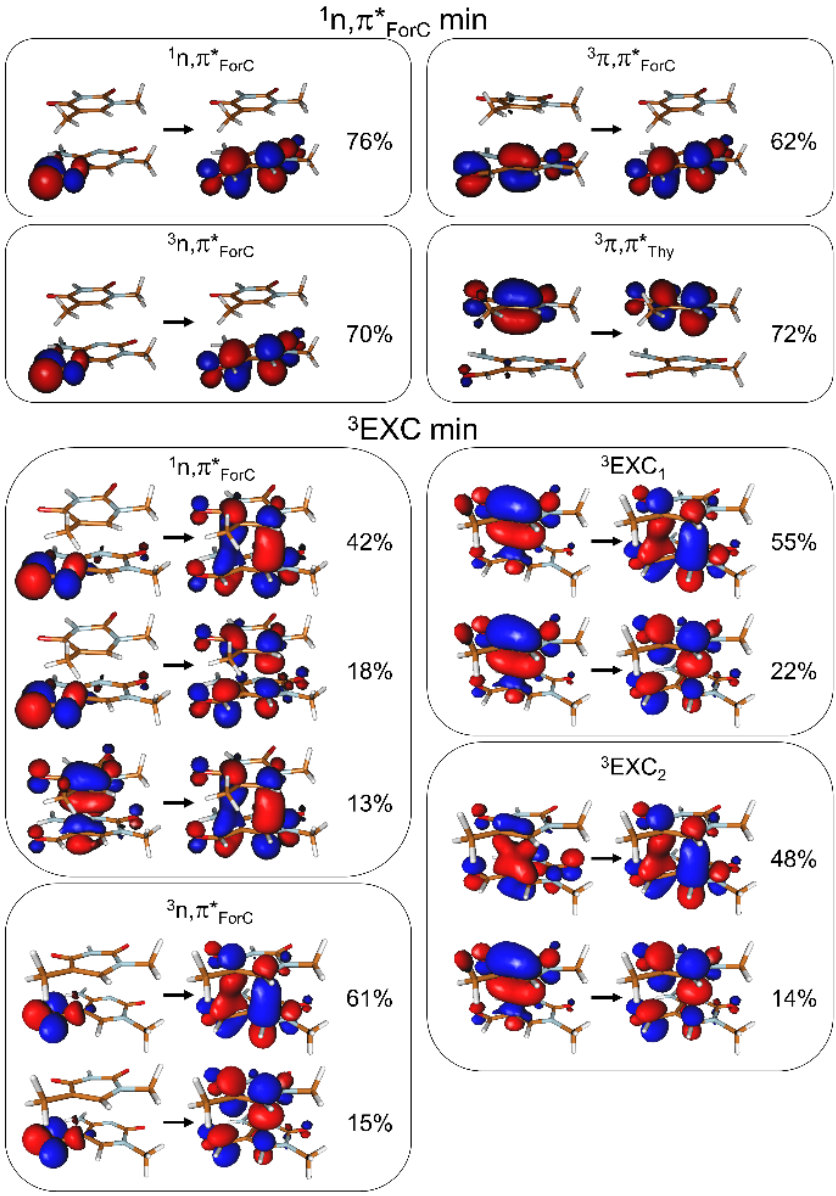

Figure 5.20. CASSCF orbitals corresponding to the highest weight electronic transitions that characterize the excited states of the ForC-Thy system. The weights of the configurations are also shown. Other transitions with much lower weights adding up to the total 100% are not reported.

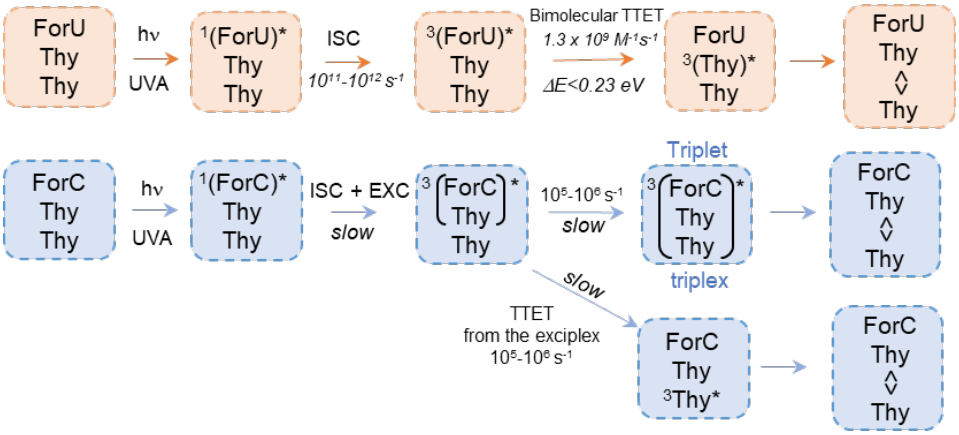

Scheme 5.2. Schematic representation of the proposed Thy<>Thy production from excitation of ForU (top) and ForC (bottom), according to our experimental and computational data. ISC = intersystem crossing, TTET = triplet-triplet energy transfer.

5.3. Conclusions

To sum up, the most important photophysical features of two oxidized nucleobases, ForU and ForC, have been unraveled and compared using a combination of molecular modeling and spectroscopic determinations. Moreover, their different capabilities to promote formation of CPD lesions through triplet-triplet energy transfer were analyzed by time-resolved and steady-state absorption spectroscopy, NMR, HPLC and theoretical calculations.

Regarding the photophysical properties, it has been shown that both oxidized nucleobases can undergo ISC, albeit with a different efficiency and

with two different mechanisms. Indeed, ForU happens to be much more efficient, with a characteristic time for the ISC that is half the one of ForC.

Concerning their photochemistry, it has been evidenced by experimental and theoretical approaches that the TTET from ForU to Thy-Thy is more favored than that from ForC. Specifically, steady-state photolysis showed a higher CPD rate production in the presence of ForU, and laser flash photolysis revealed that ForU is quenched by Thy-Thy three times faster than ForC ($k_q \sim 1.3 \times 10^9$ $M^{-1}s^{-1}$ for ^{3}ForU* and 4.6×10^8 M^{-1} s^{-1} for ^{3}ForC*). Besides, these experimental results were further supported by molecular modeling showing for ForC (*i*) a slower intersystem crossing, since the relaxation of the singlet excited state leads to a region where the triplet states are less accessible and (*ii*) a slower triplet-triplet energy transfer since exciplex states of $^3\pi,\pi^*$ (^{3}EXC) nature dominate the triplet state manifold in ForC-Thy, being identified as mediator of thymine dimerization in this system.

These results represent a step forward in the understanding of the intimate coupling between oxidative and light-induced DNA damage, responsible of the public health problem of unprotected sunlight exposure and development of malignant skin diseases.

5.4. Experimental section

5.4.1. Synthesis

Synthesis of the model Thy-Thy and its photoproduct Thy<>Thy was performed following the procedure reported in the literature.[32,43]

Synthesis of 1,1'-(propane-1,3-diyl)bis(5-methylpyrimidine-2,4(1H,3H)-dione) (1).[43]

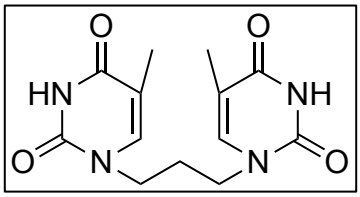

To a dry deaerated two necks round bottom flask fitted with a reflux condenser was added *O,O'*-bis(trimethylsilyl)thymine (1 g, 3.7 mmol) and 6 mL of anhydrous DMF. Then, 1,3-dibromopropane (0.19 mL, 1.8 mmol) was added and the solution was stirred at 170 ºC overnight. The resulting mixture was cooled to 0 ºC and 3 mL of MeOH were added to obtain a white precipitate, that was washed with a mixture of $CHCl_3$:MeOH (1:1, v:v) and dried under vacuum. Finally, the pure product **1** was obtained as a white solid and used as reaction intermediate without further purification. Yield: 0.420 g (77%).

^{1}H NMR (300 MHz, [d_6]-DMSO): δ (ppm) 11.21 (s, 2H), 7.52 (s, 2H), 3.65 (t, J = 6.9 Hz, 4H), 1.92-1.87 (m, 2H), 1.74 (s, 6H).

Synthesis of 1,1'-(propane-1,3-diyl)bis(3,5-dimethylpyrimidine-2,4(1H,3H)-dione) (Thy-Thy)[32]

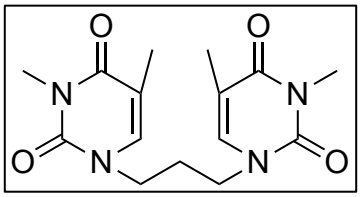

Compound **1** (0.395 g, 1.34 mmol), NaH (0.07 g, 2.94 mmol) and 9 mL of anhydrous dimethylformamide were added to a dry two necks round bottom flask fitted with a reflux condenser. This mixture was stirred at room temperature for 1h. Subsequently, the solution was cooled in an ice bath and then methyl iodide (MeI, 0.462 mL, 7.42 mmol) was added portionwise. The resulting mixture was stirred at 85 ºC overnight. Finally, the crude reaction was concentrated under reduced pressure and purified by column chromatography (DCM:MeOH, 99:1) to give the pure product Thy-Thy. Yield: 0.264 g (61%).

^{1}H NMR (300 MHz, $CDCl_3$): δ (ppm) 7.05 (s, 2H), 3.78 (t, J = 6.9 Hz, 4H), 3.33 (s, 6H), 2.13-2.04 (m, 2H), 1.92 (s, 6H).

Synthesis of 5,6a,6b,8-tetramethylhexahydro-1H-3a,5,8,9a-tetraazacyclohepta[def]biphenylene-4,6,7,9(5H,8H)-tetraone (Thy<>Thy)[32]

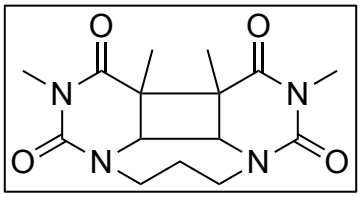

0.02 g (0.034 mmol) of compound Thy<>Thy was dissolved in acetone (30 mL). This solution was split up among three pyrex tubes which were irradiated with a medium pressure mercury lamp (750 W). The solvent was evaporated to give the pure product Thy<>Thy. Yield 0.02 g (> 98 %).

^{1}H NMR (300 MHz, D_2O:CD_3CN (1:1, v:v)) δ (ppm) 4.76-4.61 (m, 4H), 4.48 (s, 2H), 3.52 (s, 6H), 3.45-3.30 (m, 1H), 2.01 (s, 6H).

5.4.2. NMR spectra

^{1}H NMR ([d_6]-DMSO, 300 MHz)

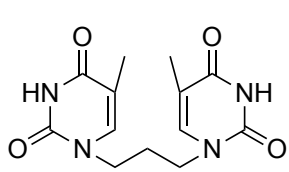

Compound 1

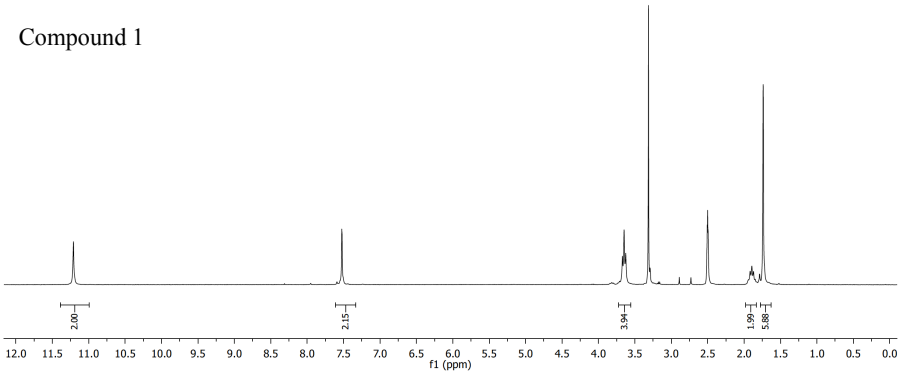

^{1}H NMR ($CDCl_3$, 300 MHz)

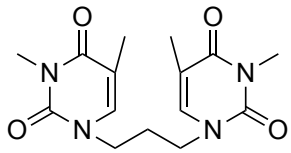

Thy-Thy

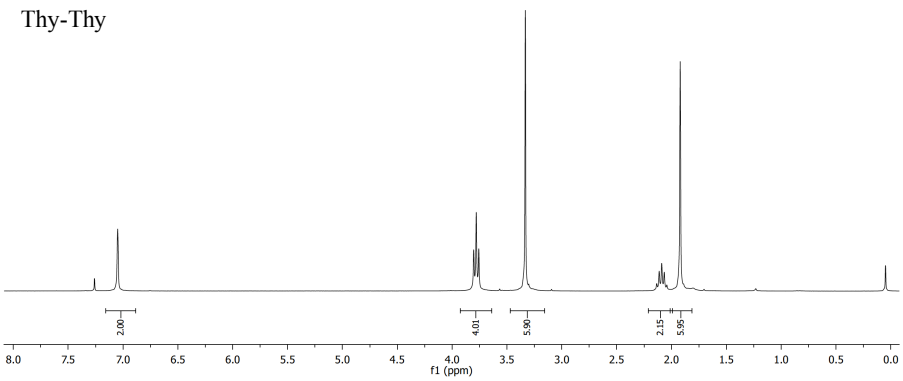

^{1}H NMR (D_2O:CD_3CN (1:1, v:v), 300 MHz)

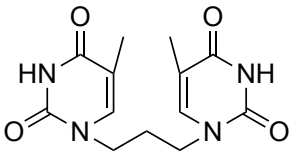

Thy<>Thy

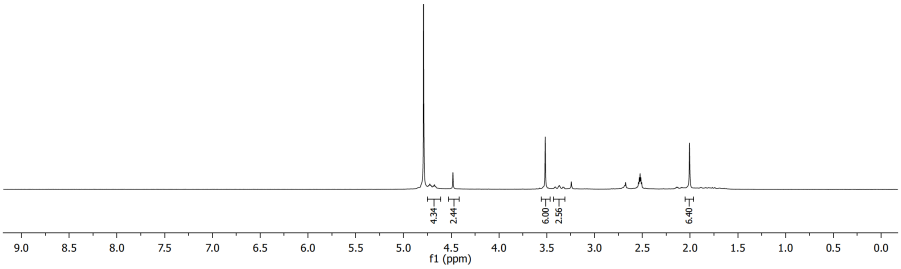

5.5. Bibliography

1 C. E. Crespo-Hernandez, B. Cohen, P. M. Hare and B. Kohler, *Chem. Rev.*, 2004, **104**, 1977–2019.

2 R. Improta, F. Santoro and L. Blancafort, *Chem. Rev.*, 2016, 116, 3540–3593.

3 L. Esposito, A. Banyasz, T. Douki, M. Perron, D. Markovitsi and R. Improta, *J. Am. Chem. Soc.*, 2014, **136**, 10838–10841.

4 H. Ikehata, T. Mori, Y. Kamei, T. Douki, J. Cadet and M. Yamamoto, *Photochem. Photobiol.*, 2020, **96**, 94–104.

5 J. Cadet and T. Douki, *Photochem. Photobiol. Sci.*, 2018, **17**, 1816–1841.

6 J. Cadet, E. Sage and T. Douki, *Mutat. Res. - Fundam. Mol. Mech. Mutagen.*, 2005, **571**, 3–17.

7 A. Francés-Monerris, H. Gattuso, D. Roca-Sanjuán, I. Tuñón, M. Marazzi, E. Dumont and A. Monari, *Chem. Sci.*, 2018, **9**, 7902–7911.

8 Y. Zhang, K. De La Harpe, A. A. Beckstead, R. Improta and B. Kohler, *J. Am. Chem. Soc.*, 2015, **137**, 7059–7062.

9 Y. Zhang, X.-B. Li, A. M. Fleming, J. Dood, A. A. Beckstead, A. M. Orendt, C. J. Burrows and B. Kohler, *J. Am. Chem. Soc.*, 2016, **138**, 7395–7401.

10 D. B. Bucher, A. Schlueter, T. Carell and W. Zinth, *Angew. Chem. Int. Ed.*, 2014, **53**, 11366–11369.

11 K. Rottger, H. J. B. Marroux, M. P. Grubb, P. M. Coulter, H. Bohnke, A. S. Henderson, M. C. Galan, F. Temps, A. J. Orr-Ewing and G. M. Roberts, *Angew. Chem. Int. Ed.*, 2015, **54**, 14719–14722.

12 M. C. Cuquerella, V. Lhiaubet-Vallet, F. Bosca and M. A. Miranda, *Chem. Sci.*, 2011, **2**, 1219–1232.

13 S. Mouret, C. Baudouin, M. Charveron, A. Favier, J. Cadet and T. Douki, *Proc. Natl. Acad. Sci. U. S. A.*, 2006, **103**, 13765–13770.

14 G. P. Pfeifer and A. Besaratinia, *Photochem. Photobiol. Sci.*, 2012, **11**, 90–97.

15 F. P. Noonan, M. R. Zaidi, A. Wolnicka-Glubisz, M. R. Anver, J. Bahn, A. Wielgus, J. Cadet, T. Douki, S. Mouret, M. A. Tucker, A. Popratiloff, G. Merlino and E. C. De Fabo, *Nat. Commun.*, 2012, **3**, 1–10.

16 A. Banyasz, T. Douki, R. Improta, T. Gustavsson, D. Onidas, I. Vayá, M. Perron and D. Markovitsi, *J. Am. Chem. Soc.*, 2012, **134**, 14834–14845.

17 C. Rauer, J. J. Nogueira, P. Marquetand and L. González, *J. Am. Chem. Soc.*, 2016, **138**, 15911–15916.

18 H. Ikehata and T. Ono, *J. Radiat. Res.*, 2011, **52**, 115–125.

19 B. Epe, *Photochem. Photobiol. Sci.*, 2012, **11**, 98–106.

20 D. Roca-Sanjuán, G. Olaso-González, I. González-Ramírez, L. Serrano-Andrés and M. Merchán, *J. Am. Chem. Soc.*, 2008, **130**, 10768–10779.

21 T. Climent, I. González-Ramírez, R. González-Luque, M. Merchán

and L. Serrano-Andrés, *J. Phys. Chem. Lett.*, 2010, **1**, 2072–2076.

22 E. Dumont and A. Monari, *Front. Chem.*, 2015, **3**, 43.

23 V. Lhiaubet-Vallet, Z. Sarabia, D. Hernández, J. V. Castell and M. A. Miranda, in *Toxicology in Vitro*, 2003, vol. 17, pp. 651–656.

24 S. Sauvaigo, T. Douki, F. Odin, S. Caillat, J.-L. Ravanat and J. Cadet, *Photochem. Photobiol.*, 2007, **73**, 230–237.

25 V. Lhiaubet-Vallet, F. Bosca and M. A. Miranda, *Photochem. Photobiol.*, 2009, **85**, 861–868.

26 M. C. Cuquerella, V. Lhiaubet-Vallet, J. Cadet and M. A. Miranda, *Acc. Chem. Res.*, 2012, **45**, 1558–1570.

27 M. Marazzi, S. Mai, D. Roca-Sanjuán, M. G. Delcey, R. Lindh, L. González and A. Monari, *J. Phys. Chem. Lett.*, 2016, **7**, 622–626.

28 E. Dumont, M. Wibowo, D. Roca-Sanjuán, M. Garavelli, X. Assfeld and A. Monari, *J. Phys. Chem. Lett.*, 2015, **6**, 576–580.

29 V. Vendrell-Criado, G. M. Rodriguez-Muniz, M. C. Cuquerella, V. Lhiaubet-Vallet and M. A. Miranda, *Angew. Chem. Int. Ed.*, 2013, **52**, 6476–6479.

30 E. Bignon, H. Gattuso, C. Morell, E. Dumont and A. Monari, *Chem. Eur. J.*, 2015, **21**, 11509–11516.

31 D. K. Rogstad, J. Heo, N. Vaidehi, W. A. Goddard, A. Burdzy and L. C. Sowers, *Biochemistry*, 2004, **43**, 5688–5697.

32 I. Aparici-Espert, G. Garcia-Lainez, I. Andreu, M. A. Miranda and V. Lhiaubet-Vallet, *ACS Chem. Biol.*, 2018, **13**, 542–547.

33 A. Francés-Monerris, C. Hognon, M. A. Miranda, V. Lhiaubet-Vallet and A. Monari, *Phys. Chem. Chem. Phys.*, 2018, **20**, 25666–25675.

34 X. Wang, Y. Yu, Z. Zhou, Y. Liu, Y. Yang, J. Xu and J. Chen, *J. Phys. Chem. B*, 2019, **123**, 5782–5790.

35 J. An, A. Rao and M. Ko, *Exp. Mol. Med.*, 2017, **49**, 323–334.

36 R. Rahimoff, O. Kosmatchev, A. Kirchner, T. Pfaffeneder, F. Spada, V. Brantl, M. Müller and T. Carell, *J. Am. Chem. Soc.*, 2017, **139**, 10359–10364.

37 A. Schön, E. Kaminska, F. Schelter, E. Ponkkonen, E. Korytiaková, S. Schiffers and T. Carell, *Angew. Chem. Int. Ed.*, 2020, **59**, 5591–5594.

38 R. L. Martin, *J. Chem. Phys.*, 2003, **118**, 4775–4777.

39 T. Etienne, X. Assfeld and A. Monari, *J. Chem. Theory Comput.*, 2014, **10**, 3896–3905.

40 M. Pastore, X. Assfeld, E. Mosconi, A. Monari and T. Etienne, *J. Chem. Phys.*, 2017, **147**, 024108.

41 F. Bosca, V. Lhiaubet-Vallet, M. C. Cuquerella, J. V. Castell and M. A. Miranda, *J. Am. Chem. Soc.*, 2006, **128**, 6318–6319.

42 V. Lhiaubet-Vallet and M. A. Miranda, in *CRC Handbook of Organic Photochemistry and Photobiology.*, eds. F. Ghetti, A. G. Griesbeck and M. Oelgemöller, CRC Press, 2012, pp. 1541–1555.

43 O. R. Alzueta, M. C. Cuquerella and M. A. Miranda, *J. Org. Chem*, 2019, **84**, 13329–13335.

44 V. Lhiaubet-Vallet, M. C. Cuquerella, J. V. Castell, F. Bosca and M. A.

Miranda, *J. Phys. Chem. B*, 2007, **111**, 7409–7414.

45 M. A. El-Sayed, *Acc. Chem. Res.*, 1968, **1**, 8–16.

46 L. Kurtz, A. Hofmann and R. De Vivie-Riedle, *J. Chem. Phys.*, 2001, **114**, 6151–6159.

47 P. Miro, V. Lhiaubet-Vallet, M. L. Marin and M. A. Miranda, *Chem. Eur. J.*, 2015, **21**, 17051–17056.

Chapter 6:

Insertion of 5-formyluracil into oligodeoxynucleotides using a photoremovable protecting group

6.1. Introduction

5-Formyluracil (ForU) is one of the oxidatively generated pyrimidine damages that can be found in bacteriophages, prokaryotes and mammalian cells.[1] This damage, together with 5-(hydroxymethyl)uracil (5hmU) and 5,6-dihydroxy-5,6-dihydrothymine (ThyGly) (Chart 6.1), arises from the action of endogenous or exogenous agents. In this context, the hydroxyl radicals, generated after exposure to γ-radiation or Fenton reaction,[2,3] are among the most important external sources giving rise to the abovementioned compounds. These highly reactive species are able to abstract a hydrogen from the C5 methyl group to yield ForU and 5hmU, or to add to the C5-C6 double bond, giving rise in this case to ThyGly.[4,5]

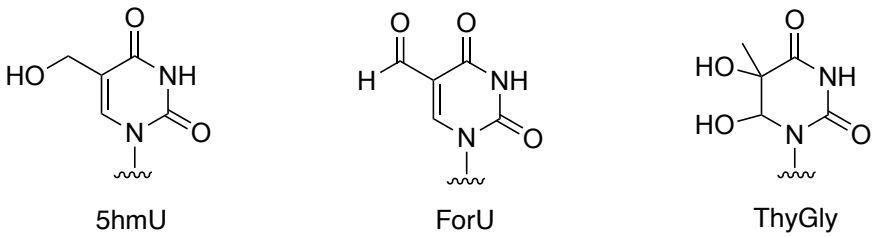

Chart 6.1. Oxidatively generated thymidine products.

Moreover, ForU can also be photochemically obtained by UVA photosensitization in the presence of Type I photosensitizers. The feasibility of this latter process has been studied with different photosensitizers, such as riboflavin, benzophenone and menadione.[6,7] From the analysis of the obtained products, it has been observed that the formation yield of ForU depends on the photosensitizer's properties. In this sense, a comparison between menadione and benzophenone has shown that ForU formation is favored in the presence of benzophenone. This can be explained based on the ability of

benzophenone to oxidize thymidine through two possible mechanisms, *i.e.* formal hydrogen abstraction at the methyl group and one-electron oxidation. Menadione, however, is only able to act through the latter mechanism, which favors the formation of ThyGly over ForU.[8,9]

Additionally, ForU, and 5hmU, can also be generated endogenously as a result of the sequential oxidation of thymine catalyzed by thymine hydroxylase (TH). This enzyme belongs to the nonheme iron α-ketoglutarate-dependent dioxygenases family, which is present in a wide range of organisms including bacteria, yeast, plants and humans.[10]

The presence of ForU has negative consequences on the correct functioning of DNA. From a chemical point of view, these consequences are mainly caused by the strong electron-withdrawing effect of the formyl group and its reactivity. Due to this effect, the *N*-glycosidic bond of ForU suffers from a higher hydrolysis rate than its parent pyrimidine. In addition, the increase of the N3 imino proton acidity affects the Watson–Crick interaction involved in base pairing with adenine,[11] and yields a higher misincorporation rate of G during replication by favoring the formation of its enolate tautomer. In this context, it has been proposed that ForU can pair with G in both its keto (Wobble base pair) and enolate forms (Watson-Crick base pair) (Figure 6.1).[12]

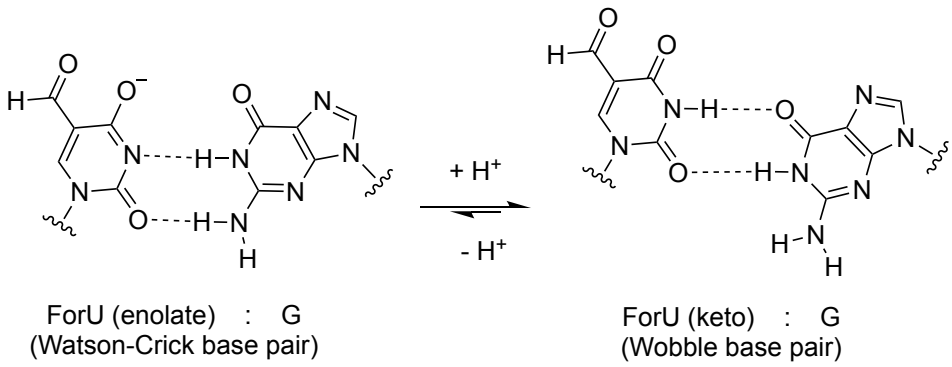

Figure 6.1. Acid-base equilibrium of the keto and enolate forms of ForU and their interactions with guanine.

Moreover, the formyl group could also interfere with the interactions between DNA and proteins.[13] In this sense, a Schiff base can be formed with lysine residues resulting in DNA-protein cross-linking.[14,15]

The formyl substitution not only impacts on the chemical properties, but also on the photochemical ones. ForU and its counterpart ForC fulfill the basic requirements to act as intrinsic photosensitizers, *i.e.* they exhibit a red shifted UV absorption spectrum and populate a sufficiently energetic triplet excited state (see Chapter 5). In this respect, their photosensitizing capabilities have been experimentally evaluated at an intermolecular level in the presence of bipyrimidine models and isolated DNA.[16] However, there is no experimental work studying these photosensitizing properties within DNA, or short oligonucleotides, although theoretical methodologies have shown that ForU triplet excited state properties are maintained within DNA.[17] Nevertheless, as recently reported for 6-4 PP,[18] the efficiency in CPD formation can differ when ForU is part of the double helix, depending on the sequence and the distance between the intrinsic photosensitizer and the Thy-Thy site.[19,20]

For the aforementioned reasons, the development of new synthetic alternatives allowing the site-specific incorporation of ForU into oligodeoxynucleotides (ODNs) is of outmost importance to get a better understanding of the genetic effect of this DNA lesion.

Regarding the incorporation of 5-formyl-2'-deoxyuridine (dForU) into ODNs, the main challenge is related to the reactivity of its formyl group towards nucleophiles and reductive or oxidative agents. As a result, its insertion into ODN under standard phosphoramidite-based synthesis proceeds in very low yields. To overcome this problem, 5-(1,2-diacetoxyethyl)-2'-deoxyuridine (dUAc, Figure 6.2 A) has been widely employed as a precursor. Then, dUAc is converted into dForU once it is incorporated into ODN after deprotection of the acetyl groups and subsequent oxidation with sodium periodate.[14,21–23]

Here, a new photochemical approach for the synthesis of ODN containing dForU has been designed. The main advantage of this new alternative is the employment of a photolabile protecting group (PPG) to cage the 5-formyl moiety. Thus, it is possible to achieve its selective conversion into dForU by means of light instead of an oxidative agent (Figure 6.2 B).

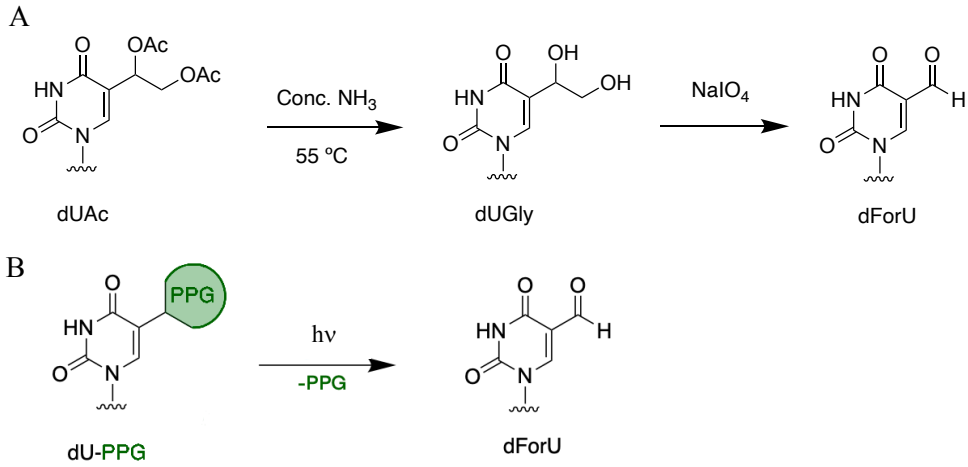

Figure 6.2. Comparison between the commonly employed dUAc conversion to afford ForU within oligodeoxynucleotides (A) and the new photochemical alternative proposed (B).

6.2. Results and discussion

6.2.1. Selection of the photolabile protecting group

As stated above, incorporation of 5-formyl-2'-deoxyuridine into ODN proceeds in low yields because of the instability of the 5-formyl group under standard phosphoramidite chemistry. For this reason, the synthesis of ODN containing dForU normally entails the use of a precursor, which is then turned into dForU after its incorporation. Traditionally, this latter modification involves an oxidative process. In this chapter, we propose a new strategy based on selective photodeprotection employing a salicyl alcohol derivative (PPG-1, Figure 6.3) as photoremovable protecting group of the 5-formyl group. In this way, the above-mentioned oxidation step is replaced with a photochemical one and does not require the use of any additional chemical. This and some other structurally related PPGs were developed by

Penfei Wang and co-workers, and have been tested for a large set of carbonyl derivatives (see Chapter 1).

The PPG selection was based on the following reasons. First of all, even though an acetal is obtained after its insertion, PPG-1 is reported to be stable under acidic conditions, and hence, it should remain unchanged during ODN synthesis, especially under standard detritylation (dichloroacetic acid, DCA) and coupling conditions (4,5-dicyanoimidazole). Besides, its removal is achievable using light of wavelength longer than 320 nm, thus allowing its selective excitation in the presence of canonical nucleobases.

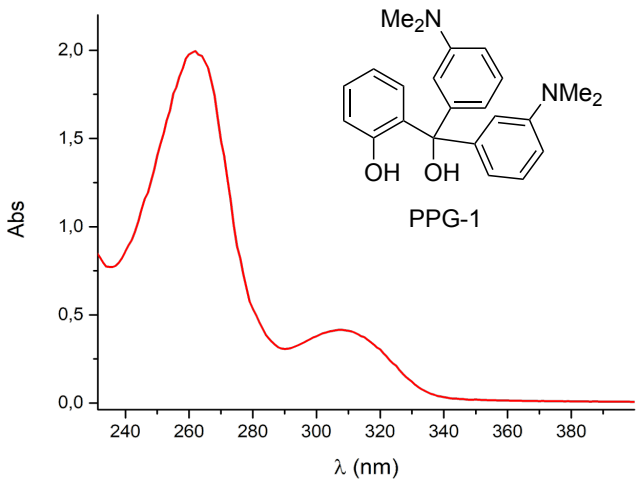

Figure 6.3. UV-Vis absorption spectrum of PPG-1 in MeCN at 6.6 x 10^{-5} M.

The PPG-1 was readily synthesized from the commercially available methyl salicylate by reacting with freshly prepared (3-(*N,N*-dimethylamino)phenyl) magnesium bromide (Scheme 6.1).[24]

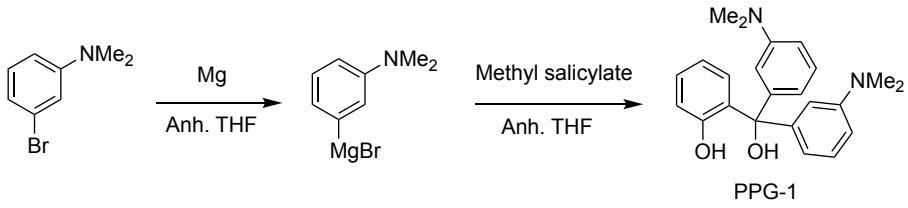

Scheme 6.1. Synthesis of the PPG-1.

6.2.2. Synthesis of the dForU building block (dForU-BB-PPG-1)

In this chapter, two different synthetic routes have been proposed for the synthesis of the α and β anomers of the protected 5-formyl-2'-deoxyuridine phosphoramidite (Schemes 6.2 and 6.3, respectively).

The synthesis of the pure α and the α:β mixture of the protected building block (dForU-BB-PPG-1) was addressed in five steps following the synthetic route depicted in Scheme 6.2. After the first step, an α:β (60:40) dForU-Tol mixture is obtained from a nucleophilic attack of the ForU at the anomeric position of the Hoffer's chlorosugar. At this point, purification of pure α dForU-Tol anomer was readily achievable by recrystallization from EtOH. In the second step, the formyl group of dForU-Tol was protected with the PPG-1 by heating both compounds in p-xylene. Then, the p-toluoyl groups were removed under basic conditions. Finally, the desired dForU-BB-PPG-1 was obtained following selective phosphitylation and tritylation of 3' and 5'-hydroxy groups, respectively.

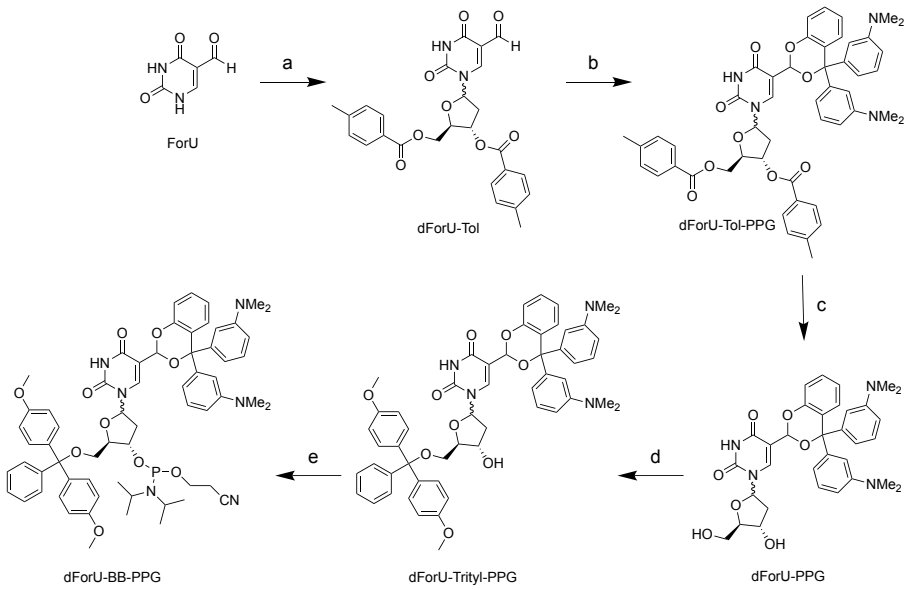

Scheme 6.2. Synthesis of α and α:β mixture anomers. (a) NaH, Hoffer's chlorosugar, anh. DMF; (b) PPG-1, p-xylene, 140 ºC; (c) NaOMe, anh. MeOH; (d) DMT-Cl, anh. Pyridine; (e) DIPEA, 2-cyanoethyl-*N,N*-di*iso*propylchlorophosphoramidite, DCM.

Unfortunately, the pure β anomer could not be isolated using this synthetic route, and hence the following studies were performed using the pure α anomer as well as the α:β (30:70) mixture obtained from the mother liquors left over after recrystallization of the α anomer. However, an alternative synthesis is currently in progress to obtain the pure β anomer following the route depicted in Scheme 6.3. The main difference from the previous one is that in this case the β 5-iodo-2'-deoxyuridine (5-IdU) is used as starting material in order to avoid formation of α:β mixture (step a, Scheme 6.2). Initially, the free OH groups of 5-IdU are protected with TBDMS. In the second step, the C5-iodo is converted to a formyl group through a metal-halogen exchange reaction followed by treatment with DMF. Next, the free

hydroxy groups are once again deprotected. After that, the three last steps are carried out following the same procedure as before.

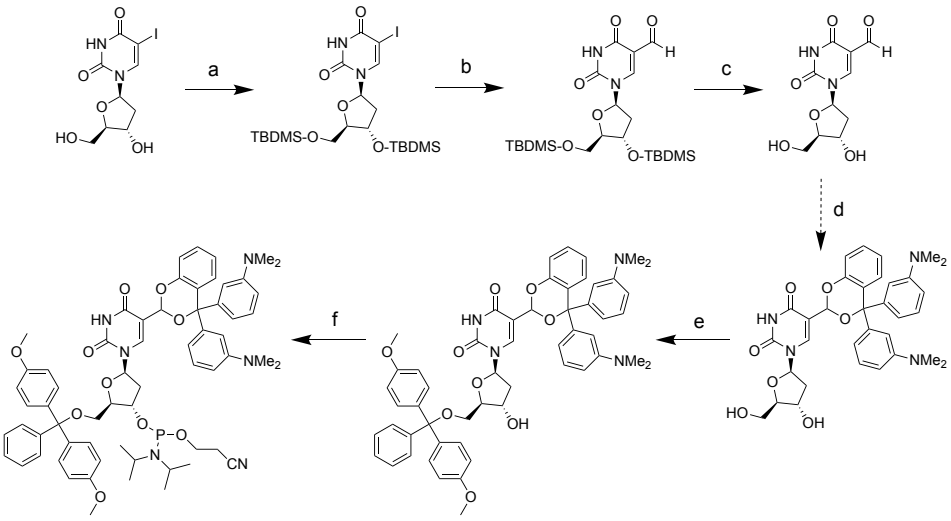

Scheme 6.3. Synthesis of the protected β-anomer. (a) Imidazole, TMDMSCl, anh. DMF; (b) (1) NaH, THF; (2) *n*BuLi, then DMF, -78 ºC; (c) TBAF, THF; (d) PPG-1, p-xylene, 140 ºC; (e) DMT-Cl, anh. pyridine; (f) DIPEA, 2-Cyanoethyl-*N,N*-di*iso*propylchlorophosphoramidite, DCM.

The configuration of both anomers was determined on the tritylated compound dForU-Trityl-PPG-1 by measuring NOESY 2D NMR spectrum. This technique shows the interactions between nuclei that are spatially close. Thus, the stereochemistry was determined by using the interaction between the hydrogens of the deoxyribose moiety highlighted in Figure 6.4. As it clearly appears, interactions between H_4/H_1 or H_5/H_1 can be used as a signature for β and α anomers, respectively.

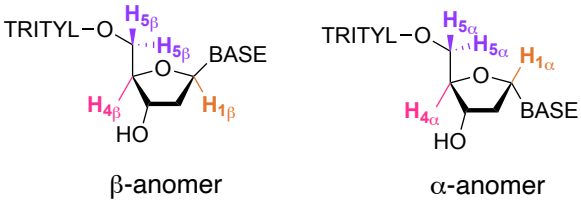

Figure 6.4. Stereochemistry of α and β anomers.

Figure 6.5 shows part of the NOESY map for pure α dForU-Trityl-PPG-1, where the observed cross-peak between $H_{1\alpha}$ and $H_{5\alpha}$ is consistent with the α configuration.

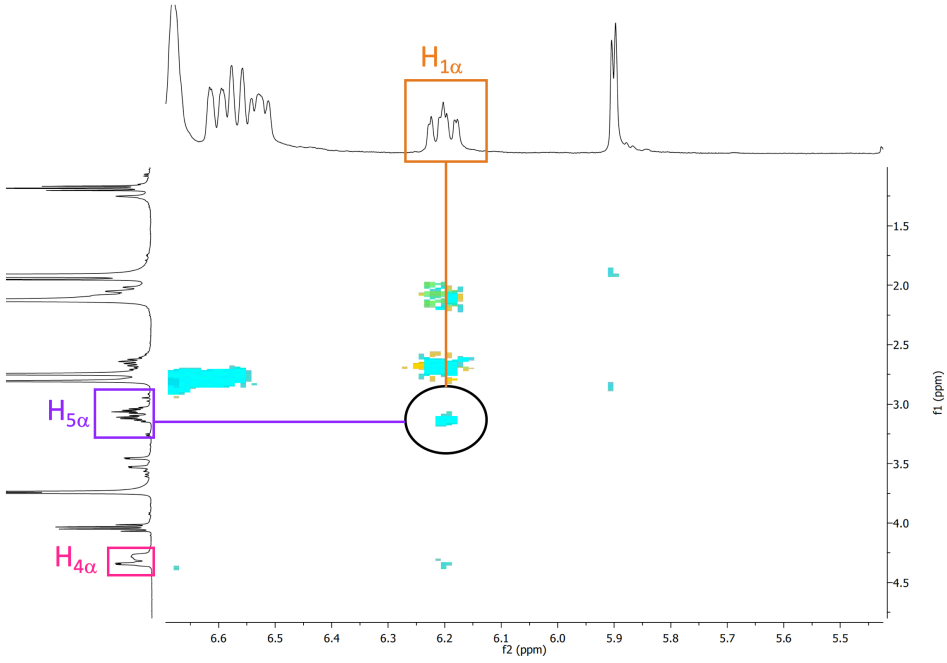

Figure 6.5. Part of the 2D NOESY correlation map of the α anomer dForU-Trityl-PPG-1. The circled spot corresponds to the correlation between $H_{1\alpha}$ and $H_{5\alpha}$, as expected for the α configuration.

The same analysis was done with the α:β (30:70) mixture (Figure 6.6) and in this case the cross-peak between $H_{1\beta}$ and $H_{5\beta}$ was not observed. Instead, a new cross-peak between $H_{1\beta}$ and $H_{4\beta}$ was detected, which agrees with β configuration.

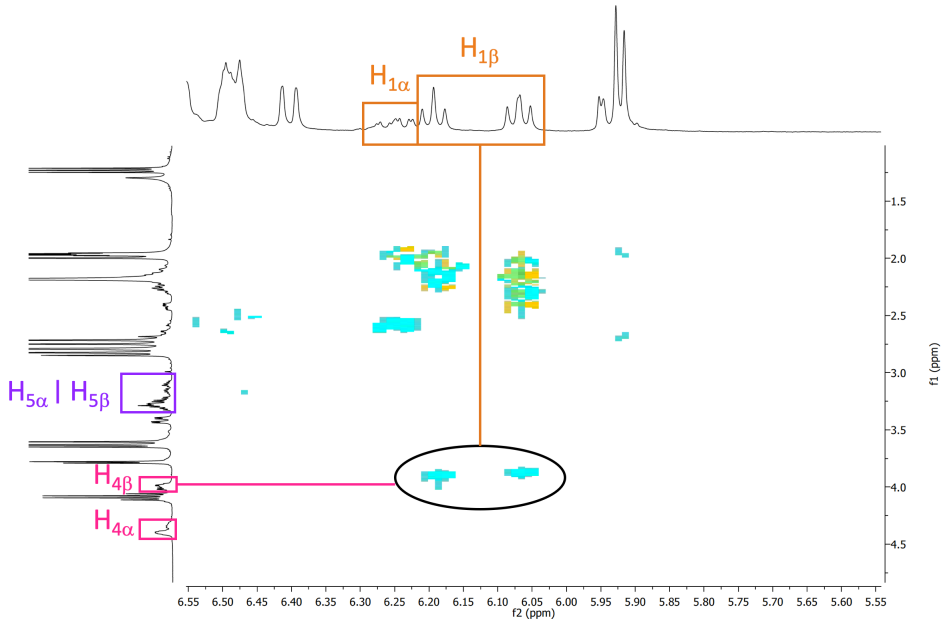

Figure 6.6. Part of the 2D NOESY correlation map of the α:β (30:70) mixture dForU-Trityl-PPG-1. The circled spot corresponds to the correlation between $H_{1\beta}$ and $H_{4\beta}$, as expected for the β configuration.

6.2.3. Steady-state studies using the nucleoside

Before its incorporation into an oligonucleotide, the α:β (60:40) dForU-Tol-PPG-1 was irradiated in MeCN:H_2O (9:1, v:v) with 6 lamps centered at *ca*. 350 nm to test the capability of the PPG-1 to release the α and β dForU-Tol. The course of the reaction was followed by HPLC. The peaks corresponding to dForU-Tol-PPG-1, eluting at *ca*. 17.6 min, and dForU-Tol,

eluting at *ca*. 3.2 and 3.8 min, were assigned by comparison with synthetic standards; for both compounds, detection of different peaks is in agreement with the presence of different isomers. After 2 h, the initial α:β mixture dForU-Tol-PPG-1 was consumed in 52% yield, giving rise to α:β (60:40) dForU-Tol in *ca*. 40% yield (Figure 6.7).

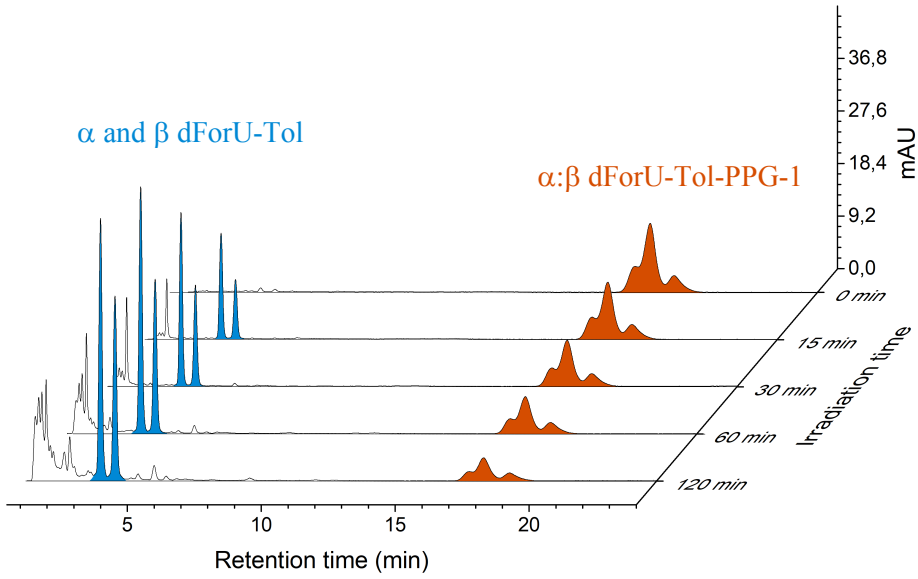

Figure 6.7. HPLC chromatograms registered at 300 nm for MeCN:H_2O (90:10, v:v) solution of α:β (60:40) dForU-Tol-PPG-1 ($2x10^{-4}$ M), upon UVA irradiation at different times.

6.2.4. Incorporation of ForU into deoxynucleotides

Next, the α:β (30:70) mixture of dForU-BB-PPG-1 (proportion calculated from the ^1H NMR of the α:β ForU-Trityl-PPG-1 mixture, see experimental section) was incorporated into an ODN to test the capability of

PPG-1 to release the corresponding dForU within the DNA. This synthesis, together with characterization of the ODNs and their steady state photolysis, was carried out during my stay in Karlsruhe (Germany) at the Karlsruhe Institute of Technology in the group of Prof. Wagenknecht.

The oligonucleotide containing the protected dForU at a specific location was prepared on an Expedite 7/99 synthesizer from PerSeptive Biosystems. The synthesis was carried out following standard phosphoramidite chemistry as depicted in Figure 6.8. According to this procedure, incorporation of each nucleobase involves 4 steps.[25] In the first step the trityl group is removed under acid conditions by dichloroacetic acid (DCA) in DCM. Then, the di*iso*propylamino group of the incoming phosphoramidite is activated towards the attack of the previously deprotected 5'-OH group. Such activation is achieved with tetrazole. Next, the unreacted 5'-OH groups are acetylated using a mixture of Cap A (acetic anhydride, pyridine in THF) and Cap B (*N*-methylimidazole in THF) to avoid the accumulation of shortmers through successive cycles. After that, the unstable phosphite triester bond is oxidized to its stable phosphate triester with a solution of iodine in pyrimidine and water. Finally, after completion of the DNA sequence, treatment with concentrated aqueous ammonia solution is performed to deprotect the β-cyanoethyl group from the phosphate triester, to remove the N-acetyl groups from the bases and to release the ODN from the solid support.

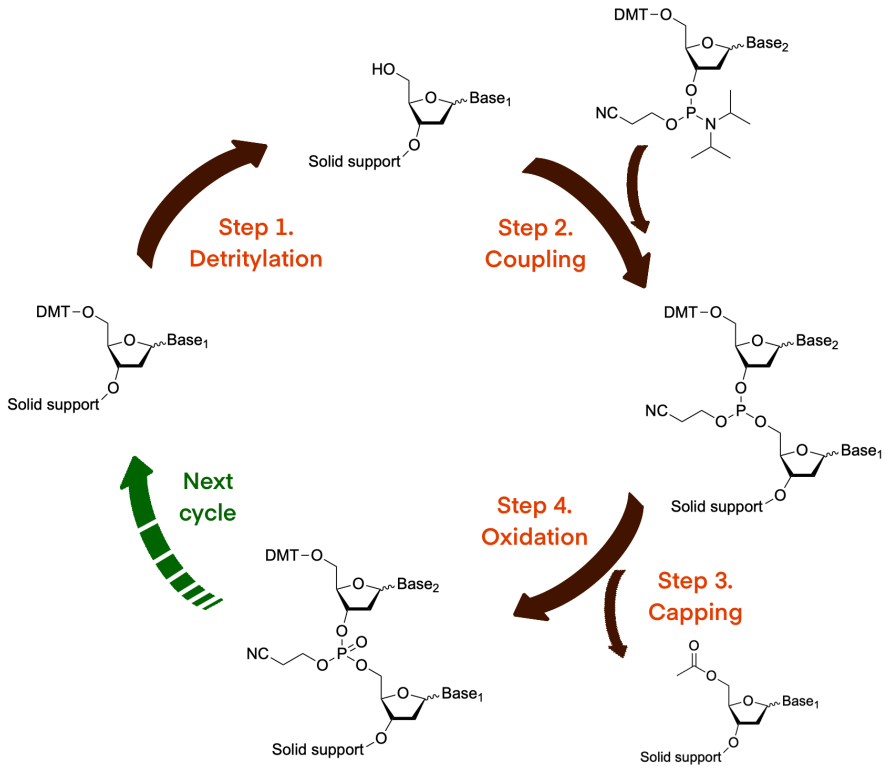

Figure 6.8. Standard protocol for solid-phase oligonucleotide synthesis.

The selected sequence is shown in Figure 6.9. For the step corresponding to dForU-Tol-PPG-1 insertion, the coupling time was enhanced from 96 s to 1400 s. The total coupling efficiency yield was *ca*. 40 %, calculated from the absorption at 495 nm of the DMT carbocation released during detritylation step.

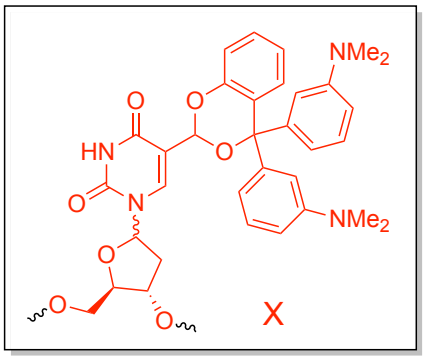

3' G-C-G-T-A-T-A-X-A-T-A-T-A-A-T-A-C-A-G 5' (19-mers)

Figure 6.9. Sequence of the synthetic oligonucleotide containing modified pyrimidine nucleobase at position X and its structure.

The oligonucleotide was purified by HPLC and the obtained fractions were analyzed by MALDI. The mass corresponding to the oligonucleotide of interest was detected at *ca.* 6184.2 Da.

Then, the oligonucleotide was lyophilized and quantified by its absorbance at 260 nm, using a molar absorption coefficient of 234000M^{-1} cm^{-1} on a Nanodrop ND-1000 spectrophotometer. For the irradiation experiments, a solution of the oligonucleotide (*ca.* 5μM) in a 250 mM NaCl and 10 mM sodium phosphate buffer was prepared. This solution was irradiated for 4 h with a LED centered at 305 nm. After that time, salts were removed using a desalting column and the resulting sample was analyzed by MALDI. Interestingly, after irradiation the mass corresponding to the 19-mers ODN containing the protected dForU was not found, whereas the mass for the sodium adduct of the deprotected oligonucleotide was detected at *ca.* 5866.4 Da. These results show the feasibility of the dForU photodeprotection process,

and thus the successful sequence specific insertion of this oxidatively generated lesion within the ODN.

6.3. Conclusion

In summary, a photolabile carbonyl protecting group has been employed to synthesize a new 5-formyl-2'-deoxyuridine derivative (dForU-BB-PPG-1). Its incorporation into an oligodeoxynucleotide (ODN) and further selective irradiation afford the desired ODN containing 5-formyluracil. Development of this new building block compared to traditional dForU precursors offers the advantage of using light for its conversion instead of oxidizing agents. The stereochemistry at the anomeric carbon of the dForU-Trityl-PPG-1 has been determined by 2D NOESY NMR. Additionally, our first results on the insertion of the α:β (30:70) dForU-BB-PPG-1 mixture into ODN and its successful photorelease to afford dForU pave the way for a new methodology to insert aldehydes within ODN sequences. This work also represents an important achievement for the study of ForU capability to act as an intrinsic DNA photosensitizer.

6.4. Experimental section

6.4.1. Synthesis

Synthesis of 2-(bis(3-(dimethylamino)phenyl)(hydroxy)methyl)phenol (PPG-1).[24]

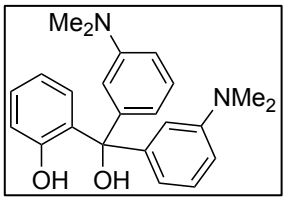

Salicylic acid methyl ester (0.4 mL, 3.1 mmol) was added dropwise to the stirred solution of 3-dimethylaminophenyl magnesium bromide (6.2 mmol), prepared from (3-bromophenyl)-dimethylamine (0.89 mL, 6.2 mmol) and magnesium (182 mg, 7.5 mmol) in 20 mL of anhydrous THF, and the resultant solution was stirred overnight. THF was removed from the obtained mixture, then redissolved using H_2O:EtOAc (1:1, v:v) and adjusted to pH 2-3 with HCl (1M). The aqueous phase was extracted three times with EtOAc, the organic phase was dried over $MgSO_4$ and filtered. Then, the solvent was removed under vacuum. Purification was performed by flash chromatography (Cy:EtOAc, 3:1; silica gel). Product PPG-1 was obtained in a 50% yield (0.56 g).

^{1}H NMR (300 MHz, $CDCl_3$): δ (ppm) 8.28 (s, 1 H), 7.21-7.15 (m, 3 H), 6.89 (dd, J = 1.2, 8.1Hz, 1 H), 6.74-6.61 (m, 6 H), 6.55-6.48 (m, 2 H), 3.50 (s, 1H), 2.86 (s, 12 H).

Synthesis of (2*R*,3*S*,5*S*)-5-(5-formyl-2,4-dioxo-3,4-dihydropyrimidin-1(2*H*)-yl)-2-(((4-methylbenzoyl)oxy)methyl)tetrahydrofuran-3-yl 4-methylbenzoate (α dForU-Tol).

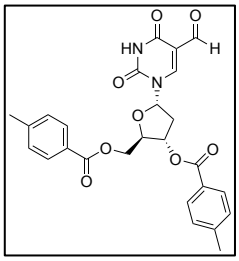

In a heat-dried and argon flushed round bottom flask, 5-formyluracil (0.5 g, 3.6 mmol) was suspended in 18 mL DMF and 142 mg NaH (3.6 mmol, 60% dispersion in mineral oil) were added. The mixture was stirred at room temperature for 40 min, then Hoffer's chlorosugar (1.7 g, 4.3 mmol) was added and the reaction was stirred overnight. The mixture was dried under reduced pressure. Purification via silica gel column chromatography (Cy:EtOAc, 2:1) yielded a mixture of diastereomeric α:β nucleosidation products in a 51% yield (0.9 g). The proportion between both nucleosides was determined as α:β (60:40) by ^{1}H NMR. Recrystallization from absolute EtOH yielded the pure α nucleoside.

^{1}H NMR (400 MHz, $CDCl_3$): δ (ppm) 9.98 (s, 1H), 8.95 (s, 1H), 8.49 (s, 1H), 7.93 (d, J = 8.2 Hz, 2H), 7.73 (d, J = 8.2 Hz, 2H), 7.28 (d, J = 8.0 Hz, 2H), 7.18 (d, J = 8.0 Hz, 2H), 6.36-6.30 (m, 1H), 5.69-5.63 (m, 1H), 5.09-5.04 (m, 1H), 4.62 – 4.44 (m, 2H), 3.06-2.94 (m, 1H), 2.57-2.48 (m, 1H), 2.43 (s, 3H), 2.39 (s, 3H).

^{13}C NMR (101 MHz, $CDCl_3$): δ (ppm) 185.8, 166.2, 165.6, 161.8, 149.2, 145.1, 144.9, 144.6, 129.9, 129.8, 129.6, 129.5, 126.5, 125.8, 110.7, 88.9, 86.2, 74.5, 63.9, 39.6, 21.9, 21.8.

Synthesis of (2*R*,3*S*,5*S*)-5-(5-(4,4-bis(3-(dimethylamino)phenyl)-4*H*-benzo[1,3]dioxan-2-yl)-2,4-dioxo-3,4-dihydropyrimidin-1(2*H*)-yl)-2-(((4-methylbenzoyl)oxy)methyl)tetrahydrofuran-3-yl 4-methylbenzoate (α dForU-Tol-PPG-1)

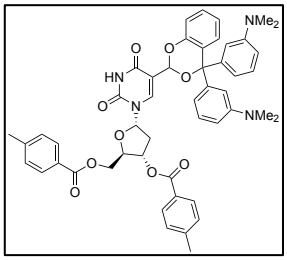

In a heat-dried and argon flushed round bottom flask, α dForU-Tol (0.33 g, 0.67 mmol), PPG-1 (0.5 g, 1.38 mmol) and 3 mL of p-xylene were stirred at 140 ºC. Upon completion, the reaction mixture was purified twice via flash column chromatography. After a first purification by normal-phase flash column chromatography (hexane:AcOEt:MeOH, 6.6:3:0.4) and a second purification by reverse-phase flash column (MeCN:H_2O, 80:20), product α dForU-Tol-PPG-1 was obtained in a 30% yield (0.17 g).

^{1}H NMR (300 MHz, $CDCl_3$): δ (ppm) 8.20 (2s, 1H), 7.94 (d, J = 8.2 Hz, 2H), 7.90 (d, J = 8.2 Hz, 1H), 7.73 (d, J = 8.2 Hz, 1H), 7.30 (d, J = 9 Hz, 2H), 7.21-6.81 (m, 6H), 6.78-6.51 (m, 6H), 6.50-6.37 (m, 1H), 6.36-6.23 (m, 1H), 6.10 (s+s, 1H), 5.75-5.60 (m, 1H), 4.99-4.86 (m, 1H), 4.66-4.45 (m, 2H), 3.11-2.91 (m, 1H), 2.84 (s+s, 6H), 2.74 (s+s, 6H), 2.65-2.49 (m, 1H), 2.43 (s, 3H), 2.16 (s+s, 3H).

^{13}C NMR (101 MHz, $CDCl_3$): δ (ppm) 166.2, 166.0, 161.0, 160.7, 152.1, 152.0, 149.8, 149.7, 144.8, 144.5, 139.0, 138.8, 129.9, 129.9, 129.6,

129.5, 128.7, 128.6, 128.5, 128.2, 126.7, 126.0, 125.8, 120.6, 117.3, 117.3, 111.8, 111.1, 89.6, 89.5, 88.8, 88.1, 86.1, 86.1, 86.0, 85.0, 74.6, 64.3, 64.2, 40.8, 39.7, 39.5, 21.9, 21.7.

Synthesis of 5-(4,4-bis(3-(dimethylamino)phenyl)-4*H*-benzo[1,3]dioxan-2-yl)-1-((2*S*,4*S*,5*R*)-4-hydroxy-5-(hydroxymethyl)tetrahydrofuran-2-yl)pyrimidine-2,4(1*H*,3*H*)-dione (α dForU-PPG-1)

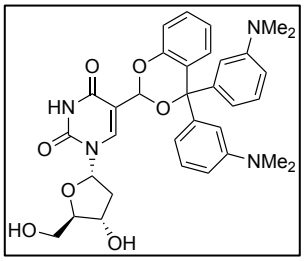

In a heat-dried and argon flushed round bottom flask, α dForU-Tol-PPG-1 (0.24 g, 0.28 mmol) was dissolved in 2.8 mL of anhydrous MeOH. After that, 3 mL of a freshly prepared 0.5 M NaOMe solution were added dropwise and the reaction mixture was stirred for 4 h. Then, the resulting mixture was neutralized with a solution of AcOH (2M) in MeOH, dried under reduced pressure and purified by flash column chromatography (hexane:AcOEt:MeOH, 4.75:4.75:5) to afford α dForU-PPG-1 in a 89% yield (0.153 g).

^{1}H NMR (400 MHz, $CDCl_3$): δ (ppm) 9.13 (s+s, 1H), 8.36 (s+s, 1H), 7.23-7.03 (m, 3H), 6.98 – 6.74 (m, 5H), 6.73-6.56 (m, 4H), 6.19-6.08 (m, 1H), 6.05 (s+s, 1H), 4.45 – 4.22 (m, 2H), 3.69 – 3.46 (m, 2H), 2.90-2.75 (m, 12H), 2.72-2.55 (m, 1H), 2.24 – 2.08 (m, 1H).

^{13}C NMR (101 MHz, $CDCl_3$): δ (ppm) 161.7, 152.1, 152.0, 150.5, 150.4, 146.9, 146.7, 143.9, 141.8, 141.6, 129.8, 129.7, 128.7, 128.5, 125.8, 125.6, 120.5, 118.7, 117.4, 117.3, 114.4, 114.3, 113.0, 112.7, 111.4, 111.3, 90.0, 89.8, 89.5, 89.4, 88.5, 85.8, 85.7, 71.9, 63.0, 41.6, 41.4, 41.0, 40.8.

Synthesis of 5-(4,4-bis(3-(dimethylamino)phenyl)-4*H*-benzo[1,3]dioxan-2-yl)-1-((2*S*,4*S*,5*R*)-5-((bis(4-methoxyphenyl)(phenyl)methoxy)methyl)-4-hydroxytetrahydrofuran-2-yl)pyrimidine-2,4(1*H*,3*H*)-dione (α dForU-Trityl-PPG-1)

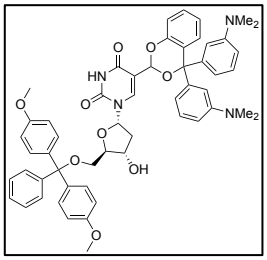

In a heat-dried and argon flushed round bottom flask, α dForU-PPG-1 (0.13 g, 0.22 mmol) was dissolved in 2.1 mL of anhydrous pyridine. Then, 4,4'-dimethoxytrityl chloride (84 mg, 0.25 mmol) was added. The reaction mixture was stirred at room temperature for 21 h, dried under reduced pressure and purified by flash column chromatography (hexane:AcOEt:MeOH, 4.75:4.75:5) to afford α dForU-Trityl-PPG-1 in a 28% yield (57 mg).

^{1}H NMR (400 MHz, CD_3CN): δ (ppm) 9.04 (s, 1H), 8.45 (s+s, 1H), 7.58-7.44 (m, 2H), 7.44-7.32 (m, 6H), 7.32-7.20 (m, 3H), 7.19-7.08 (m, 1H), 7.07-6.09 (m, 1H), 7.00-6.86 (m, 6H), 6.84-6.73 (m, 3H), 6.72-6.49 (m, 3H), 6.33-6.20 (m, 1H), 5.98 (s+s, 1H), 4.55-4.24 (m, 2H), 3.82 (s+s, 6H), 3.27-3.02 (m, 2H), 2.90-2.75 (m, 12H), 2.77-2.67 (m, 1H), 2.14-2.07 (m, 1H).

^{13}C NMR (101 MHz, CD_3CN): δ (ppm) 159.7, 153.1, 151.6, 151.4, 151.0, 147.6, 147.5, 146.0, 146.0, 145.3, 145.2, 142.1, 142.1, 136.9, 130.9, 130.6, 129.5, 129.4, 129.4, 129.4, 129.3, 129.0, 128.8, 127.8, 121.2, 117.3,

114.1, 113.9, 113.2, 113.2, 113.1, 112.7, 112.7, 111.0, 111.0, 90.4, 90.4, 89.7, 89.6, 88.2, 88.2, 87.2, 86.6, 86.4, 72.6, 65.0, 64.9, 55.9, 41.3, 41.3, 40.7, 40.7, 40.6.

MS (MALDI-TOF) *m/z,* $C_{54}H_{54}N_4O_9$ calculated for 902.38; found: 901.77.

Synthesis of (2*R*,3*S*)-5-(5-(4,4-bis(3-(dimethylamino)phenyl)-4*H*-benzo[1,3]dioxan-2-yl)-2,4-dioxo-3,4-dihydropyrimidin-1(2*H*)-yl)-2-((bis(4-methoxyphenyl)(phenyl)methoxy)methyl)tetrahydrofuran-3-yl (2-cyanoethyl) diisopropylphosphoramidite (α:β dForU-BB-PPG-1 mixture)

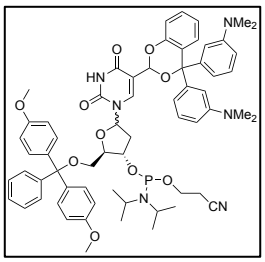

In a heat-dried and argon flushed round bottom flask, the diastereomeric mixture α:β (30:70) dForU-Trityl-PPG-1 (55 mg, 0.06 mmol) was dissolved in 3.2 mL of anhydrous DCM. Di*iso*propylethylamine (36.6 μL, 0.21 mmol) was added and the resulting mixture was stirred at room temperature for 6 min before 2-cyanoethyl-*N,N*-di*iso*propylchlorophosphoramidite (20.1 μL, 0.09 mmol). Then, the mixture was stirred at room temperature for 4 h. In the meantime, same amount of di*iso*propylethylamine and 2-cyanoethyl-*N,N*-di*iso*propylchlorophosphoramidite was added twice. The reaction mixture was dried under reduced pressure and purified by flash column chromatography using dry SiO_2 (DCM:acetone, 9:1 + 1% TEA) to afford dForU-BB-PPG-1 in a 93% yield (62 mg).

^{31}P NMR (162 MHz, [d_6]-DMSO) δ (ppm) 147.73, 147.50, 147.46, 147.21.

MS (MALDI-TOF) *m/z,* $C_{63}H_{71}N_6O_{10}P$ calculated for 1102.49; found: 1102.37

6.4.2. NMR spectra

^{1}H NMR ($CDCl_3$, 300 MHz)

PPG

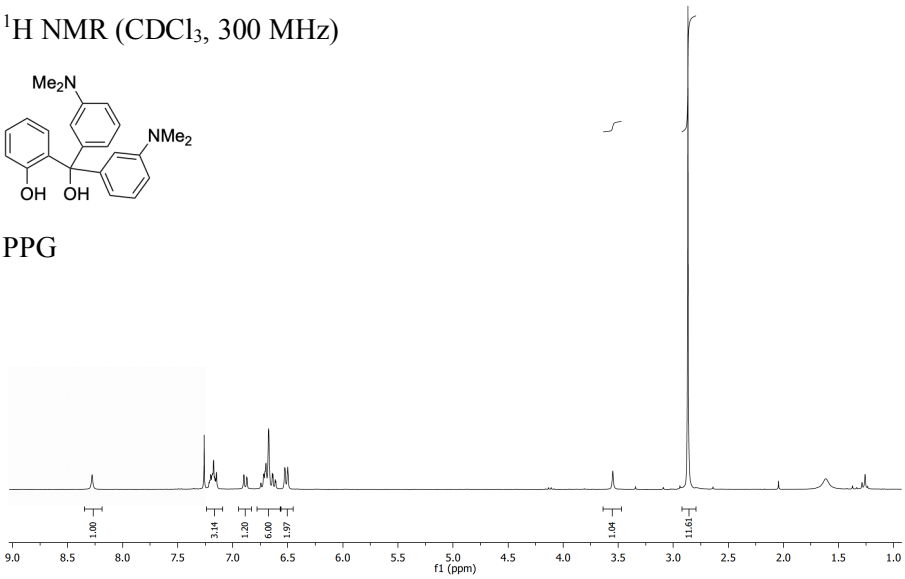

^{1}H NMR ($CDCl_3$, 400 MHz)

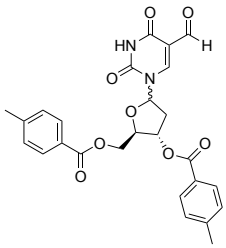

α:β (30:70) dForU-Tol

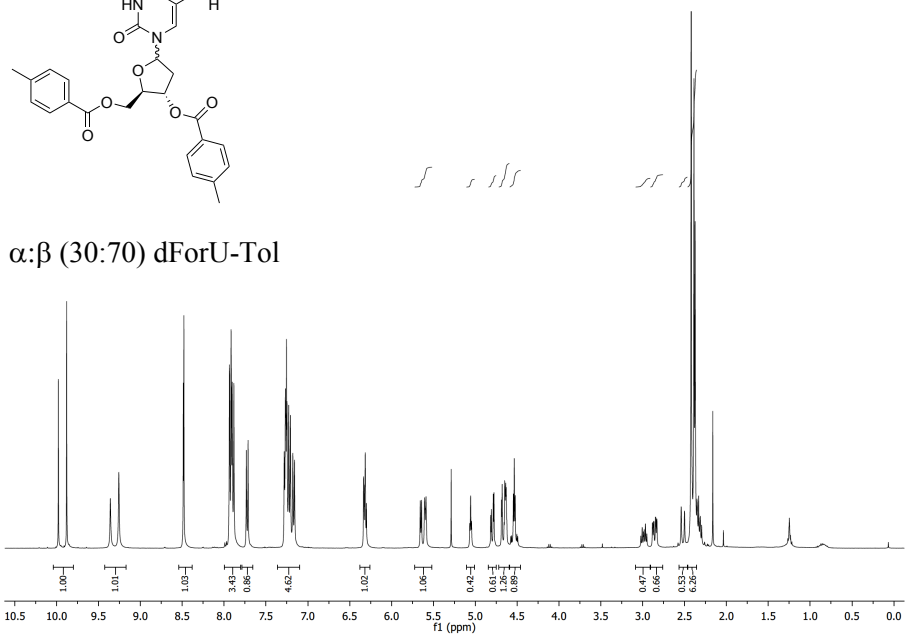

^{1}H NMR ($CDCl_3$, 400 MHz)

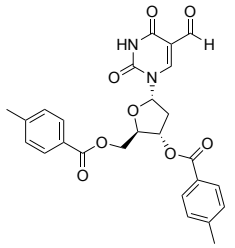

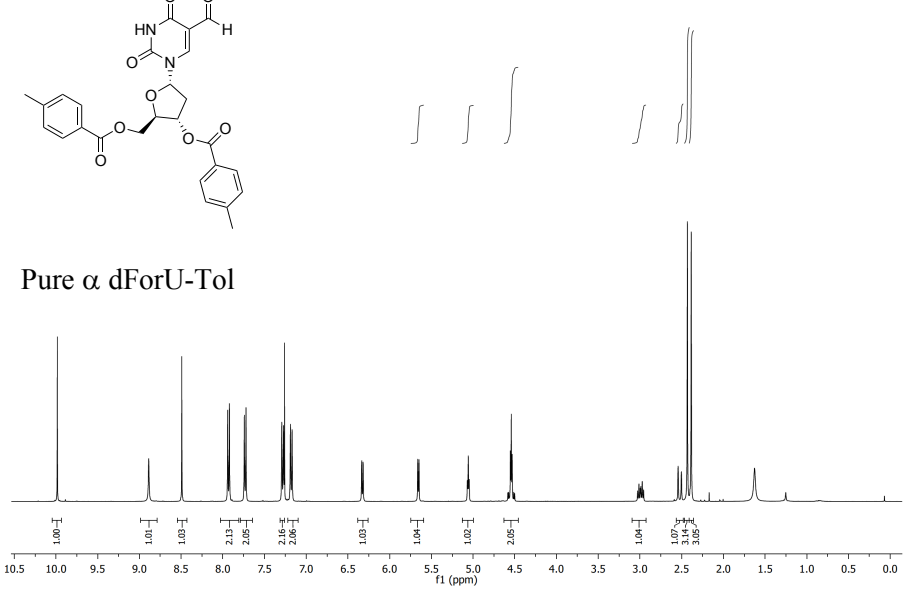

Pure α dForU-Tol

^{13}C NMR ($CDCl_3$, 101 MHz)

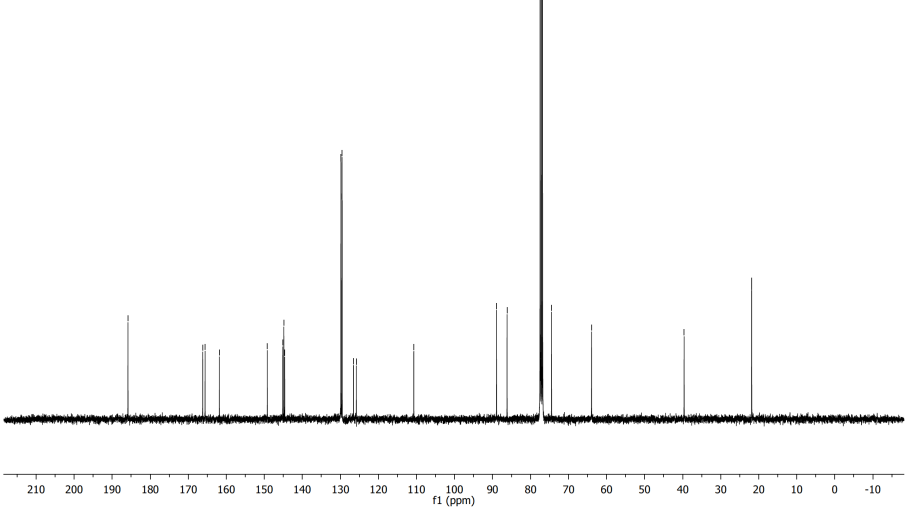

^{1}H NMR ($CDCl_3$, 300 MHz)

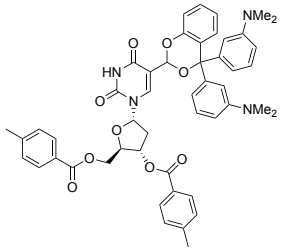

Pure α dForU-Tol-PPG-1

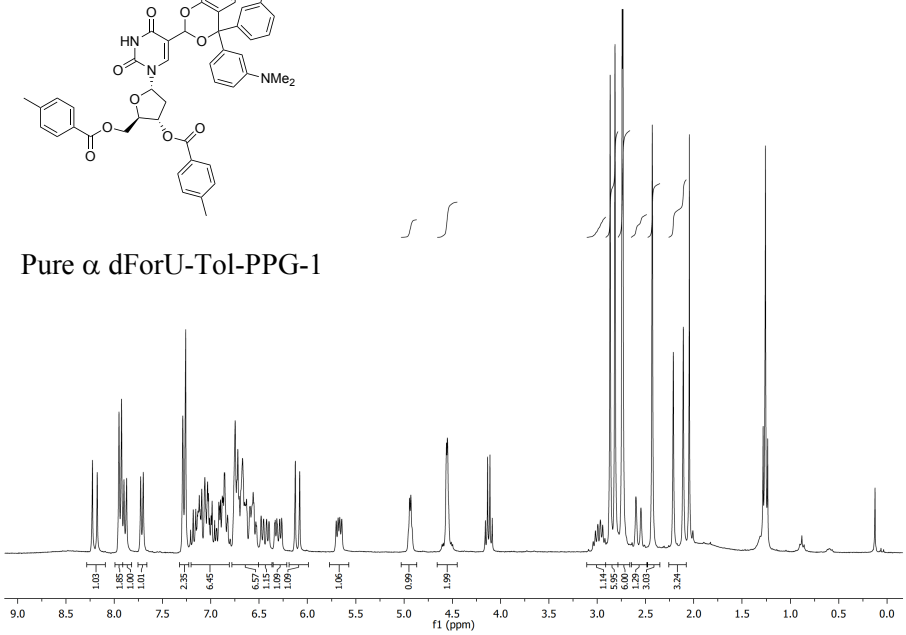

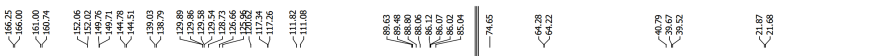

^{13}C NMR ($CDCl_3$, 101 MHz)

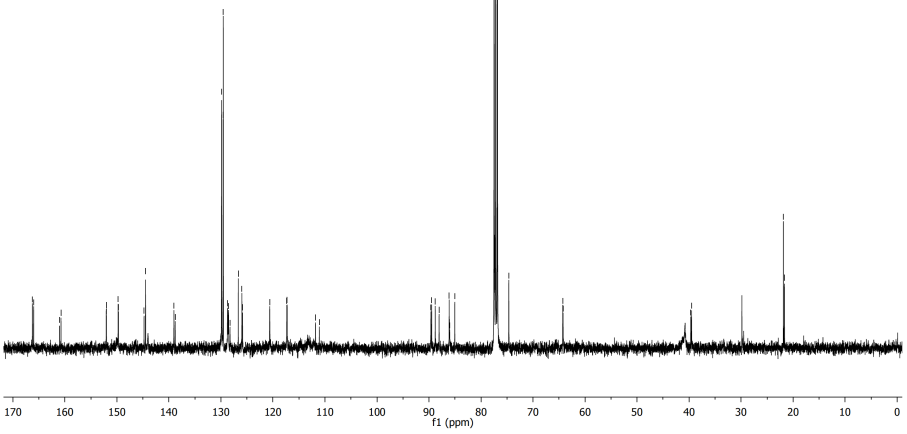

^{1}H NMR ($CDCl_3$, 400 MHz)

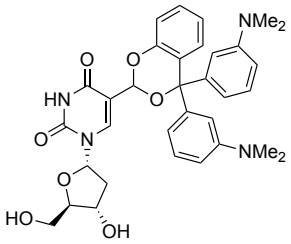

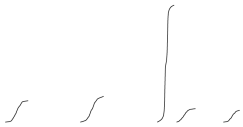

Pure α dForU-PPG-1

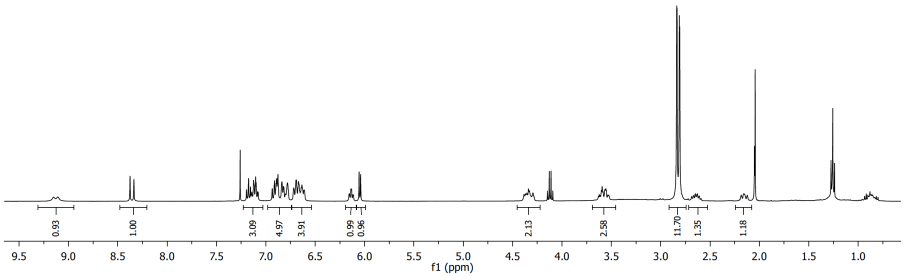

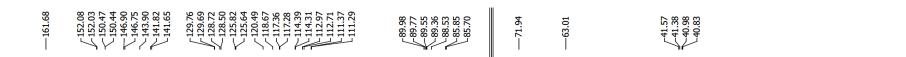

^{13}C NMR ($CDCl_3$, 101 MHz)

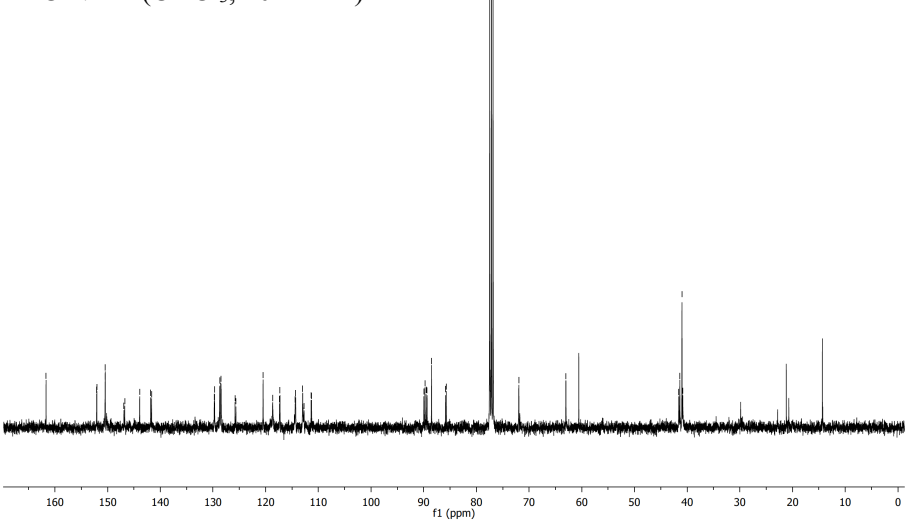

^{1}H NMR (CD_3CN, 400 MHz)

Pure α dForU-Trityl-PPG-1

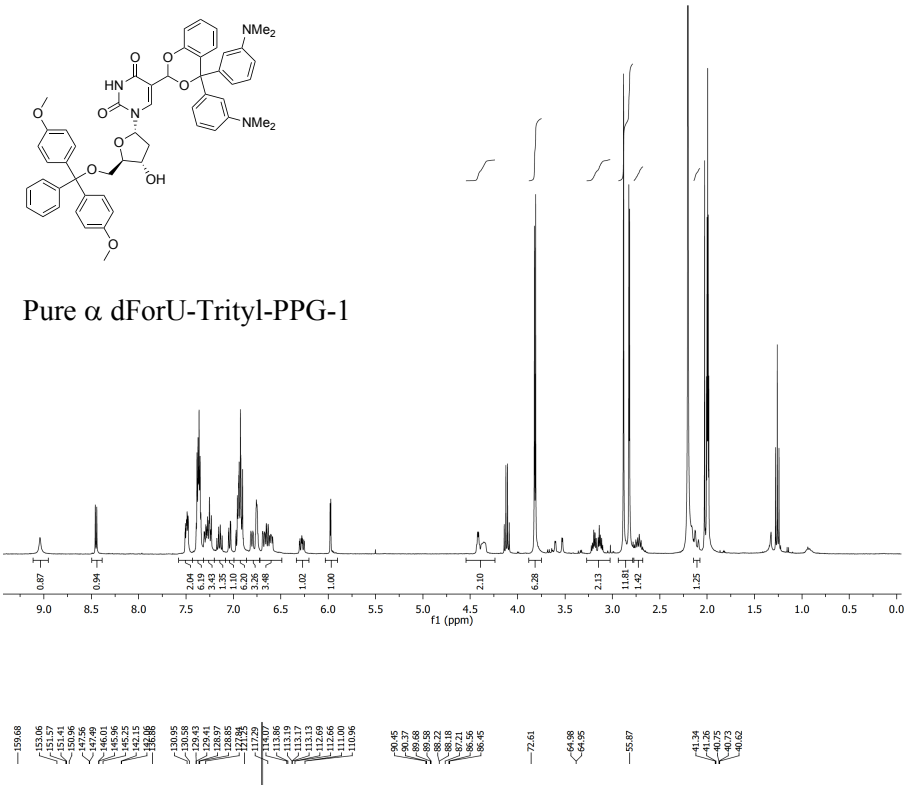

^{13}C NMR (CD_3CN, 101 MHz)

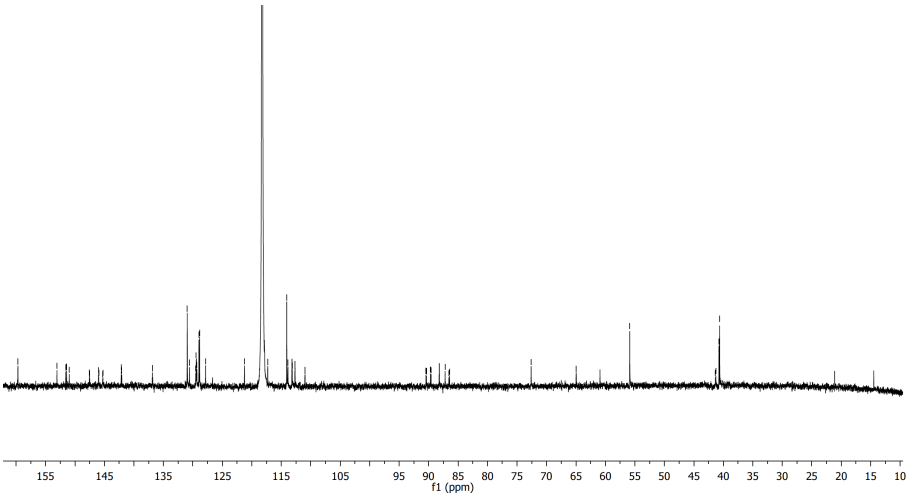

HSQC (CD_3CN)

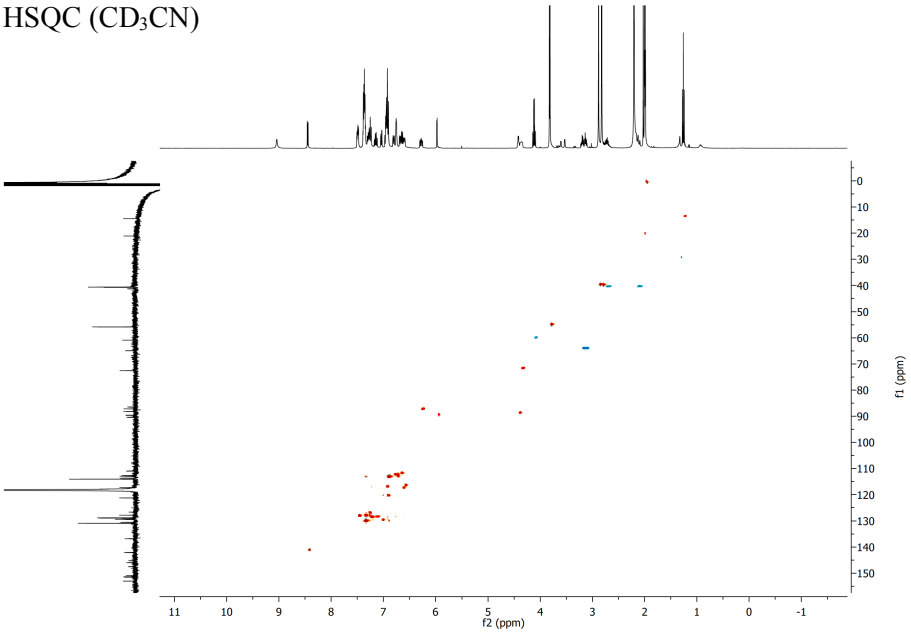

NOESY (CD_3CN)

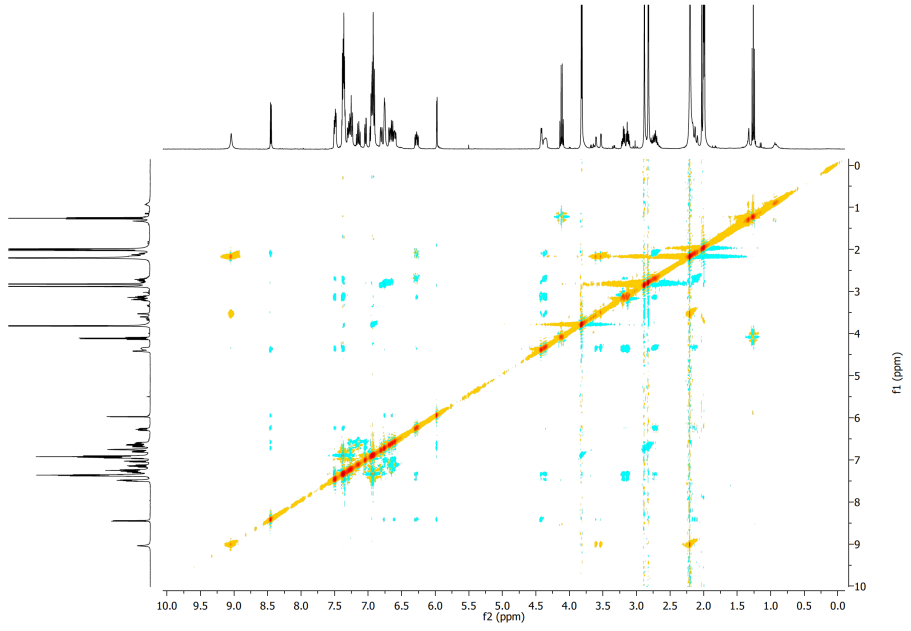

^{1}H NMR (CD_3CN, 400 MHz)

α:β (30:70) dForU-Trityl-PPG-1

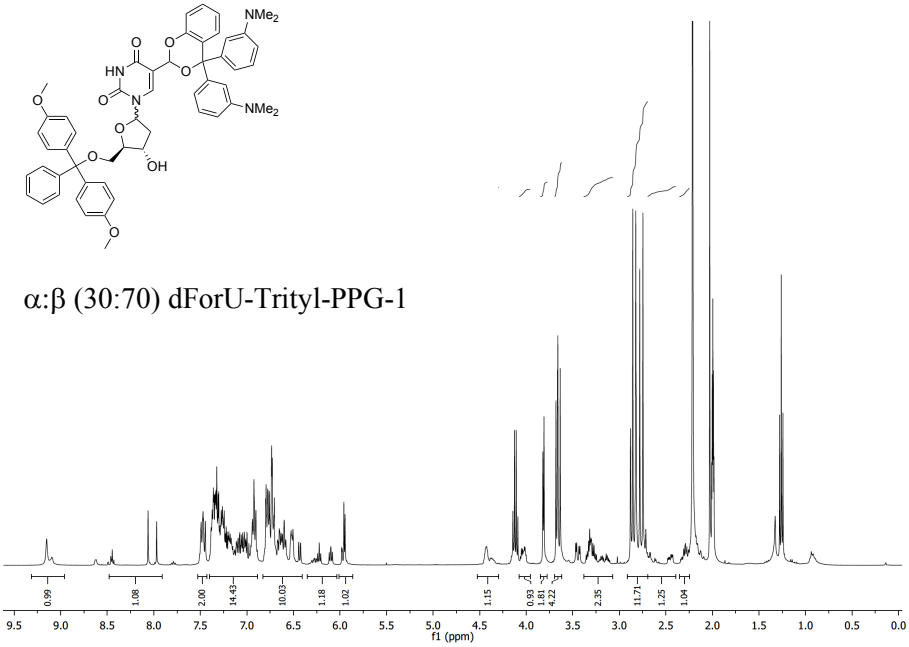

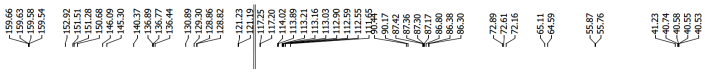

^{13}C NMR (CD_3CN, 101 MHz)

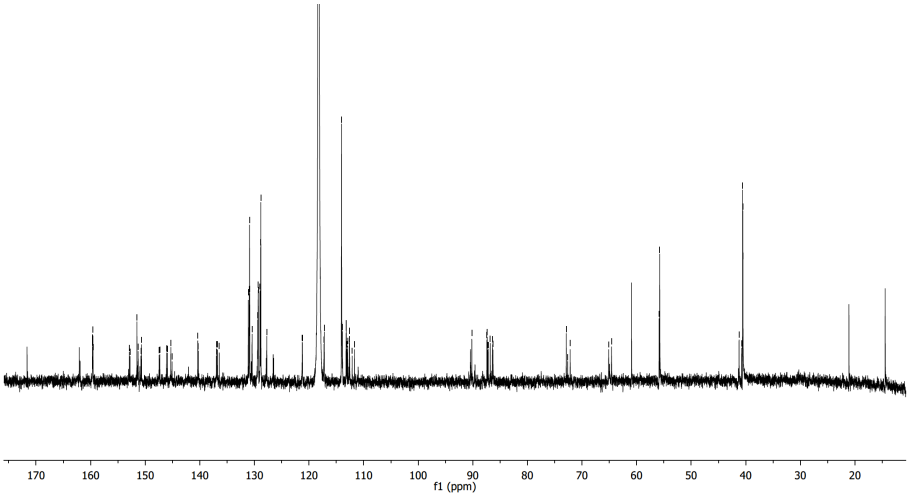

HSQC (CD_3CN)

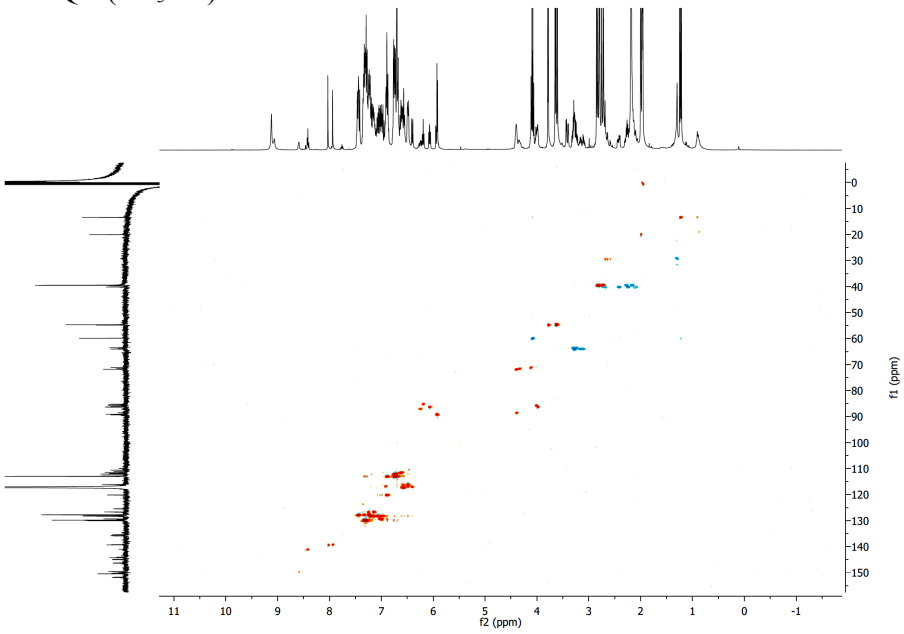

NOESY (CD_3CN)

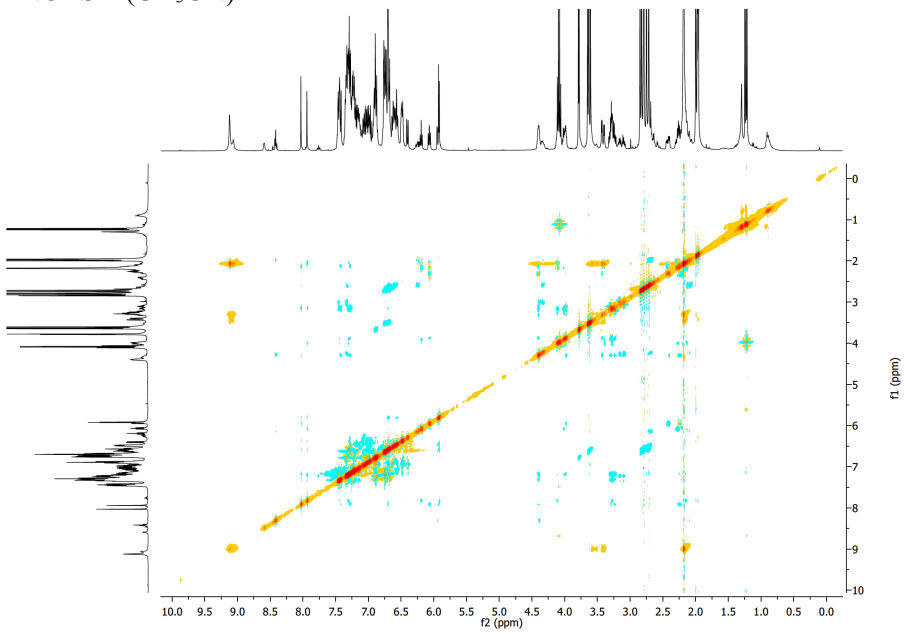

^{31}P NMR ([d_6]-DMSO, 162 MHz)

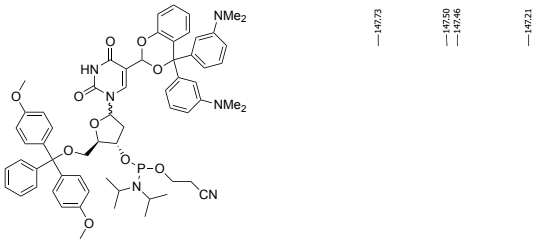

α:β dForU-BB-PPG-1 mixture

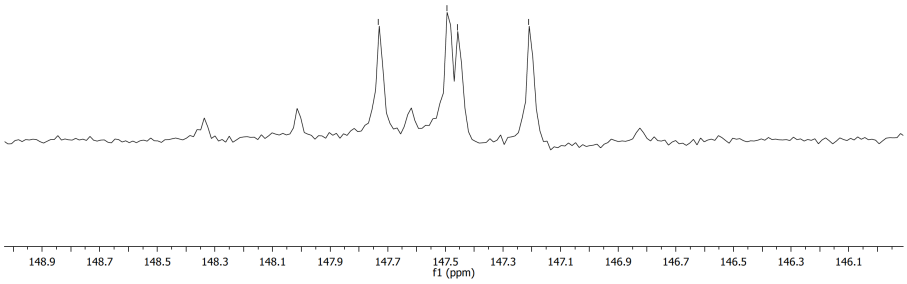

6.5. Bibliography

1 Y. Wang, X. Zhang, G. Zou, S. Peng, C. Liu and X. Zhou, *Acc. Chem. Res.*, 2019, **52**, 1016–1024.

2 W. K. Pogozelski and T. D. Tullius, *Chem. Rev.*, 1998, **98**, 1089–1107.

3 J. Cadet, S. Mouret, J. L. Ravanat and T. Douki, *Photochem. Photobiol.*, 2012, **88**, 1048–1065.

4 T. Douki, T. Delatour, F. Paganon and J. Cadet, *Chem. Res. Toxicol.*, 1996, **9**, 1145–1151.

5 H. Hong, H. Cao, Y. Wang and Y. Wang, *Chem. Res. Toxicol.*, 2006, **19**, 614–621.

6 T. Douki and J. Cadet, *Int. J. Radiat. Biol.*, 1999, **75**, 571–581.

7 I. Saito, M. Takayama and S. Kawanishi, *J. Am. Chem. Soc.*, 1995, **117**, 5590–5591.

8 T. Delatour, T. Douki, C. D'Ham and J. Cadet, *J. Photochem. Photobiol. B Biol.*, 1998, **44**, 191–198.

9 M. C. Cuquerella, V. Lhiaubet-Vallet, J. Cadet and M. A. Miranda, *Acc. Chem. Res.*, 2012, **45**, 1558–1570.

10 J. W. Neidigh, A. Darwanto, A. A. Williams, N. R. Wall and L. C. Sowers, *Chem. Res. Toxicol.*, 2009, **22**, 885–893.

11 E. J. Privat and L. C. Sowers, *Mutat. Res. - Fundam. Mol. Mech. Mutagen.*, 1996, **354**, 151–156.

12 A. Masaoka, H. Terato, M. Kobayashi, Y. Ohyama and H. Ide, *J. Biol. Chem.*, 2001, **276**, 16501–16510.

13 D. K. Rogstad, J. Heo, N. Vaidehi, W. A. Goddard, A. Burdzy and L. C. Sowers, *Biochemistry*, 2004, **43**, 5688–5697.

14 A. Kittaka, C. Horii, H. Tanaka, T. Miyasaka, K. T. Nakamura, R. Kuroda and T. Sugiyama, *Heterocycles*, 2004, **64**, 367–382.

15 H. Kasai, A. Iida, Z. Yamaizumi, S. Nishimura and H. Tanooka, *Mutat. Res. Lett.*, 1990, **243**, 249–253.

16 I. Aparici-Espert, G. Garcia-Lainez, I. Andreu, M. A. Miranda and V. Lhiaubet-Vallet, *ACS Chem. Biol.*, 2018, **13**, 542–547.

17 A. Francés-Monerris, C. Hognon, M. A. Miranda, V. Lhiaubet-Vallet and A. Monari, *Phys. Chem. Chem. Phys.*, 2018, **20**, 25666–25675.

18 T. Douki, *ChemPhotoChem*, 2020, **4**, 294–299.

19 L. Antusch, N. Gaß and H. A. Wagenknecht, *Angew. Chem. Int. Ed.*, 2017, **56**, 1385–1389.

20 A. Kuhlmann, L. Bihr and H. A. Wagenknecht, *Angew. Chem. Int. Ed.*, 2020, **59**, 17378–17382.

21 K. Sato, W. Hirose and A. Matsuda, *Curr. Protoc. Nucleic Acid Chem.*, 2008, 1–19.

22 H. Sugiyama, S. Matsuda, K. Kino, Q. M. Zhang, S. Yonei and I. Saito, *Tetrahedron Lett.*, 1996, **37**, 9067–9070.

23 A. Tran, S. Zheng, D. S. White, A. M. Curry and Y. Cen, *Chem. Sci.*,

2020, **11**, 11818–11826.

24 H. Yang, X. Zhang, L. Zhou and P. Wang, *J. Org. Chem.*, 2011, **76**, 2040–2048.

25 N. D. Sinha, J. Biernat, J. McManus and H. Köster, *Nucleic Acids Res.*, 1984, **12**, 4539–4557.

Chapter 7:

Instrumentation

7.1 Absorption measurements

All UV-Vis absorption spectra were registered with a simple beam spectrophotometer (Varian Cary 50 o 60) with a quartz cell of 1 cm optical path length.

7.2 Emission measurements

7.2.1. Fluorescence

The steady-state fluorescence measurements were performed using a fluorimeter Photon Technology International (PTI), LPS-220B model, equipped with a Xenon lamp of 75 W and a monochromator that covers a range from 200 to 700 nm. Measurements were registered after having adjusted the compound absorbance between 0.03 and 0.1 at the excitation wavelength.

7.2.2. Phosphorescence

The phosphorescence spectra were registered with a phosphorimeter Photon Technology International (PTI, TimeMaster TM/2003) equipped with a pulsed Xenon lamp. The equipment worked in time-resolved mode with a delay time of 500 μs. All solutions were prepared in ethanol, adjusting their absorbance at *ca.* 0.8 at the excitation wavelength (with a cuvette of 1 cm optical pathway), then measurements were performed in a quartz tube (0.5 mm diameter) at 77 K.

7.3. Steady-state photolysis

Irradiations of the samples were run using 4 different systems:

- A Xenon lamp (150 W) equipped with a monochromator from Photon Technology International (PTI) for monochromatic irradiations.

- A medium pressure mercury lamp (750 W).

- A Luzchem photoreactor (model LZC-4V, 8 W) with a variable number of lamps with a maximum output at 350/254 nm for UVA/UVC irradiations.

- A Thermo Oriel Newport (91192-1000) solar simulator equipped with a 1000 W Xenon arc for simulated sunlight irradiations (SSL). The output was filtered to better match the solar emission spectrum using an AM 1.5 G global filter; its output was *ca.* 860 $mWcm^{-2}$.

Irradiations were performed under anaerobic or aerobic conditions in quartz cells of 1 cm optical path or pyrex tubes.

7.4. Laser Flash Photolysis (LFP)

Laser Flash Photolysis experiments were performed by exciting at 355 and 266 nm, using the 3^{rd} and 4^{th} harmonic, respectively, of a pulsed laser Nd:YAG (L52137V LOTIS TII) with a pulse duration of ca. 10 ns. The full system comprises a pulsed laser, a Xenon lamp (Lo 255 Oriel), a monochromator (Oriel 77200), a photomultiplier (Oriel 70705) and an oscilloscope (TDS-640A Tektronic). The output signal from the oscilloscope was transferred to a personal computer. All experiments were performed in a quartz cell of 1 cm optical path length. All components concentration was

adjusted in order to have an absorbance of *ca*. 0.3-0.4 in the excitation wavelength. Before running the experiment, solutions were flushed with N_2, O_2 or N_2O for 15 min. Laser energies ranging from 20 to 49 mJ per pulse were used.

In Chapter 4, 1-methylnaphthalene (MNP) solution was prepared at 11mM in MeCN for the quenching experiments of OB-BP.

7.5. Femtosecond transient absorption spectroscopy

The transient absorption spectra were recorded using a typical pump-probe system. The femtosecond pulses were generated with a mode-locked Ti-sapphire laser of a compact Libra HE (4W power at 4 kHz) regenerative amplifier delivering 100 fs pulses at 800 nm (1 mJ/pulse). The output of the laser was split into two parts to generate the pump and the probe beams. Thus, tunable femtosecond pump pulses were obtained by directing the 800 nm light into an optical parametric amplifier. In the present case, the pump was set at 355 nm and passed through a chopper prior to focus onto a rotating cell containing the solutions under study. The white light used as probe was produced after part of the 800 nm light from the amplifier travelled through a computer controlled 8 ns variable optical delay line and impinge on a CaF_2 rotating crystal. This white light is in turn, split in two identical portions to generate reference and probe beams that then are focused on the rotating cell containing the sample. The pump and the probe are made to coincide to interrogate the sample. A computer-controlled imaging spectrometer is placed after this path to measure the probe and the reference pulses and obtain the transient absorption decays/spectra. Samples were prepared with an absorbance of *ca*. 1 at the pump wavelength, using an optical pathway of 1 mm.

7.6. Nuclear Magnetic Resonance (NMR)

NMR spectra were measured using a 300 MHz or a 400 MHz instrument. All compounds have been characterized by ^{1}H and ^{13}C NMR, except those already described in the literature which have been characterized by ^{1}H NMR. $CDCl_3$, CD_3OD, D_2O and $(CD_3)_2SO$ were used as solvents for the spectra, and their signals were taken as the reference using the following chemical shifts:

-$CDCl_3$: 7.26 ppm and 77.16 ppm, for ^{1}H NMR and ^{13}C NMR, respectively.

-CD_3OD: 3.31 ppm and 49.00 ppm, for ^{1}H NMR and ^{13}C NMR, respectively.

-CD_3CN: 1.94 ppm and 118.36 ppm (or 1.32 ppm), for ^{1}H NMR and ^{13}C NMR, respectively.

-D_2O: 4.79 ppm for ^{1}H NMR (used in Chapter 5, section 5.2.4, as a reference signal in D_2O:CD_3CN (1:1, v:v) mixtures)

-[d_6]-DMSO: 2.5 ppm and 39.52 ppm, for ^{1}H NMR and ^{13}C NMR, respectively.

All coupling constants (J) are given in Hz.

7.7. HPLC analyses

All irradiation mixtures were analyzed on an Agilent 1100 Series HPLC set-up equipped with a diode-array detector covering a detection range from 200 to 400 nm. Analysis were performed using two different columns: a

Zorbax Eclipse Plus C18 (100 x 4.6 mm, 3.5 μm) column (ZC) and a Mediterranean Sea C18 column (250 x 4.6 mm, 5 μm) (MC). In all cases, the H_2O mobile phase was acidified at a pH of *ca*. 3 and the flow rate was set at 1 $mL \cdot min^{-1}$. The percentage yields were determined in all cases from calibration curves of pure compounds.

In Chapter 4, the MC column was used to analyze OB-BP, OB-BP-C, OB-KP, OB-TL and OB-AP. For all of them, an isocratic mixture of MeCN:H_2O (70:30, v:v) was used, except for OB-KP, which was measured using an isocratic mixture of MeCN:H_2O (55:45, v:v). In this chapter, the ZC column was also used for the analysis of OB-CBP and OB-CBP-C, which were analyzed using an isocratic mixture of MeCN:H_2O (65:35, v:v).

In Chapter 5, all samples were analyzed using the MC column, and the chromatographic conditions were an isocratic mixture of MeCN:H_2O (20:80, v:v).

7.8. UPLC-HRMS analyses

Exact mass values were determined by means of a QToF spectrometer coupled with a liquid chromatography system. Separations were accomplished by UPLC on a Zorbax Eclipse Plus C18 column (4.6x100 mm, 3.5 μm). The ESI source was operated in positive ionization mode with a capillary voltage of 3 kV. The source and desolvation temperatures were set at 80 and 400ºC, respectively. The cone and desolvation gas flows were 20 and 800 $L \cdot h^{-1}$, respectively. All data were collected in centroid mode. Leucine-enkephalin was used as the lock mass, generating an $[M+H]^+$ ion (m/z 556.2771) at a concentration of 250 $pg \cdot mL^{-1}$ and a flow rate of 50 $mL \cdot min^{-1}$ to ensure accuracy during the MS analysis.

In Chapter 4, section 4.2.5.2, the mobile phase was applied as a gradient composed of 0.1% aqueous formic acid solution (component A) and 0.1% formic acid in acetonitrile (component B). The column was equilibrated with A:B (80:20, v/v) as the mobile phase at a flow rate of 0.5 $mL \cdot min^{-1}$. The amount of component A was maintained at this composition for 3 min, then decreased from 80 to 0% over 7 min, kept at 0% for 5 min, restored to the initial composition over 2 min, and finally maintained at this composition for 3 min.

7.9. Computational details

The following computational data are part of the theoretical studies performed in Chapters 3 and 5, which have been done in collaboration with Prof. A. Monari and Dr. A. Francés-Monerris from University of Lorraine (France).

In Chapter 3, all geometry optimizations were performed at the Density Functional Theory (DFT) level using ωB97-XD as exchange correlation functional and the 6-31G(d) basis set. Solvation (ethanol and hexane) has been taken into account implicitly *via* the continuum polarizable method (PCM) as implemented in the Gaussian 09 software using the default parameters. Excited-state energies and equilibrium geometries have been obtained using the Time-Dependent DFT (TD-DFT) method making use of the Tamm-Dancoff Approximation (TDA) in order to avoid triplet instability problems. The singlet and triplet electronic densities have been analyzed in terms of Natural Transition Orbitals (NTOs) making use of the NANCY_EX code.

In Chapter 5, TD-DFT and CASPT2 methods are used. For that reason, it is important to clarify the difference between both of them. CASPT2 (complete-active-space second-order perturbation theory) is an electronic structure method based on the resolution of the time-independent Schrödinger equation for chemical systems in which all possible excitations are computed within a limited number of orbitals (denoted as active space), and the energies are further refined by means of perturbation theory. For this reason, this method is classified as multiconfigurational and is especially suited for the calculation of excited states and degeneracies between electronic states. In contrast, an alternative approach is to quantify the electron density of the system and use it as a descriptor of its electronic structure, instead of solving the Schrödinger equation. This is the principle of the density functional theory (DFT). While this method is much faster than CASPT2, a drawback is the abscence of a universal functional. As a consequence, many approximate functionals (such as ωB97-XD or B3LYP) have been designed to treat specific chemical families or properties, and the use of one or another requires knowledge and adequate validation. Whereas this method only describes the ground state of molecules, the time-dependent extension of the method (TD-DFT) allows the determination of excited states by computing all single excitations from the ground state determinant. Both methods should be considered as complementary. Both allow the determination of the electronic structure of a system and its properties, for example, molecular orbitals, energies, oscillator strengths, dipolar moments, energy gradients, or vibrational modes, although at different levels of accuracies and computational costs. It is therefore the researcher who has to decide their use and interpret the data considering the nature and size of the chemical system and scientific goals of the study.

In this chapter, geometry optimizations on a π-stacked ForC-Thy model system were conducted using the density functional theory (DFT) method for the ground state (S_0) and its time-dependent extension (TD-DFT) for the excited states (S_1 and T_1), making use of the dispersion-corrected hybrid DFT/ωB97-XD functional and the Pople 6-31+G** basis set, as implemented in the Gaussian 09 program. The Tamm-Dancoff approximation was used for all TD-DFT computations. Note that all the calculations have been performed in gas-phase. As a general comment, while the performance of the ωB97-XD exchange-correlation functional has been benchmarked against *ab initio* CASPT2 computations in our previous work, the role of dispersion is crucial since we are dealing with stacked dimers for which geometries obtained by non-dispersion corrected functionals are largely inaccurate. This can be seen as a supplementary argument in favor of the use of the ωB97-XD functional that natively includes dispersion corrections. Finally, no conformational study has been performed since the dimer has been built in such a way to reproduce the orientation of the two chromophores in a B-DNA disposition.

Energies were recomputed on top of the optimized geometries by means of the multiconfigurational complete-active-space self-consistent field/complete-active-space second-order perturbation theory (CASSCF/CASPT2) method and the ANO-S-VDZP as implemented in the OpenMolcas software. The CASSCF wave functions were built distributing 14 electrons into 13 molecular orbitals [hereafter, CAS(14,13)]. The active space is composed by the three most important π and π* orbitals localized over each molecule, *i.e.* six p-like molecular orbitals of ForC and 6 of Thy, and the lone pair on the oxygen of the aldehyde group of ForC. This extension of the widely used CAS(12,12) for DNA nucleobase dimers plus the mentioned lone pair, to allow n,π* transitions, is chemically intuitive and has

been proved as accurate in the ForU-Thy system. Twelve singlet states and twelve triplet states were computed in the state-average (SA)-CASSCF procedures.

The necessary electron dynamic correlation has been computed at the CASPT2 level using the CAS(14,13) wave functions as a reference. The original zeroth-order Hamiltonian has been used throughout (IPEA=0.0 au), whereas an imaginary level shift of 0.2 au has been used to avoid the presence of weakly intruder states.

Chapter 8:

General conclusions

In this Doctoral Thesis, three classes of photoremovable protecting groups (PPG) have been studied and employed for different biological applications. The first two PPGs correspond to sunscreen based photocages and allow the simultaneous photorelease of photosensitive compounds along with solar filters, whereas the third PPG has been used for the insertion of 5-formyl pyrimidine derivatives into oligodeoxynucleotides (ODN). The conclusions of each chapter can be summarized as follows:

1) In Chapter 3, the photophysics of two prodrug/profilter systems formed by linking the avobenzone (AB) solar filter to two different nonsteroidal anti-inflammatory drugs (NSAIDs) has been thoroughly assessed and compared with that of their basic constituents by means of experimental and theoretical approaches. From these results it has been concluded that:

➤ *The relative energy of the AB triplet manifold, ^{3}AB(K)*, with respect to its caged compound is of utmost importance. In this regard, ^{3}AB(K)* has to possess the lowest energy, otherwise it would be deactivated through triplet-triplet energy transfer, resulting in the inactivation of the photouncaging process.*

2) In Chapter 4, a new class of photoremovable carbonyl protecting group has been designed based on the oxybenzone (OB) solar filter. Moreover, additional information has been gained from the synthesis and study of different OB-systems, which also allows extending the scope of this PPG to other ketone derivatives. In this sense:

➤ *The photophysical and photochemical properties of two model systems, formed by caging the benzophenone and the 4-carboxybenzophenone, have been analyzed. Based on that information, the photorelease mechanism has been proposed to occur*

through a first 1,5-hydrogen abstraction leading to a cyclic intermediate, this is followed by photoionization and subsequent incorporation of oxygen and water.

➢*This novel PPG has been applied for the release of the NSAID ketoprofen and two model ketones, namely acetophenone and α-tetralone.*

3) In Chapter 5, the photophysical and photochemical properties of two oxidatively generated DNA damages, 5-formyluracil (ForU) and 5-formylcytosine (ForC), have been studied by means of experimental and theoretical approaches. These studies have revealed that:

➢*Both bases are able to populate their triplet excited state, although with different efficiencies and by different mechanisms. In this context, ForU happens to be much more efficient, with a characteristic time for the intersystem crossing (ISC) that is much shorter than that of ForC.*

➢*The triplet-triplet energy transfer (TTET) from ForU to Thy dimer models (Thy-Thy) is more favored than that from ForC. In this sense, higher cyclobutane pyrimidine dimers (CPD) yield and quenching rate constants have been observed with ForU than with ForC.*

4) In Chapter 6, a new photochemical approach for the synthesis of oligodeoxynucleotides (ODN) containing ForU has been designed, which represents an important achievement for the study of the photosensitizing properties of ForU within the DNA environment. This new synthetic approach offers two advantages: (*i*) Protection of the carbonyl group towards standard phosphoramidite conditions during its incorporation into ODN and (*ii*)

selective removal of the PPG to afford the desired ODN containing ForU by using light instead of an oxidative agent. The obtained results show that:

➢*The synthesis of the oligodeoxynucleotide containing ForU is achievable by the new proposed strategy.*

Chapter 9:

Summary/Resumen/Resum

Summary

The solar spectrum is composed of a wide range of electromagnetic radiations which have different impacts on life on earth. Among them, those belonging to the ultraviolet region are of utmost importance when we refer to photobiology, since they can interact with biomolecules through both direct and photosensitized processes. As a result, these biomolecules can undergo modifications that do not always have beneficial effects. In this context, photoinduced DNA damage is of great relevance as it is closely related to the increasing incidence of skin cancer. Therefore, it is necessary both to investigate the mechanisms involved in these processes and to develop new strategies to avoid them. In this Thesis these issues have been addressed through the development and use of photolabile protecting groups (PPG).

The first part of this Thesis involves the development of new PPG based on solar filters. Once released, these PPG offer the advantage of acting as ultraviolet shields. In this context, Chapter 3 looks into the photophysical and photochemical properties of those systems formed by avobenzone as PPG of carboxylic acids, more specifically ketoprofen (KP) and naproxen (NPX). In this study, the influence on the photorelease process of the relative energetic location of the avobenzone triplet manifold in its diketo form, ^{3}AB(K)*, with respect to that of its caged compound, is duly analyzed by means of molecular modeling and spectroscopic techniques. In this sense, it has been observed that ^{3}AB(K)* has to be the lowest in energy in the system in order to prevent its deactivation through a triplet-triplet energy transfer (TTET) towards the carboxylate moiety resulting in the inactivation of the photouncaging process. Following this same line of work, a new PPG capable of releasing oxybenzone (OB) solar filter along with carbonyl compounds has been developed in Chapter 4. Firstly, mechanistic studies have been carried out using two model systems formed by linking the OB filter to benzophenone

(OB-BP) and to 4-carboxybenzophenone (OB-CBP). From these studies, the formation of a cyclic intermediate has been observed. Moreover, the release of both components has been proposed to occur after photoionization and subsequent incorporation of water and oxygen. Secondly, the use of OB as PPG has been extended to other carbonyl compounds such as KP, acetophenone (AP) and α-tetralone (TL).

The second part of this Thesis focuses on the "Trojan Horse" concept, which establishes that certain DNA lesions can act as endogenous photosensitizers, thus generating new lesions in their neighborhood. In this context, in Chapter 5 the photosensitizing properties of two oxidatively generated DNA damages, namely 5-formyluracil (ForU) and 5-formylcytosine (ForC), have been studied by means of experimental and theoretical approaches. Here, special emphasis has been placed on unraveling their capacity to photoinduce the formation of cyclobutane pyrimidine dimers (CPD). These studies have shown that both DNA damages are capable of populating their triplet states, although through different mechanisms and with different efficiencies. In this sense, ForU has turned out to be the most efficient with a characteristic time for the ISC that is half that of ForC. Regarding the formation of CPD, the results show a triplet-triplet energy transfer to thymine dimer models more favored from ForU than from ForC. In this regard, a higher quenching rate constant and a higher CPD production rate have been observed for ForU. Finally, in Chapter 6 a new synthetic alternative for the incorporation of ForU into oligodeoxynucleotides (ODN) has been developed. Due to the instability of the aldehyde group, this synthesis is generally carried out by incorporating a precursor which is subsequently converted into ForU by the action of an oxidative agent. On the contrary, in the new approach, the aldehyde is protected with a PPG, so that once inserted into the ODN, the aldehyde is selectively released through the

use of light. These results show the viability of this new alternative, having achieved both the synthesis of the oligodeoxynucleotide containing the protected ForU and its subsequent photodeprotection. This work entails a step forward in the study of the photosensitizing properties of ForU, offering a new tool for their evaluation within the DNA environment.

Resumen

El espectro de la luz solar está compuesto por una amplia gama de radiaciones electromagnéticas las cuales tienen diferentes impactos sobre la vida en la tierra. Entre ellas, las pertenecientes a la región ultravioleta toman un papel principal cuando nos referimos a la fotobiología, ya que pueden interactuar con las biomoléculas por medio de procesos tanto directos como fotosensibilizados. Como resultado, estas biomoléculas pueden sufrir modificaciones que no siempre tienen efectos beneficiosos. En este contexto, los daños fotoinducidos al ADN son de gran relevancia ya que están estrechamente relacionados con la creciente incidencia de cáncer de piel. Por ello, es necesario investigar tanto los mecanismos involucrados en dichos procesos como el desarrollo de nuevas estrategias para combatirlos. En la presente tesis se da respuesta a estas necesidades mediante el desarrollo y empleo de grupos protectores fotolábiles (PPG).

En una primera parte se avanza en el desarrollo de nuevos PPG basados en filtros solares. Estos ofrecen la ventaja de actuar, una vez liberados, como un escudo protector frente a la radiación ultravioleta. En este contexto, en el Capítulo 3 se profundiza en las propiedades fotofísicas y fotoquímicas de los sistemas formados por la avobenzona como PPG de ácidos carboxílicos, más concretamente del ketoprofeno (KP) y del naproxeno (NPX). En este estudio se analiza por medio de modelado molecular y técnicas

espectroscópicas la influencia que tiene la energía relativa del triplete de la avobenzona en su forma dicetónica, ^{3}AB(K)*, respecto a la de los compuestos protegidos en el proceso de liberación. En este sentido se ha observado que para que la desprotección tenga lugar de forma eficiente el ^{3}AB(K)* tiene que ser el más bajo en energía del sistema, ya que de lo contrario éste se desactivaría mediante transferencia de energía triplete-triplete (TTET). Siguiendo en esta misma línea de trabajo, en el Capítulo 4 se ha desarrollado un nuevo PPG capaz de liberar el filtro solar oxibenzona (OB) junto con compuestos carbonílicos. En primer lugar, se han realizado estudios mecanísticos empleándose para ello los sistemas modelo formados por la unión de la OB a la benzofenona (OB-BP) y a la 4-carboxibenzofenona (OB-CBP). De estos estudios se ha observado la formación de un intermedio ciclado desde el cual tiene lugar la liberación de ambos componentes tras fotoionización y posterior incorporación de agua y oxígeno. En segundo lugar, se ha extendido el uso de la OB como PPG a otros compuestos carbonílicos como son el KP, la acetofenona (AP) y la α-tetralona (TL).

En una segunda parte, el foco de atención se ha puesto en el concepto de "Caballo de Troya", el cual establece que ciertas lesiones del ADN pueden actuar a su vez como fotosensibilizadores endógenos generando así nuevas lesiones en su entorno. En este contexto, en el Capítulo 5 se han estudiado, mediante métodos tanto experimentales como teóricos, las propiedades fotosensibilizantes de dos de los daños oxidativos del ADN, el 5-formiluracilo (ForU) y la 5-formilcitosina (ForC), poniendo especial énfasis en la capacidad de estos para poblar sus estados tripletes, así como de inducir la formación fotosensibilizada de dímeros ciclobutánicos de pirimidina (CPD). En estos estudios se ha demostrado que ambos daños del ADN son capaces de poblar sus estados tripletes, aunque por medio de diferentes mecanismos y con diferentes eficiencias. En este sentido el ForU ha resultado ser el más eficiente

con una constante de tiempo de cruce intersistema (CIS) correspondiente a la mitad de la calculada para la ForC. Respecto a la formación de CPD, los resultados muestran que la transferencia de energía triplete-triplete a diadas timina-timina está también más favorecida en el caso del ForU, observándose para éste una mayor constante de desactivación y una mayor velocidad de formación de CPD. Por último, en el Capítulo 6 se ha desarrollado una nueva alternativa sintética para la incorporación del ForU en oligonucleótidos. Debido a la inestabilidad del grupo aldehído, esta síntesis se lleva a cabo generalmente mediante la incorporación de un precursor el cual es posteriormente convertido en el ForU mediante la acción de un agente oxidante. Por el contrario, en la nueva alternativa planteada el aldehído es protegido con un PPG, de manera que una vez insertado en el ODN, el aldehído es liberado de forma selectiva mediante el empleo de luz. Los resultados presentados en este último Capítulo muestran la viabilidad de dicho planteamiento, habiéndose logrado tanto la síntesis del oligonucleótido con el ForU protegido como la posterior fotodesprotección del mismo. Este trabajo supone un avance en el estudio de las propiedades fotosensibilizantes del ForU ofreciendo una nueva herramienta para la evaluación de las mismas en un entorno más cercano al del ADN.

Resum

L'espectre de la llum solar està compost per una àmplia gamma de radiacions electromagnètiques les quals tenen diferents impactes sobre la vida en la terra. Entre elles, les pertanyents a la regió ultraviolada prenen un paper principal quan ens referim a la fotobiologia, ja que poden interactuar amb les biomolècules per mitjà de processos tant directes com fotosensibilitzats. Com a resultat, aquestes biomolècules poden patir modificacions que no sempre

tenen efectes beneficiosos. En este context, els danys fotoinduits a l'ADN són de gran rellevància ja que estan estretament relacionats amb la creixent incidència de càncer de pell. Per això, és necessari tant d'investigar els mecanismes involucrats en els processos com el desenvolupament de noves estratègies per a combatre'ls. En la present tesi es dóna resposta a aquestes necessitats per mitjà del desenvolupament i ús de grups protectors fotolàbils (PPG).

En una primera part s'avança en el desenvolupament de nous PPG basats en filtres solars. Estos ofereixen l'avantatge d'actuar, una vegada alliberats, com un escut protector enfront de la radiació ultraviolada. En este context, en el capítol 3 s'aprofundeix en les propietats fotofísiques i fotoquímiques dels sistemes formats per l'avobenzona com PPG d'àcids carboxílics, més concretament del ketoprofé (KP) i del naproxé (NPX). En este estudi s'analitza per mitjà de modelatge molecular i tècniques espectroscòpiques la influència que té en el procés d'alliberament l'energia relativa del triplet de l'avobenzona en la seua forma dicetònica, ^{3}AB(K)*, respecte a la dels compostos protegits. En este sentit s'ha observat que per a què la desprotecció tinga lloc de forma eficient el ^{3}AB(K)* ha de ser el d'energia més baixa en el sistema, ja que en cas contrari este es desactivaria per mitjà de transferència d'energia triplet-triplet (TTET). En esta mateixa línia de treball, en el capítol 4 s'ha desenvolupat un nou PPG capaç d'alliberar el filtre solar oxibenzona (OB) junt amb compostos carbonílics. En primer lloc, s'han realitzat estudis mecanístics emprant els sistemes model formats per la unió de l'OB a la benzofenona (OB-BP) i a la 4-carboxibenzofenona (OB-CBP). D'estos estudis s'ha observat la formació d'un intermedi ciclat des del qual té lloc l'alliberament dels dos components després de fotoionització i posterior incorporació d'aigua i oxigen. En segon lloc, s'ha estés l'ús de l'OB

com PPG a altres compostos carbonílics com són el KP, l'acetofenona (AP) i la α-tetralona (TL).

En una segona part, el focus d'atenció s'ha posat en el concepte de "Cavall de Troia", el qual estableix que certes lesions de l'ADN poden actuar al seu torn com fotosensibilitzadors endògens generant així noves lesions en el seu entorn. En este context, en el capítol 5 s'han estudiat, per mitjà de mètodes tant experimentals com teòrics, les propietats fotosensibilitzants de dos dels danys oxidatius de l'ADN, el 5-formiluracil (ForU) i la 5-formilcitosina (ForC), posant especial èmfasi tant en la capacitat d'estos per a poblar els seus estats triplet, com d'induir la formació fotosensibilitzada de dímers ciclobutànics de pirimidina (CPD). En aquestos estudis s'ha demostrat que ambdós danys de l'ADN són capaços de poblar els seus estats triplets, encara que per mitjà de diferents mecanismes i amb diferents eficiències. En aquest sentit el ForU ha resultat ser el més eficient amb una constant de temps d'encreuament intersistema (ISC) corresponent a la meitat de la calculada per al ForC. Respecte a la formació de CPD, els resultats mostren que la transferència d'energia triplet-triplet a diades timina-timina està també més afavorida en el cas del ForU, observant-se per a aquest una major constant de desactivació i una major velocitat de formació de CPD. Finalment, en el capítol 6 s'ha desenvolupat una nova alternativa sintètica per a la incorporació del ForU en oligonucleòtids. A causa de la inestabilitat del grup aldehid, esta síntesi es duu a terme generalment per mitjà de la incorporació d'un precursor el qual és posteriorment convertit en el ForU per mitjà de l'acció d'un agent oxidant. Al contrari, en la nova alternativa plantejada l'aldehid és protegit amb un PPG, de manera que una vegada inserit en l'oligonucleòtid, l'aldehid és alliberat de forma selectiva per mitjà de l'ús de llum. Els resultats presentats en este últim capítol mostren la viabilitat del plantejament, havent-se aconseguit tant la síntesi de l'oligonucleòtid amb el ForU protegit com la

posterior fotodesprotecció del mateix. Este treball suposa un avanç en l'estudi de les propietats fotosensibilitzants del ForU i ofereix una nova ferramenta per a l'avaluació de les mateixes en un entorn més pròxim al de l'ADN.

Chapter 10:

Scientific contribution

10.1. Contribution to Conferences

❖ M. Lineros-Rosa, M. A. Miranda and V. Lhiaubet-Vallet. "Looking into the Trojan Horse concept. Comparison between the oxidatively generated DNA lesions of thymine and 5-methylcytosine". 2nd ITQ Winter Meeting, Valencia, Spain, 19th December, **2019**. Oral presentation.

❖ M. Lineros-Rosa, M. A. Miranda and V. Lhiaubet-Vallet. "Mechanistic study and application of a new sunscreen-based photocaged system for the photorelease of carbonyl groups". XVI Simposio de Jóvenes Investigadores de la Real Sociedad Española de Química, Valencia, Spain, 4th-7th November, **2019**. Oral presentation.

❖ M. Lineros-Rosa, M. A. Miranda and V. Lhiaubet-Vallet. "Oxidatively generated DNA lesions of thymine and 5-methylcytosine as potential intrinsic photosensitizers". 3rd Workshop on DNA Damage and Repair. Chemistry, Biology, and Medicine, Valencia, Spain, 25th-26th September, **2019**. Oral presentation.

❖ M. Lineros-Rosa, M. A. Miranda and V. Lhiaubet-Vallet. "Design of a new sunscreen-based photocaged system. A mechanistic study based on a model and its application in a ketoprofen-oxybenzone model". 17th Congress of the International Union of Photobiology and 18th Congress of the European Society for Photobiology, Barcelona, Spain, 25th-30th August, **2019**. Oral presentation.

❖ M. Lineros-Rosa, M. A. Miranda and V. Lhiaubet-Vallet. "The development of a new sunscreen-based photocaged system. Its application in a ketoprofen-oxybenzone dyad". 1st ITQ Winter Meeting, Valencia, Spain, 17th December, **2018**. Poster presentation.

❖ M. Lineros-Rosa, M. A. Miranda and V. Lhiaubet-Vallet. "The development of a new sunscreen-based photocaged system. Its application in a ketoprofen-oxybenzone dyad". VIth Jornadas Ibéricas de Fotoquímica, Aveiro, Portugal, 11th-14th September, **2018**. Poster presentation.

❖ M. Lineros-Rosa, M. A. Miranda and V. Lhiaubet-Vallet. "Simultaneous photorelease of photosensitizing drugs and solar filters. Its application in a ketoprofen-oxybenzone dyad". 5th ESP Photobiology School, Bressanone, Italy, 10th-16th June, **2018**. Poster presentation.

10.2. Publications

10.2.1. Related to this Doctoral Thesis

❖ M. Lineros-Rosa, M. A. Miranda and V. Lhiaubet-Vallet. "A Sunscreen-Based Photocage for Carbonyl Groups". *Chem. Eur. J.*, **2020**, 26, 7205–7211.

❖ A. Francés-Monerris, M. Lineros-Rosa, M. A. Miranda, V. Lhiaubet-Vallet and A. Monari. "Photoinduced intersystem crossing in DNA oxidative lesions and epigenetic intermediates". *Chem. Commun*., **2020**, 56, 4404–4407.

❖ M. Lineros-Rosa, A. Francés-Monerris, A. Monari, M. A. Miranda and V. Lhiaubet-Vallet. "Experimental and theoretical studies on thymine photodimerization mediated by oxidatively generated DNA lesions and epigenetic intermediates". *Phys. Chem. Chem. Phys.,* **2020**, 22, 25661–25668.

❖ M. Lineros-Rosa, M. C. Cuquerella, A. Francés-Monerris, A. Monari, M. A. Miranda and V. Lhiaubet-Vallet. "Triplet stabilization for

enhanced drug photorelease from sunscreen-based photocages". *Org. Biomol. Chem*., **2021**, 19, 1752-1759.

10.2.2. Other publications

❖ G. Nardi, M. Lineros-Rosa, F. Palumbo, M. A. Miranda and V. Lhiaubet-Vallet. "Spectroscopic characterization of dipicolinic acid and its photoproducts as thymine photosensitizers". *Spectrochim. Acta A Mol. Biomol. Spectrosc*., **2021**, 245, 118898–118906.